

**SoLID (Solenoidal Large Intensity Device)
Updated Preliminary Conceptual Design Report**

The SoLID Collaboration

May 22, 2017

1 Contents

2	1 Executive Summary of the Responses to the Recommendations from the JLab Director's Review Committee	1
3		
4	1.1 Overview	1
5	1.2 Physics Program	2
6	1.2.1 SIDIS Production of Charged Pions	2
7	1.2.2 PVDIS	2
8	1.2.3 J/ψ	3
9	1.3 Plan for Possible Expansion in Physics Reach	4
10	1.3.1 GPD	4
11	1.3.2 SIDIS Production of Charged Kaons	5
12	1.4 Experimental Design, Simulation and Feasibility	5
13	1.4.1 Solenoidal Magnet	5
14	1.4.2 Acceptance, Efficiency and Systematics	6
15	1.4.3 Rates and Data Acquisition	7
16	1.5 Summary	8
17	2 Introduction and Overview of SoLID Experimental Programs	9
18	2.1 SoLID Project Introduction/Overview	9
19	2.1.1 Base Equipment Description	9
20	2.1.2 Dependencies to Base Equipment	9
21	2.1.3 Experiment-specific Dependencies	10
22	2.1.4 Research Program	10
23	2.2 SIDIS Program	11
24	2.2.1 Introduction	11
25	2.2.2 Transverse Structure and Semi-Inclusive Deep Inelastic Scattering	13
26	2.2.3 The Phenomenology TSSAs and TMDs	15
27	2.2.4 Overview of SIDIS program	16
28	2.2.5 Beam Time and Projections	17
29	2.2.6 Comparisons with SBS and CLAS12 SIDIS programs	19
30	2.3 PVDIS Program	26
31	2.3.1 Motivation for PVDIS	26
32	2.3.2 Review of the Theory	26
33	2.3.3 Charge Symmetry Violation	28
34	2.3.4 Higher Twist	30
35	2.3.5 Data Sample and analysis	31
36	2.3.6 Beam Time Request	32
37	2.4 J/ψ Program	34
38	2.4.1 Motivation	34
39	2.4.2 Program Overview	38
40	2.4.3 Beam Time and Projection	39
41	2.5 Possible Expansion in Physics Reach	41
42	2.5.1 GPD Program	41
43	2.5.2 SIDIS Production of Charged Kaons	42

44	3	Technical Requirements and Experimental Setup	44
45	3.1	Summary of Requirements	44
46	3.2	SIDIS- ³ He Experiments	49
47	3.3	SIDIS-proton Experiment	52
48	3.4	PVDIS Experiment	54
49	3.5	J/ψ Experiment	56
50	4	Magnet	60
51	4.1	Requirements	60
52	4.2	SoLID magnet	60
53	4.3	Planned Modifications	61
54	4.4	Current Status and Planned Test	63
55	5	Targets	66
56	5.1	Polarized ³ He Target	66
57	5.2	Transversely Polarized Proton Target	66
58	5.3	Cryogenic Target for PVDIS	69
59	6	Baffles	72
60	7	GEM Tracker	78
61	7.1	Design	78
62	7.2	GEM tracker R&D	82
63	7.2.1	GEM chamber R&D program in UVa	82
64	7.2.2	GEM chamber R&D programs in China	85
65	7.3	Collaboration Status and Construction Outlook	88
66	8	Light Gas Čerenkov	90
67	8.1	Design	90
68	8.1.1	Tank and Čerenkov Gas	90
69	8.1.2	Mirrors	90
70	8.1.3	PMTs	91
71	8.1.4	Magnetic Shielding and Winston Cones	92
72	8.2	Tank Support	93
73	8.3	Simulations	94
74	8.3.1	Collection Efficiencies	94
75	8.3.2	Background Rates	94
76	8.3.3	Pion Rejection	94
77	9	Heavy Gas Čerenkov	99
78	9.1	Optical System Design	99
79	9.2	Simulation	99
80	9.2.1	Photoelectron Yield	99
81	9.2.2	Pion Detection Efficiency and Kaon Rejection Factor	100
82	9.3	Performance of the PMTs in Magnetic Field	101
83	9.4	Engineering Design	102

84	10 Electromagnetic Calorimeter	105
85	10.1 Overview	105
86	10.2 Shower Detector Design Considerations	107
87	10.2.1 Total Length of the Calorimeter	107
88	10.2.2 Sampling Ratio of the Shower Detector	108
89	10.2.3 Lateral Size of the Calorimeter Module	109
90	10.3 Preshower Detector	110
91	10.4 Layout and Support	112
92	10.5 Light Readout	112
93	10.6 Radiation Effects	114
94	10.7 Performance	114
95	10.7.1 Intrinsic electron-pion separation	114
96	10.7.2 PID performance under realistic background simulation	117
97	10.7.3 Trigger capability	119
98	10.7.4 Shower Position Measurement	122
99	10.7.5 Supplemental Information: PID Selection Cuts	122
100	10.8 Scintillator Pad Detector for SIDIS Experiments	124
101	10.9 EC Collaboration Status and Construction Outlook	125
102	11 MRPC	128
103	11.1 Overview	128
104	11.2 Structure of the MRPC Prototype	128
105	11.3 Cosmic Ray Test	129
106	11.4 Beam Test at Hall A	129
107	11.5 Beam Test Results	131
108	11.5.1 HV Scan	131
109	11.5.2 Rate Scan	132
110	11.6 Conclusions	132
111	11.7 R&D Plan for Better Time Resolution	132
112	12 Simulation and Reconstruction	139
113	12.1 End-to-End Software Framework	139
114	12.2 Simulation	140
115	12.2.1 Simulation Software	140
116	12.2.2 Simulation Status	142
117	12.2.3 Physics Event Generators	143
118	12.2.4 GEM Digitization	144
119	12.3 Reconstruction	147
120	12.3.1 Tracking	147
121	12.3.2 Additional Reconstruction Algorithms	149
122	13 Integration and Expected Performance	150
123	13.1 Overview	150
124	13.2 SIDIS Program	150
125	13.3 PVDIS Program	154
126	13.3.1 Acceptances, efficiencies, and systematic uncertainties for PVDIS	154
127	13.3.2 Kinematics, Resolution and Calibration for PVDIS	156
128	13.4 J/ψ Program	160

129	14 Data Acquisition	163
130	14.1 Introduction and Requirements	163
131	14.1.1 SIDIS Trigger and Rate Estimate	163
132	14.1.2 J/ψ Trigger and Rate Estimate	164
133	14.1.3 PVDIS Trigger and Rate Estimate	164
134	14.2 DAQ Hardware and Trigger	165
135	14.2.1 GEM readout	165
136	14.2.2 SIDIS Configuration	167
137	14.2.3 PVDIS Configuration	170
138	14.3 Event size from FADC	171
139	14.4 Data rates,event size and L3 Farm	171
140	14.5 Hall DAQ installation	172
141	14.5.1 Experiment switch over	172
142	14.6 Managing data rates	172
143	14.7 Summary and Pre R&D plans	173
144	15 Radiation damage estimates and Activation	178
145	15.1 Radiation damage to GEM electronics	178
146	15.2 Power deposited	179
147	15.2.1 Power in 1st baffle (due to Möllers), (Cooling, activation)	180
148	15.2.2 Power in exit hole in magnet (elastics) (Cooling, activation)	180
149	15.2.3 Power in the entrance surface of the magnet (Cooling, activation) (external target configurations)	181
150	15.2.4 Heat load in magnet cryostat	182
152	15.3 Estimates for radiation damage in the Hall	183
153	15.3.1 Radiation damage to electronics in Hall	183
154	15.3.2 Radiation from beam pipe	184
155	15.3.3 Radiation with external targets	185
156	16 Slow Controls	192
157	16.1 General Requirements	192
158	16.2 Frontend GUIs	192
159	16.3 High/Low Voltage Controls	193
160	16.4 DAQ Crate Control	193
161	16.5 Gas Systems Requirements	193
162	16.6 Detector Systems	193
163	17 Electron Beam Polarimetry	194
164	17.1 Compton Polarimetry	194
165	17.2 The Hall A Compton Polarimeter Baseline Upgrade	194
166	17.3 Upgrades Beyond the Baseline	196
167	17.3.1 Laser System and Luminosity	197
168	17.3.2 Alternative Laser System	199
169	17.3.3 Chicane Magnet Modification	201
170	17.3.4 Photon Detection	201
171	17.4 Systematic Uncertainties	202
172	17.4.1 Sources of Correlated Error	202
173	17.4.2 Systematic Errors for the Electron Detector	202

174	17.4.3 Systematic Errors for the Photon Detector	205
175	17.5 Summary of Compton Polarimetry	206
176	17.6 Møller Polarimetry	206
177	17.7 The Hall A Upgrade: “High Field” Iron Foil Targets	207
178	17.7.1 Ferromagnetic Foil Targets	208
179	17.7.2 Simplified Møller Scattering Target Assembly	210
180	18 Supports and Infrastructure	212
181	18.1 Magnet Support	212
182	18.2 Endcap Support Structure and Motion Mechanism	212
183	18.3 Support Structure for Equipment Located Inside Cryostat Bore	212
184	18.4 Power Requirements	212
185	19 Installation	214
186	19.1 Experimental Layout	214
187	19.2 Magnet Moving and Placement	214
188	19.3 Helium Dewar Support and Upper Access Platform	218
189	19.4 Endcap Forward Angle Detector Package Installation Structure	218
190	19.5 Large Angle Detector and Baffle Installation Mechanism	218
191	19.6 Light Gas Cherenkov Installation Structure	219
192	20 Project Status and Proposed Management Organization	220
193	20.1 Collaboration and Organization	220
194	20.2 Cost estimation	222
195	Bibliography	223
196	Appendices	239
197	Appendix A Summary of Recommendations from the 2015 SoLID Director’s Review and	
198	the Responses (Where Are They Addressed in the Main Text)	239
199	A.1 On the physics relevance and risks	239
200	A.2 On the viability of approach and the experimental technique	240
201	A.3 On the understanding, completeness, and credibility of the resources needed for the	
202	SoLID project.	241
203	Appendix B Summary of Subsystems	243
204	B.1 Magnet	243
205	B.2 GEM	243
206	B.3 Light Gas Čerenkov	244
207	B.4 Heavy Gas Čerenkov	244
208	B.5 Electromagnetic Calorimeter and Scintillator-Pad Detector	244
209	B.6 MRPC	245
210	B.7 DAQ	245
211	Appendix C Software Development Effort Estimate	247

1 Executive Summary of the Responses to the Recommendations from the JLab Director's Review Committee

1.1 Overview

To exploit the full potential of the JLab 12 GeV energy upgrade, a large acceptance high luminosity device, SoLID (Solenoidal Large Intensity Detector), was proposed for a rich vibrant set of experiments. Five SoLID experiments, one PVDIS, three SIDS and one J/ψ production, were approved with high ratings in 2010–2012 by the JLab Program Advisory Committee. After years of work by the collaboration, a preliminary conceptual design report (pCDR) was submitted to the JLab Director in 2014. A Jefferson Lab Director's Review for SoLID was held in February 2015. The review committee felt that SoLID was in a good state to move forward, but also identified a number of areas where additional work would be needed. Thirty-six recommendations were made in total (summarized in Appendix A of this document), with some aiming at longer term efforts of the type requisite to any project of this magnitude, and others more specifically relevant for the nearer term. After discussions with the Physics Division and Jefferson Lab management, the collaboration aimed as a first step to address those recommendations that were necessary to proceed with a Science Review as required for a DOE Critical Decision CD-0. While continuing to also address the longer term recommendations to the extent possible, the collaboration has completed this first step.

This chapter summarizes the preparatory work to reach this milestone. It includes the experiment specific recommendations related to the three core measurements (SIDIS, PVDIS and J/ψ production), as well as the ones related to the general performance of the instrumentation to reach the scientific goals. For PVDIS, the viability of the calibration procedure to determine Q^2 was studied including realistic misalignments. The design of the baffles was re-examined, including the choice of materials. For SIDIS, careful studies were performed to show the impact of SoLID compared to the world data, including comparisons to Jefferson Lab 12 GeV era projected data from the CLAS12 and SBS programs. Examples of physics reach, such as the transversity/tensor charge, were simulated and are presented. For J/ψ , bin migration effects and the trigger rate were simulated. Studies of promising additional science reach facilitated by SoLID, such as Generalized Parton Distributions and kaon identification, were also recommended and considered.

Realistic simulations, as well as tracking and data acquisition development, have shown that the performance of the instrumentation will allow realization of the SoLID scientific goals with the proposed instrumentation. The acceptances, efficiencies and systematic uncertainties were simulated in detail for each of the three core measurements. Meticulous magnet field modeling confirmed that the forces are tolerable and the fringe field at the polarized target location can be controlled to the desired level. The effects of possible radiation damage were carefully evaluated. Significant progress has also been made in the development of a full analysis simulation and software framework.

Beyond the above, which were deemed critical to the near term path to a Science Review, work is continuing on the many recommended fronts. The coils and cryostat of the CLEO-II magnet have arrived at JLab and the exterior steel is being shipped. Other activities include the development of GEM foil production in China and assessment of the risk factor, communication with expert groups in calorimeter design and R&D, and stability testing of the conductivity of MRPC glass. An initial study of the slow control system has been performed. A pre-R&D plan was developed with input from Jefferson Lab management, and has been submitted to the DOE. Pre-R&D activities are continuing with some detector pre-R&D activities supported by the international collaboration (China and Canada).

This work has been summarized in the next few subsections and/or merged into the original pCDR along with a map in Appendix A pointing to where the changes are in the document to

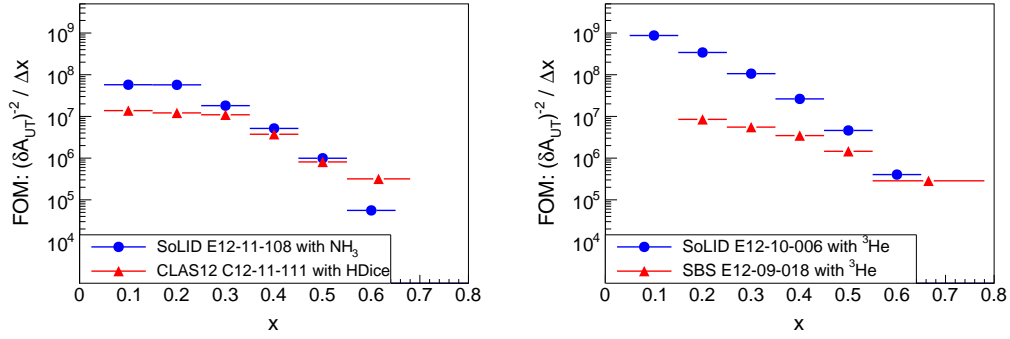


Figure 1: Comparisons of the FOM, defined as the sum of the inverse square of the statistical uncertainties of the single spin asymmetry (roughly proportional to statistics). The SoLID SIDIS experiment with the NH_3 target is compared with CLAS12 experiment in the left panel. The SoLID SIDIS experiments with the ^3He target are compared with the SBS experiment in the right panel. In both comparisons, the kinematic cuts of $W > 2.3 \text{ GeV}$ and $0.3 < z < 0.7$ are applied.

258 address each recommendation.

259 As a whole, the collaboration considers the progress on SoLID to be adequately substantive and
 260 positive to enable the next phase to begin, in particular a DOE Science Review. We therefore submit
 261 this revised pCDR as a first formal response to the 2015 Director’s Review, and look forward to the
 262 committee’s evaluation and subsequent guidance from the laboratory.

263 1.2 Physics Program

264 1.2.1 SIDIS Production of Charged Pions

265 The SoLID SIDIS program includes three approved experiments, using transversely and longitudi-
 266 nally polarized ^3He targets and a transversely polarized proton (NH_3) target. With the combination
 267 of high luminosities and large acceptance including a full azimuthal coverage, the SoLID SIDIS
 268 experiments will allow measurements in 4-dimensional bins with high statistics and well controlled
 269 systematics. Compared to CLAS12 and SBS SIDIS programs, SoLID has better FOM, correspond-
 270 ing to higher statistics, in the region $x = (0.05, 0.55)$, as shown in Figure 1. To demonstrate the
 271 physics impact of SoLID SIDIS program, we perform the transversity extractions based on the
 272 works of [5, 6] with simulated data of CLAS12, SBS and SoLID, and then compare them in Fig-
 273 ure 2. SoLID can improve the error of the transversity for u (d) quark by a factor of 3 (7) more
 274 than CLAS12, and by a factor of 5 (10) more than SBS. The tensor charge determination will have
 275 similar improvements which together with nEDM measurements will provide constraints on quark
 276 EDMs and thus new physics models. It is clear that the projected high precision results from SoLID
 277 will provide powerful tests of Lattice QCD, and much more quantitative information about TMDs
 278 and quark OAMs inside the nucleon.

279 1.2.2 PVDIS

280 The unique feature of SoLID, combining high luminosity and large acceptance, makes it possible to
 281 reach the high precision needed to have a high impact by using PVDIS to probe physics beyond the
 282 Standard Model. A measurement of PVDIS in deuterium will determine the fundamental coupling

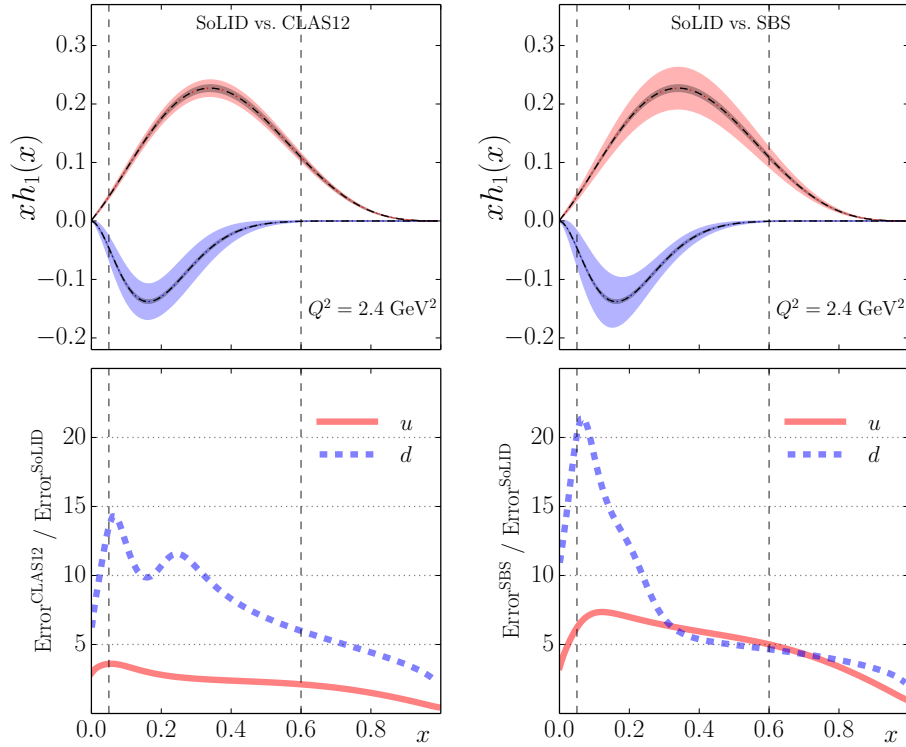


Figure 2: Comparisons of the impact on transversity extractions, as the extension of published works [5, 6]. The left column shows the comparison between SoLID and CLAS12, and the right column shows the comparison between SoLID and SBS. In the upper panels, the light shade bands show the uncertainties after SBS/CLAS12, and the dark shade bands show the uncertainties after SoLID. Curves in the lower panels show their ratios. Both u and d quark results are presented. All results are plotted at a typical JLab12 scale $Q^2 = 2.4 \text{ GeV}^2$.

283 constant $2C_{2u} - C_{2d}$ that is inaccessible with other means. PVDIS measurements can also access a
 284 number of topics in QCD physics, including searching for charge symmetry violation in the parton
 285 distribution functions, determining the d/u ratio in the proton without nuclear effects, and a clean
 286 extraction of higher-twist effects due to quark-quark correlations. The 6-GeV PVDIS collabora-
 287 tion [1] has recently published in Nature a new experimental result $2C_{2u} - C_{2d} = -0.145 \pm 0.068$,
 288 the first measurement sufficiently sensitive to show that the C_{2q} are non-zero as predicted by the
 289 SM. One way to quantify the reach of various experiments is to quote mass limits suitable for com-
 290 posite models [2], where the couplings are on the order of $4\pi/\Lambda^2$ where Λ is the compositeness
 291 mass scale. Such limits for the 6-GeV PVDIS collaboration and the SoLID PVDIS experiment [3]
 292 are shown in Figure 3. The sensitivity to be reached by SoLID is at the same level as LHC's for
 293 non-parity-violating couplings.

294 1.2.3 J/ψ

295 The impressive luminosity offered by SoLID combined with large acceptance detection opens new
 296 opportunities for the measurement of rare processes with unprecedented precision impacting di-
 297 rectly our understanding of QCD. In particular the measurement of the elastic production of J/ψ
 298 on the proton near threshold could provide the unique and much needed information on the pure

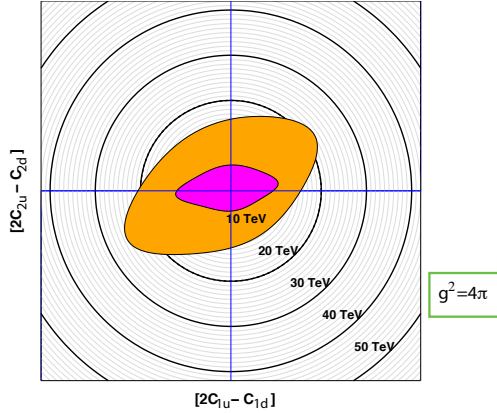


Figure 3: Projected mass limits for composite models. Purple region is excluded by published data and the orange region is the projected reach with SoLID and final Qweak result.

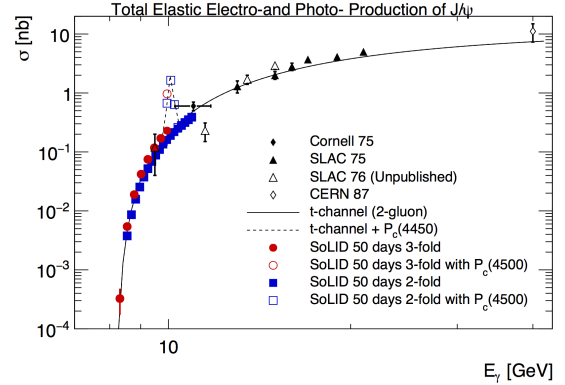


Figure 4: Projected uncertainties of total elastic J/ψ electro and photo-production cross sections based on a 2-gluon exchange model including a projection of the LHCb pentaquark production assuming a coupling of 5%.

299 gluonic component of the QCD interaction, as well as the verification of the nature of the recently
 300 observed charmed “pentaquark” states at the LHCb [151]. A measurement very close to the thresh-
 301 old (Figure 4) where the cross section drops rapidly can provide important information on the trace
 302 anomaly, a key component responsible for the mass of the nucleon. Hadrons, the emergent phe-
 303 nomena of QCD, are in the realm of the strong interaction regime where much of its dynamics
 304 remains to be understood. While significant progress has been achieved in exploring QCD in its
 305 asymptotically free regime, the theory in the strong coupling regime is hardly tractable without nu-
 306 merical techniques. For example, an impressive success was achieved with the recent lattice QCD
 307 determination of the low-lying levels of the baryon spectrum [4] but there is a long road ahead to
 308 fully grasp the implications of QCD in this regime. One aspect is the decomposition of the mass
 309 of the nucleon in terms of its constituents quarks and gluons. The threshold region of electro- and
 310 photo-production of J/ψ could very well shed light on the anomaly responsible for a large fraction
 311 of the proton mass.

312 1.3 Plan for Possible Expansion in Physics Reach

313 1.3.1 GPD

314 The unique features of SoLID’s large acceptance and high luminosity make it an attractive device
 315 for the experimental study of GPDs. A number of groups have been working on developing a
 316 SoLID-GPD program. There are several GPD experiments in different stages of study/approval. A
 317 run-group proposal of Time-like Compton Scattering (TCS) from an unpolarized LH2 target has
 318 been approved to test the universality of GPD, explore the underlying principles of factorization
 319 and quantify the importance of higher twist effects. Double Deeply Virtual Compton Scattering
 320 (DDVCS) in the di-lepton channel on an unpolarized LH2 target was reviewed by the JLab PAC as
 321 a Letter-Of-Intent and the collaboration was encouraged to develop it into a two-stage program with
 322 an initial focus to have a first significant DDVCS measurement (over a limited kinematic region)
 323 using the baseline SoLID setup. Measurements of DVCS and Deep Exclusive Meson Production
 324 (DEMP) with the transversely polarized ^3He target are under development and the DEMF run-group
 325 proposal was reviewed by the SoLID Collaboration and received a strong encouragement. These

326 measurements, together with the planned CLAS12 and Hall A/C GPD experiments, will make a
 327 significant contributions in disentangling different GPDs in the JLab 12-GeV kinematic region.

328 1.3.2 SIDIS Production of Charged Kaons

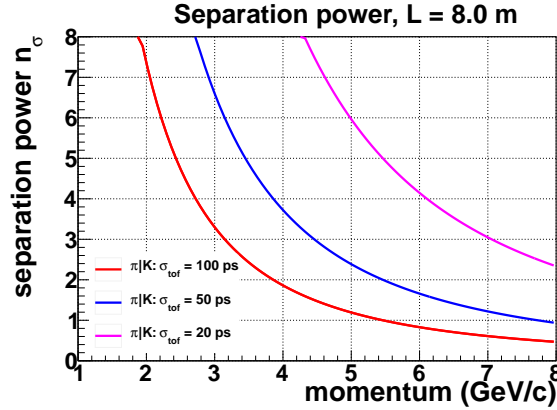


Figure 5: Kaon identification by TOF.

329 We have studied kaon identification for SoLID to potentially extend its physics programs. A full
 330 RICH detector for kaon detection is likely to be too costly to consider. High resolution TOF is a
 331 more practical solution. SoLID needs kaon identification over a momentum range of 1 GeV/c to 7
 332 GeV/c. Given the ~ 8 meter flight distance, a TOF time resolution of 20 ps is required to obtain a 3
 333 sigma separation between pions and kaons as shown in Figure 5. A promising avenue is to improve
 334 the timing of the planned SoLID TOF-MRPC detector. The baseline MRPC is designed to reach 80
 335 ps time resolution in the SoLID high-rate environment. Bench testings of thin-gap MRPC prototype
 336 detectors demonstrated the potential to reach a resolution of sub-20 ps [9, 10]. A planned R&D
 337 effort by a Chinese collaboration (Tsinghua University, USTC and CCNU) on the next generation
 338 MRPC jointly for SoLID, sPHENIX and EIC is being pursued, aiming for 20 ps resolution in a
 339 high-rate environment. The plan is to develop a prototype and readout electronics system next year.
 340 Beam test and finalization of the detector and electronics will be done in the following year.

341 1.4 Experimental Design, Simulation and Feasibility

342 1.4.1 Solenoidal Magnet

343 The CLEO II magnet was removed from the CESR beamline by Cornell University and JLAB
 344 personnel during the 2016 summer down. All ancillary power, cryogenic and control services were
 345 disconnected from the magnet in preparation for iron removal. The iron was removed layer by
 346 layer and stored at Cornell's laydown yard until 2017 when it will be shipped to JLAB. With the
 347 cryostat exposed, the axial transport brackets were installed and the cryostat moved to the transport
 348 frame. The service turret and neck were removed to reduce the height of the cryostat for safe
 349 highway transit. The entire unit was wrapped in marine grade shrink wrap to provide a weather
 350 barrier for the trip to JLAB. Three-axis accelerometers were mounted to the cryostat to monitor
 351 loads during the road trip. All loads remained under allowable thresholds specified in the Oxford
 352 CLEO II Operating Manual. Upon arrival at JLAB in November 2016, the magnet was rolled into

353 the Test Lab for climate controlled storage, as shown in Figure 6. We are making plans for testing
 354 the magnet with a new power supply and in-situ mapping.



Figure 6: CLEO II magnet at JLab.

355 **1.4.2 Acceptance, Efficiency and Systematics**

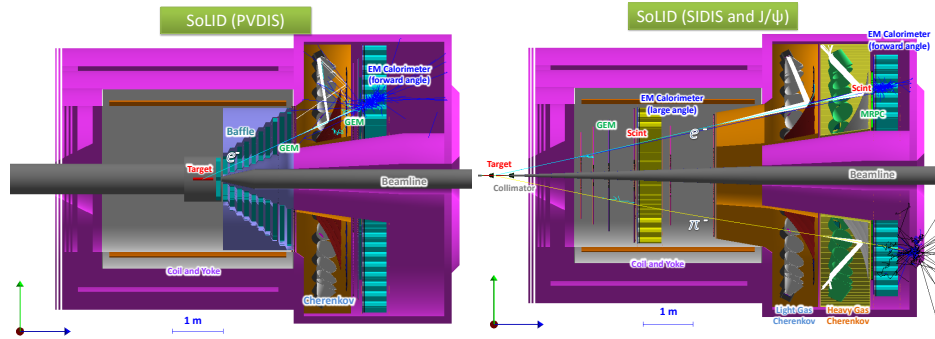


Figure 7: Left: SoLID PVDIS setup. Right: SoLID SIDIS and J/ψ setup.

356 The SoLID setups [8] for the PVDIS and the SIDIS and J/ψ configurations are shown in Figure 7.
 357 Substantial progress has been made in developing a SoLID simulation package with realistic sub-
 358 system responses that includes all elements of the apparatus, EM showers in the electromagnetic
 359 calorimeter, optical processes in the two Cherenkov detectors, energy deposition in the GEMs and
 360 MRPC and their digitizations. A new event generator has been used for the estimation of hadron
 361 background rates. The simulation package allowed detailed simulations of the performance and
 362 feasibility of all core measurements, namely the PVDIS, SIDIS and J/ψ measurements.

Table 1: Average electron detection efficiencies of all SoLID sub-detectors and the total SoLID efficiency.

Detector	EC	Cerenkov	Scintillator pad and MRPC	GEM tracking	Total
average efficiency	95%	95%	98%	90%	80%

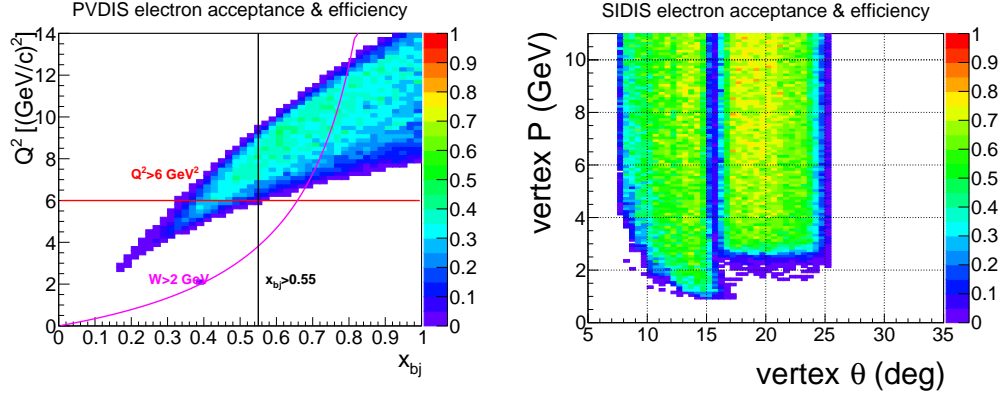


Figure 8: Left panel: electron acceptance and efficiency (except tracking) of SoLID PVDIS with the 40 cm LD2 target and baffle. Curves show bounds of the kinematic range with $Q^2 > 6 \text{ GeV}^2$, $W > 2 \text{ GeV}$, and $x_{bj} > 0.55$. Right panel: electron acceptance and efficiency (except tracking) of SoLID SIDIS with the 40 cm ^3He target and two target window collimators. The result for J/ψ has a similar shape, but higher values because it has a 15 cm long target and no collimator.

363 A Kalman Filter based track finding and fitting algorithm is being developed and tested with
 364 digitized GEM simulation data. Tracking resolution from the simulated tracking fitting results in-
 365 cluding all material effects was studied. With background taken into account, tracking efficiency
 366 was obtained with the simulation. We have good electron detection efficiency from all sub-detectors.
 367 They vary slightly across the phase space and the average efficiency values are shown in Table 1.
 368 The PVDIS setup with its 40 cm long LD2 target has acceptance ~ 0.35 due to the baffle and the
 369 SIDIS setup with its 40 cm long ^3He target has acceptance ~ 0.7 due to the two target window col-
 370 limators. Figure 8 shows the combined effect of acceptance and efficiency (except tracking) for the
 371 two configurations. Systematic uncertainties for PVDIS and SIDIS are summarized in Table 2. The
 372 total systematic uncertainty for J/ψ is about 11%, dominated by acceptance, and the bin-migration
 373 effect is expected to be small. These results were used as the inputs to the physics projections.

Table 2: The systematic uncertainties on the asymmetry measurements of PVDIS and SIDIS.

PVDIS Systematic (rel.)		SIDIS Systematic (abs.)		SIDIS Systematic (rel.)	
Polarimetry	0.4%	Raw asymmetry	0.0014	Target polarization	3%
Q^2	0.2%	Detector resolution	< 0.0001	Nuclear effect	(4 – 5)%
Radiative corrections	0.2%			Random coincidence	0.2%
Reconstruction errors	0.2%			Radiative correction	(2 – 3)%
				Diffractive meson	3%
Total	0.6%	Total	0.0014	Total	(6 – 7)%

374 1.4.3 Rates and Data Acquisition

375 The trigger rates were simulated with the full background (Table 3). The SIDIS configuration,
 376 with an expected trigger rate of 100 kHz and total data rate of over 3 GB/s, represents the greatest
 377 challenge for SoLID data acquisition. Recent performance of the GlueX and HPS DAQs with
 378 extrapolations by the JLab data acquisition and fast electronics groups give confidence that trigger

379 rates of 100 kHz and above are achievable. Data for each of the 30 sectors of SoLID will pass
 380 through two readout controllers (ROCs), a PC based ROC for GEM data, and a VME ROC for all
 381 other detectors. The portion of the total data rate for non-GEM detectors, about 400 MB/s, is less
 382 than 15 MB/s per VME crate, so will not limit the trigger rate at 100 kHz. GEM detector trigger
 383 rates of 50 kHz have been obtained by HPS using an APV25 sample size of six. With a planned
 384 sample size of one for SIDIS, the GEM readout will not be limited to 100 kHz. The overall data
 385 rate required by SIDIS, which exceeds the rate currently achieved by GlueX, can be recorded by
 386 multiplexing data from the readout controllers to multiple event building computers. Designing a
 387 DAQ system with 60 ROCs that can handle data rates of several GB/s will require some R&D,
 388 including firmware and software improvements, but is feasible using technology currently in use at
 389 JLab.

Table 3: Rates, run times and data total estimates for the PVDIS, SIDIS and J/Ψ experiments. For PVDIS, there are 30 sectors each of which has a separate DAQ.

Experiment	PVDIS	SIDIS ^3He	J/ψ
Trigger rate (expected) (kHz)	15×30	100	30
Data rate (GB/s)	0.2×30	3.2	2.5
Running time (days)	169	125	60
Total data (PB)	175	70	25

390 1.5 Summary

391 The strong and unique physics programs with PVDIS, SIDIS and J/ψ production are presented
 392 in the context of the worldwide effort. The science related recommendations from the Director's
 393 Review committee have been addressed. The science reach, unique strength and feasibility of the
 394 SoLID program demonstrate that we are ready for the next step: the anticipated Science Review by
 395 DOE.

2 Introduction and Overview of SoLID Experimental Programs

2.1 SoLID Project Introduction/Overview

2.1.1 Base Equipment Description

The SoLID (Solenoidal Large Intensity Device) project will develop a large acceptance spectrometer/detector system capable of handling very high rates. It is designed to satisfy the requirements of five approved high-scientific rated experiments, four A and one A-, as well as to become base equipment for a continued program of physics in the 12 GeV era at Jefferson Lab that requires both high luminosity and large acceptance. The base equipment composing the SoLID project includes two configurations: the “SIDIS” (Semi-Inclusive Deep Inelastic Scattering) configuration and the “PVDIS” (Parity-Violating Deep Inelastic Scattering) configuration. Although the geometrical layouts for the detectors are not the same in the two configurations, most of the following items are common:

1. A solenoidal magnet with a power supply and cryogenic system, identified as the CLEO-II magnet. With some modifications as described in the magnet section, this magnet meets the experimental requirements. The coils and cryostat of the CLEO-II magnet have arrived at JLab in 2016 and the exterior steel is arranged to be shipped to JLab in the summer of 2017.
2. An electromagnetic calorimeter for electron identification. (In the SIDIS configuration, it is separated into two sectors, a forward sector and a large-angle sector).
3. A light gas Cherenkov detector for electron identification.
4. A heavy gas Cherenkov detector for pion (hadron) identification. This is for the SIDIS configuration only.
5. A set of baffles. This is for the PVDIS configuration only.
6. A data acquisition system (DAQ). Part of the DAQ electronics, mainly FADCs, will be from the JLab Physics Division Shared Electronics Pool (see next section on Dependencies to Base Equipment).
7. Supporting structures for the magnet and the detectors.
8. Requisite Hall A infrastructure to accommodate the functioning of the above — cooling, cabling, and the like.

2.1.2 Dependencies to Base Equipment

The following items are requisite outside contributions to the SoLID base equipment:

1. GEM detectors for tracking: These are planned to be provided by a SoLID Chinese Collaboration. Five Chinese institutions (USTC, CIAE, Tsinghua, Lanzhou and IMP), in collaboration with UVa (Nilanga Liyanage group), have committed to perform R&D and apply for full funding from the Chinese funding agencies to construct the full set of GEMs for the SoLID project.
2. A MRPC (Multi-Gap Resistive Plate Chamber) detector serving as a time-of-flight (TOF) detector for pion (hadron) identification: Two Chinese groups (Tsinghua University and USTC) have committed to perform R&D and apply for full funding to construct the required MRPC

434 detector for the SoLID project. The Chinese groups, in collaboration with US institutions,
435 will also apply for separate funding for MRPC electronics.

436 3. DAQ electronics: JLab intends to have an electronics pool to share basic DAQ electronics
437 among the four experimental halls. Some of these electronics, mainly FADCs, will be utilized
438 by SoLID.

439 4. Magnet: JLab formally requested the CLEO-II magnet and received a positive response from
440 Cornell University. JLab, in coordination with Cornell, had the magnet coils and cryostat be
441 transported to JLab in the fall of 2016 and plans to have the steels be shipped to JLab in the
442 Summer of 2017.

443 5. Beamline: The Hall A beam line with standard instrumentation is assumed to be in operational
444 condition and is not included in the SoLID base equipment.

445 **2.1.3 Experiment-specific Dependencies**

446 The five approved experiments in the SoLID research program would require the SoLID base equip-
447 ment, as well as the development of components outside the base equipment of the SoLID project.
448 The following lists such additional equipment that is either standard and existing at JLab or that will
449 be available for experiments planned before the SoLID experiments:

450 1. For SIDIS transverse ^3He and longitudinal ^3He : The existing polarized ^3He target with per-
451 formance already achieved from the 6 GeV transversity (E06-010) experiment is required.
452 However, modifications to the stand, supports, and service may be required to accommodate
453 integration into SoLID.

454 2. For J/Ψ the standard cryogenic LH2 target system is assumed. This is standard Hall A
455 equipment, however the SoLID SIDIS configuration will require re-arrangement of the de-
456 tector system for the target and there may be significant modifications required for both to
457 accommodate integration into SoLID.

458 3. For PVDIS: A Compton polarimeter and a super-conducting Moller polarimeter (both also
459 required by MOLLER and to be employed for PREX also) are assumed to be available.

460 For completeness, though not as general dependencies for SoLID base equipment, the following
461 experiment-specific items which will require additional resource/funding are listed:

462 1. For PVDIS: a custom, high-power cryotarget is required. ESR2 is assumed to be available
463 (required by the Moller project).

464 2. For SIDIS transverse proton: a transversely polarized proton target will need development.
465 An initial study has been performed by Oxford which concluded that such a target is feasible.

466 **2.1.4 Research Program**

467 The five currently-approved, high-impact experiments approved for the SoLID project are as fol-
468 lows:

469 1. SIDIS-transverse ^3He : Semi-inclusive deep-inelastic-scattering of electron beam on a trans-
470 versely polarized ^3He target. It is focusing on charged pion production to study transverse
471 spin (transversity) and other transverse momentum dependent parton distributions (TMDs). It

472 will provide a 4-d (x, z, P_T, Q^2) mapping of the Collins, Sivers and pretzelosity asymmetries
473 of the neutron in the valance quark region with high precision. Combined with the SIDIS
474 measurement on the proton and the world e^+e^- data, the Collins asymmetries will allow for
475 an extraction of one of the fundamental properties of the nucleon, the tensor charge of the
476 u and d quarks to better than 10%, providing a benchmark test of lattice QCD. The Sivers
477 and Pretzelosity asymmetries will allow an extraction of the Sivers function and pretzelosity
478 function, providing crucial information on the quark orbital motion.

479 2. SIDIS-longitudinal ^3He : Semi-inclusive deep-inelastic-scattering of electron beam on a lon-
480 gitudinally polarized ^3He target. It is focusing on charged pion production to study TMDs.
481 Combined with transversely polarized ^3He target experiment, it will provide a precision 4-d
482 (x, z, P_T, Q^2) mapping of the two worm-gear asymmetries of the neutron in the valance quark
483 region, allowing an extraction of the two so-called worm-gear TMDs (g_{1T} , longi-transversity
484 and h_{1L}^\perp , trans-helicity) with high precision, providing crucial information on the quark orbital
485 motion and the spin-orbital correlations.

486 3. SIDIS-transverse proton: Same as in 1) but on the proton.

487 4. PVDIS on the deuteron and the proton: PVDIS on the deuteron will provide a precision test
488 of the Standard Model. It provides the best measurement of the C_2 coupling and also provides
489 a precision measurement of $\sin^2 \theta_W$ at an intermediate value of Q^2 . The broad kinematical
490 range enables the separation of the testing of the Standard Model and the study of fundamental
491 hadron properties, including a precision measurement of possible charge symmetry violation
492 at the partonic level and a unique measurement of the higher-twist effect (twist-4 term). The
493 proton measurement provides a clean measurement of the d-quark over u-quark ratio in the
494 high- x region without nuclear effects.

495 5. J/Ψ production near threshold: This fully exclusive measurement of the electroproduction
496 of J/Ψ mesons from protons near threshold will be sensitive to the non-perturbative gluonic
497 interaction between the J/ψ and nucleon, and might reveal an enhancement of the cross
498 section just above the production threshold. This in turn could be a manifestation of the
499 important role of the conformal anomaly. A further consequence is whether or not J/ψ -
500 nuclear bound states would exist in nature. This experiment could open a new window to
501 study QCD in the non-perturbative region using charmonium in a multi-phase program.

502 All proposals are available at

503 http://www.jlab.org/exp_prog/generated/12GeV/halla.html

504 **2.2 SIDIS Program**

505 **2.2.1 Introduction**

506 Deep inelastic lepton-nucleon scattering (DIS) experiments have played a fundamental role in de-
507 scribing the partonic momentum structure of hadrons. The unpolarized parton distribution functions
508 (PDF) have been extracted with excellent precision over a large range of x and Q^2 from DIS, Drell-
509 Yan and other processes after several decades of experimental and theoretical efforts. The compari-
510 son of the structure functions in the large Q^2 range with QCD evolution equations has provided one
511 of the best tests of QCD.

512 When the target and/or beam are polarized the essential properties of spin-angular momentum
513 structure of hadrons is probed. Three decades of intensive experimental and theoretical investiga-
514 tion have resulted in a great deal of knowledge on the partonic origin of the nucleon spin structure.



515 Motivated by the “spin crisis” from the European Muon Collaboration experiment in the 1980s [11],
 516 the longitudinal polarized parton distribution functions have been determined with significantly im-
 517 proved precision over a large region of x and Q^2 from polarized deep-inelastic (DIS) experiments
 518 carried out at CERN, SLAC, DESY in the last two decades, and more recently at JLab and at RHIC
 519 from polarized proton-proton scattering (see [12, 13] for reviews and compilation of references).
 520 In particular, considerable knowledge has been gained from inclusive DIS experiments on the lon-
 521 gitudinal structure – the x -dependence and the helicity distributions – in terms of the unpolarized
 522 (denoted $q^a(x)$ or $f_1^a(x)$) and helicity (denoted $\Delta q^a(x)$ or $g_1^a(x)$) parton distribution functions for
 523 the various flavors (indicated by a).

524 In more recent experimental and theoretical studies, it has become evident that precise knowl-
 525 edge of the transverse structure of partons is essential to unfold the full momentum and spin
 526 structure of the nucleon. This concerns in particular the investigations of the chiral-odd trans-
 527 versely polarized quark distribution function or transversity [14] (denoted as $\delta q(x)$, $h_1(x)$ or also
 528 $\Delta_T q(x)$) which is probed in transverse spin polarization experiments. Like the axial charge $\Delta q^a =$
 529 $\int_0^1 dx (g_1^a(x) + g_1^{\bar{a}}(x))$, the tensor charge $\delta q^a = \int_0^1 dx (h_1^a(x) - h_1^{\bar{a}}(x))$ is a basic property of the
 530 nucleon. The essential role of the transversity distribution function emerges from a systematic ex-
 531 tension of the QCD parton model to include transverse momentum and spin degrees of freedom.
 532 In this context, semi-inclusive deep-inelastic lepton nucleon scattering (SIDIS) has emerged as an
 533 essential tool to probe both the longitudinal and transverse momentum and spin structure of the nu-
 534 cleon. The azimuthal dependence in the scattering of leptons off transversely polarized nucleons is
 535 explored through the analysis of transverse single spin asymmetries (TSSAs). Recent work [15–17]
 536 predicts that these observables are factorized convolutions of leading-twist transverse momentum
 537 dependent parton distributions (TMDs) and fragmentation functions (FFs) at low transverse momen-
 538 tum. These functions provide *essential non-perturbative* information on the partonic sub-structure
 539 of the nucleon; they offer a rich understanding of the motion of partons inside the nucleon, of the
 540 quark orbital properties, and of spin-orbit correlations. They also provide essential information on
 541 multi-parton correlations at leading-twist, allowing us to explore and uncover the dynamics of the
 542 quark-gluon structure of the nucleon.

543 At leading twist if we integrate over the transverse momenta of quarks, the three quark distri-
 544 bution functions remain: the unpolarized parton distribution f_1 , the longitudinal polarized parton
 545 distribution g_1 , and the quark transversity distribution h_1 . Besides f_1 , g_1 and h_1 , there are five
 546 more transverse momentum dependent distribution functions [15, 16]. Fig. 9 tabulates all these
 547 eight TMDs according to the polarizations of the quark (f, g, h) and nucleon (U, L, T). Since these
 548 TMDs provide the description of the parton distributions beyond the collinear approximation, they
 549 depend not only on the longitudinal momentum fraction x , but also on the transverse momentum,
 550 k_T . An intuitive interpretation of the k_T dependent transversity distribution, h_1 , is that it gives the
 551 probability of finding a transversely polarized parton inside a transversely polarized nucleon with
 552 certain longitudinal momentum fraction x and transverse momentum k_T . The JLab 12 GeV up-
 553 grade provides a unique opportunity to extend our understanding of nucleon spin and momentum
 554 structure by carrying out multi-dimensional precision studies of longitudinal and transverse spin
 555 and momentum degrees of freedom from SIDIS experiments with high luminosity in combination
 556 with large acceptance detectors. Such a program will provide the much needed kinematic reach to
 557 unfold the momentum and flavor structure of the nucleon. In the next section, we summarize the
 558 essential role that transverse polarization studies play in unfolding this structure in SIDIS.

559 **2.2.2 Transverse Structure and Semi-Inclusive Deep Inelastic Scattering**

560 The transverse spin and momentum structure of the nucleon was first discussed in 1970s [18, 19]
 561 followed by renewed interest in late 1980s [14, 20]. The transversity function is a chirally odd quark
 562 distribution function, and the least known among the three leading twist parton distribution func-
 563 tions. It describes the net quark transverse polarization in a transversely polarized nucleon [20]. In
 564 the non-relativistic limit, the transversity distribution function $h_1(x, Q^2)$ is the same as the longi-
 565 tudinal quark polarization distribution function, $g_1(x, Q^2)$. Therefore, the transversity distribution
 566 function probes the relativistic nature of the quarks inside the nucleon.

Leading Twist TMDs  : Nucleon Spin  : Quark Spin


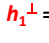



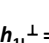





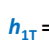

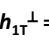

		Quark polarization		
		Un-Polarized (U)	Longitudinally Polarized (L)	Transversely Polarized (T)
Nucleon Polarization	U	$f_1 = $ 		$h_1^\perp = $  -  Boer-Mulder
	L		$g_1 = $  -  Helicity	$h_{1L}^\perp = $  - 
	T	$f_{1T}^\perp = $  -  Sivers	$g_{1T}^\perp = $  - 	$h_{1T} = $  -  Transversity $h_{1T}^\perp = $  - 

Figure 9: Leading twist TMDs classified according to the polarizations of the quark (f, g, h) and nucleon (U, L, T).

567 There are several interesting properties of the quark transversity distribution. First it does not
 568 mix with gluons; that is, it evolves as a non-singlet distribution [21] and doesn't mix with gluons
 569 under evolution and thus has valence-like behavior [22]. Secondly in the context of the parton model
 570 it satisfies the Soffer bound [23], which is an inequality among the three leading twist distributions,
 571 $|h_1^q| \leq \frac{1}{2}(f_1^q + g_1^q)$, based on unitarity and parity conservation. QCD evolution of transversity was
 572 studied in Ref. [24], where it was shown that Soffer's inequality holds up to next to leading order
 573 (NLO) QCD corrections. In the past [25] and more recently [26], studies have been performed that
 574 consider the violation of this bound. Therefore, it is interesting to experimentally test the Soffer's
 575 inequality as a function of Q^2 . Lastly, the lowest moment of h_1^q is the tensor charge, which has been
 576 calculated from lattice QCD [27] and various models [28–33]. Due to the valence-like nature of the
 577 transversity distribution, measuring transversity in the high- x region (JLab kinematics) is crucial to
 578 determine tensor charge of quarks. The experimental determination of the transversity function is
 579 challenging - it is not accessible in polarized inclusive DIS measurements when neglecting quark
 580 masses - h_1 decouples at leading twist in an expansion of inverse powers of the hard scale in in-
 581 clusive deep-inelastic scattering due to the helicity conserving property of the QCD interactions.
 582 However, paired with another hadron in the initial state *e.g.* double polarized Drell-Yan processes

583 (two transversity distributions) [19], or in the final state, *e.g.* semi-inclusive deep-inelastic [34] scat-
 584 tering (transversity and Collins fragmentation function), leading twist h_1 can be accessed without
 585 suppression by a hard scale.

586 The most feasible way to access the transversity distribution function is via an azimuthal sin-
 587 gle spin asymmetry, in semi-inclusive deep-inelastic lepto-production of mesons on a transversely
 588 polarized nucleon target, $eN^\uparrow \rightarrow e\pi X$. In this case the chiral-odd partner is the Collins frag-
 589 mentation function, H_1^\perp [34], which has been extracted from charged pion pair production from
 590 e^+e^- annihilation [35]. Assuming factorization, schematically this transverse single spin asymme-
 591 try (TSSA) contains h_1 and H_1^\perp , $A_{UT} \sim h_1 \otimes H_1^\perp$ ($U \equiv$ unpolarized lepton beam, $T \equiv$ transversely
 592 polarized target) [16].

593 The first evidence of non-trivial transverse spin effects in SIDIS has been observed in the trans-
 594 verse single spin asymmetries measured by the HERMES [36–38], and the COMPASS [39, 40]
 595 experiments from a transversely polarized proton or deuteron target, where an unpolarized lepton
 596 beam is scattered off $lp^\uparrow \rightarrow l'hX$. Besides the non-zero Collins asymmetry, which contains h_1
 597 and H_1^\perp discussed previously, another non-zero asymmetry (Sivers asymmetry), was also observed.
 598 The Sivers asymmetry is associated with a naive T-odd transverse momentum dependent (TMD)
 599 parton distribution function [41]. More recently, results on Collins and Sivers asymmetries on neu-
 600 tron were reported for the first time using a polarized ^3He target at Jefferson Lab [42]. In contrast
 601 to inclusive deep-inelastic lepton-nucleon scattering where transverse momentum is integrated out,
 602 these processes are sensitive to the transverse-momentum scale, P_T , which is on the order of the
 603 intrinsic quark momentum, k_T ; that is $P_T \sim k_T$. This is evident by considering the generic struc-
 604 ture of the TSSA for a transversely polarized nucleon target which is characterized by interference
 605 between helicity flip and helicity non-flip amplitudes $A_{UT} \sim \text{Im}(f^{*+}f^-)$. In the collinear limit of
 606 QCD, partonic processes conserve helicity and Born amplitudes are real [43]. For this structure to
 607 be non-zero at leading twist we must go beyond the collinear limit where such a reaction mechanism
 608 requires a recoil scale sensitive to the intrinsic quark transverse momentum. This is roughly set by
 609 the confinement scale $k_T \sim \Lambda_{\text{QCD}}$ [44]. Because strongly interacting processes conserve parity
 610 transverse spin asymmetries are described by T-odd correlations between transverse spin \mathcal{S}_T , longi-
 611 tudinal momentum \mathbf{P} and intrinsic quark momentum \mathbf{k}_T [34, 41], which are depicted by the generic
 612 vector product $i\mathcal{S}_T \cdot (\mathbf{P} \times \mathbf{k}_\perp)$. These correlations imply a leading twist reaction mechanism which
 613 is associated with a naive T-odd transverse momentum dependent (TMD) parton distribution [41]
 614 and fragmentation [34] function (PDF & FF).

615 A crucial theoretical breakthrough [45–47] was that the reaction mechanism is due to non-trivial
 616 phases arising from the color gauge invariant property of QCD. This leads to the picture that TSSAs
 617 arise from initial and final state interactions [48–50] (ISI/FSI) of the active quark with the soft
 618 distribution or fragmentation remnant in SIDIS, which manifests itself as a gauge link that links
 619 the bilocal quark configuration. This gauge link gives rise to the final state gluonic interactions
 620 between the active quark and target remnant. Thus, T-odd TMDs are of crucial importance because
 621 they possess transverse spin polarization structure as well as the necessary phases to account for
 622 TSSAs at leading twist. Further work on factorization theorems for SIDIS indicate that there are two
 623 leading twist T-odd TMDs; the Sivers function, denoted as f_{1T}^\perp , describing the probability density
 624 of finding unpolarized partons inside a transversely polarized proton, is one of these functions. All
 625 these aforementioned ingredients (TMD, FF, gauge link) enter the factorized [17] hadronic tensor
 626 for semi-inclusive deep-inelastic scattering.

627 Exploring the transverse spin structure of the TMD PDFs reveals evidence of a rich spin-orbit
 628 structure of the nucleon. When the transverse spin and momentum correlations are associated with
 629 the nucleon, where the quark remains *unpolarized*, the Sivers function [41] describes the helicity
 630 flip of the nucleon target in a helicity basis. Since the quark is unpolarized in the Sivers func-

tion, the orbital angular momentum of the quarks must come into play to conserve overall angular momentum in the process [51, 52]. Indeed a partonic description of the Sivers and Boer-Mulders functions requires wave function components with nonzero orbital angular momentum and thus provides information about the correlation between the quark orbital angular momentum (OAM) and the nucleon/quark spin, respectively [48, 53].

Unlike the Sivers function, which provides a clean probe of the QCD FSI, the functions g_{1T} and h_{1L}^\perp are (naive) T-even, and thus do not require FSI to be nonzero. Nevertheless, they also require interference between wave function components that differ by one unit of OAM and thus require OAM to be nonzero. Recently, a first ever determination of g_{1T} was reported [54] using a polarized ^3He target at Jefferson Lab, in which a positive azimuthal asymmetry for π^- production on ^3He and the neutron was observed, while the π^+ asymmetries are consistent with zero. Finally, the pretzelosity h_{1T}^\perp requires interference between wave function components that differ by two units of OAM (e.g. p-p or s-d interference). Combining the wealth of information from all these functions could be invaluable for disentangling the spin orbit correlations in the nucleon wave function, thus providing important information about the quark orbital angular momentum.

Complementary to Generalized Parton distributions (or Impact Parameter Dependent distributions), which describe the probability of finding a parton with certain longitudinal momentum fraction and at certain transverse position b (1-D momentum space and 2-D coordinate space), TMDs give a description of the nucleon structure in 3-D momentum space. Furthermore, by including the transverse momentum of the quark, the TMDs reveal important information about the nucleon/parton spin-orbital angular momentum correlations.

2.2.3 The Phenomenology TSSAs and TMDs

All eight leading twist TMDs can be accessed in SIDIS. The transversity, Sivers, and pretzelosity TMDs can be accessed through a transversely polarized target. There are three mechanisms which can lead to the single (transversely polarized target) spin azimuthal asymmetries, which are the Collins asymmetry, the Sivers asymmetry, and the pretzelosity asymmetry. As mentioned previously, the quark transversity function in combination with the chiral-odd Collins fragmentation function [34] gives rise to an azimuthal (Collins) asymmetry in $\sin(\phi_h + \phi_S)$, where azimuthal angles of both the hadron (pion) (ϕ_h) and the target spin (ϕ_S) are with respect to the virtual photon axis and relative to the lepton scattering plane. The Sivers asymmetry [41, 55, 56] refers to the azimuthal asymmetry in $\sin(\phi_h - \phi_S)$ due to the correlation between the transverse target polarization of the nucleon and the transverse momentum of the quarks, which involves the orbital angular momentum of the unpolarized quarks [48, 51]. The pretzelosity asymmetry is similar to Collins asymmetry except it is due to quarks polarized perpendicularly to the nucleon spin direction in the transverse plane in a transversely polarized nucleon. It has an azimuthal angular dependence of $\sin(3\phi_h - \phi_S)$. One can disentangle these angular distributions by taking the azimuthal moments of the asymmetries as has been done by the HERMES Collaboration [38], the COMPASS Collaboration [40], and most recently by the Jefferson Lab E06-010 collaboration [42]. With a longitudinally polarized lepton beam, and a transversely polarized target, the double spin asymmetry from SIDIS has an azimuthal angular dependence of $\cos(\phi_h - \phi_S)$ that allows for the determination of the g_{1T} TMD as was done in [54]. With a longitudinally polarized target, the single target spin asymmetry with an azimuthal angular dependence of $\sin(2\phi_h)$ is sensitive to h_{1L}^\perp , while the double spin asymmetry allows for the determination of the helicity TMD, g_1 .

In recent years a great deal of understanding of transverse spin effects, final state interactions, and the spin orbit structure of partonic-hadronic interactions has been gained from model calculations of the TMDs and fragmentation functions. In particular the final state interactions in TSSAs

677 through the Sivers function has been studied in spectator models and the light-cone wave func-
 678 tion approach [48–50, 57–61] as well as the bag model [62] and the NJL jet model [66]. The
 679 Collins function has been calculated in [63–65] while studies of the universality of T-odd fragmen-
 680 tation functions have been carried out in [67–69]. The Boer-Mulders function has been calculated
 681 in [50, 59, 61, 70, 71] and the spin orbit effects of the pretzelosity function have been studied in both
 682 light-cone constituent quarks models [72–75], while model predictions of azimuthal and transverse
 683 spin asymmetries have been predicted in [59, 76, 77].

684 The first model dependent extractions of the transversity distribution have been carried out [78]
 685 by combining SIDIS [37, 38, 79, 80] data with e^+e^- data [35] on the Collins function. Within
 686 the uncertainties, the Soffer bound is respected. In addition, the extraction of the Sivers func-
 687 tion [81–85] has been performed by combining SIDIS data from the HERMES [38] on the proton
 688 and COMPASS data [40] on the deuteron. Complementing the data from the HERMES [37, 38],
 689 COMPASS [80], and BELLE [35] experiments, the recent results from the Jefferson Lab Hall A
 690 experiment E06-010 [42] on the neutron (with polarized ^3He) will facilitate a flavor decomposition
 691 of the transversity distribution function, h_1 [20, 86] and the Sivers distribution function f_{1T}^\perp [41]
 692 in the overlapping kinematic regime. However a model-independent determination of these leading
 693 twist functions requires data in a wider kinematic range with high precision in *four dimensions* of
 694 (Q^2, x, z, P_T) .

695 2.2.4 Overview of SIDIS program

696 The 12-GeV energy upgrade at CEBAF together with the newly proposed SoLID opens a great new
 697 window to perform precision studies of the transverse spin and transverse-momentum-dependent
 698 structure in the valence quark region for both the proton and the neutron. The experimental program
 699 on TMDs is one of the main thrusts of the 12-GeV physics program at Jefferson Lab.

700 Currently, there are three A rated SoLID experiments (E12-10-006 [87], E12-11-007 [88], and
 701 E12-11-108 [89]) on TMD physics with two involving a transversely (longitudinally) polarized
 702 ^3He (neutron) target, and one employing a transversely polarized NH_3 (proton) target. To extract
 703 TMDs with precisions from single and double spin asymmetry measurements, the detection system
 704 should have the capability to handle large luminosities, a full azimuthal angular coverage, good
 705 kinematic coverage in terms of Q^2, x, z, P_T for SIDIS, and good particle identification for electrons
 706 and charged pions. Further, the influence due to the residual magnetic field of the spectrometer
 707 magnet needs to be negligible for polarized targets. SoLID is such a device that has been proposed
 708 and designed for these newly approved SIDIS experiments.

709 These new SIDIS experiments employ a superconducting solenoid magnet, a detector system
 710 consisting of forward-angle detectors and large-angle detectors, and a high-pressure polarized ^3He
 711 target or a polarized NH_3 target positioned upstream of the magnet. The polarized ^3He target is
 712 based on the technique of spin-exchange optical pumping of hybrid Rb-K alkali atoms. Such a
 713 target was used successfully in the recently completed SSA experiment [42, 54] with a 6-GeV
 714 electron beam at JLab and an in-beam polarization of 55-60% was achieved. For the polarized
 715 proton experiment E12-11-108, an upgraded version of the JLab/UVa/SLAC polarized NH_3 target
 716 will be used. The main upgrade will involve using a new magnet to replace the aging Helmholtz-
 717 coil magnet and to have fast spin-flip capability with the Adiabatic Fast Passage (AFP) technique.
 718 Preliminary design study has been carried out for such a magnet with a vertical opening angle of \pm
 719 25° to satisfy the requirement of the experiment. The target is based on the principle of dynamic
 720 nuclear polarization (DNP) by using microwave pumping to reach high proton polarizations [90,
 721 91]. The CLEO-II magnet with new end caps and modification of the yolks has been identified
 722 as the magnet of the choice for SoLID based on both the requirements of the experiments and the

723 availability of the magnet. Six layers of GEM detectors will be placed inside the coils as tracking
 724 detectors. A combination of an electromagnetic calorimeter, gas Čerenkov counters, a layer of
 725 Multi-gap Resistive Plate Chamber (MRPC) and a thin layer of scintillator will be used for particle
 726 identification in the forward-angle region. As only electrons will be identified in the large-angle
 727 region, a shashlyk-type [92, 93] electromagnetic calorimeter will be sufficient to provide the pion
 728 rejection. More details about SoLID experimental setup, kinematic coverage, particle identification,
 729 and other important considerations for SIDIS can be found in Section 3.2 and 3.3.

730 2.2.5 Beam Time and Projections

731 **E12-10-006** Experiment E12-10-006 was approved 90 days of total beam time with 15 μA , 11/8.8
 732 GeV electron beams on a 40-cm long, 10 amgs transversely polarized ^3He target. 69 days is for
 733 beam on the polarized ^3He target, and 10 days for a dedicated study of the $x - z$ factorization with
 734 Hydrogen and Deuterium gas using a reference target cell. Additional 3.0 days is requested with
 735 a longitudinal target polarization to study the systematics of potential A_{UL} contamination, where
 736 U stands for an unpolarized beam and L for a longitudinally polarized target. A total overhead
 737 time of 8 days is requested. This overhead time will be shared among activities such as unpolarized
 738 target runs, target spin flip and target polarization measurements, as has been done in the past during
 739 other Hall A polarized ^3He target experiments. Although beam polarization is not required for the
 740 proposed SSA measurements, polarized beam with polarization of 85% or higher will be used for
 741 for parasitic measurements of A_{LT} , which can be used to access, g_{1T} as demonstrated in [54].

742 Projected data from E12-10-006 are binned into 4-dimensional (x, P_h, z, Q^2) bins. For a typical
 743 z and Q^2 bin ($0.40 < z < 0.45$, $2 \text{ GeV}^2 < Q^2 < 3 \text{ GeV}^2$), data projections for Siverts asymmetry
 744 measurements, left panel for π^+ and right panel for π^- , are shown in Fig. 10 as examples. Also
 745 shown are results from the 6-GeV experiment E06-010 [42], and predictions of Siverts asymmetries
 746 from Anselmino *et al.* [94] with model uncertainties. For complete projections which consist of
 747 1400 data points, we refer to the proposal [87].

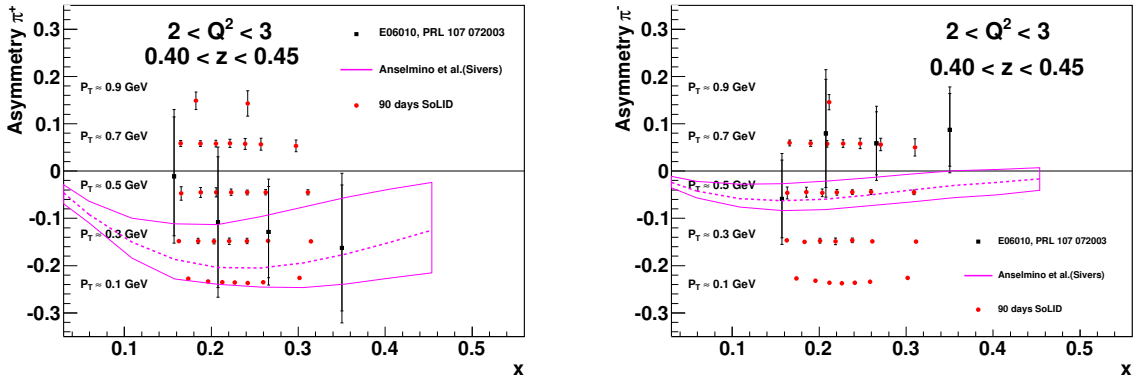


Figure 10: The left panel shows the projected Siverts asymmetry measurement for π^+ for a typical z and Q^2 bin ($0.40 < z < 0.45$, $2 \text{ GeV}^2 < Q^2 < 3 \text{ GeV}^2$) as a function of x with different ranges of the hadron transverse momentum labeled. The right panel shows the projection for the corresponding π^- Siverts asymmetry measurement. Also shown are the results from the 6-GeV experiment E06-010 [42].

748 **E12-11-007** Experiment E12-11-007 was approved 35 days of total beam time with 15 μA , 11/8.8
 749 GeV electron beams on a 40-cm long, 10 amgs longitudinally polarized ^3He target to match about

750 50% statistics of experiment E12-10-006. When combined with experiment E12-10-006, this exper-
 751 iment will not require any beam time for calibration data, including reference cell runs and detector
 752 calibrations.

753 A maximum likelihood method [95] was used to extract angular modulations with combined,
 754 projected data sets from both E12-11-007 and E12-10-006. Projected data are binned into 4-
 755 dimensional (x, P_h, z, Q^2) bins. For a typical z and Q^2 bin ($0.40 < z < 0.45$, $2 \text{ GeV}^2 < Q^2 <$
 756 3 GeV^2 , one of the total 48 $z - Q^2$ bins), data projections are shown in Fig. 11 as examples. For
 757 complete projections, we refer to the proposal [88].

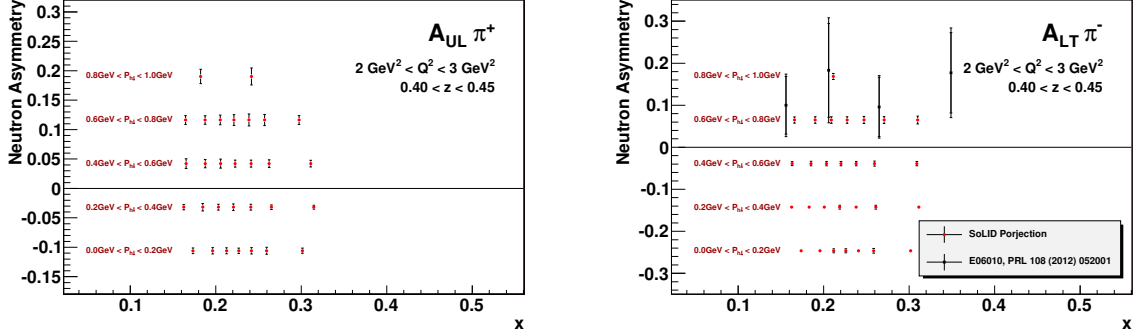


Figure 11: The left panel shows the projection for a typical z and Q^2 bin ($0.40 < z < 0.45$, $2 \text{ GeV}^2 < Q^2 < 3 \text{ GeV}^2$, one of the total 48 $z - Q^2$ bins) for the π^+ single target spin asymmetry $A_{UL}^{\sin(2\Phi_h)}$ measurement as a function of x with different ranges of the hadron transverse momentum labeled. The right panel shows the projection for the corresponding $z - Q^2$ bin for the π^- double spin asymmetry $A_{LT}^{\cos(\Phi_h - \Phi_S)}$ measurement. Also shown are the results from the 6-GeV experiment E06-010 [54].

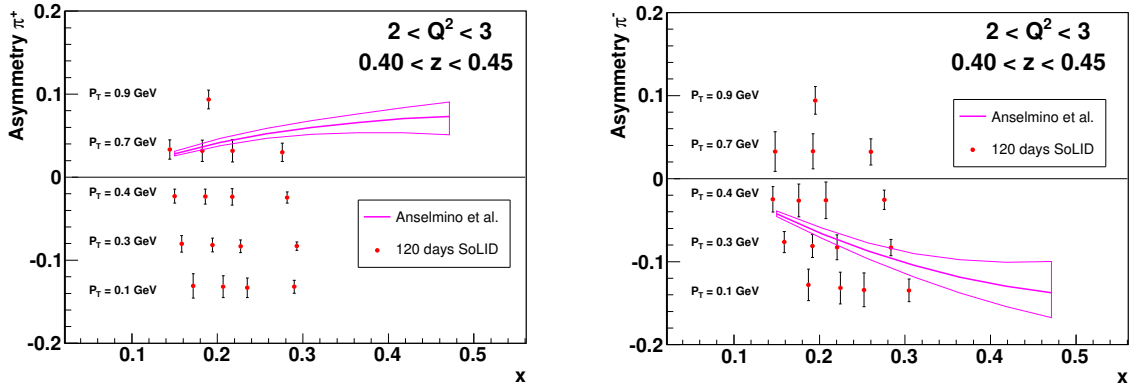


Figure 12: The left panel shows the projection for a typical z and Q^2 bin ($0.40 < z < 0.45$, $2 \text{ GeV}^2 < Q^2 < 3 \text{ GeV}^2$) for the π^+ Collins asymmetry measurement as a function of x with different ranges of the hadron transverse momentum labeled. The right panel shows the projection for the corresponding $z - Q^2$ bin for the π^- measurement. Also shown are predictions of Collins asymmetries from Anselmino *et al.* [94] with model uncertainties.

758 **E12-11-108** Experiment E12-11-108 was approved 94 days of total beam time with 100 nA,
 759 11/8.8 GeV electron beams on a 3-cm long, polarized NH_3 target. The 8.8 GeV beam energy will

760 provide precision data on the radiative corrections along with the increased Q^2 coverage. 90 days
761 are for beam on a transversely polarized NH_3 target including 7.5 days for dilution measurements,
762 optics, and detector calibrations. Also 4 days are requested with a longitudinal target polarization to
763 study the systematics of potential A_{UL} contamination. Although beam polarization is not required
764 for the proposed SSA measurements, a longitudinally polarized beam will be used for a parasitic
765 measurement of the A_{LT} , which can be used to access g_{1T} . In addition, there will be an overhead
766 time of 26 days for regular target annealing which does not need an electron beam.

767 Projected data from E12-11-108 are binned into 4-dimensional (x, P_h, z, Q^2) bins. For a typical
768 z and Q^2 bin ($0.40 < z < 0.45, 2 \text{ GeV}^2 < Q^2 < 3 \text{ GeV}^2$), data projections for Collins asymmetry
769 measurements, left panel for π^+ and right panel for π^- , are shown in Fig. 12 as examples. Also
770 shown are predictions of Collins asymmetries from Anselmino *et al.* [94] with model uncertainties.
771 For complete projections of E12-11-108, we refer to the proposal [89].

772 The combination of these three experiments will allow for accessing important information
773 about TMDs from proton and neutron, and the flavor separation of the TMDs (transversity, Sivers,
774 pretzelosity, and g_{1T}) for u and d quark. A good example based on a study in Ref. [96] to demon-
775 strate the impact of this program is shown in Fig. 13 in which the projected transversity distributions
776 for u and d quarks are shown at a typical $Q^2 = 2.4 \text{ GeV}^2$ based on the up-to-date knowledge of
777 evolution of the transverse momentum dependent distribution and fragmentation functions. The ex-
778 pected improvement in the knowledge of the transversity distribution is enormous: from the wide
779 error bands based on the current knowledge to the narrow bands from the SoLID program, and the
780 access to the valence quark region, which has been essentially unexplored as of now. In fact the
781 proposed SoLID SIDIS program will allow for studies of the k_T dependence, and the Q^2 evolution
782 of the TMDs also. Furthermore, the SoLID SIDIS program will provide precise information on the
783 tensor charge of the nucleon, an important property of the nucleon like spin or magnetic moment,
784 and is determined by the valence quarks inside the nucleon. A quantitative study [96] demonstrates
785 that the SoLID SIDIS program will improve the accuracy of the tensor charge determination by one
786 order of magnitude, and allows for benchmark tests of lattice QCD predictions. The high impact of
787 these data on the extraction of the tensor charge of the u and d quark is shown in Fig. 14.

788 2.2.6 Comparisons with SBS and CLAS12 SIDIS programs

789 In Table 4, we compare the experimental conditions of the SIDIS experiments with SoLID, SBS
790 and CLAS12. The values of solid angle coverage in the table are simplified descriptions. A more
791 realistic acceptance from GEMC is used for the estimation of the physics impact. Compared with
792 SBS, the statistics of SIDIS events with SoLID are much better due to the large acceptance. This
793 will allow us to have 4-dimensional bins with SoLID, while SBS will only have 3-dimensional bins.

794 A comparison of the Figure of Merit (FOM), which is calculated by the sum of the inverse
795 square of the statistical uncertainties of the SSA, is shown in Figure 15 and Figure 16. In these
796 comparisons, we applied the same kinematic cuts of $W > 2.3 \text{ GeV}$ and $0.3 < z < 0.7$. Compared
797 with CLAS12, SoLID has higher statistics in smaller x region and has comparable (or slightly lower)
798 statistics in larger x region. Compared with SBS, SoLID has higher statistics up to about $x \sim 0.55$,
799 while SBS has more coverage in large x region.

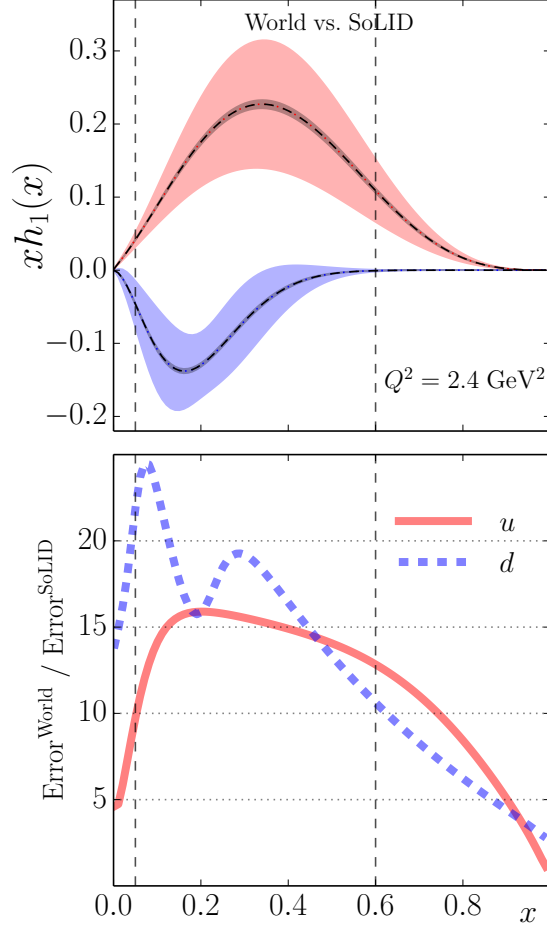


Figure 13: The impact on u and d quark transversity distributions by the SIDIS program using SoLID. The wide error bands show the current knowledge from the global analysis of the world data, and the narrow error bands show the SoLID projections. The lower panel shows the improvements, which are the ratios between the current errors and the projected errors.

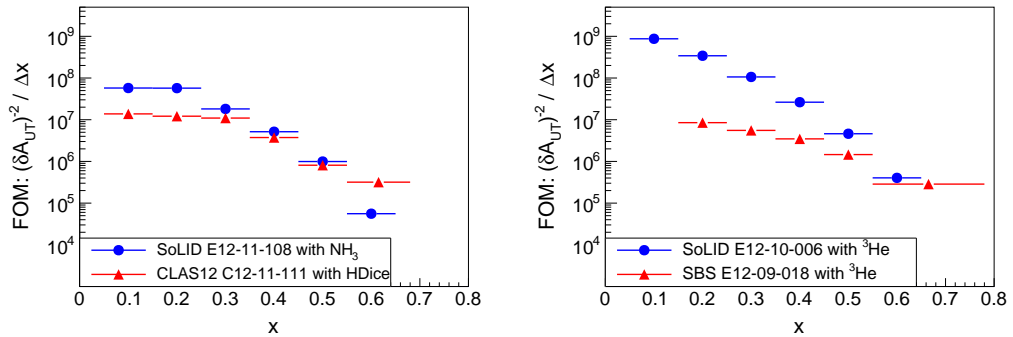


Figure 15: Comparison of the FOM at different x regions. SoLID SIDIS experiment with the proton target is compared with CLAS12 in the left panel. SoLID SIDIS experiments with the neutron target are compared to the SBS experiment in the right panel. In both comparisons, the same kinematic cuts of $W > 2.3$ GeV and $0.3 < z < 0.7$ are applied.

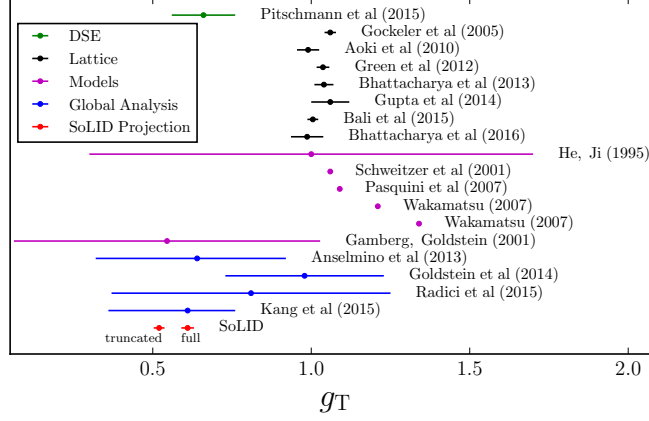


Figure 14: The impact of the projected SoLID measurement of the tensor charge together with current knowledge from models, Dyson-Schwinger equations, global analyses, and lattice QCD simulations.

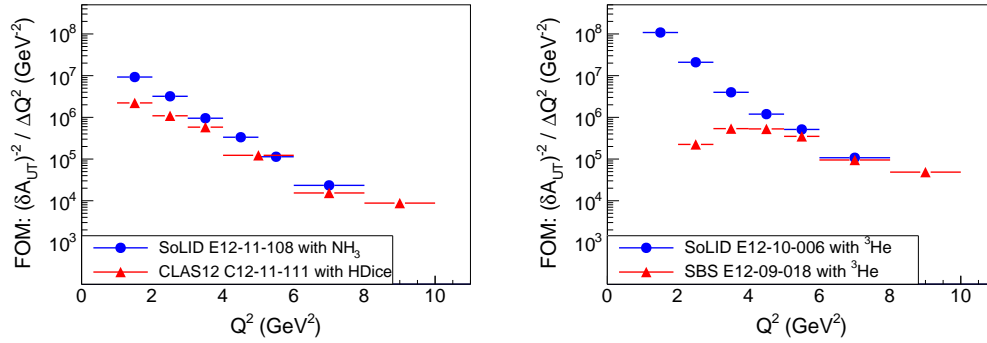


Figure 16: Comparison of the FOM at different Q^2 regions. SoLID SIDIS experiment with the proton target is compared with CLAS12 in the left panel. SoLID SIDIS experiments with the neutron target are compared to the SBS experiment in the right panel. In both comparisons, the same kinematic cuts of $W > 2.3$ GeV and $0.3 < z < 0.7$ are applied.

800 The physics impact of SoLID is the precise measurement of the TMDs in the valance region.
801 One highlight is the Collins SSA, which is related to the transversity distribution, which in turn is
802 dominated by the valance quark distribution. It is related to quark transversity distribution, which
803 is valance quark dominant. To compare the improvement on the determination of transversity,
804 we model the transversity distributions with the recent global fit of [5], which includes the TMD
805 evolution effect. We estimate the errors with the standard Hessian method [287]. The Hessian is
806 the second derivatives of the χ^2 with respect to the parameters at the least χ^2 point. It reflects not
807 only the uncertainties of the parameters but also the correlations of the parameters. The Hessian of
808 the world data is obtained from the covariant matrix of the global fit [5]. The Hessians of SoLID,
809 CLAS12, and SBS are calculated with the simulated data. To ensure that the SIDIS events are in the
810 current fragmentation region, which can be described by TMD factorization, we adopt the recent
811 theoretical study on the criteria of the current fragmentation kinematics [7] and only use the bins
812 in the current fragmentation region to study the physics impact. The impacts on the transversity

	SoLID	SBS	SoLID	CLAS12
Experiment	E12-10-006 Approved (A)	E12-09-018 Approved (A-)	E12-11-108 Approved (A)	C12-11-111 Conditional
Targets	^3He (“n”)	^3He (“n”)	NH_3 (“p”)	HDice (“p”)
Polarization (P)	65% (60% in beam)	65% (<60% in beam)	70%	60%
Dilution (f)	0.15~0.3	0.15~0.3	0.13	0.33×80%
Luminosity ($L \text{ cm}^{-2}\text{s}^{-1}$)	1.0×10^{36}	2.7×10^{36}	1.0×10^{35}	1.4×10^{33}
Solid angle ($\Omega_e \times \Omega_h \text{ sr}^2$)	0.482×0.139	0.044×0.063	0.482×0.139	1.14×1.16

Table 4: Comparison of the experimental conditions of SoLID, SBS, and CLAS12.

813 extractions are compared in Figure 17. In the comparison, only statistical uncertainties are used to
814 compare with CLAS12 and SBS. The improvement from SoLID data including systematic errors
815 is also shown in Figure 17. To remove the model dependence as much as possible, we take the
816 ratio between the prior uncertainties and the post uncertainties to show the improvements from the
817 SoLID, CLAS12, and SBS SIDIS experiments.

818 The tensor charge, which is the integral of transversity distributions, is a fundamental quantity
819 in QCD. It describes the coupling between a nucleon and a tensor current. Note that in QCD, this
820 correlation is different from the correlation between the longitudinal quark spin with the longitudinal
821 spin of the nucleon which is measured by the structure function g_1 . The impact of the determination
822 of the tensor charge from SoLID, CLAS12, and SBS are compared in Table 5. The improvements
823 are shown in two ways, the typical measured x region by JLab-12 experiments and the full x region.

	World vs. SBS+CLAS12	World vs. SoLID	SBS+CLAS12 vs. SoLID	World vs. SoLID including systematics
$\delta u^{\text{measured}}$	6.1	16	2.8	6.7
$\delta d^{\text{measured}}$	1.9	17	9.3	11
δu^{full}	5.4	16	3.0	5.9
δd^{full}	1.8	17	10	10

Table 5: Comparison of improvements to tensor charge extractions. “World” represents all world available data by 2015. In the first three comparisons, only statistical errors are used, while in the last comparison both statistical and systematic errors are included. The values in the table give the ratio between the prior error and the post error. The measured region is the integral over x from 0.05 to 0.6, and the full region is the integral over x from 0 to 1.

824 One of the advantages of SoLID SIDIS experiments is that the high statistics allows us to have
825 four-dimensional bins. This will help study TMDs, which are three dimensional distributions. To
826 show the impact of SoLID on TMD measurements, we take the Sivers function as an example. In
827 the analysis, we do a global fit with both unpolarized multiplicity data and Sivers asymmetry data.
828 The fitting result is used as the input model for future SoLID, CLAS12, and SBS pseudo-data. The

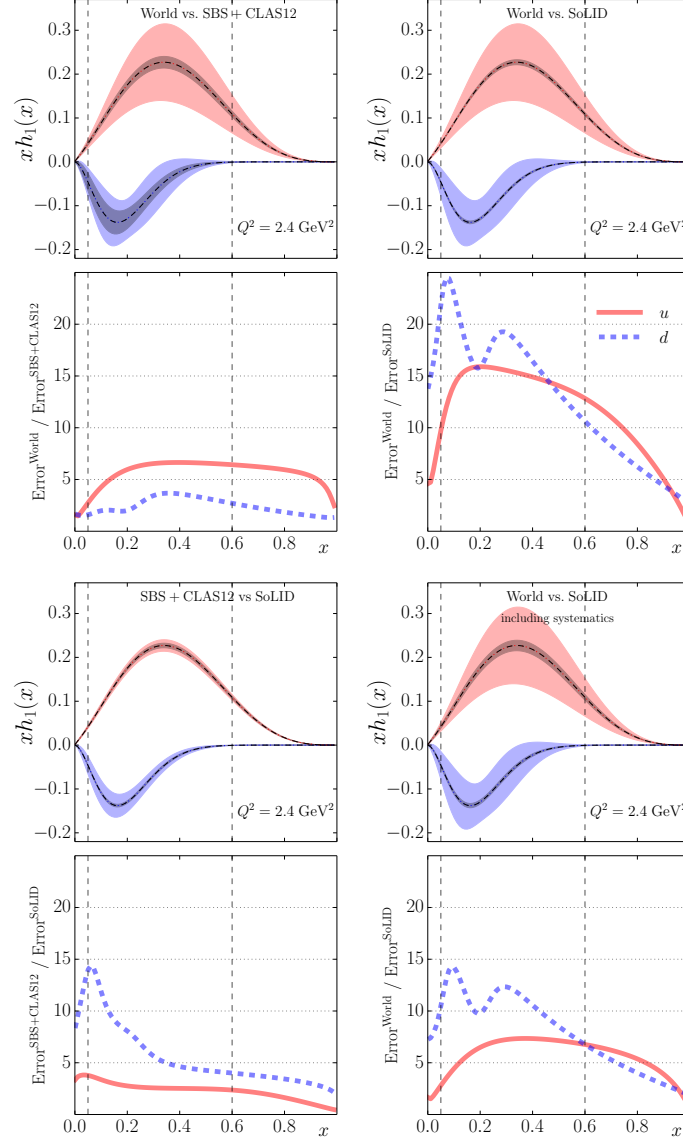


Figure 17: Comparison of the impact on the transversity extractions. The “World” represents all world available data by 2015. The upper left panel shows the improvement from future JLab12 data, i.e. SBS and CLAS12, before SoLID on the base of world available data by 2015. The upper right panel shows the improvements from SoLID data. The lower left panel shows the further improvement from SoLID data after the expected SBS and CLAS12 data. The lower right panel shows the improvements from SoLID data including the systematic uncertainties. The current uncertainties are from the global fit [5], and the future uncertainties are obtained by including the pseudo-data from these experiments with only statistical errors for the first three, and with both statistical and systematic errors for the last one. The curves in the lower panels show the improvement, which is the ratio between the prior uncertainties and the post uncertainties. The x -range between the two vertical dashed lines is directly measured by SoLID.

829 uncertainties from the world data and from inclusion of SoLID, CLAS12, and SBS are estimated in
830 the same framework. Similar to the case of transversity extraction, we only select the bins that pass
831 the kinematic cuts of the current fragmentation criteria. In Figure 18, we show the improvement
832 from SoLID on the extraction of the Sivers function, and compare it with CLAS12 and SBS.

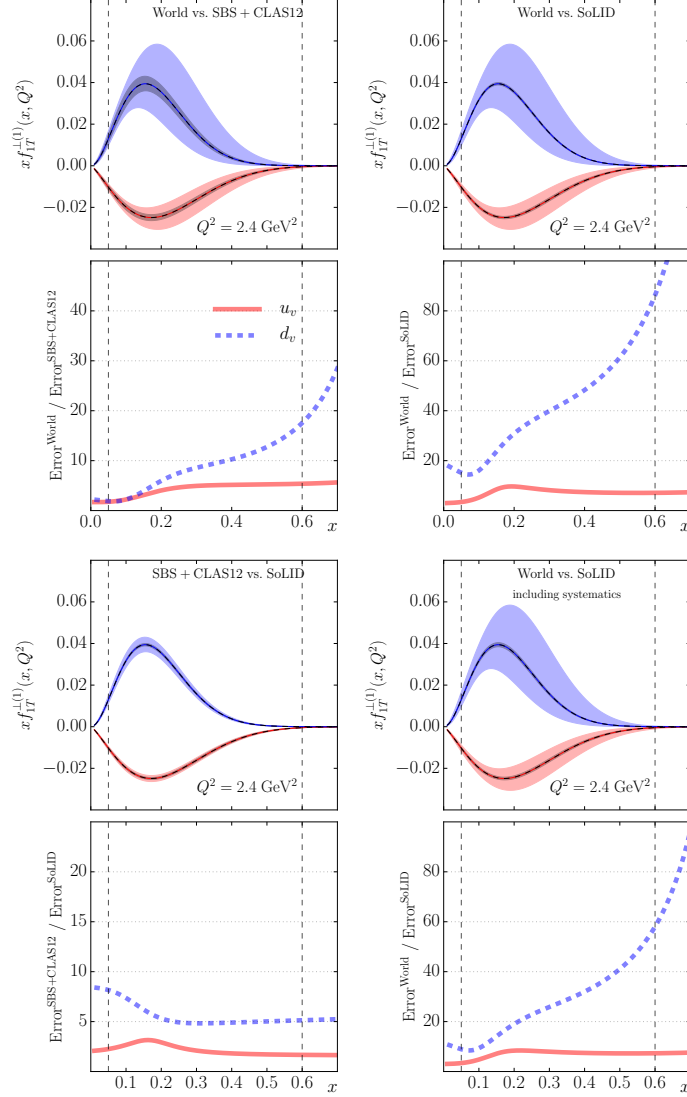


Figure 18: Comparison of the impact on the first transverse moment of the Sivens function. The “World” represents all world available data by 2015. The upper left panel shows the improvement from future SBS and CLAS12 data before SoLID beyond the base of world available data by 2015. The upper right panel shows the improvements from SoLID data. The lower left panel shows the further improvement from SoLID data after the expected JLab-12 data before SoLID. The lower right panel shows the improvements from SoLID data including the systematic uncertainties. The current uncertainties are from our new global fit to both unpolarized multiplicity data and Sivens asymmetry data, and the future uncertainties are obtained by including the pseudo-data from these experiments with only statistical errors for the first three, and with both statistical and systematic errors for the last one. The curves in the lower panels show the improvement, which means the ratio between the prior uncertainties and the post uncertainties. The x -range between the two vertical dashed lines is directly measured by SoLID.

833 2.3 PVDIS Program

834 2.3.1 Motivation for PVDIS

835 The unique opportunities for experiments on parity violation at JLab with the 12 GeV upgrade were
 836 recognized in the NSAC long-range planning exercises. The experiment was approved by PAC 35.
 837 Quoting the PAC 35 report, “the PAC believes the mission of this and future experiments using
 838 SoLID are sufficiently important that the Laboratory should make every effort to assist in securing
 839 the necessary funding.”

840 We reiterate here the physics topics that become accessible with the advent of a longitudinally
 841 polarized 11 GeV electron beam via measurements of the parity-violating asymmetry A_{PV} in deep
 842 inelastic scattering (DIS) in the kinematic region of large Bjorken $x = Q^2/2M\nu$. A_{PV} is defined
 843 to be:

$$A_{PV} = \frac{\sigma_R - \sigma_L}{\sigma_R + \sigma_L} \quad (1)$$

844 where $\sigma_R(\sigma_L)$ is the cross section for incident right-(left-) handed electrons.

845 The primary motivation of PVDIS is to search for new interactions beyond the Standard Model
 846 (SM). PVDIS is unique in that it is sensitive to fundamental axial-hadronic currents but does not have
 847 large radiative corrections that involve soft hadronic physics and are impossible to make reliably.

848 We propose to obtain data over a broad kinematic range, with $x > 0.2$, $2 < Q^2 < 10$. With a
 849 deuterium target, the asymmetry is approximately independent of kinematics and insensitive to the
 850 structure function. However, it is possible that the following physics could be observed in our data:

- 851 1. Charge Symmetry violation (CSV) at the quark level.
- 852 2. Higher-twist effects in the parity-violating asymmetry. Significant higher-twist effects are
 853 observed in DIS cross sections, but in PVDIS large higher-twist contributions can only be
 854 due to quark-quark correlations.

855 If these effects are large, they will constitute an important discovery. If they are small, our test of
 856 the SM will be quite reliable.

857 It has been suggested that there is additional CSV in heavier nuclei. By obtaining data with a
 858 lead target, we could test this hypothesis. Such an effect would have profound implications for our
 859 understanding of the EMC effect.

860 By switching the target to hydrogen, we can also measure the d/u ratio in the proton, without
 861 requiring any nuclear corrections.

862 2.3.2 Review of the Theory

863 The general expression for A_{PV} for $Q^2 \ll M_Z^2$ is [97]

$$A^{PV} = - \left(\frac{G_F Q^2}{4\sqrt{2}\pi\alpha} \right) \left[g_A^e Y_1 \frac{F_1^{\gamma Z}}{F_1^\gamma} + \frac{g_V^e}{2} Y_3 \frac{F_3^{\gamma Z}}{F_1^\gamma} \right] = - \left(\frac{G_F Q^2}{4\sqrt{2}\pi\alpha} \right) (Y_1 a_1 + Y_3 a_3). \quad (2)$$

864 Here the F_i^γ are the electromagnetic structure functions and the $F_i^{\gamma Z}$ are structure functions for the
 865 parity-violating interference term. The Y_i are functions of the kinematic variable $y = \nu/E$ and the
 866 ratios of structure functions $R^j(x, Q^2)$:

$$Y_1(x, y, Q^2) = \frac{1 + (1-y)^2 - y^2(1-r^2/(1+R^{\gamma Z})) - 2xyM/E}{1 + (1-y)^2 - y^2(1-r^2/(1+R^\gamma)) - 2xyM/E} \left(\frac{1+R^{\gamma Z}}{1+R^\gamma} \right) \quad (3)$$

$$Y_3(x, y, Q^2) = \frac{1 - (1 - y)^2}{1 + (1 - y)^2 - y^2(1 - r^2/(1 + R^\gamma)) - 2xyM/E} \left(\frac{r^2}{1 + R^\gamma} \right) \quad (4)$$

867 The above expressions are quite general.

868 In order to account for possible violations of the Standard Model, it is essential to express the
869 parity-violating part of the electron-hadron interaction in terms of general phenomenological four-
870 fermion contact interactions

$$\mathcal{L}^{PV} = \frac{G_F}{\sqrt{2}} [\bar{e}\gamma^\mu\gamma_5 e (C_{1u}\bar{u}\gamma_\mu u + C_{1d}\bar{d}\gamma_\mu d) + \bar{e}\gamma^\mu e (C_{2u}\bar{u}\gamma_\mu\gamma_5 u + C_{2d}\bar{d}\gamma_\mu\gamma_5 d)]$$

871 with additional terms as required for the heavy quarks. Here C_{1j} (C_{2j}) gives the vector (axial-
872 vector) coupling to the j^{th} quark. For the Standard Model:

$$C_{1u} = g_A^e g_V^u \approx -\frac{1}{2} + \frac{4}{3} \sin^2 \theta_W \approx -0.19 \quad (5)$$

$$C_{1d} = g_A^e g_V^d \approx \frac{1}{2} - \frac{2}{3} \sin^2 \theta_W \approx 0.34 \quad (6)$$

$$C_{2u} = g_V^e g_A^u \approx -\frac{1}{2} + 2 \sin^2 \theta_W \approx -0.030 \quad (7)$$

$$C_{2d} = g_V^e g_A^d \approx \frac{1}{2} - 2 \sin^2 \theta_W \approx 0.025 \quad (8)$$

873 The numerical values include electroweak radiative corrections. The key point is that the C_{1i} are
874 about an order of magnitude larger than the C_{2i} , which makes the a_1 term dominant. Recently, the
875 JLab PVDIS collaboration published in the journal Nature[98] the result that the C_{2i} 's are indeed
876 nonzero. The results are shown in Figure 19.

877 As recently pointed out by Mantry, et al., [99] for the deuteron where $I = 0$, $Y_1 = 1$ and

$$a_1^D(x) = g_A^e \frac{F_1^{D\gamma Z}}{F_1^{D\gamma}} = a_1^D(x) = \frac{6}{5} (2C_{1u} - C_{1d}) \left(1 + \frac{2s^+}{u^+ + d^+} \right)$$

878 The only corrections to these formulae are physics beyond the Standard Model, CSV and quark-
879 quark correlations, which form the motivation for the experiment, and known corrections including
880 strange quarks and target mass corrections.

881 For the a_3 term, we use the quark-parton model (QPM), which describes the structure functions
882 in terms of parton distribution functions (PDF's) functions $f_i(x)$ ($\bar{f}_i(x)$), which are the probabilities
883 that the i^{th} quark (antiquark) carries a fraction x of the nucleon momentum. With the definitions
884 $f_i^\pm = f_i \pm \bar{f}_i$, $y = \nu/E$, the structure functions are given by

$$F_1^\gamma = \frac{1}{2} \sum_i e_i^2 (f_i(x) + \bar{f}_i(x))$$

$$885 \quad F_1^{\gamma Z} = \sum_i e_i g_V^i (f_i(x) + \bar{f}_i(x))$$

$$886 \quad F_3^{\gamma Z} = 2 \sum_i e_i g_A^i (f_i(x) - \bar{f}_i(x)),$$

887 where e_i is the electromagnetic charge of the i^{th} quark. Then

$$a_3^D(x) = \frac{g_V^e F_3^{\gamma Z}}{2 F_1^\gamma} = 2 \frac{\sum_i C_{2i} e_i f_i^-(x)}{\sum_i e_i^2 f_i^+(x)} = \frac{6}{5} (2C_{2u} - C_{2d}) \left(\frac{u^+ - d^+}{u^+ + d^+} \right) + \dots$$

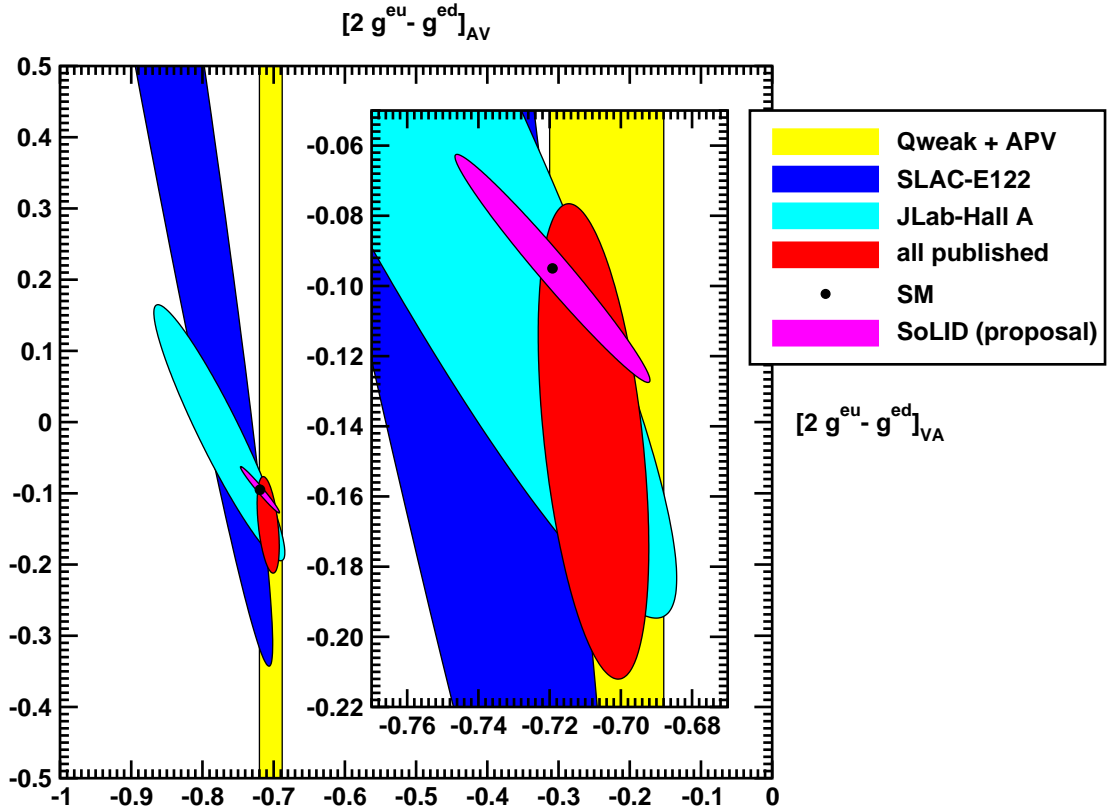


Figure 19: Results from the JLab PVDIS collaboration together with the projected results from the SoLID PVDIS experiment.

888 Contributions due to higher twist to this term can be obtained from neutrino scattering. The contri-
 889 bution of R^γ to A_{PV} is given in the Y_3 factor.

890 The key is that since $(2C_{2u} - C_{2d})$ is small, there is less sensitivity to the hadronic physics,
 891 whereas $(u^+ - d^-)(u^+ + d^+) \sim 1$ so that we are sensitive to new physics contributions to the C_{2i} .

892 The main goal of the experiment is to place a narrow error band on the C_{2i} plots of Figures
 893 20 and 19. An example of new physics that can contribute to the C_{2i} but not to the C_{1i} that have
 894 been precisely measured by Qweak and atomic parity violation in Cs, is a leptophobic Z' [100] as
 895 illustrated in Fig. 21. At the LHC, such a particle would be swamped by background. The proposed
 896 data will also improve the mass limits for generic models for composite for quarks and leptons [101]
 897 as shown in Figure 22.

898 2.3.3 Charge Symmetry Violation

899 The subtle violation of fundamental symmetries in hadronic systems can often provide important
 900 insights into the dynamics at work in those systems. The famous Nolen-Schiffer anomaly has
 901 played a significant role in nuclear structure for decades. When it comes to hadron structure charge
 902 symmetry violation is of great interest because of its link to the role of di-quarks in non-perturbative
 903 parton distribution functions [102–104].

904 The NuTeV experiment published a discrepancy with the Standard Model [105] with a signifi-
 905 cance of about three sigma. The result stirred a lot of controversy, resulting in a serious re-evaluation

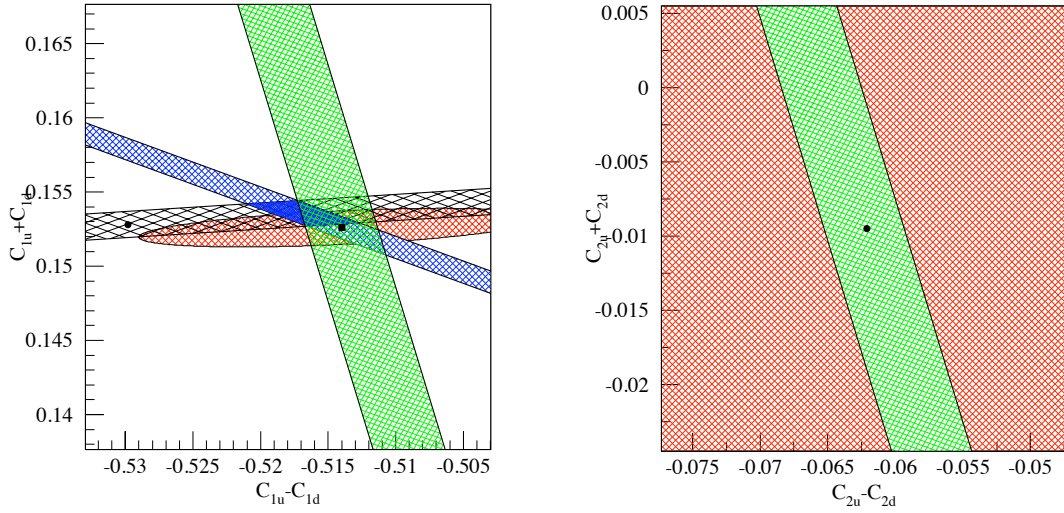


Figure 20: Green band: limits projected for this experiment. The blue band is the Qweak experiment and the black is the Cs APV.

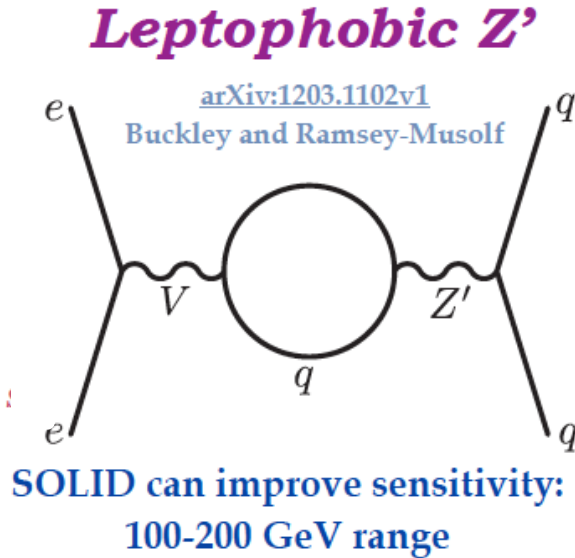


Figure 21: Diagram of a leptophobic Z' that can contribute to the C_{2i} and few other observables.

906 of the work. Additional corrections, including changes in the Cabibbo angle, strange sea, and im-
 907 proved radiative corrections, have recently been made, but have changed the result very little.

908 One possible explanation of the NuTeV result is charge symmetry violation (CSV) in the PDF's.
 909 This was overlooked in the NuTeV analysis, even though estimates which suggested how important
 910 it could be had existed in the literature for almost a decade [103, 104]. Various authors [106–108]
 911 have also presented the case that this is a reasonable explanation.

912 Our experiment is also sensitive to CSV. If the x -dependence of the CSV falls slower than the

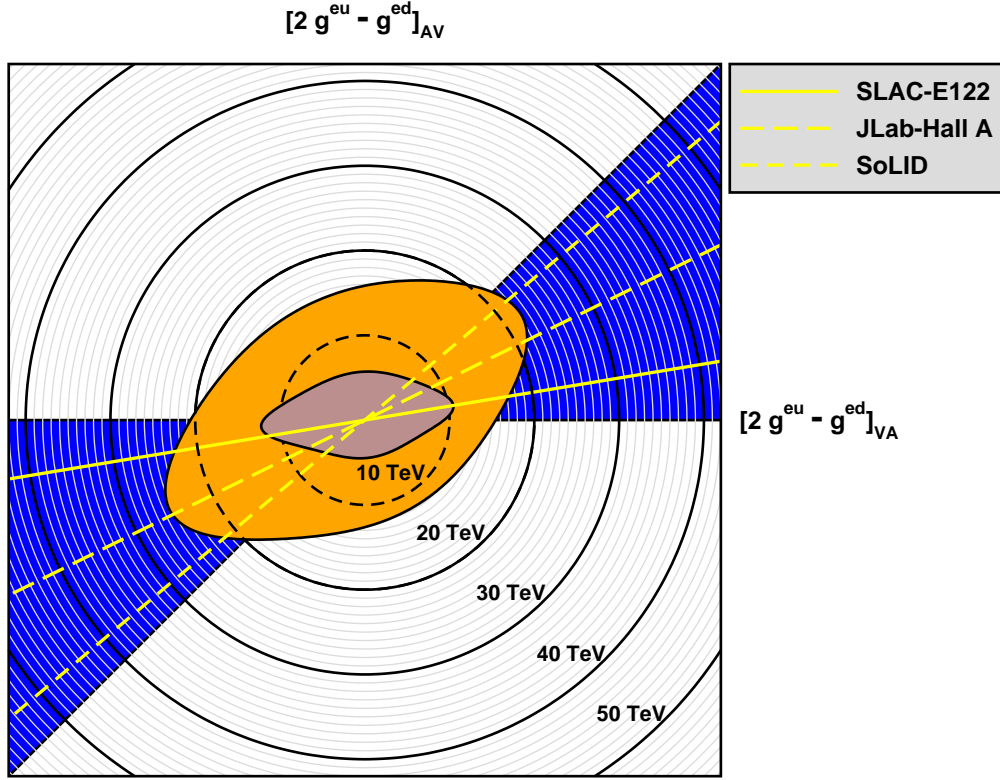


Figure 22: Polar plot for limits on composite models. The gray ellipse includes the published results from the PVDIS and Qweak collaborations. The orange ellipse gives the projected limits with the full Qweak statistics and the SoLID data.

913 PDF's as suggested by the curves in Figure 23 our asymmetry should display a clear x -dependence.
 914 Moreover, these results will provide an important test of the CSV explanation for NuTeV.

915 Another interesting possible contribution to the NuTeV anomaly is the isovector EMC ef-
 916 fect [109], which occurs for heavy nuclei. Measuring PVDIS in a target such as Pb would be
 917 able to demonstrate this effect.

918 2.3.4 Higher Twist

919 A recent paper has examined the contribution of higher twist (HT) effects to the dominant $Y_1 a_1$
 920 term in A_{PV} . [99] The correction can be parameterized as a fractional contribution $R_1(HT)$ by

$$Y_1 a_1 \approx Y_1 a_1 (1 + R_1(HT) + \dots)$$

921 where the ellipsis refers to other corrections including CSV. It turns out that the only contribution
 922 comes from the operator

$$\mathcal{O}_{ud}^{\mu\nu} = \frac{1}{2} [\bar{u}(x) \gamma^\mu u(x) d(0) \gamma^\nu d(0) + (u \leftrightarrow d)]$$

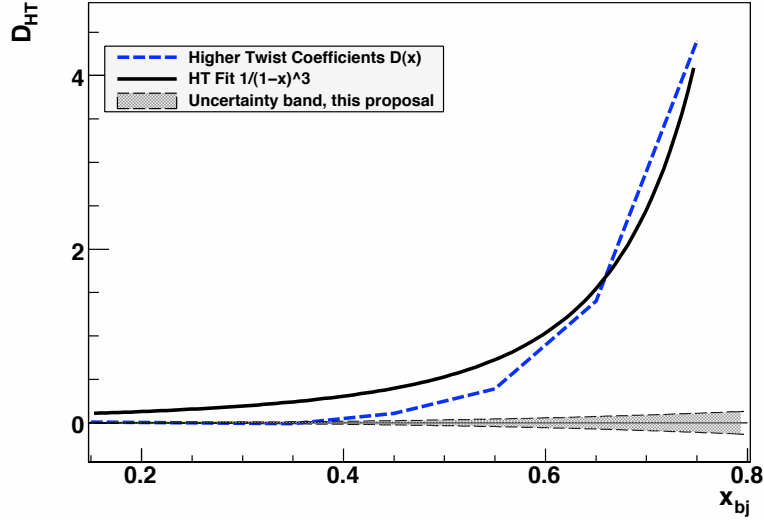


Figure 23: Possible contribution to A_{PV} due to CSV

923 which arises only from quark-quark correlations, or in other words, di-quarks in the nucleon. Higher
 924 twist contributions involving gluons cancel in the ratio. The special feature of A_{PV} is that it is the
 925 only practical experiment that can isolate higher twist due to four quarks.

926 The result is

$$R_1(HT) = -\frac{4}{5} \frac{[(9 - 20 \sin^2 \theta_W) F_1^{\gamma;4q} - 5 F_1^{\gamma Z;4q}]}{(1 - \frac{20}{9} \sin^2 \theta_W)[u_p(x) + d_p(x)]}$$

927 where $F_1^{\gamma;4q}$ and $F_1^{\gamma Z;4q}$ are the four-quark higher twist contributions to the structure functions.

928 2.3.5 Data Sample and analysis

929 The observation of CSV is possible with our apparatus only if the effect varies with x . An x -
 930 independent CSV effect would be indistinguishable from a change in the C_{1q} 's. It is quite natural,
 931 however, to expect that the x -dependence is similar to that shown in Figure 23, and we will make that
 932 assumption in our further discussion. From observations of higher-twist contributions to DIS cross
 933 sections, it is also natural to assume that Q^2 -dependent effects will also increase with increasing x .

934 If indeed either higher twist effects or CSV are clearly seen, the experiment will be a success.
 935 If they are absent, we plan to untangle the effects of hadronic and electroweak physics by fitting the
 936 asymmetries to a function of the form

$$A_{PV}^D = A_{PV}^{EW} \left(1 + \beta_{HT} \frac{1}{(1-x)^3 Q^2} + \beta_{CSV} x^2 \right) \quad (9)$$

937 Since the size of the hadronic effects is small, the sensitivity to the exact form is not important. The
 938 resulting statistical errors on the fit parameters are:

$$\delta A_{PV}^{EW} / A_{PV}^{EW} = 0.3\%; \quad \delta \beta_{HT} = 0.0026; \quad \delta \beta_{CSV} = 0.017$$

939 With this method, we use the full statistical power of the data set. However, the result has some
 940 sensitivity to the exact form of the chosen fitting functions. Under the scenario where the hadronic

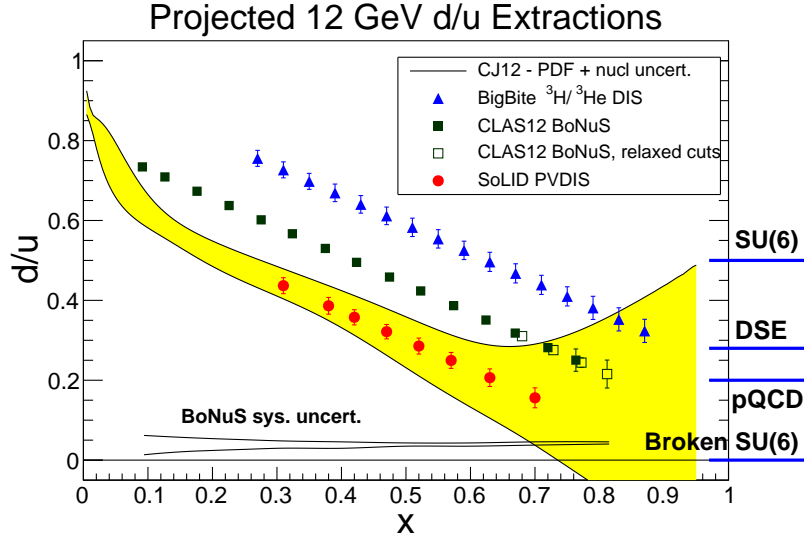


Figure 24: Anticipated precision for d/u measurement with SoLID as well as other proposed experiments.

941 effects are small, these errors are negligible as long as we assume that CSV and higher twist effects
 942 depend strongly on x , as expected. The one-sigma band for the CSV term is plotted in Figure 23.

943 If the pattern of higher twist effects is the same for A_{PV} as it is for the cross sections, then at
 944 $x = 0.6$ the asymmetries at the different Q^2 values will differ by 15%. In that scenario, the rapid
 945 x -dependence of the higher-twist coefficients for the cross section would imply that higher twist
 946 effects would still be negligible at $x = 0.4$. With a comparable x -dependence, a Q^2 -dependent
 947 effect as small as $\sim 3\%$ of the effect seen in cross-section measurements would be easily identifiable
 948 given our statistical precision.

949 **Measuring d/u at high x** Hydrogen is another useful target. Since it is not isoscalar, the structure
 950 functions do not cancel in the expression for $a(x)$. In particular,

$$a(x) \approx \frac{3}{4} \left[\frac{6C_{1u}u(x) - 3C_{1d}d(x)}{u(x) + \frac{1}{4}d(x)} \right] \sim \left[\frac{u(x) + 0.912d(x)}{u(x) + 0.25d(x)} \right]$$

951 and we see that $a(x)$ is sensitive to the ratio d/u . The determination of this for the proton is a topic
 952 of considerable interest at large values of x [110–113]. The ratio is difficult to determine from cross
 953 section data because at large x complicated nuclear physics effects become important for deuterium
 954 targets. Alternative methods include comparing ^3He and tritium or detecting the recoil proton from
 955 deuteron. Projected errors for all three approaches are shown in Fig. 24.

956 2.3.6 Beam Time Request

957 For the deuterium data, we have based our sensitivity on 180 days of production running at $50 \mu\text{A}$,
 958 with 1/3 of the data at 6.6 GeV and the rest at 11 GeV. Approximately 27 additional days, run
 959 at various currents, will be required for checkout and calibrations. An additional 18 days will be
 960 required at 4.4 GeV and $50 \mu\text{A}$ for radiative correction measurements. The total beam request at

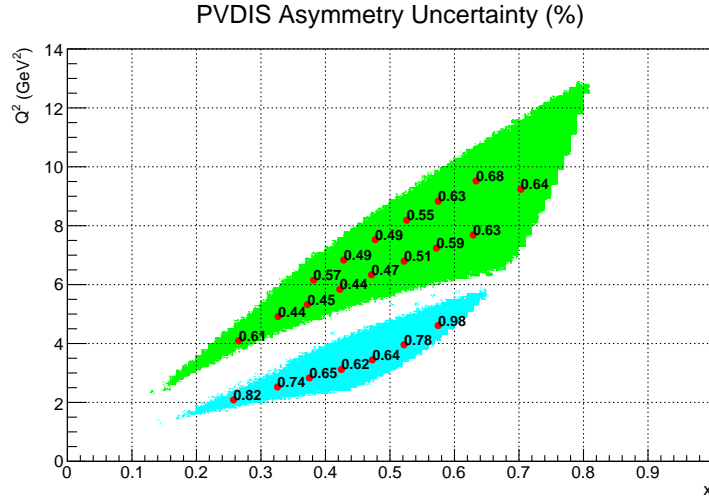


Figure 25: Anticipated statistical precision for A_{PV} in percent versus Q^2 and x . 11 GeV data (green region) are based on a simulation including the electron calorimeter trigger. For the 6.6 GeV data the effect of the trigger is estimated.

961 all energies for the deuterium measurement is 225 days, with about 25 of those days run mostly at
 962 reduced beam currents. Projected statistical uncertainties in A_{PV} are shown in Fig. 25.

963 For the hydrogen measurement, 90 days are needed for production data at 11 GeV, about 9 days
 964 are required at 4.4 GeV to control radiative corrections and another 14 days will be required for
 965 calibration. The running time requested for hydrogen totals to 113 days. We have been approved
 966 for 180 days total. The plan is to first take half the deuterium data. If nothing exciting appears, we
 967 will switch to hydrogen.

968 In the future, we would also anticipate requesting an additional comparable run for a heavy
 969 nucleus such as Pb.

970 2.4 J/ψ Program

971 2.4.1 Motivation

972 One of the fundamental goals of modern nuclear physics is to understand hadrons and nuclei starting
973 with the basic ingredients of QCD namely quarks and gluons and their interactions. While signifi-
974 cant progress has been made in exploring the theory in its perturbative region much remains to be
975 understood in the strong region, particularly where gluonic exchanges dominate. Strong gluonic
976 field configurations and interactions are responsible for most of the mass of nucleons and nuclei.
977 Fundamental approaches such as lattice QCD, effective field theories or dual string theories (that
978 would match QCD) could in principle shed light on confinement of hadrons and perhaps make
979 predictions of novel phenomena of strong interactions.

980 We plan to explore this strong interaction using a particular system that emphasizes the multi-
981 gluon exchange between two color neutral particles which do not share a common valence quark,
982 namely nucleons/nuclei and charmonia. It has long been argued that the force acting between nu-
983 cleon/nucleus and J/ψ is an attractive force, which has negligible mesonic ($D\bar{D}$) or multi-mesonic
984 ($\rho\pi$) exchange contribution at low energies [114]. Since the nucleon/nucleus and J/ψ are color
985 neutral, this force is dubbed as color Van der Waals force in analogy with the atomic-molecular
986 physics case. This situation is unique in nuclear physics where a force exchanged between nucleons
987 or hadrons is purely gluonic especially at low energy. A direct consequence of such an attractive
988 force is the possible existence of a nuclear bound quarkonium state which was proposed more than
989 20 years ago by Brodsky, Schmidt and de Teramond [115] but has yet to be observed. A calculation
990 using the operator product expansion (OPE) [116] to describe the low energy interaction of quarko-
991 nium with nuclei, in the limit where the mass of the charm quark is infinite, found that the J/ψ
992 binds in nuclear matter with about 10 MeV but the authors caution about possible large corrections
993 due to confinement effects.

994 Due to the lack of experimental data, a timid but sustained theoretical activity on the subject fol-
995 lowed over the past twenty years. For example, Kaidalov and Volkovitsky [117] argued that S-wave
996 quarkonia can be found in nuclei with $A \geq 10$ and with binding energy of few MeV, while de Tera-
997 mond et al. [118] in an update to his original paper with Brodsky [115] estimated a binding energy
998 of 2 MeV in ^{12}C and 10 MeV in ^{208}Pb , while Shevchenko [119] pointed in a later work that the
999 interaction of charmonium-nucleon is so small that the potential depth for nuclear bound state may
1000 only be possible for nuclei with $A > 200$. Applying QCD sum rules Hayashigaki [120] finds a 4 to
1001 7 MeV binding of the J/ψ in nuclear matter. Yokokawa, Sasaki, Hatsuda and Hayashigaki [121]
1002 performed a first lattice study in the quenched approximation of low energy charmonium-hadron
1003 interaction to determine the scattering length. But more recently Kawanai and Sasaki [122] calcu-
1004 lated the charmonium-nucleon potential from the equal-time Bethe-Salpeter amplitude through the
1005 effective Schrödinger equation and found that the charmonium-nucleon potential is weakly attrac-
1006 tive at short distances and exponentially screened at large distances. Finally, Tsushima, Lu, Krein
1007 and Thomas [123, 124] have recently explored the J/ψ -nuclear bound states and found that the
1008 attractive potential that originate from the D and D^* meson loops in the J/ψ in nuclear medium
1009 should produce bound states.

1010 Many of the J/ψ photoproduction experiments that have been performed at high photon ener-
1011 gies and low t or in the case of electroproduction at large center of mass energy s and low t (see
1012 Refs. [125–132]) are usually considered as a diffractive production. Experiments in the thresh-
1013 old region are few and were performed soon after the discovery of the J/ψ particle more than 35
1014 years ago [133–136]. In particular, the measurements of Cornell [134] and SLAC [136] show large
1015 discrepancies at photon energy around 10 GeV.

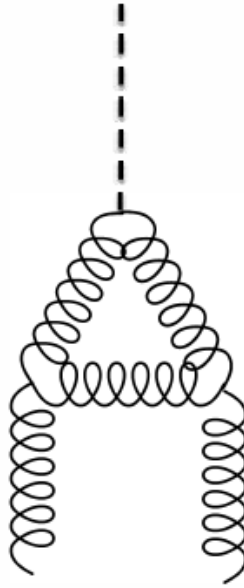


Figure 26: Anomaly diagram which dominate the cross section interaction at threshold.

1016 It is fair to say that not much is known in the region where the energy of the photon is just
 1017 above 8.2 GeV and where t is about 2 GeV, namely the threshold region. With Jefferson Lab at
 1018 12 GeV, we enter a new kinematic domain where the electro/photo-production of charmed hadrons
 1019 near threshold becomes possible. It is precisely a region well suited for the investigation of the
 1020 QCD Van der Waals interaction, since as we approach the threshold and due to the conformal scale
 1021 anomaly of the low energy J/ψ -nucleon interaction [137, 138] the non-perturbative part of the
 1022 interaction vanishes more slowly than the perturbative part. In his paper of 1998 [138], Kharzeev
 1023 considered explicitly the possible enhancement of the threshold cross section due to this conformal
 1024 scale anomaly which corresponds to a diagram where the coupling of the quarkonium to the nucleon
 1025 occurs through triangle gluonic lines (see Fig. 26). As shown in Fig. 27, the scattering amplitude in
 1026 the threshold region is also dominated by its real part in contrast to the case of high energy.

1027 Later Brodsky, Chudakov, Hoyer and Laget [139] discussed the photoproduction of charm near
 1028 threshold and invoked the two-gluon exchange mechanism in the production. These authors also
 1029 considered the possible enhancement of the cross section at threshold due to a strong interaction
 1030 beyond two-gluon exchanges as shown in Fig. 28. Whereas Sibirtsev, Krewald and Thomas [140]
 1031 attributed the mechanism of the J/ψ photoproduction at low energies and large t to a mechanism
 1032 different from pomeron or two-gluon exchange. They considered the possibility of the exchange
 1033 of an axial vector trajectory that couples with the axial form factor of the nucleon in this case also
 1034 enhancing the cross section at threshold.

1035 At first, the charmonium production near the threshold region would not seem to lend itself to
 1036 calculations using pQCD similar to the case of deep inelastic scattering at large Q^2 . However, a
 1037 closer look reveals a new scale at play, namely the mass of heavy quarks, which when compared to
 1038 Λ_{QCD} enables a perturbative approach to evaluate the scattering amplitude of the process. This fact
 1039 was used a while ago to derive charm photoproduction sum rules in a way similar to deep inelastic
 1040 scattering [141–143].

1041 In the reaction $\gamma^* + N \rightarrow J/\psi + N$, the production mechanism at threshold can be viewed in a

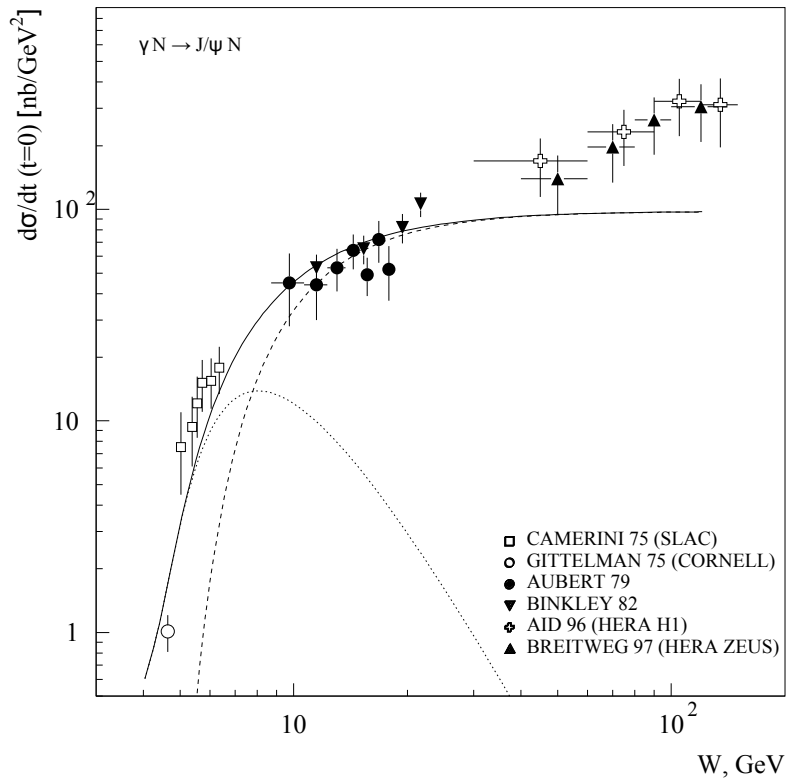


Figure 27: Forward J/ψ photoproduction data compared to the results of [138] with (solid line) and without (dashed line) the real part of the amplitude.

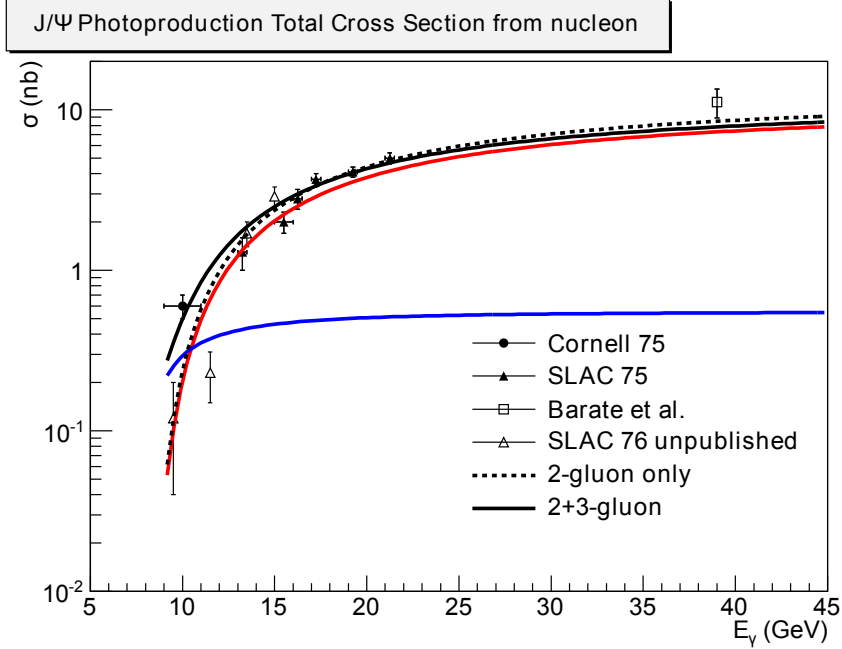


Figure 28: The 2-gluon model is shown as dotted black line. The (2+3)-gluon model is shown as solid black line. Furthermore, the 2-gluon contribution and 3-gluon contribution in the (2+3)-gluon model are shown as red and blue lines as well. Data are from “Cornell 75” [134], “SLAC 75” [133], “SLAC 76” [136] and “Barate et al.” [128].

1042 way similar to the J/ψ elastic scattering off a nucleon at small relative velocity. The coupling of the
 1043 soft gluonic fields to the nucleon, at low Q^2 is determined by the low-energy theorem in QCD based
 1044 on the anomaly in the trace of the energy-momentum tensor. The J/ψ -nucleon scattering amplitude
 1045 is proportional to the nucleon matrix element of the following gluon operator [144]:

$$\langle N | \frac{1}{2} \vec{E}^a \cdot \vec{E}^a | N \rangle = \frac{4\pi^2}{b} \langle N | \theta_\mu^\mu | N \rangle + 2\pi\alpha_s \langle N | \theta_G^{00} | N \rangle, \quad (10)$$

1046 where \vec{E}^a represents the chromo-electric field, $\theta_G^{\mu\nu}$ is the energy-momentum tensor of the gluon
 1047 field, θ_μ^μ is the anomalous trace of the full energy-momentum tensor in QCD in the chiral limit, b is
 1048 the coefficient in the QCD beta function with three light (massless in the chiral limit) quarks and α_s
 1049 is the QCD coupling.

1050 It is argued [144] that this matrix element is bound by

$$\langle N | \frac{1}{2} \vec{E}^a \cdot \vec{E}^a | N \rangle \geq \frac{4\pi^2}{b} 2m_N^2 \quad (11)$$

1051 In a measurement of electroproduction close to the threshold region, and unlike at high energy,
 1052 the real part of the scattering amplitude contribution dominates compared to the imaginary part
 1053 even though the allowed exchanges are purely gluonic. This contribution probes the matrix element
 1054 represented by $\langle N | \theta_\mu^\mu | N \rangle = 2m_N^2$. Hence, in a threshold measurement we probe the conformal
 1055 anomaly contribution to the low energy $J/\psi - N$ interaction comparable to a Higgs-like coupling¹.

¹The coupling of the contact term is sensitive to the entire mass of nucleon, and as such is similar to the Higgs coupling.

1056 Furthermore, the determination of an upper limit of the strength of this interaction will help de-
1057 termine whether or not a nucleon- J/ψ bound state due to the Van der Waals color forces would
1058 exist.

1059 2.4.2 Program Overview

1060 The high luminosity and large solid angle offered by the Jefferson Lab 12 GeV energy upgrade
1061 combined with the SoLID detector in Hall A is a unique tool to start an investigation program of the
1062 J/ψ -nucleon interaction.

1063 In a first phase, measurements of the cross section of electro- and photo-production of J/ψ on a
1064 nucleon near threshold will take place with experiment E12-12-006[152] using SoLID. These mea-
1065 surements at threshold have not been revisited since the 70s. The precision and energy range close to
1066 threshold of the proposed measurements will best probe the possible enhancement of the cross sec-
1067 tion due to the contribution of the conformal anomaly very close to the threshold photon energy of
1068 J/ψ production. Threshold enhancements due to on-shell rescattering or quasi-bound states around
1069 threshold have been observed in several processes such as $e^+e^- \rightarrow p\bar{p}, \Lambda\bar{\Lambda}, \Sigma^0\bar{\Sigma}_0, \Lambda\bar{\Sigma}_0$ [145] as
1070 well as in the J/ψ radiative decays, e.g. $J/\psi \rightarrow p\bar{p}\gamma$ [146]. The experiment E12-12-006 aims
1071 at observing such enhancement in the J/ψ -proton system and offers the capability to explore the
1072 region below threshold if there are hints of an enhancement of the cross section just above thresh-
1073 old. Furthermore, the proposed cross section measurement could also shed light on the existence of
1074 predicted super-heavy N^* with hidden charm with a mass around 4.3 GeV [148].

1075 In a second phase we shall explore the interference of the Bethe-Heitler amplitude with that
1076 of the J/ψ electroproduction to attempt a determination of the relative contribution of the real
1077 and the imaginary part of the scattering amplitude. Moreover, a study of the angular distribution
1078 of the J/ψ decay can reveal whether the J/ψ was originally produced from an octet or singlet
1079 state. Recently a phenomenological analysis of the forward $J/\psi - p$ scattering amplitude within a
1080 dispersive framework [147] resulted in a ψ binding energy in nuclear matter of 2.7 ± 0.3 MeV. The
1081 latter number uncertainty would be dramatically improved with more accurate cross section data in
1082 the threshold region. Furthermore, in the same reference a path towards unraveling the ratio of real
1083 to imaginary part of the J/ψ -nucleon scattering amplitude is described through the measurement of
1084 the $\gamma p \rightarrow e^+e^-p$ forward-backward asymmetry in the vicinity of the J/ψ resonant amplitude. This
1085 forward-backward asymmetry is sizable due to the interference of the Bethe-Heitler amplitude with
1086 the J/ψ production amplitude.

1087 Finally, studies of J/ψ production and propagation in the nuclear medium is the natural exten-
1088 sion of the proposed measurements on a nucleon. The study of multi-gluon QCD Van der Waals
1089 forces in nuclei is believed to shed new light on their possible role in J/ψ -nuclear bound states
1090 [115, 115–122]. Another related challenge is the in-medium properties of charmonia as well as the
1091 possible restoration of the chiral symmetry in the nuclear medium, which is closely connected to the
1092 modifications of masses and widths of mesons when embedded in the nuclear environment [123].
1093 For these studies, it is important to find the appropriate kinematical conditions to produce J/ψ near
1094 rest, or with small momentum relative to the nucleus. Therefore, measurements near threshold and
1095 even sub-threshold look promising [149].

1096 At JLab Hall C, a photoproduction experiment (E03-008) was performed in the *subthreshold*
1097 regime using the CEBAF at 6 GeV. Unfortunately no signal was observed after one week of beam
1098 on a ^{12}C target [149]. This experiment allowed to set a limit on the cross section, which was found to
1099 be consistent with the quasi-free production. The experiment used a bremsstrahlung beam produced
1100 on a copper radiator by the 6 GeV incident electron beam. The pair of spectrometers (HMS and
1101 SOS) of Hall C were used to detect the pair of leptons resulting from the decay of the J/ψ . A

1102 proposal "A-dependence of J/ψ photoproduction near threshold" [150] for the 12 GeV upgrade
1103 of Hall C was also considered by the PAC32 and conditionally approved. The authors proposed
1104 the use of bremsstrahlung photon beam created in a radiator to look at the photoproduction near
1105 threshold in a series of nuclei. The physics goal was to measure the photoproduction cross section
1106 on hydrogen and then investigate the A dependence of the propagation of the J/ψ in the nuclear
1107 medium. In this proposal, only the J/ψ is detected through the detection of the decay leptonic pair.
1108 The experiment E12-12-006[152] as the first phase of the program, will utilize the SoLID spec-
1109 trometer to measure the cross section of the full exclusive electro- and photo-production of J/ψ
1110 near threshold ($4.05 \text{ GeV} < W < 4.45 \text{ GeV}$ and $|t - t_{min}| < 2.5 \text{ GeV}^2$) to study QCD in the
1111 non-perturbative regime with luminosity of $10^{37} \text{ cm}^{-2} \text{ s}^{-1}$.

1112 **2.4.3 Beam Time and Projection**

1113 The experiment E12-12-006 was approved by Jefferson Lab PAC39 with total 60 PAC days[152].
1114 Among them, 50 days will be used for production run with $3 \mu\text{A}$, and 11 GeV electron beam on a 15
1115 cm long liquid hydrogen target. The other 10 days will be shared among activities, such as detector
1116 calibration, data taking with Al dummy target, and special low luminosity running for understanding
1117 the trigger efficiency and normalization for the cross section measurement.

1118 Our projections for the total elastic cross sections of electro- and photo-production are plotted
1119 against the effective photon energy in Fig. 29. Together, we have also plotted the world data of
1120 J/ψ photoproduction near threshold. The fit of 2-gluon exchange only model is shown as well with
1121 a solid line. In our projections we also included the possible photoproduction of the LHCb "pen-
1122 taquark" [161]. It is clear that the proposed measurements will significantly advance our knowledge
1123 of electroproduction of J/ψ near the threshold region.

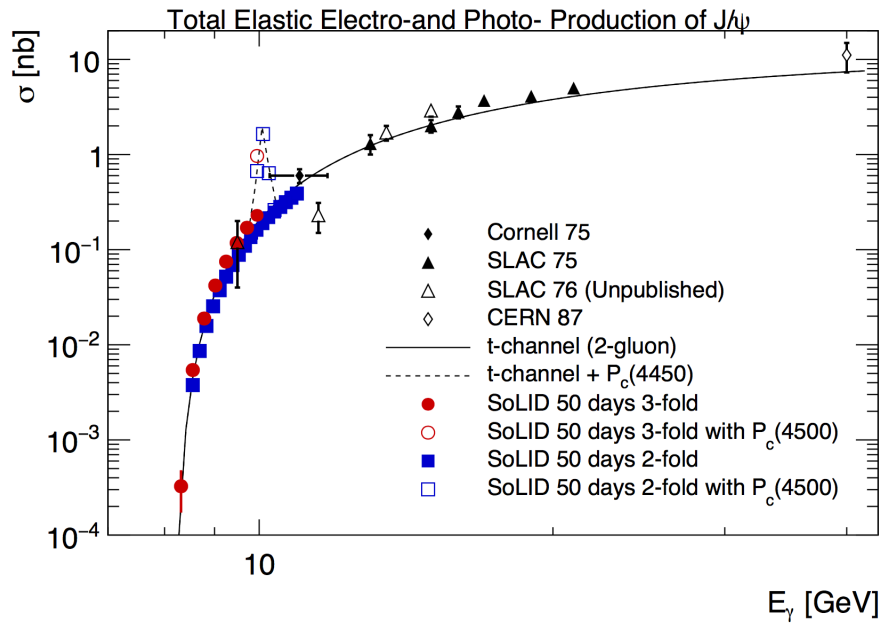


Figure 29: Projected uncertainties on the total elastic J/ψ electro-and photo-production cross sections. Our projections are based on the 2-gluon exchange model. The central values of our projections are positioned at 1.2 times or 0.8 times of the predicted total cross section of the 2-gluon exchange model in order to differentiate our projections from SLAC76 [136] points. The electro-production data is plotted against effective photon energy. We have also included the projection of the LHCb pentaquark photoproduction with a 5% coupling according to [151]

1124 **2.5 Possible Expansion in Physics Reach**

1125 **2.5.1 GPD Program**

1126 There are several GPD experiments in different stages of study/approval. As has been remarked
 1127 elsewhere, a variety of hard exclusive measurements are needed to disentangle the contributions of
 1128 the different GPDs, with the general Compton processes (DVCS, TCS, DDVCS) sensitive to various
 1129 real and imaginary combinations of all four leading twist GPDs (Fig. 30), vector-meson Deep Ex-
 1130 clusive Meson Production (DEMP) sensitive to the spin-average H and E GPDs and pseudoscalar-
 1131 meson Demp sensitive to the spin-difference \tilde{H} and \tilde{E} GPDs. The SoLID GPD program under
 1132 investigation includes many of these reactions, and has the potential to improve greatly our under-
 1133 standing of nucleon structure.

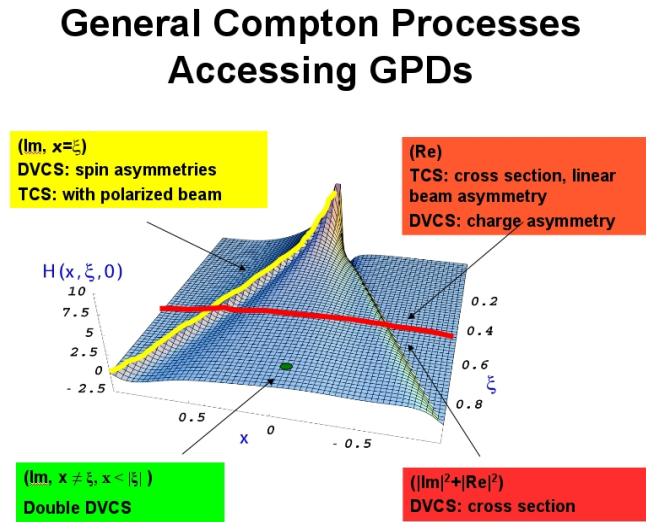


Figure 30: General Compton processes accessing GPDs.

1134 Timelike Compton Scattering (TCS) from an unpolarized LH_2 target can provide information
 1135 on the real (imaginary) parts of the Compton amplitude using unpolarized (circularly polarized)
 1136 photons. In this case, the produced lepton pair sets the hard scale ($Q^2 > 4 \text{ GeV}^2$) and the az-
 1137 imuthal asymmetry of the $\ell^+\ell^-$ plane with respect to the q -vector allows the separation of the GPD
 1138 and Bethe-Heitler contributions. This has been approved as a run group experiment with the J/ψ
 1139 experiment (E12-12-006A).

1140 Double Deeply Virtual Compton Scattering (DDVCS) in the di-lepton channel on an unpolar-
 1141 ized LH_2 target has been reviewed by PAC43 as LOI12-12-005. The solenoidal configuration is
 1142 ideal for high luminosity, with a fully parasitic proposal (as part of the J/ψ run group) for the e^+e^-
 1143 channel under preparation. Once this experiment has run, a later phase of measurements might
 1144 include the $\mu^+\mu^-$ channel. A workshop at ECT Trento to refine the TCS and DDVCS physics
 1145 program was held for October 24-28, 2016.

1146 A possible Deeply Virtual Compton Scattering (DVCS) experiment on polarized ^3He is also
 1147 under study. The 12 GeV polarized DVCS experiments to date utilize longitudinally (E12-06-119)
 1148 and transversely (C12-12-010) polarized proton targets. No polarized neutron-DVCS experiment
 1149 has been proposed at JLab to date, and SoLID could make a unique contribution here once the

1150 reaction exclusivity requirements and possible backgrounds are better understood. A complete set of
1151 SoLID DVCS data with both proton and neutron targets at varied polarization would be essential to
1152 control systematic uncertainties, perform flavor decomposition, and disentangle the different GPDs.

1153 Deep Exclusive Meson (π^-) Production (DEMP) using a transversely polarized ^3He (neutron)
1154 target looks very promising. The transverse single-spin asymmetry in exclusive charged π pro-
1155 duction has been identified as the most sensitive observable to probe \tilde{E} . In this case, one fits the
1156 $\sin(\phi - \phi_S)$ dependence, where $(\phi - \phi_S)$ is the azimuthal difference between the π^- reaction plane
1157 and the polarized target. Theoretical calculations suggest higher twist corrections likely cancel in
1158 the asymmetry, allowing access to GPDs at much lower value of Q^2 than typically required in
1159 DEMP reactions. This measurement has been proposed as a run group experiment with the trans-
1160 versely polarized ^3He SIDIS experiment (PR12-10-006B), and detailed studies on the expected
1161 uncertainties are underway.

1162 This summary makes clear that the SoLID-SIDIS setup is indeed very attractive in terms of
1163 acceptance and luminosity, and will allow a Phase 1 GPD program to be initiated with minimal
1164 impact on the approved SoLID program. Once this has been executed, one could envision a later
1165 Phase 2 suite of GPD experiments with additional recoil detectors near the target (such as low
1166 momentum proton tagging for DEMP), dedicated configurations (for DDVCS), or improved EC
1167 resolution (to allow exclusive vector meson and π^0 measurements). These would require much
1168 more study, and are clearly beyond the scope of the present proposals.

1169 2.5.2 SIDIS Production of Charged Kaons

1170 The extension of the SIDIS production of charged pion to the SIDIS production of charged kaons is
1171 under study. Because the kaon contains a valence strange/antistrange quark, the SIDIS production
1172 of charged kaons is more sensitive to the strange distributions. Compared to the pion data, the kaon
1173 data are very limited. Lacking the knowledge of the strange quark distributions will prevent us from
1174 fully understanding the spin structures of the nucleon. Taking advantage of high luminosities and
1175 large acceptance, SoLID could be ideal to measure the SIDIS production of charged kaons with
1176 high statistics. The combination of the proton and the neutron (^3He) targets, and the detection of
1177 charged pions and charged kaons in a similar kinematic region helps us to have flavor separations of
1178 all light quark distributions, *i.e.*, u , \bar{u} , d , \bar{d} , s , and \bar{s} . As kaon is heavier than pion, the SoLID kine-
1179 matics covers a intermediate region from target-fragmentation to current-fragmentation. A precise
1180 measurement in this region will allow us to understand how the factorization breaks down.

1181 A full RICH detector for kaon detection is likely to be too costly to consider. A high resolution
1182 TOF is a more practical solution. SoLID needs to do kaon identification over a momentum range
1183 of 1 GeV/c to 7 GeV/c. Given the 8 m flight distance, a TOF time resolution of 20 ps is required
1184 to obtain a 3-sigma separation between pions and kaons, as shown in Figure 31. Two detector
1185 technologies that could give high resolution TOF are being investigated.

1186 The Large Area Picosecond Photodetector (LAPPD) collaboration [179] is developing large area
1187 detectors capable of time resolutions in the picosecond range. Such detectors use Micro Channel
1188 Plate photomultipliers, which have small paths for electrons, achieving better timing resolution than
1189 traditional PMTs. Resolutions of 20 ps for a single photoelectron have been achieved and resolutions
1190 of under 10 ps could be obtained for multiple photoelectrons. The main drawback of Micro Channel
1191 Plate PMTs is the high cost per area. The LAPPD project is aiming to producing large area MCP
1192 PMTs with a cheaper microchannel plate, significantly reducing the cost for large area of detectors.
1193 Depending on the ultimate costs, this could be an option for SoLID.

1194 A second TOF option is improving the timing performance of the MRPC detector in SoLID.
1195 The baseline MRPC is designed to reach 80 ps. Improvement of the MRPC timing resolution would

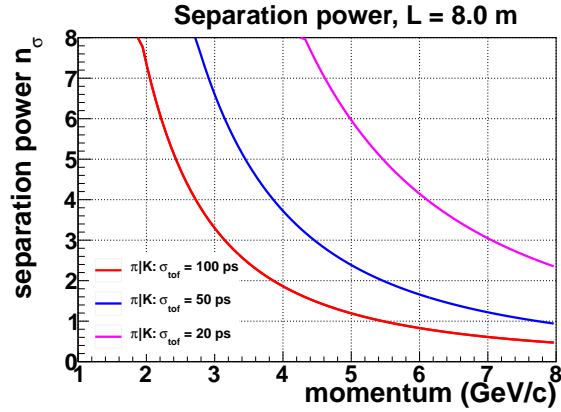


Figure 31: Kaon identification by TOF.

1196 extend the momentum range of π/K identification to the full momentum range. Beam tests showed
 1197 that current MRPC designs can reach 50 ps with test beam and 80 ps in high background area.
 1198 There is ongoing EIC R&D [180] on Multi Gap Resistive Plate to improve the timing resolution. A
 1199 thin gap MRPC prototype has been built and tested by BNL and University of Illinois, achieving a
 1200 resolution of 20 ps. The R&D plan is described in the MRPC section.

1201 **3 Technical Requirements and Experimental Setup**

1202 **3.1 Summary of Requirements**

1203 The minimum requirements of the base equipment for SoLID are summarized below and also listed
1204 in Table 6,

- 1205 • Magnet: Outer diameter is 3 meters (to fit in Hall A), inner diameter is 1 meter and length is
1206 greater than 3 meters. Field strength is greater than 1.35 tesla and integrated BdL is 5 tesla-
1207 meters. Acceptance in azimuthal angle (ϕ) is 2π , in polar angle (θ) is 8° to 24° for the SIDIS
1208 configuration and 22° to 35° for the PVDIS configuration. Momentum range is 1–7 GeV, and
1209 momentum resolution (combined with 100-micron tracking resolution) is 2%. Fringe field at
1210 the front end after endcap (shielding) is less than 5 gauss (for polarized target operation).
- 1211 • GEM Tracking Chambers: Six planes for SIDIS and five for PVDIS. Total area is 37 m^2 , total
1212 number of channels 165K. Tracking efficiency is greater than 90%. Radial position resolution
1213 reaches 0.1 mm. Works in high rate environment.
- 1214 • EM Calorimeter: Shashlyk sampling (lead-scintillator/fiber) calorimeter. Total 1800 modules
1215 of shower (18 radiation length) and 1800 pre-shower (2 radiation length), with an area of 100
1216 cm^2 for each module. Energy resolution is $10\%/\sqrt{E}$. Reaches $50 : 1$ π suppression with
1217 electron efficiency better than 90%. Reaches $5 : 1$ photon suppression. Radiation hard (gain
1218 decreasing less than 20% after 400 KRad). Combined EC and Cherenkov for PVDIS trigger
1219 rate to be below 600 KHz (20 KHz/sector). In front of the EM Calorimeter, there are 300
1220 pieces of scintillator pad detectors (SPDs) with thickness of 5 mm or 20 mm to help with
1221 photon rejection.
- 1222 • Light Gas Cherenkov: 2 meters long with 1 atm CO_2 gas for SIDIS and 1 meter long with
1223 1 atm CO_2 for PVDIS. Contains 60 mirrors and 270 PMTs. The total area is 20 m^2 . Pro-
1224 vides number of photo-electrons larger than 10 and electron efficiency greater than 90%. π
1225 suppression is greater than 500 for momentum less than 4 GeV (SIDIS) or less than 3.2 GeV
1226 (PVDIS). Works in moderate field up to 200 gauss (< 100 gauss after mu-metal shielding).
1227 Combined EC and Cherenkov for PVDIS trigger rate to be below 600 kHz (20 KHz/sector).
- 1228 • Heavy Gas Cherenkov: 1 meter long 1.5-atm $\text{C}_4\text{F}_8\text{O}/\text{C}_4\text{F}_{10}$ gas, with 30 mirrors and 480
1229 PMTs. Total area is 20 m^2 (active 8.5 m^2) and the number of photo-electrons is greater than
1230 10. With an efficiency for π better than 90%, kaon suppression is greater than 10:1. Works in
1231 moderate field up to 200 gauss (< 100 gauss after mu-metal shielding)
- 1232 • MRPC: 50 super-modules, each of which contains 3 MRPC modules. There are totally 1650
1233 strips and 3300 readout channels, covering an area of 10 m^2 . Timing resolution is better
1234 than 100 ps. Kaon suppression is about 20:1 for momentum from 2.5 to 7 GeV and photon
1235 suppression is as high as 10:1. Works at a high rate up to $10\text{ KHz}/\text{cm}^2$.
- 1236 • DAQ: 282 FADC sampling at 250 MHz. 32 high-speed pipeline VME switched Series (VXS)
1237 system. 30 GEM Scalable-read-out system (SRS). Can handle trigger rate of 100 KHz for
1238 SIDIS with event size of 2.6 KBytes and trigger rate of 600 KHz (20 KHz per sector) for
1239 PVDIS with event size of 48 KBytes
- 1240 • Baffles: Eleven planes of lead blocks, 30 sectors in each plane, thickness of 9 cm, with az-
1241 imuthal angle opening for each block to be more than 4° out of 12° ($360^\circ/30$). One additional

1242 plane of lead blocks with thickness of 5 cm is placed in front of the EM Calorimeter at the
1243 small radius region ($110 \text{ cm} < r < 200 \text{ cm}$). The design is optimized to block low energy
1244 particle, photon and hadron backgrounds to an acceptable level (total trigger rate below 600
1245 kHz (20 KHz/sector) for the PVDIS configuration).

1246 A summary of the detector requirements of all approved experimental programs is given in
1247 Table 7. The key parameters of the approved programs are in Table 8. The experimental setup of
1248 PVDIS, SIDIS- ^3He , SIDIS-proton and J/ψ are shown in the next few subsections.

Table 6: Summary of Minimum Requirements of SoLID Base Equipment. Items listed in brackets are particularly for SoLID-PVDIS requirements.

Equipment	dimension/description	description	performance, eff	performance, rej	conditions
Magnet	OD 3m, ID 1m, L > 3m	B > 1.35 T, BDL > 5 T-m	2 π , 8 to 24° (22 to 35°)	P: 1-7 GeV, Res 2%	Fringe field < 5 G
GEMs	6 planes (5 planes)	Total 37 m ² , Chan 165K	Track Eff > 90%	Posi res 100 μ m	high rate
EM Calorimeter	1800 \times 100 cm ²	18 RL + 2 RL + 5 mm SPD	E res 10%, eff > 90%	50:1 π , 5:1 γ	rad hard
Light Cherenkov	2m CO2 (1m C4F8O/N2)	60 mirr, 270 PMTs, 20 m ²	γ -e > 10, Eff > 90%	π 500:1 < 4.5/3.2 GeV	100 G field
Heavy Cherenkov	1m 1.5 atm C4F8O	30 mirr, 480 PMTs, 20 m ²	γ -e > 10, Eff > 90%	K 10:1 2.5-7 GeV	100 G field
MRPC	50 \times 3 modules, 10 m ²	1650 strips, 3300 chan.	Time res < 100 ps	K 20:1 < 2.5 GeV, γ 10:1	high rate
DAQ	282 FADC @ 250 MHz	32 pipeline VXS, 30 SRS	Trig 100 KHz \times 2.6 KB	Trig 30 \times 20 KHz \times 48 KB	high noise
Baffle	11 \times 30 blocks, 9 cm	5 cm, r 110-200 cm	area open ϕ > 4° / 12°	reduce background	

Table 7: Detector Summary for Approved Experiments

Experiments	PVDIS	SIDIS- ^3He	SIDIS-Proton	J/ψ
Target Length	LH ₂ /LD ₂ 40 cm	^3He 40 cm	NH ₃ 3 cm	LH ₂ 15 cm
Target Polarization	N/A	$\sim 60\%$	$\sim 70\%$	N/A
Target Spin Flip	N/A	≤ 20 mins	≤ 4 hours	N/A
GEM Tracking Chambers	5 chambers	6 chambers	6 chambers	6 chambers
E&M Calorimeter	Forward angle	Forward + Large angle	Forward + Large angle	Forward + Large angle
Light Gas Čerenkov	1 m long	2 m long	2 m long	2 m long
Baffles	Yes	N/A	N/A	N/A
Heavy Gas Čerenkov	N/A	1 m long	1 m long	N/A
MRPC (TOF)	N/A	100 ps resolution	100 ps resolution	100 ps resolution
Beam Polarimetry	0.4% determination	$< 3\%$	$< 3\%$	N/A
Target Polarimetry	N/A	$\sim 3\%$	$\sim 3\%$	N/A
DAQ	Single trigger	Coincidence trigger	Coincidence trigger	Coincidence trigger

Table 8: Summary of Key Parameters for Approved Programs

Experiments	PVDIS	SIDIS- ^3He	SIDIS-Proton	J/ψ
Reaction channel	$p(\vec{e}, e')X$	$(e, e'\pi^\pm)$	$(e, e'\pi^\pm)$	$e + p \rightarrow e' + J/\Psi(e^-, e^+) + p$
Approved number of days	169	125	120	60
Target	LH ₂ /LD ₂	^3He	NH ₃	LH ₂
Unpolarized luminosity ($\text{cm}^{-2}\text{s}^{-1}$)	$0.5 \times 10^{39} / 1.3 \times 10^{39}$	$\sim 10^{37}$	$\sim 10^{36}$	$\sim 10^{37}$
Momentum coverage (GeV/c)	2.3-5.0	0.8-7.0	0.8-7.0	0.6-7.0
Momentum resolution	$\sim 2\%$	$\sim 2\%$	$\sim 2\%$	$\sim 2\%$
Polar angle coverage (degrees)	22-35	8-24	8-24	8-24
Polar angle resolution	1 mr	0.6 mr	0.6 mr	0.6 mr
Azimuthal angle resolution	-	5 mr	5 mr	5 mr
Trigger type	Single e^-	Coincidence $e^- + \pi^\pm$	Coincidence $e^- + \pi^\pm$	Triple coincidence $e^- e^- e^+$
Expected DAQ rates	$\sim 20 \text{ kHz} \times 30$	$< 100 \text{ kHz}$	$< 100 \text{ kHz}$	$< 10 \text{ kHz}$
Backgrounds	Negative pions, photons	$(e, \pi^- \pi^\pm)$ $(e, e' K^\pm)$	$(e, \pi^- \pi^\pm)$ $(e, e' K^\pm)$	BH process Random coincidence
Major requirements	Radiation hardness 0.4% Polarimetry π^- contamination Q^2 calibration	Radiation hardness Detector resolution Kaon contamination DAQ	Shielding of <i>sheet-of-flame</i> Target spin flip Kaon contamination	Radiation hardness Detector resolution

1249 3.2 SIDIS-³He Experiments

1250 The E12-10-006 [182] (E12-11-007 [183]) is designed to measure the single/double spin asymme-
1251 tries through the semi-inclusive deep-inelastic scattering (SIDIS) ($e, e'\pi^\pm$) with the SoLID spec-
1252 trometer and the transversely (longitudinally) polarized ³He target. The layout of the experiment is
1253 shown in Fig. 32 and Fig. 33. The entire detector system consists of two parts: the forward-angle
1254 detectors and the large-angle detectors.

1255 At forward angle, there are five layers of GEM detectors inside the coils to provide the forward-
1256 angle tracking, and the first three of them are shared with the large-angle detectors. A 2 m long
1257 light gas Čerenkov counter is installed after the GEM detectors to discriminate the scattered elec-
1258 trons from the produced pions. A 1 m long heavy gas Čerenkov counter right after the light gas
1259 Čerenkov counter can separate kaons and protons from the pions at momenta larger than 2.5 GeV/c.
1260 One layer of Multi-gap Resistive Plate Chamber (MRPC) is placed after the heavy gas Čerenkov
1261 counter to provide timing information and particle identification of hadrons at low momentum ($<$
1262 2.5 GeV/c), as well as to suppress photon background. A “Shashlyk”-type forward-angle Electro-
1263 magnetic calorimeter (FAEC) will be used for electron/pion separation. One layer of scintillator pad
1264 detector (SPD) is placed in front of the FAEC to reject photons and reduce the calorimeter-based
1265 trigger rates. The polar angular coverage for the forward-angle detectors ranges from 8° to 14.8°
1266 and the momentum coverage extends from 0.8 GeV/c to 7.0 GeV/c. A combination of the FAEC,
1267 the gas Čerenkov counter, and the MRPC will be used for electron and pion identifications.

1268 To cover the large electron scattering angles, there are four layers of GEM detectors placed
1269 inside the coils, with the last three layers shared with the forward angle detectors. Following a layer
1270 of SPD, another “Shashlyk”-type large-angle Electromagnetic calorimeter (LAEC) will be placed
1271 inside the coils to separate electrons and hadrons. The large-angle detectors are mainly used for
1272 electron detection in a momentum range of 3.5-6.0 GeV/c where the expected π^-/e ratio smaller
1273 than 1.5. The polar angle coverage ranges from 15.7° to 24°.

1274 The standard Hall A polarized ³He target will be used in its transverse mode. A higher than
1275 60% target polarization with a faster than 20 minutes target spin flip is expected at the full polarized
1276 luminosity of 10^{36} N cm⁻² s⁻¹, which is corresponding to the unpolarized luminosity of 10^{37} N
1277 cm⁻² s⁻¹. The target polarization is expected to be limited by the magnetic field gradient in the
1278 target region, which is dominated by the leakage field from the SoLID magnet. Therefore, the
1279 design of the magnet yokes is important to achieve the required target polarization. As shown
1280 in Fig. 32 and Fig. 33, the target will be located about 70 cm upstream of the front yoke. Two
1281 target collimators will be placed close to two windows of the 40 cm long target in order to reduce
1282 backgrounds generated from both windows. The expected kinematic coverage includes: i) 0.05
1283 $< x < 0.6$ which comprises the majority of the valence quark region; ii) $0.3 < z < 0.7$ in which the
1284 leading order $x - z$ factorization is expected to hold; iii) maximum pion transverse momentum P_T
1285 up to 1 GeV/c, where the TMD framework is valid; and iv) $1 \text{ GeV}^2 < Q^2 < 8 \text{ GeV}^2$ with about 2
1286 GeV^2 coverage in ΔQ^2 at fixed x . These kinematic coverages can be achieved by combining data
1287 with incident electron energies of 11 and 8.8 GeV.

1288 In order to achieve the proposed precision in asymmetries, the negative pion contamination in
1289 the electron sample needs to be controlled to below 1%. At forward angle, it is achieved by a
1290 combination of the FAEC and the light gas Čerenkov detector. At large angle, the LAEC alone will
1291 be enough to provide the required pion rejection, since the expected pion to electron ratio is small.
1292 Furthermore, the coincidence detection of electron and leading pion in the SIDIS kinematics would
1293 further reduce the pion contamination in the electron sample.

1294 The particle identification of the leading pion (forward angle detector only) will be achieved by
1295 a combination of time-of-flight (TOF) from the MRPC and the heavy gas Čerenkov detector. The

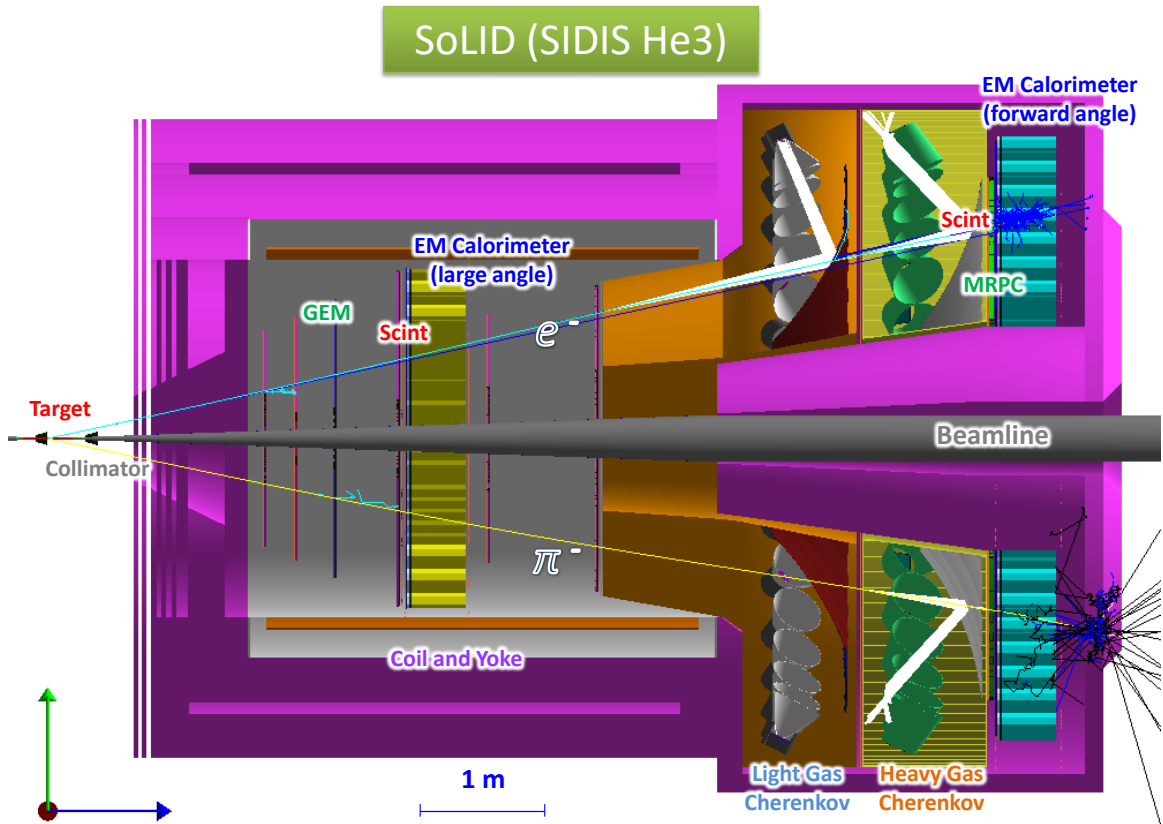


Figure 32: The experimental layout of the SoLID SIDIS- ^3He setup based on the CLEO magnet. The scattered electrons are detected by both forward-angle and large-angle detectors. The leading pions are detected by the forward-angle detector only. The polarized ^3He target will be placed upstream in front of the spectrometer entrance.

1296 electron, kaon, and proton contaminations in the pion samples are all required to be kept below the
 1297 1% level. The electron rejection will be achieved by the combination of the FAEC and the light
 1298 gas Čerenkov counter. With the expected 100ps TOF resolution from the MRPC, a separation of
 1299 3 standard deviations (6 standard deviations from peak to peak) between pions and protons can be
 1300 achieved for momenta up to $4\text{ GeV}/c$. Pions with momenta higher than $2.5\text{ GeV}/c$ will trigger the
 1301 heavy gas Čerenkov detector, while the momentum threshold for kaons to trigger the same detector
 1302 is $7.6\text{ GeV}/c$. Therefore, the heavy gas Čerenkov detector would provide additional rejection of
 1303 protons when the pion momenta are larger than $2.5\text{ GeV}/c$. For pions with momenta below 2.5
 1304 GeV/c , the TOF would provide a separation better than 2 standard deviations (4 standard deviations
 1305 from peak to peak) between pions and kaons. Since the kaon to pion ratio is expected to be about 0.1,
 1306 a combination of the TOF and the heavy gas Čerenkov detector would easily satisfy the requirement
 1307 of below 1% kaons contamination.

1308 The extraction of various TMD asymmetries relies on the ϕ_S and ϕ_h angular dependence of
 1309 the measured single/double spin azimuthal asymmetries in each kinematic bin of the 4-D (x , Q^2 ,
 1310 z , and P_T) phase space. Since the kinematics of interests are in the deep-inelastic-scattering (DIS)
 1311 region, the requirements on the resolution of the reconstructed kinematic variables are modest. For

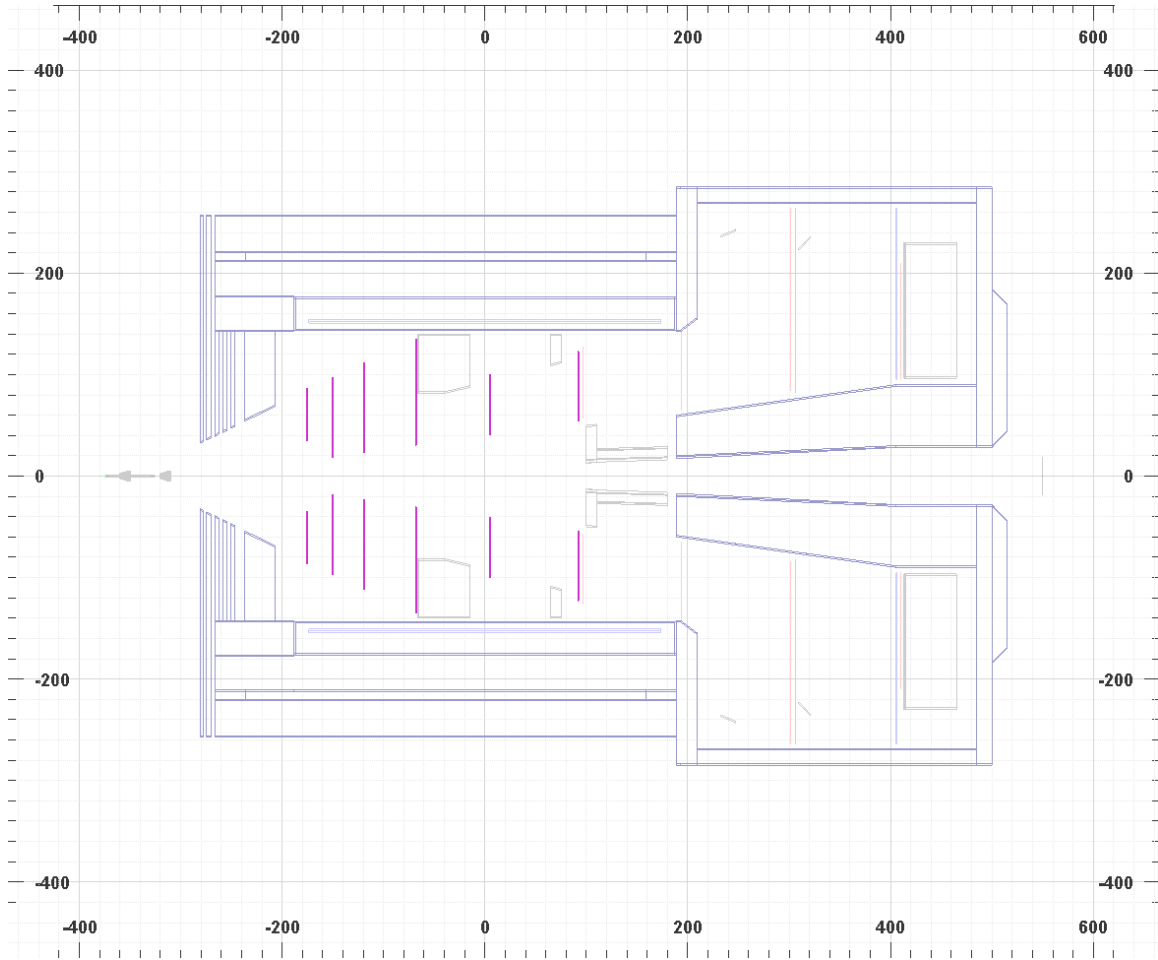


Figure 33: A 2D representation of the experimental layout of SoLID SIDIS-³He setup based on the CLEO magnet.

1312 example, a better than a few percent momentum resolution, a better than a few mrad polar angular
 1313 resolution, a better than 10 mrad azimuthal angular resolution, and a 1-2 cm reconstructed vertex
 1314 resolution would satisfy the needs of these experiments.

1315 With similar reaction channels, E12-10-006 [182], E12-11-007 [183], and E12-11-108 [184]
 1316 (see next section) will share the same design of the DAQ system. The required overall luminosity
 1317 of E12-10-006 and E12-11-007 is 10^{37} N/cm²s⁻¹, which is an order of magnitude higher than that
 1318 of E12-11-108. The goal of the SIDIS DAQ is to satisfy the requirement of ~ 100 kHz trigger rate.

1319 The SIDIS process requires the detection of both the scattered electron and the leading pion.
 1320 Therefore, a single electron trigger or a coincidence trigger of electron and hadron would satisfy
 1321 this need. The electron trigger at the large-angle detectors will be provided by the LAEC at an
 1322 energy threshold of about 3 GeV. Such a trigger would be sensitive to both high energy electrons
 1323 and high energy photons (mostly from the π^0 decay). With the large angle SPD being incorporated
 1324 into the trigger, the electron-like triggers can be significantly suppressed. The electron trigger at the
 1325 forward angle detector will be formed by a coincidence between the light gas Čerenkov detector, the
 1326 FAEC, the SPD and the MRPC. Considering the kinematic information of the scattered electrons
 1327 from the DIS process (e.g. $Q^2 > 1$ GeV²), a position dependent energy threshold with a low limit

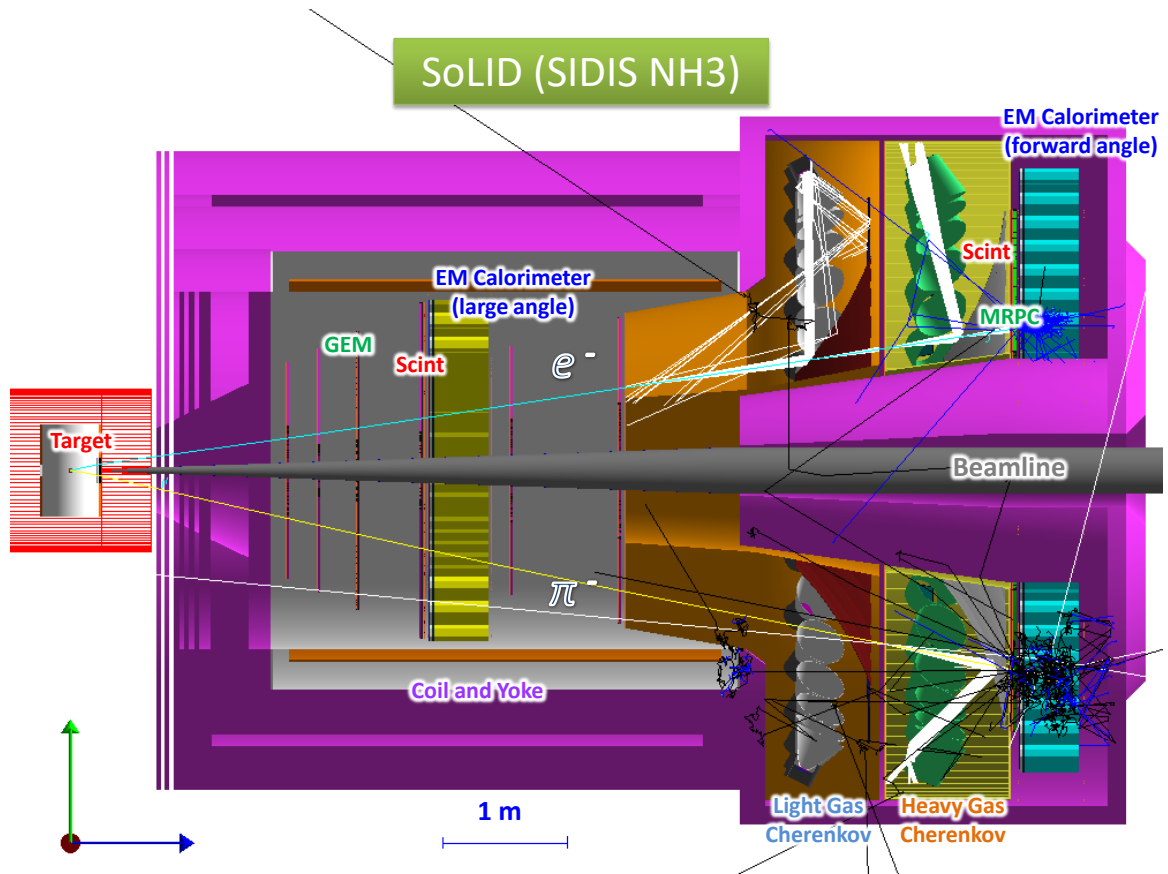


Figure 34: The experimental layout of the SoLID SIDIS-proton setup based on the CLEO magnet. It's the same like SIDIS- ^3He setup, except the ^3He target is replaced by transversely polarized NH_3 target upstream in front of the spectrometer entrance. The scattered electrons are detected by both forward-angle and large-angle detectors. The leading pions are detected by the forward-angle detector only.

1328 at 0.8 GeV in FAEC could significantly reduce the trigger rate. The charged hadron trigger at the
 1329 forward angle will be formed with a coincidence between the FAEC, the SPD and the MRPC. The
 1330 coincidence trigger is given by overlapping the electron trigger and the hadron trigger within a
 1331 narrow time window. If the single electron trigger can not satisfy the requirement of ~ 100 kHz
 1332 trigger rate, the coincidence trigger could retain more SIDIS events. Therefore, it is important to
 1333 include the coincidence trigger in the baseline design of the SIDIS DAQ system.

1334 3.3 SIDIS-proton Experiment

1335 The E12-11-108 [294] is designed to measure the single/double spin asymmetries through the semi-
 1336 inclusive deep-inelastic scattering (SIDIS) ($e, e'\pi^\pm$) with the SoLID spectrometer and a transversely
 1337 polarized proton target. The layout of the experiment is same as ^3He program except the target as
 1338 shown in Fig. 34. The entire detector system consists of two parts: the forward-angle detectors and
 1339 the large-angle detectors. The overall luminosity in this case is smaller compared to that of using
 1340 the polarized ^3He target.

1341 An improved version of JLab/UVa/SLAC polarized NH_3 target (shown in Fig. 35) will be used.

1342 The main upgrade is to replace the aging Helmholtz-coil magnet with a new magnet and to have a
 1343 fast spin-flip capability with the AFP technique to minimize the systematic uncertainty in the single
 1344 spin asymmetry measurement. In order to satisfy the requirements of phase space coverage, the
 1345 new design will further allow both transverse and longitudinal direction to have a nominal forward
 1346 opening of more than $\pm 25^\circ$, while maintaining the same maximum field (5 Tesla) and a uniform
 1347 field region in the center. The target polarization is required to be higher than 70% with the spin flip
 1348 every few hours.

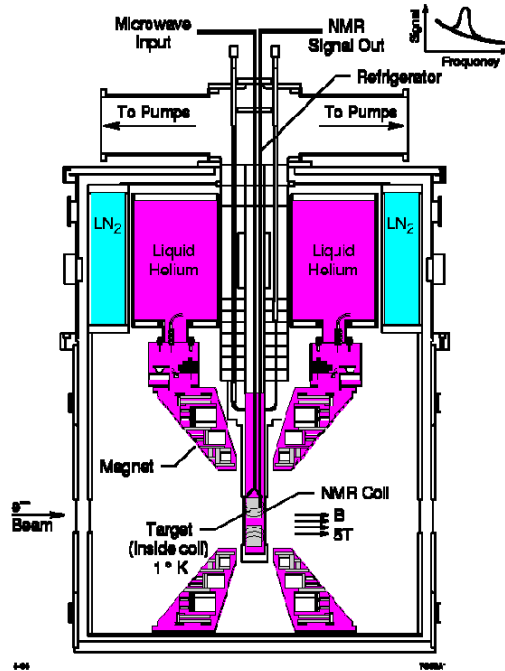


Figure 35: Polarized target system.

1349 Due to the large magnetic field in the transverse direction, this experiment suffers from a dif-
 1350 ferent kind of background compared to the low field polarized ^3He experiment, known as *sheet-*
 1351 *of-flame*. The main feature of such a background is that a very high rate of charged particles with
 1352 momentum range between 1-2 GeV will be localized in a very narrow region of the acceptance.
 1353 Fig 36 shows this background on all six GEM planes in the SoLID. The GEM chambers in regions
 1354 outside of the *sheet-of-flame* location see a background rate of less than 1.0 KHz/mm^2 on, whereas
 1355 the regions inside have much higher rates. In order to handle this background and avoid damage to
 1356 the apparatus, detector sectors in the direct line-of-sight of this *sheet of flame* will be removed or
 1357 turned off during the proton experiment.

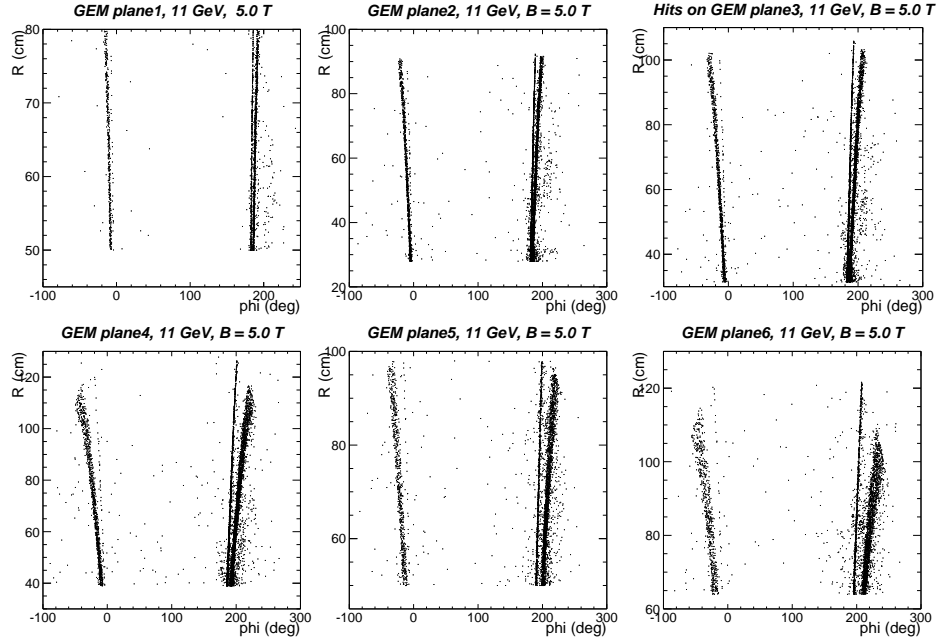


Figure 36: GEANT3 simulation results of background with NH_3 target field ON. The x -axis is the azimuthal angle in lab frame. The y -axis is the radius of GEM chambers (1-6). Narrow regions of high rate (compared to rest of the acceptance) are clearly seen as a function of azimuthal angle ϕ .

1358 3.4 PVDIS Experiment

1359 Experiment E12-10-007 [181] is designed to measure the parity violating asymmetries (A_{PV})
 1360 through the inclusive deep-inelastic scattering (DIS) $p(\vec{e}, e')X$ with the SoLID spectrometer. The
 1361 layout of the experiment is shown in Fig. 37 and Fig. 38. In order to eliminate high energy ($\sim\text{GeV}$)
 1362 photons, a lead baffle will be placed downstream of the target to block direct lines of sight to the
 1363 detector system. The detector system consists of four layers of GEM chambers for particle tracking,
 1364 a 107 cm long light gas Čerenkov counter for electron/pion separation, and a “shashlyk”-type elec-
 1365 tromagnetic calorimeter system for the trigger and additional electron/pion separation. The GEM
 1366 chambers will be divided into two groups, with one group placed in front of the gas Čerenkov
 1367 counter and the other group behind it. This configuration will maximize the detector resolution,
 1368 leading to about 2% momentum and 1 mr polar angle resolutions. The entire detector system will
 1369 be divided into 30 independent sectors in the azimuthal angle.

1370 The polar angle and momentum coverages of the detector system are from 22° to 35° on an
 1371 extended (40 cm) target and from 1.5 GeV/c to 5 GeV/c, respectively. These coverages transform
 1372 into kinematic coverages of $0.2 < x < 0.8$ and $2 (\text{GeV}/c)^2 < Q^2 < 12 (\text{GeV}/c)^2$. The overall
 1373 luminosity is required to be larger than $5 \times 10^{38} \text{ N cm}^{-2} \text{ s}^{-1}$ in order to reach about 0.5% relative
 1374 statistical uncertainties on the parity violating asymmetries A_{PV} in each of the kinematic bins (see.
 1375 Fig. 25). Such a high luminosity places specific requirements on the radiation hardness of the
 1376 detector system.

1377 To leading order, the physics asymmetry A_{PV}^{phys} is related to the measured asymmetry $A_{PV}^{measured}$

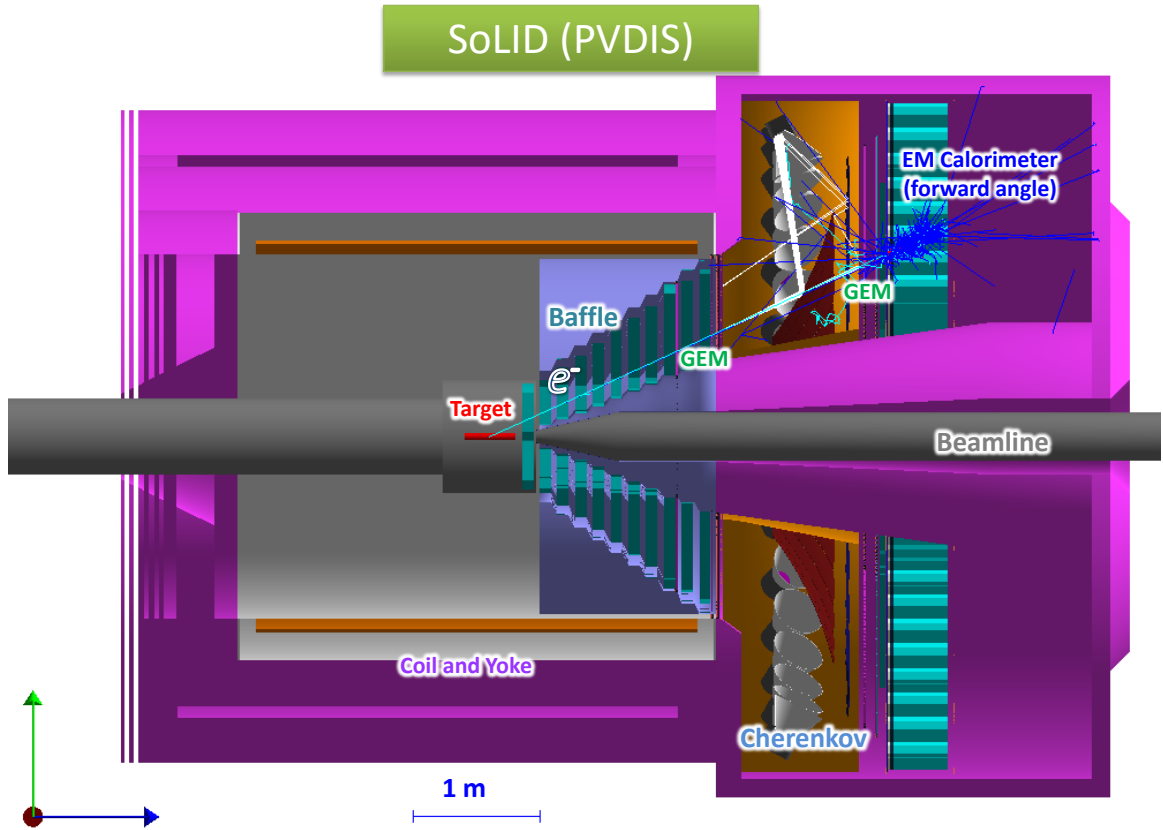


Figure 37: The experimental layout of SoLID PVDIS setup based on the CLEO magnet.

1378 by

$$A_{PV}^{phys} \sim \frac{1}{Q^2 \cdot P_{beam}} \cdot \frac{A_{PV}^{measured} - f \cdot A_{PV}^{\pi^-}}{1 - f} \quad (12)$$

1379 where P_{beam} is the polarization of the electron beam, and f and $A_{PV}^{\pi^-}$ are the pion contamination and
 1380 the parity violating asymmetry of pions, respectively. The proposed high precision measurement of
 1381 A_{PV} (about 0.5% in each kinematic bin) requires high accuracy. The uncertainty of the electron
 1382 beam polarization is required to be smaller than 0.4%. Since A_{PV} for produced pions is expected to
 1383 be similar to that of scattered electrons, the contamination of negative pions in the electron sample
 1384 needs to be determined to about a 10^{-3} level. Furthermore, the uncertainty in Q^2 also must be
 1385 controlled to below 0.1% using a precise and comprehensive optics calibration program.

1386 Since only the scattered electrons are detected in this experiment, each sector of the detector
 1387 system can employ an independent DAQ system. Thus the requirement on the DAQ system for this
 1388 experiment is modest. The average trigger rate for each sector is estimated to be less than 20 kHz,
 1389 leading to a total trigger rate less than 600 kHz.

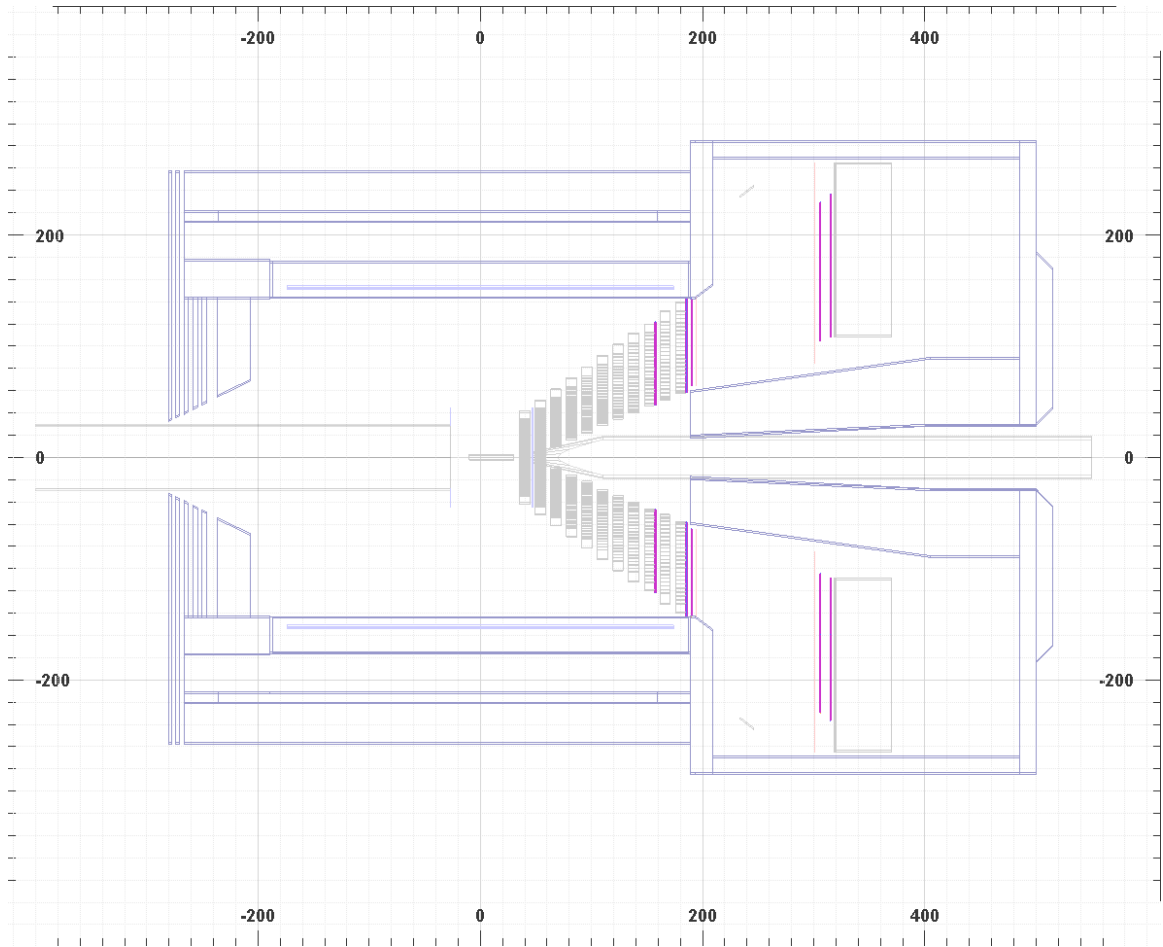


Figure 38: A 2D representation of the experimental layout of SoLID PVDIS.

1390 **3.5 J/ψ Experiment**

1391 The E12-12-006 experiment [196] is designed to measure the cross section of J/ψ electroproduction
 1392 near threshold. The reaction of interest is $e + p \rightarrow e' + J/\Psi(e^-, e^+) + p$ where J/ψ is detected
 1393 through its decay in a lepton pair (e^+, e^-) with 5.94% branching ratio. Primary detection channels
 1394 include a 4-fold coincidence, which consists of a detection of the scattered electron, the recoil
 1395 proton, and the leptonic pair (e^+e^-) from the J/ψ decay, a 3-fold coincidence, which is similar
 1396 to the 4-fold coincidence but without the either scattered electron or the proton detection, and a
 1397 2-fold coincidence of the leptonic pair (e^+e^-) from the J/ψ decay only. In the 3-fold coincidence
 1398 channel, the full kinematics of the recoil proton can be reconstructed through energy and momentum
 1399 conservation. Since the recoil proton is not detected, the total number of events and the kinematic
 1400 coverage are greatly enhanced compared to the 4-fold coincidence channel. Possible background in
 1401 the 3-fold coincidence channel can be investigated fully with the 4-fold coincidence channel which
 1402 offers a better signal to noise ratio. Because the electrons, positrons, as well as protons are required
 1403 to be detected in coincidence, the configuration of SoLID will be similar to that of SIDIS. Fig. 39
 1404 and Fig. 40 illustrates the layout of the experiment. The scattered electron and the recoil proton
 1405 will be detected mostly by the forward angle detector, while the electron-positron pair from J/ψ
 1406 decay will be mostly detected by the large-angle detector. Compared to the SoLID-SIDIS setup,

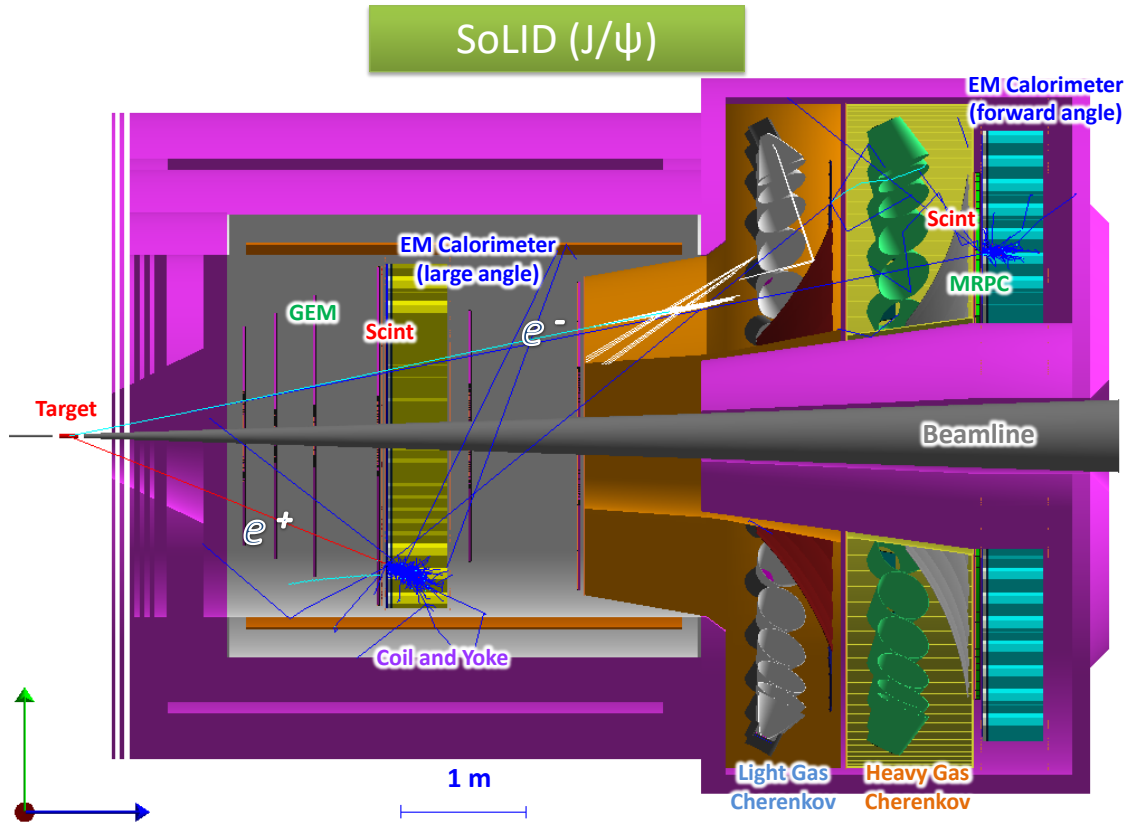


Figure 39: The experimental layout for the SoLID J/ψ setup based on the CLEO magnet. It's the same like SIDIS- ^3He setup, except the ^3He target is replaced by the standard Hall A 15 cm liquid Hydrogen target upstream in front of the spectrometer entrance.

1407 the polarized target will be replaced by the standard Hall A 15 cm liquid Hydrogen target, but its
 1408 position will be located about 35 cm more downstream relative to the target center of the SIDIS
 1409 setup to improve the acceptance.

1410 The approved beam time for this experiment is 60 PAC days at an unpolarized luminosity of 10^{37}
 1411 $\text{N cm}^{-2} \text{s}^{-1}$. The kinematic coverage will be $4.05 \text{ GeV} < W < 4.45 \text{ GeV}$ and $|t - t_{min}| < 2.5$
 1412 GeV^2 . Depending on the cross section model, the expected physics counts with 50 days production
 1413 data for 4-fold (3-fold) coincidence range from $\sim 0.7\text{k}$ (2.1k) to $\sim 2.9\text{k}$ (8.1k) at the proposed lumi-
 1414 nosity. Since this measurement is limited by statistics due to the rare nature of the J/ψ production
 1415 near threshold process, a higher luminosity ($> 10^{37} \text{ N cm}^{-2} \text{ s}^{-1}$) is strongly desired.

1416 The primary trigger is a triple coincidence of scattered electron, J/ψ decay electron, and J/ψ
 1417 decay positron. With a 100 ns coincidence window, the trigger rate would be dominated by the
 1418 random coincidence events with a rate of about 3 kHz, which is far below the required ~ 100 kHz
 1419 trigger rate of SoLID-SIDIS. Therefore, the main requirement of SoLID- J/ψ is the capability of
 1420 forming hardware coincidence trigger.

1421 Since we are interested in the exclusive electroproduction of J/ψ , the resolution of the J/ψ
 1422 setup is important in rejecting different backgrounds. Currently the expected resolutions are similar
 1423 between SIDIS and J/ψ setups and it would satisfy the requirement of this experiment. We are
 1424 working on improving the J/ψ resolution further.

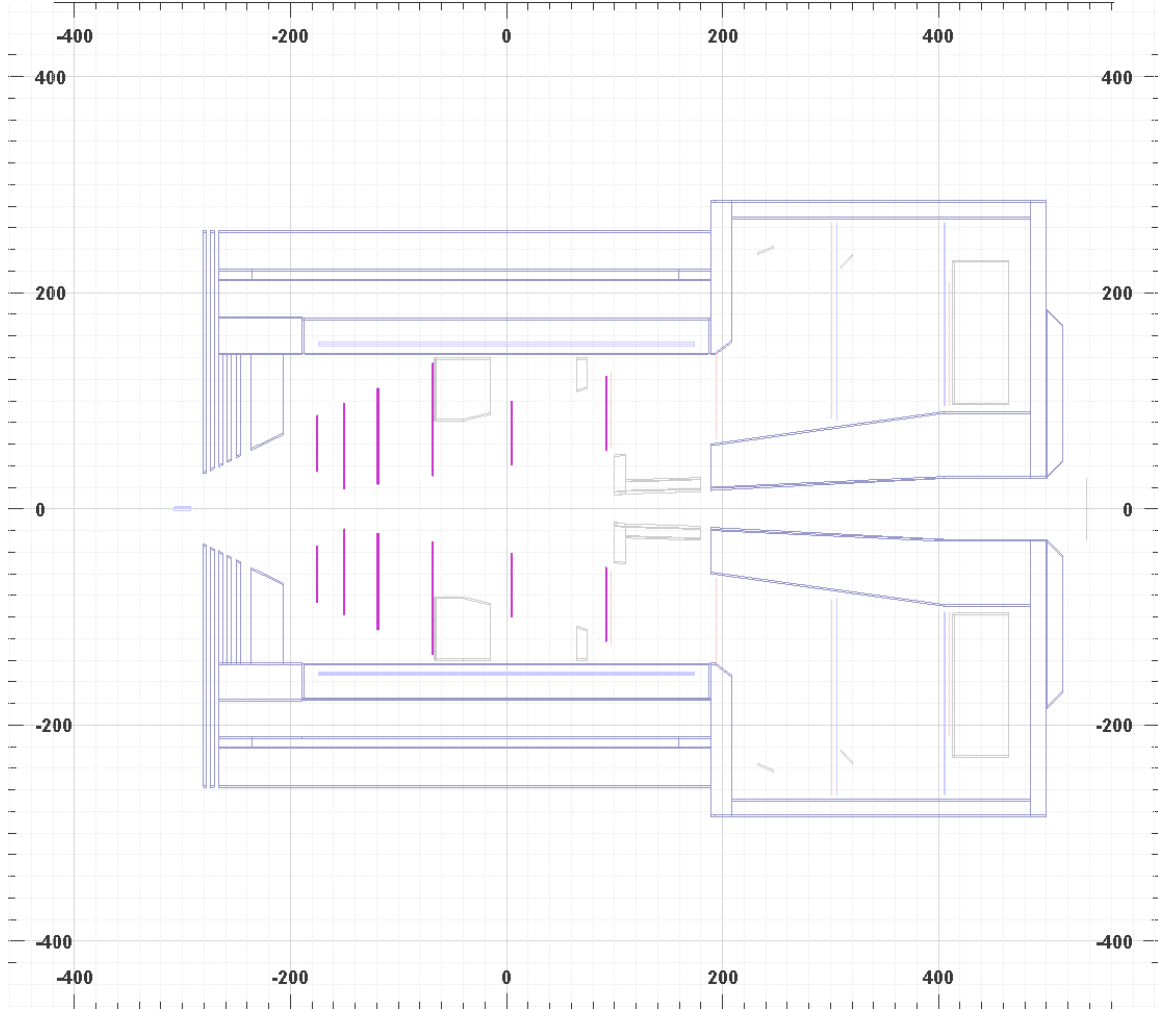


Figure 40: A 2D representation of the experimental layout of SoLID J/ψ setup.

1425 The particle identification of the recoil proton for the 4-fold coincidence relies on the time-
 1426 of-flight (TOF) from the MRPC. The highest momentum of the recoil proton is about 3 GeV/c.
 1427 With the designed 100 ps resolution in TOF, protons can be separated from kaons at 2 standard
 1428 deviations (4 standard deviations from peak to peak). In addition, protons can be separated from
 1429 pions at 6 standard deviations (12 standard deviations from peak to peak). The requirement on the
 1430 exclusive kinematics in the off-line data analysis would further strengthen the particle identification
 1431 of protons.

1432 There are two major types of backgrounds. The main physics background originates from the
 1433 Bethe-Heitler (BH) process. At the proposed kinematics, the BH background is expected to be
 1434 smaller than the physics J/ψ events by 1-2 order of magnitude in average ². The cross section
 1435 associated with the BH background can be directly measured by choosing the invariant mass of the
 1436 electron-positron pair to be away from the J/ψ peak. The other major background is the random
 1437 coincidence of a J/ψ (normally photo-produced) and a scattered electron. The random coinci-

²Due to the rapid decrease of the cross section near threshold for the physics J/ψ events, the BH background becomes comparable at low W.

1438 dence background is expected to be 1-2 orders of magnitude smaller than the physics events with
1439 the proposed setup. In addition, the random coincidence backgrounds can also be directly mea-
1440 sured/subtracted through the commonly used off-window method.

1441 **4 Magnet**

1442 **4.1 Requirements**

1443 The SoLID spectrometer is designed to have large acceptance in polar angle, azimuthal angle, and
1444 momentum acceptance, and also operate at high luminosity. A solenoid magnet is a natural choice in
1445 this case. The magnetic field is symmetric around the beamline, confining the copious low energy
1446 charged background particles to the beam pipe region. The detectors are placed symmetrically
1447 around the beamline, both within the solenoid and in the end cap region. The approved experiments
1448 all have some requirements on the magnet. They are summarized below:

1449 • The PVDIS experiment requires polar angle coverage for the center of the target from 22° to
1450 35° . Its hydrogen and deuterium targets can operate in the magnetic field. To operate the detectors
1451 at the design luminosity of $10^{39}/\text{cm}^2/\text{s}$, a set of baffles is required to block unwanted photons and
1452 hadrons originating in the target. The magnetic field must then be strong enough to spiral the several
1453 GeV DIS electrons through the gaps in the baffles and also provide sufficient curvature in the tracks
1454 so that their momentum can be reconstructed. Both requirements can be met with a field integral
1455 along the flight path on order of 2.5 T-m.

1456 • Both SIDIS proton and neutron experiments need polar angle coverage from 8° to 24° . The
1457 ^3He and NH_3 targets must be located just upstream of the solenoid where the fringe fields before
1458 additional shielding are on the order of 5 G. The NH_3 targets require a uniform 5 T field and the
1459 ^3He targets require uniform fields on the order of a 25 Gauss. There are two sets of detectors. The
1460 forward detectors, located in the end cap, cover particles with angles below 15° . This requires the
1461 solenoid to be on the order of 3-4 m long. The large angle detectors are located near the center of
1462 the magnet, requiring a diameter on the order of 3 m. The field integral needs to be on the order of
1463 5 T-m in order to provide sufficient momentum resolution from the GEM tracking system.

1464 • The J/ψ experiment must detect the electron-positron pair from the J/Ψ decay as well as the
1465 scattered electron. With a liquid hydrogen target placed upstream of the magnet, the configuration
1466 for the SIDIS experiment meets the requirements.

1467 Overall, the ideal SoLID solenoid needs to have an outer radius < 3 m to fit in the experimental
1468 hall, an inner radius > 1 m, a length of 3-4 m, and a field integral on the order of 5 T-m.

1469 **4.2 SoLID magnet**

1470 We have chosen the CLEO II magnet for the SoLID spectrometer. It is a solenoidal magnet with a
1471 uniform axial central field of 1.5 T, a large inner space with a clear bore diameter of 2.9 m and a
1472 coil of 3.1 m diameter. With a coil length of 3.5 m, its magnetic field uniformity is $\pm 0.2\%$. It was
1473 built in the 1980s by Oxford in England and installed for CLEO II in 1989 [198, 199].

1474 The coil is made of $5 \times 16 \text{ mm}^2$ aluminum stabilized superconductor and run at 3266 A with
1475 an average current density of 1.2 MA/m. The large conductor size provides simpler construction
1476 and ease of protection. A 3.8 m long cryostat encloses the coil and cools it with a thermosyphon
1477 system. The return yoke has 3 layers with 36 cm thickness each and is octagonally divided. There
1478 are 2 collars 60 cm thick supporting not only the return yokes, but also the coil with 4 rods. The
1479 magnet has good stability, low cryogenic heat load, passive cooling, and passive protection. This
1480 gave it the flexibility to be frequently de-energized for maintenance and accelerator studies. It has
1481 been kept in good condition since stopping beam. The coils and cryostat of the CLEO-II magnet
1482 have arrived at JLab in 2016 and the exterior steel is being shipped as of Spring 2017. To use the
1483 CLEO magnet for SoLID, we will reuse the coil and cryogenic system, but the downstream collar
1484 and return yoke will be modified to allow the PVDIS acceptance up to 35° . New endcap and front

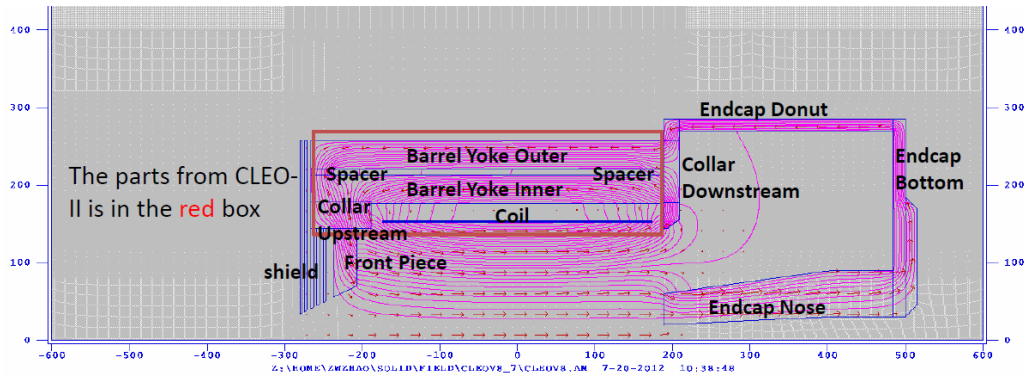


Figure 41: Design of the CLEO II magnet yoke for SoLID.

1485 pieces will be fabricated.

1486 The design of the yoke for SoLID with the CLEO II magnet is shown in Figure 41. There are
 1487 two layers of barrel flux return and an upstream collar which are kept from the original CLEO-II
 1488 magnet. The simulation has shown that the original third layer of barrel flux return is not needed
 1489 for SoLID and the field in the rest of two layers is well below saturation. The downstream collar
 1490 is either modified or a new part. All other parts including the endcap, the front piece and the target
 1491 shielding need to be built.

1492 The B field for the CLEO II magnet with the SoLID yoke is shown in Figure 42. The strongest
 1493 field is within the solenoid and drops sharply in the endcap and upstream opening. The magnetic
 1494 field was calculated using the 2D Poisson Superfish program.

1495 The B_z and B_r fields along the beamline are shown in Figure 43. The B_z field at the center is
 1496 about 1.4 T, dropping to 0.8 T at the exit of the coil.

1497 The axial force for the 3 section of coils and all parts of yoke are shown in Figure 44. There are
 1498 two strong forces compressing the coil. These forces can be balanced so that the net force on the
 1499 coil is small. It can be adjusted by moving the location of the front piece, where the force varies by
 1500 3–5 t/cm.

1501 4.3 Planned Modifications

1502 The CLEO magnet will require some modifications to its design for use in the SoLID experiments.
 1503 Much of the CLEO magnet will be reused in its original condition. However, SoLID will not use
 1504 the outermost muon ring. It will use the inner two rings, each consisting of 8 slabs of iron to make
 1505 up the 8-sided ring. Each of these slabs will have to be shortened to allow the proper position of
 1506 the endcap. The original upstream coil collar will be reused. Spacers between the slabs will also be
 1507 reused. The downstream coil collar will be modified if an economical way of reducing its thickness
 1508 can be found without wasting a majority of its unwanted material. If a solution is not found then a
 1509 new downstream coil collar will be created. Additional pieces of iron will need to be fabricated to
 1510 allow for the proper mating of the endcap with the barrel yoke. The existing outer and inner shower
 1511 counters that mount inside of the coil collars do not appear to be reusable as the upstream coil cup
 1512 that will reside inside the upstream coil collar. All supporting structure for the magnet barrel yoke
 1513 and detector endcap will be new fabrications. Please refer to the study in Ref. [197].

1514 The endcap, which consists of the outer cylindrical ring, the backplate, and endcap nose, will
 1515 all be made from new material. The endcap is designed to be part of the magnetic flux return yoke
 1516 and house the downstream forward angle detector package. The endcap will be split vertically into

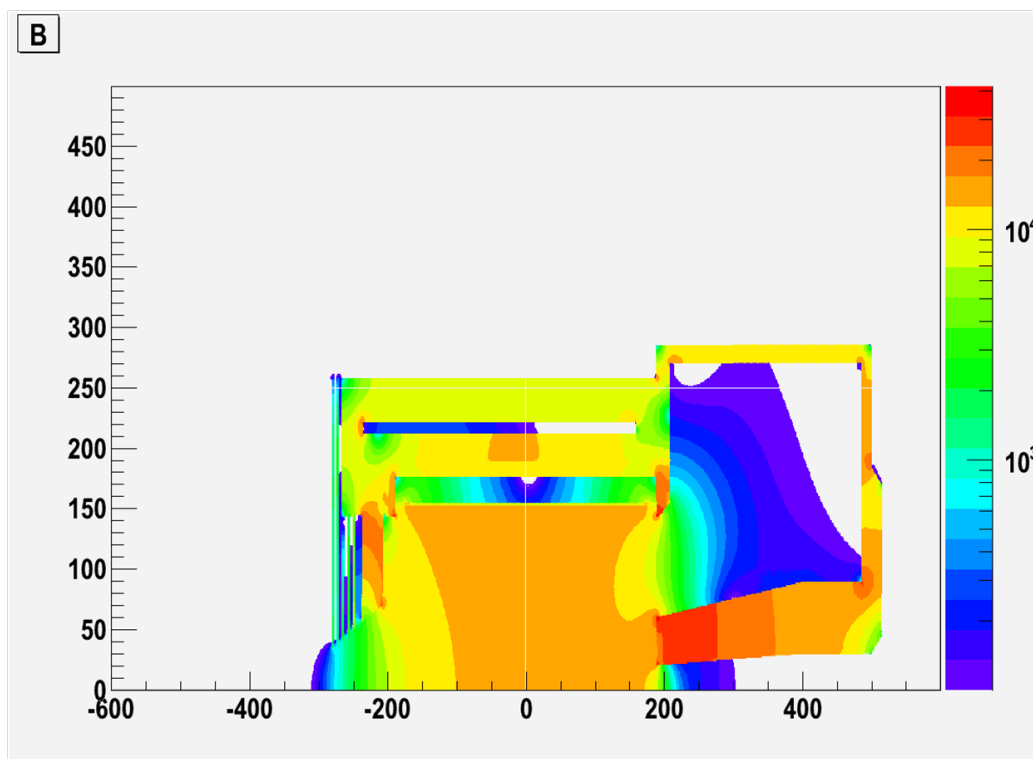


Figure 42: SoLID CLEO magnet field $B > 100G$.

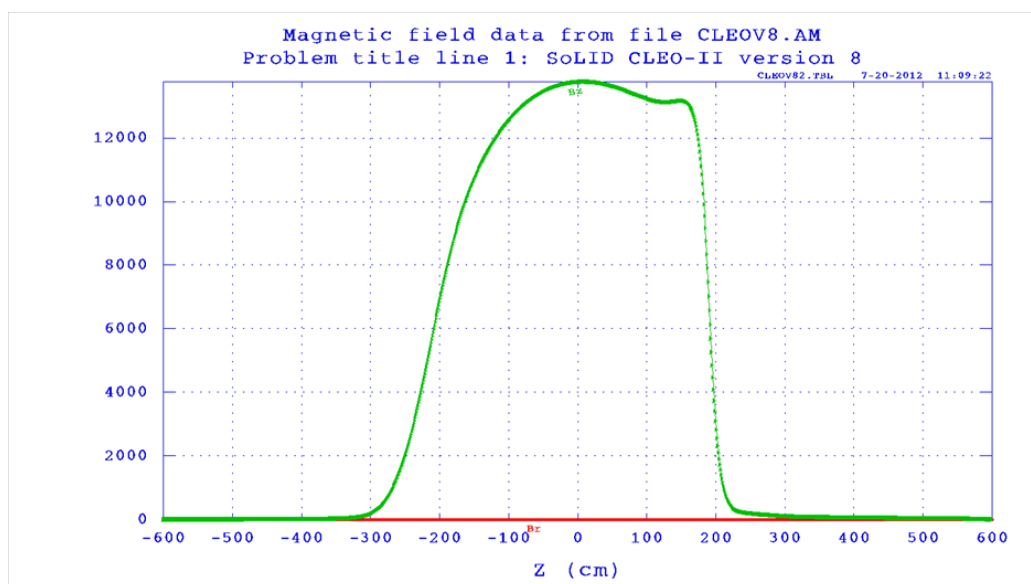


Figure 43: SoLID CLEO magnet field along beamline.

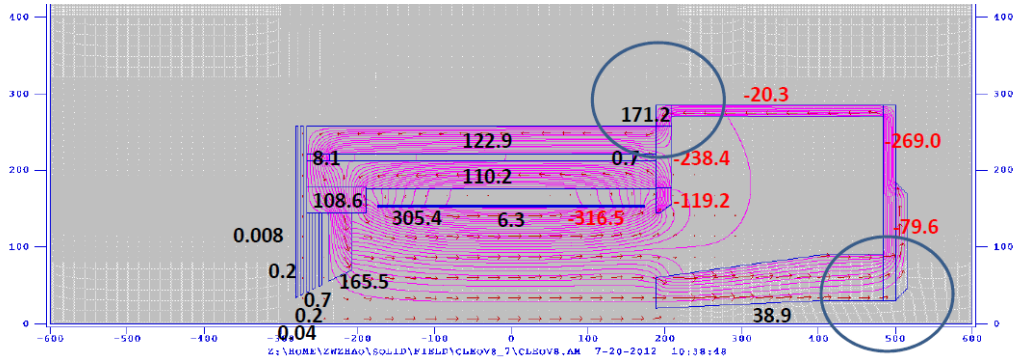


Figure 44: SoLID CLEO axial force in metric t. The two circles show where the force changes direction.

1517 halves and capable of separation to allow for access to the detector package, see Figure 45. The
 1518 endcap nose with a secondary backing plate will be a cast two piece design to allow for separation.
 1519 Each section of the nose will bolt to the main backplate which consists of a two piece round disk.
 1520 The two halves of the cylindrical outer ring will bolt to the corresponding backplate. The structural
 1521 support and motion mechanism for the endcap will be discussed in Section 18.

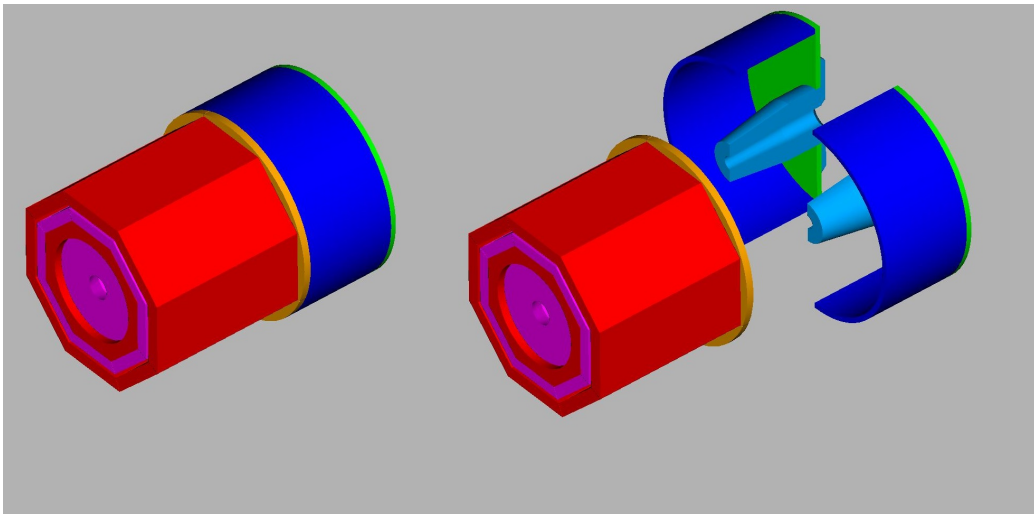


Figure 45: The endcap will be split vertically and also have the capability of separating in the lateral direction

1522 4.4 Current Status and Planned Test

1523 Jefferson Lab will develop a cold test requirements document and implementation plan prior to
 1524 installing the magnet in Hall A. The cold test will be done without the iron yoke and thus at reduced
 1525 operating parameters.

1526 A new magnet power supply cost has been added to the SoLID costs. Cost basis is from recent
 1527 purchases.

1528 Mapping the magnetic field and evaluating the data will require an additional 4–6 weeks in

1529 schedule with use of 2 technicians and 1 scientist/engineer for the duration. Additional funding will
1530 be required for the mapping apparatus, \$200k.

1531 Scheduling of the SoLID experiments will allow 1 year prior to installation for testing of the
1532 magnet.

1533 We have included the cost for new power supply, controls, transfer lines and supports. The only
1534 reuse will be some magnet yoke steel and the cryostat.

1535 Work on the dismantling of the CLEO II magnet was started by Cornell University in the sum-
1536 mer of 2015 with the disconnection of power, cryogen and control lines for the magnet from the
1537 building infrastructure. Several of the large return iron blocks were also removed to provide practi-
1538 cal experience for the Cornell rigging crew and the project management team to develop a compre-
1539 hensive schedule for the 2016 removal.

1540 The 2016 summer down period started with the removal of the 700 liter helium dewar and outer
1541 steel cladding. The leads, cooling supply and return lines as well as instrumentation cables needed
1542 to be severed at the top of the service turret to allow the dewar to be lifted away. Next, the beamline
1543 and detectors that resided in the bore of the magnet were uninstalled and the return iron was removed
1544 layer by layer.

1545 Upon completion of the iron removal, including the coil collars, the axial transport brackets
1546 were installed to protect the coils during movement. The cryostat housing the coils could then be
1547 moved to the transport frame. The service turret and neck could then be removed from the top of the
1548 cryostat. The neck required disassembly to separate the continuous leads from the thermal shielding
1549 and cooling lines. The above mentioned disassembly steps adhered to the recommendations of the
1550 Oxford Operating Manual for the CLEO II Magnet. The leads were packaged for protection and
1551 secured to the side of the cryostat for safe transport. A stainless steel cover was fabricated and
1552 attached to the flange on the top of the cryostat providing protection for the ends and the cryo lines
1553 and leads. Any remaining openings were sealed to prevent contaminants from entering the vacuum
1554 space. Prior to loading on a flatbed truck the entire cryostat was wrapped in fire retardant marine
1555 grade shrink wrap to keep the unit weathertight for the trip to JLAB.

1556 After arrival at JLAB the cryostat was rolled into the high bay area of the Test Lab for climate
1557 controlled storage until future use. Inspection indicated the cryostat remained sealed through trans-
1558 port. Loads on the magnet were monitored during transport using (2) three-axis accelerometers and
1559 remained under the maximum safe threshold indicated in the Oxford Manual. The two coil collars
1560 accompanied the cryostat in the November 2016 delivery and were stored in the Test Lab, as shown
1561 in Figure 46. The remaining return iron was stored at Cornell and will be shipped in fiscal year
1562 2017. The Test Plan for characterizing the magnet and integrating it into the JLAB systems remains
1563 to be developed.



Figure 46: CLEO II magnet at JLab.

1564 **5 Targets**

1565 There are five approved SoLID experiments. Two semi-inclusive DIS experiments (E12-10-006
1566 and E12-11-007) use a polarized ^3He target with the achieved performance. One SIDIS experi-
1567 ment (E12-11-108) uses a transversely polarized proton (NH_3) target. The parity-violating DIS
1568 experiment (E12-10-007) uses a 40-cm cryogenic liquid deuterium (hydrogen) target system. The
1569 J/Psi experiment uses the standard cryogenic liquid hydrogen target. The following subsections will
1570 describe the polarized ^3He target, the polarized proton (NH_3) target and the PVDIS cryotargets.

1571 **5.1 Polarized ^3He Target**

1572 The polarized ^3He target is based on the technique of spin-exchange optical pumping of hybrid
1573 Rb-K alkali atoms. Such a target was used successfully in the recently completed SIDIS experi-
1574 ment [200] with a 6-GeV electron beam at JLab. Three sets of Helmholtz coils provide a 25 Gauss
1575 holding field for any direction, supporting polarization in transverse (for E12-10-006) or longitu-
1576 dinal (for E12-11-007) direction. Target cells were 40-cm long with density of about 10 amg (10
1577 atm at 0°). The luminosity was about 10^{36} nuclei/s/cm with a beam current of $15 \mu\text{A}$. An in-beam
1578 polarization of up to 60% was achieved. Both achieved luminosity and figure-of-merit are the
1579 world-best so far. Two kinds of polarimetry, NMR and EPR (paramagnetic-Resonance), were used
1580 to measure the polarization of the target. The precision for each method was about 5% (relative) and
1581 the methods agreed well within uncertainties. It is expected to be able to reach 3% with the planned
1582 improvements.

1583 Frequent target polarization direction reversal is needed to minimize target-spin-correlated sys-
1584 tematic uncertainties. The fast target spin reversal was achieved in a few seconds for the 6 GeV
1585 SIDIS experiment by using RF AFP technique. The frequency of the spin reversal was kept to 20
1586 minutes to minimize the polarization loss due to AFP. The additional polarization loss due to fre-
1587 quent spin reversal was kept at $< 10\%$ (relative). The above quoted maximum in-beam polarization
1588 achieved for the 6 GeV experiment (up to 60%) included the loss due to spin reversal. A new method
1589 using field rotation for spin reversal was tested and a nearly no polarization-loss result was achieved
1590 and will result in an improved performance. It will allow to have more frequent (a few minutes
1591 instead of 20 minutes) spin reversal to help further improve the target-spin-correlated systematics.

1592 The upstream endcap plate will keep the magnetic field and its gradients under control in the
1593 target region. In this design, the absolute magnetic field strength in the target region is about a few
1594 Gauss with field gradients 50 mG/cm. Correction coils around the target will further reduce field
1595 gradients to the desired level of 30 mG/cm.

1596 A collimator, similar to the one used in 6 GeV experiment, will be placed next to the target cell
1597 window to minimize the target cell contribution to the total events.

1598 In addition to the polarized ^3He target, the current target system has a multi-foil ^{12}C target for
1599 spectrometer optics study, a BeO target for beam tuning and a reference target cell system, which
1600 allows to have different target gases, hydrogen, deuterium, ^3He and nitrogen, be used to measure
1601 unpolarized cross sections, for calibration and dilution study.

1602 Upgrades are planned for other polarized ^3He experiments before the SoLID experiments. These
1603 upgrades are not required for the SoLID experiments but will benefit them.

1604 **5.2 Transversely Polarized Proton Target**

1605 The SoLID collaboration proposes to measure single spin asymmetries in the semi-inclusive, deep-
1606 inelastic ($e, e'\pi^\pm$) reaction using a transversely polarized proton target. The target to be used is the

1607 dynamically polarized ammonia target that has been used at SLAC and at Jefferson on numerous
1608 occasions [201]. Its last use was in 2012 for the g2p/Gep experiments, which took place in Hall
1609 A [202]. Proton luminosities of $10^{35} \text{ cm}^{-2}\text{s}^{-1}$ have been achieved with this target, in conjunction
1610 with electron beam currents up to 100 nA. In order to meet requirements of the SoLID measurements
1611 however, a new superconducting magnet must be procured, as discussed below.

1612 Dynamic nuclear polarization (DNP) has been used to polarize solid targets for nuclear and
1613 particle experiments for more than four decades. To realize DNP, a paramagnetic species is im-
1614 planted into the target material, either by dissolving a stable radical into the material (if the latter
1615 is liquid at room temperature), or by producing radicals directly within the material using ionizing
1616 radiation. The unpaired electrons are highly polarized by cooling the sample to a low temperature
1617 and exposing it to a high magnetic field. For example, at the 1 K and 5 T operating conditions of
1618 the JLab target, the electron polarization is -99.8%. Off-center microwave saturation of the radicals
1619 Electron Spin Resonance (ESR) frequency is used to transfer this polarization to nearby nuclear
1620 spins, with one or more mechanisms, such as the solid effect, thermal mixing or the cross effect, be-
1621 ing responsible for the polarization transfer. Spin diffusion then transports the nuclear polarization
1622 throughout the bulk of the sample. The polarization may be positive or negative, depending upon
1623 whether the microwave frequency is below or above the ESR frequency. In well-designed systems,
1624 proton polarizations exceeding 95% [203] and deuteron polarizations approaching 90% [204] have
1625 been achieved.

1626 Frozen ammonia (NH_3) has been the target material of choice for electron beam experiments at
1627 Jefferson Lab. Proton polarizations in excess of 90% are routinely achieved in ammonia, and it has
1628 a relatively high ratio of polarizable-to-nonpolarizable nucleons (17.6%). Additionally, ammonia
1629 displays a very high resistance to radiation damage, and simply warming the material to about
1630 100 K for a few minutes can largely repair the damage that does occur. Prior to the experiment,
1631 paramagnetic radicals (chiefly NH_2) are created within the ammonia by irradiating the material
1632 (under liquid argon) with an electron beam. For convenience, this irradiation is typically done off
1633 site, and the material is then stored under liquid nitrogen until required for the experiment. The JLab
1634 target system, as utilized in Hall A, is shown in Fig 47. It consists of a 5 T split-coil superconducting
1635 magnet, a ^4He evaporation refrigerator with a cooling power of about 1 W at 1 K, and a target
1636 insert containing two samples of frozen ammonia along with additional targets for background and
1637 dilution studies. These reside in a purpose-built, evacuated scattering chamber with thin windows
1638 around its perimeter for beam entrance and exit. Equipment outside the chamber includes a large set
1639 of vacuum pumps for the evaporation refrigerator, microwave electronics for polarizing the target
1640 sample, and a NMR system for measuring its polarization. Liquid helium is provided to the target
1641 from a nearby 500 L dewar.

1642 Before its use in the g2p/Gep experiments, numerous upgrades were made to the polarized target
1643 in order to improve its performance, reliability, and safety:

- 1644 • An entirely new refrigerator was constructed at JLab according to the safety regulations dic-
1645 tated by 10 CFR 851;
- 1646 • The quench-relief piping system for the superconducting magnet was upgraded to replace
1647 leaking rubber seals with copper gaskets, and also made compliant to 10 CFR 851;
- 1648 • The pumping system and controls were overhauled;
- 1649 • A more robust sample insert and motion mechanism were constructed to address problems
1650 that were encountered in previous experiments;

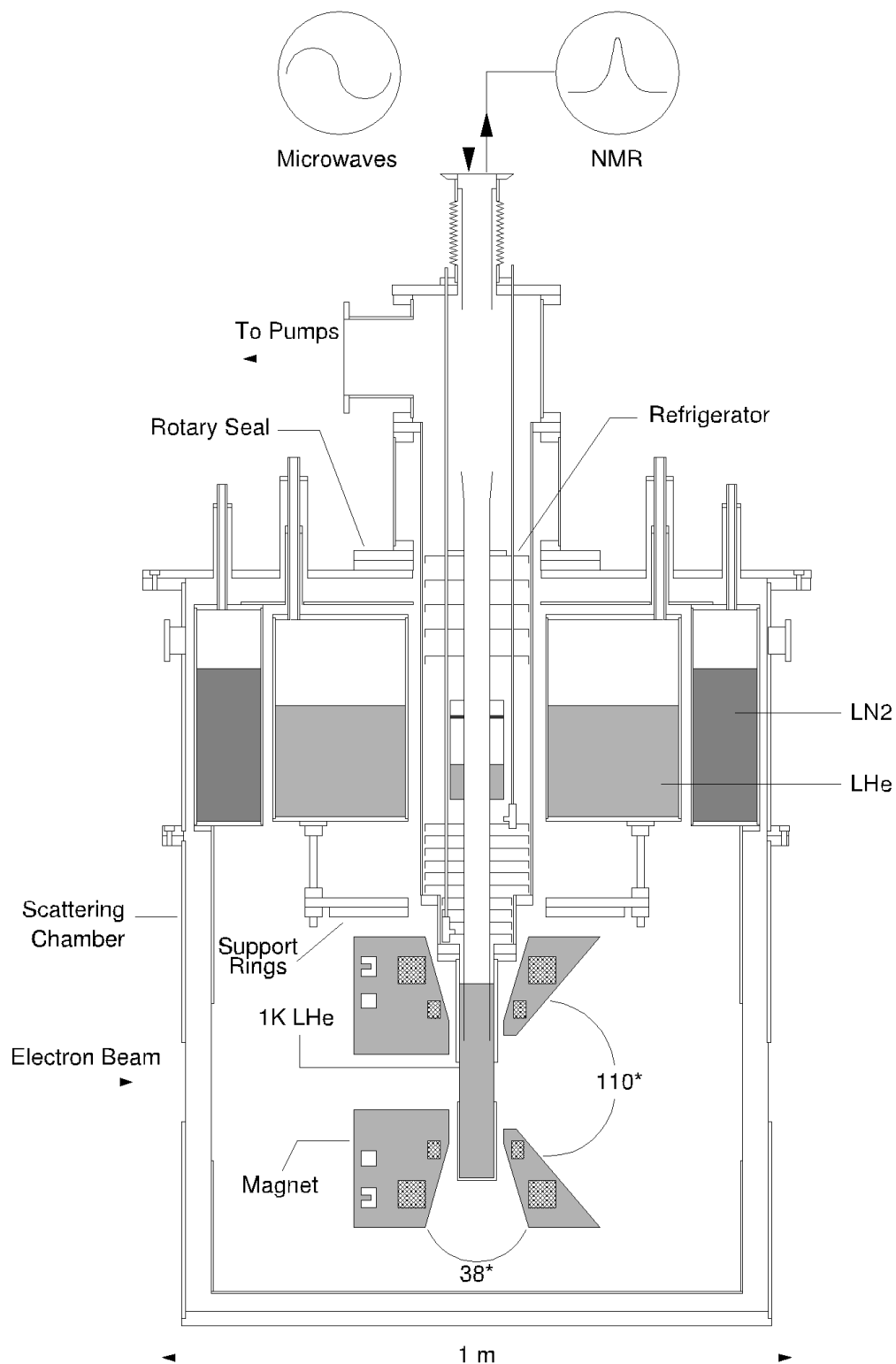


Figure 47: The dynamically polarized target, as utilized in Hall A. The cryostat can rotate 90° about the vertical axis, thus providing either longitudinal or transverse polarization with respect to the electron beam. The longitudinal orientation is shown.

- 1651 • A new rotary vacuum seal was implemented that significantly reduces the time required to
1652 rotate the magnet between its longitudinal and transverse orientations. With the new seal,
1653 there is no longer a need to disconnect the refrigerator pumping line, nor remove and replace
1654 the sample insert;
- 1655 • The 5 T magnet suffered irreparable damage during the final systems tests, and was replaced
1656 with a similar magnet removed from the Hall B polarized target [205].

1657 It should be noted that both the original and Hall B magnets were primarily designed to provide
1658 longitudinal polarization, while still permitting limited use for transverse polarization. As such,
1659 each magnet possesses an opening angle of 110° ($\pm 55^\circ$) in the direction parallel to the magnetic
1660 field, compared to only $\pm 17^\circ$ perpendicular to it (see Fig. 47). Because the SoLID proposal requests
1661 transverse polarization with an opening angle $\pm 25^\circ$ or greater, a new magnet will be necessary.

1662 Oxford Instruments (manufacturer of both the Hall B and original magnet) has performed a
1663 detailed feasibility study and concludes that they can build a 5 T split-coil magnet with both a $\pm 25^\circ$
1664 split angle and the homogeneity required for DNP [206]. The SoLID collaboration and JLab Target
1665 Group will work alongside the eventual vendor to ensure the magnet can be easily incorporated into
1666 the existing JLab cryostat. This will greatly reduce the time and cost required to field a transversely
1667 polarized target for SoLID.

1668 **5.3 Cryogenic Target for PVDIS**

1669 The proposed target consists of 40 cm liquid hydrogen/deuterium cell. This cell will be filled with
1670 either hydrogen or deuterium as needed. The heat load on this target will be much more modest
1671 than the Qweak target that was employed from 2010 to 2012 at JLAB. A conceptual design of the
1672 target is shown in the figure. The current concept allows for remote placement of a single cryogenic
1673 cell and a dummy cell with several solid targets necessary for calibrations. Such a target has the
1674 following basic elements:

- 1675 1. Heat exchanger (HX)
- 1676 2. Insulating vacuum chamber (IVC)
- 1677 3. Target stack
 - 1678 (a) Cell
 - 1679 (b) Dummy target
 - 1680 (c) Solid targets
- 1681 4. Recirculating pump
- 1682 5. Cryostat
- 1683 6. Temperature stabilizing heater
- 1684 7. Positioning system
- 1685 8. Gas handling system and gas storage
- 1686 9. Instrumentation
- 1687 10. Depolarizer

1688 All components in the system must comply with 10 CFR 851 with regard to pressure, electrical,
1689 and fire safety. The majority of these components will remain outside the high magnetic field of the
1690 solenoid. The cell and connecting piping together with the rest of the target stack are necessarily
1691 placed in the magnetic field of the solenoid. Selection of materials for these components shall
1692 consider this.

1693 The insulating vacuum chamber will consist of two main sections. One section will be inside
1694 the bore of the solenoid and a section similar to the IVC for the standard Hall A cryogenic target
1695 will be upstream of the magnet. This later section will contain the motion system, heat exchanger,
1696 etc. The section in the magnet will only contain the target stack and connecting piping. Materials
1697 for the chamber section inside the solenoid must be compatible with the magnetic field inside the
1698 solenoid. The exit of the chamber will be compatible with the acceptance of the detector.

1699 Careful attention must be given to the design of the cell. While the requirements of this target
1700 regarding density fluctuations are much less stringent than those imposed on either the Qweak or G0
1701 targets, it is of some concern. Analysis of the cell design using computational fluid dynamics (CFD)
1702 will be employed to ensure an acceptable cell design. Based on experience with previous targets
1703 at JLAB, noise associated with density fluctuations is not expected to be significant compared to
1704 counting statistics. To reduce the background from Al-e- asymmetries, the sections of the cell upon
1705 which the beam impinges will be thin. Thicknesses of 120 μm are commonly available and are
1706 adequate for the needs of the experiment. The remainder of the cell will be designed to optimize
1707 boiling performance, detector acceptance, and pressure safety. High strength aluminum alloys such
1708 as AL-7075 and AL-2219 (used on welded components) shall be used on critical parts of the cell.
1709 Through extensive experience it has been shown that cell and cell block assemblies are much more
1710 reliable when welds and mechanical joints such as conflat (CF) are employed. This avoids the
1711 issues with solder and other sealing techniques. This approach also accelerates the design and
1712 prototyping phase and simplifies testing and assembly.

1713 To avoid interference between the exiting particles at maximum scattering angle of 35° and the
1714 upper and lower target components, the cell and dummy target must be separated by a minimum of
1715 28 cm plus half the width of the cell and dummy target. Similarly the dummy and the solid targets
1716 (positioned at $Z = 0$) will require 14 cm of separation plus half the width of the dummy target and
1717 first solid target frame. A total stack height of more than 70 cm is expected. The motion system
1718 must accommodate this height and allow for some alignment adjustments. The standard Hall A
1719 cryogenic target has over 70 cm of travel, thus a similar mechanism will be suitable.

1720 Dummy and solid targets can be selected and installed as needed. The thickness of the dummy
1721 target will be chosen to match the radiation length of the liquid cell. Solid targets required for optics
1722 studies, background measurements and alignment checks will also be installed.

1723 The cryogenic liquid hydrogen and deuterium target must accommodate a beam current of
1724 50 μA on a 40 cm long cell. The estimated beam heat load for this is $\sim 800\text{W}$. The pump, heater
1725 overhead, transfer line and other losses require an additional estimated $\sim 250\text{W}$. During the Qweak
1726 experiment, more than 3 kW of power at 20K was dissipated by the heat exchanger. This design
1727 made use of both 15K and 4K refrigerant from the End Station Refrigerator (ESR) and the Central
1728 Helium Liquefier (CHL). A careful study of the target heat load and ESR/CHL refrigerators will
1729 be necessary to design the heat exchanger. However, it is expected that the heat exchanger will not
1730 need to dissipate more than 1500 W which includes a comfortable operating margin. Operationally,
1731 only $\sim 1\text{kW}$ of refrigeration will be required by one or more refrigerator.

1732 The hydrogen and deuterium target fluids may become slightly polarized in the magnetic field
1733 of the solenoid. This would result in an asymmetry unrelated to the physics of interest. This effect
1734 can be mitigated in the case of deuterium with an RF-depolarizer. In the case of hydrogen, pure
1735 para-hydrogen would reduce this effect. A catalyst (such as an iron oxide bed) would enhance the

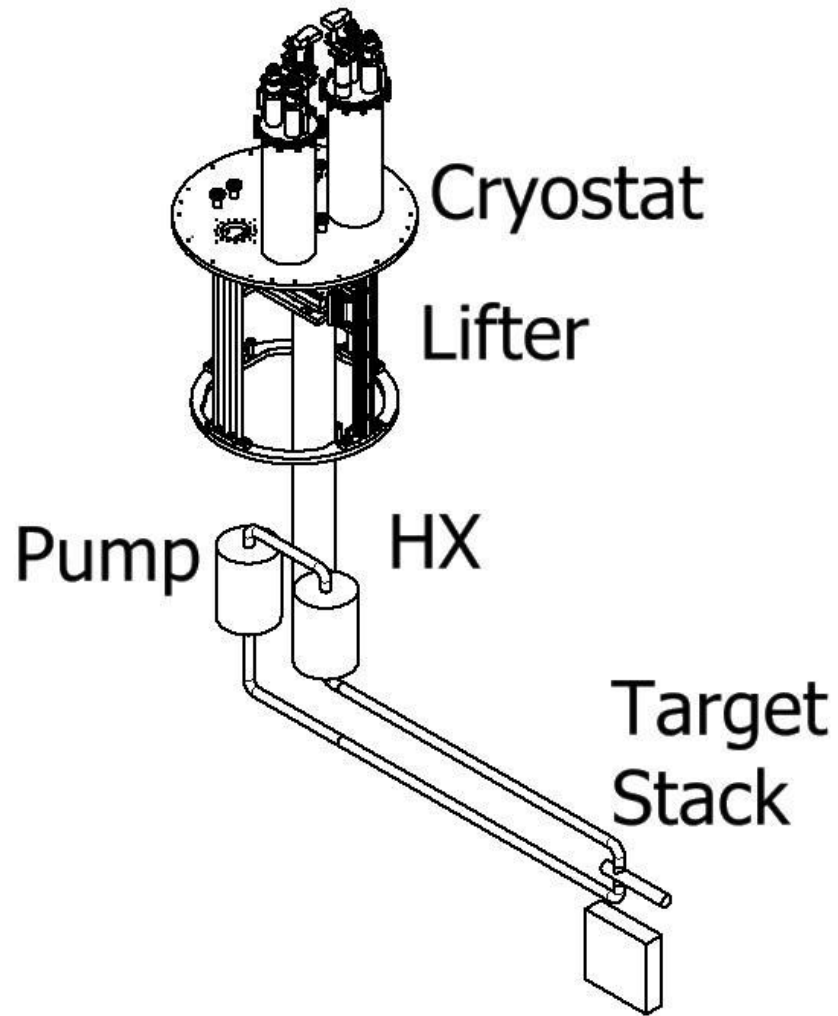


Figure 48: Cryogenic Target for PVDIS

1736 para to ortho fraction.

1737 6 Baffles

1738 In order for the detectors in the PVDIS experiment to operate at the design luminosity, a set of
1739 baffles is required that passes a reasonable fraction of the DIS electrons while blocking as much of
1740 the background as possible. The baffles provide curved channels through which only the spiraling
1741 high energy negative particles can pass. Most line-of sight photons and positively charged hadrons
1742 are blocked.

1743 The design of the baffles requires careful optimization since there are many sources of back-
1744 ground and the different detectors respond differently to the different backgrounds. The dominant
1745 background in the GEM's is soft photons, especially those between 1 and 2 MeV. The GEM's are rel-
1746 atively inefficient for lower energy photons. Sources of these photons include beam bremsstrahlung,
1747 forward radiation from wide-angle 30-100 MeV Møller electrons generated in the target, and pho-
1748 tons from showers in the baffles induced by neutral pions. The light gas Cerenkov is sensitive to pair
1749 production from photons above 20 MeV or so which can come from neutral pions produced in the
1750 target to bremsstrahlung from the wide-angle Møller electrons. The ECal is sensitive the positive
1751 hadron punch-through and high energy photons from neutral pion decay.

1752 To design the baffles for a specific magnetic field and detector configuration, ray-tracing of
1753 simulated DIS electrons is performed for the desired momentum range. For a uniform solenoidal
1754 field, high momentum electrons have a trajectory in $\phi - z$ space that is linear and the $\theta - z$ trajectory
1755 is independent of the field. The design process takes simulated electrons in a realistic field and
1756 exploits this approximate behavior to define pathways for ranges of electron momenta. This allows
1757 for a relatively simple design process involving an extended target where one considers radial rings
1758 of restricted scattering angle and places blocking material to only allow these trajectories. The
1759 number of sectors to be used for this experiment is driven by the azimuthal angle ϕ traversed by the
1760 minimum momentum particles, which for these kinematics is about 12° , hence 30 sectors.

1761 To block line-of-sight photons, there must be sufficient material to block line particles that have
1762 a constant trajectory in ϕ . Due to the fact that the target is extended, the simple model does not
1763 completely hold, allowing some fraction to leak through.

1764 We recently have undertaken studies of our baffle design including evaluation of materials, ac-
1765 ceptance, and background reduction. While our baseline baffle design uses lead, other possibilities
1766 include copper or tungsten. These materials vary by a factor of four in radiation length. The varia-
1767 tion in nuclear interaction length is smaller, as shown in Table 9. Tungsten's high density and short
1768 interaction length is advantageous, however its cost is higher, and solid tungsten is difficult to ma-
1769 chine. An easier approach to construction would be to use powdered tungsten which can be easily
1770 molded and glued.

1771 We have performed studies of trigger rates in the EC, rates of neutrons entering the EC, and rates
1772 of photons striking the last GEM with baffles constructed of different materials, but with the same
1773 geometry. All show fairly small differences, seen in Table 9. Lead provides a slightly lower photon
1774 rate than copper, while copper's hadron rates are slightly better. Powdered tungsten has a density
1775 only about 60% of solid tungsten, and consequently provides little or no performance advantage
1776 over lead.

1777 An important background is photons from π^0 decay interacting in the baffles. When photons
1778 strike the baffles close to the "hot" edge of a slit, shower products can escape into the slit and from
1779 there thread through the slits in the remaining baffle plates. A modification we have considered is to
1780 remove material amounting to 0.6° in angular width from the hot edges on baffle plates 2, 4, 6, 8 and
1781 10, allowing photons that would have hit near these slits to strike instead further from the hot edges
1782 on the next plate. Our simulations show a 16% reduction in photon rates above $p = 1 \text{ GeV}/c$, and
1783 26% reduction for $p > 10 \text{ GeV}/c$. Removal of this material would increase the pion background,

	Copper	Lead	Tungsten powder	Solid tungsten
Radiation length (cm)	1.436	0.5612	0.583	0.3504
Nuclear interaction length (cm)	15.32	17.59	16.58	9.946
Machinability	Easy	Soft, needs support	Easy to mold and glue	Hard
Cost	Low	Low	High	High
EC trigger rate (kHz)	4.78×10^3	5.45×10^3	5.25×10^3	4.59×10^3
Neutron rate in EC (kHz)	3.35×10^7	4.7×10^7	4.0×10^7	2.9×10^7
Photon rate in last GEM (GHz/sector)	2.98	2.59	—	—

Table 9: Properties and performance of copper, lead, tungsten powder and solid tungsten as baffle materials.

1784 but by less than 10%.

1785 We have performed detailed studies of track trajectories through the baffles to identify places
1786 where improvements in the baffle geometry can be made. One finding was that, for the upstream
1787 baffle plates, the solid ring at the inner radius and an angular constriction at small radius interfere
1788 with the acceptance for electrons produced at the downstream end of the target. For vertices at the
1789 upstream end of the target, acceptance was being lost due to the too-small outer radii of the upstream
1790 baffle plates.

1791 Based on these studies we have developed an improved baffle design, shown in in Fig. 49.
1792 Inner rings and angular constrictions on the first few plates have been removed, and outer radii
1793 of these plates have been increased. Shapes of the slits in all the plates were optimized, keeping
1794 the overall aperture in polar angle unchanged, but tightening up slits that were slightly too wide.
1795 The outcome of this program was a geometrical design, having modest acceptance improvements
1796 over our previous baffles while not significantly affecting photon rejection, which we believe to be
1797 optimal; see Figures 50 and 51.

1798 A detailed study of the activation of different materials suitable for the baffle has been carried
1799 out. Radiation levels for each material were studied for three different durations of beam exposure,
1800 and possible shielding configurations were evaluated. The final selection of the baffle material will
1801 likely be driven less by performance and more by activation and ease of construction.

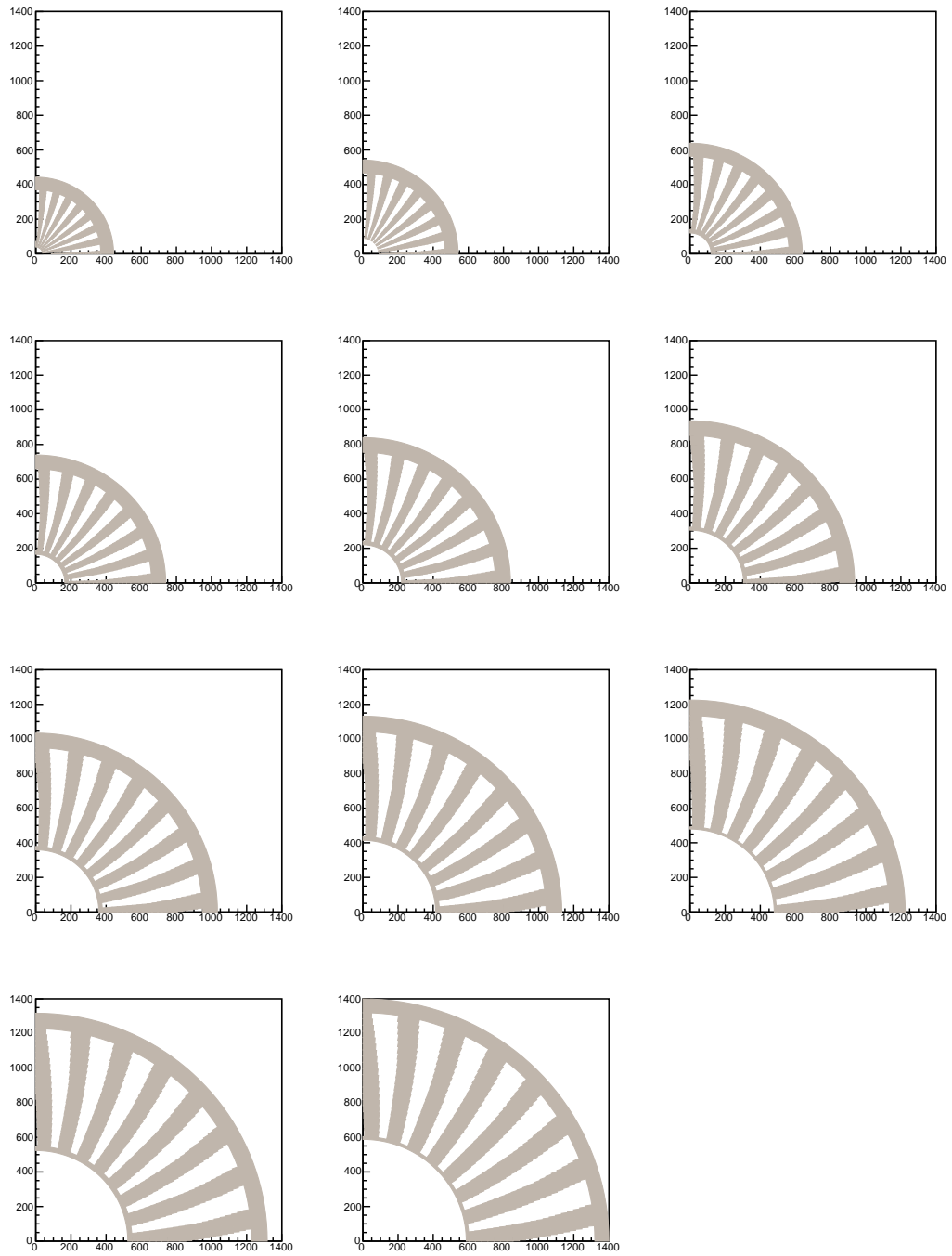


Figure 49: Face on views (first quadrant only) of the 11 plates in the PVDIS baffle system.

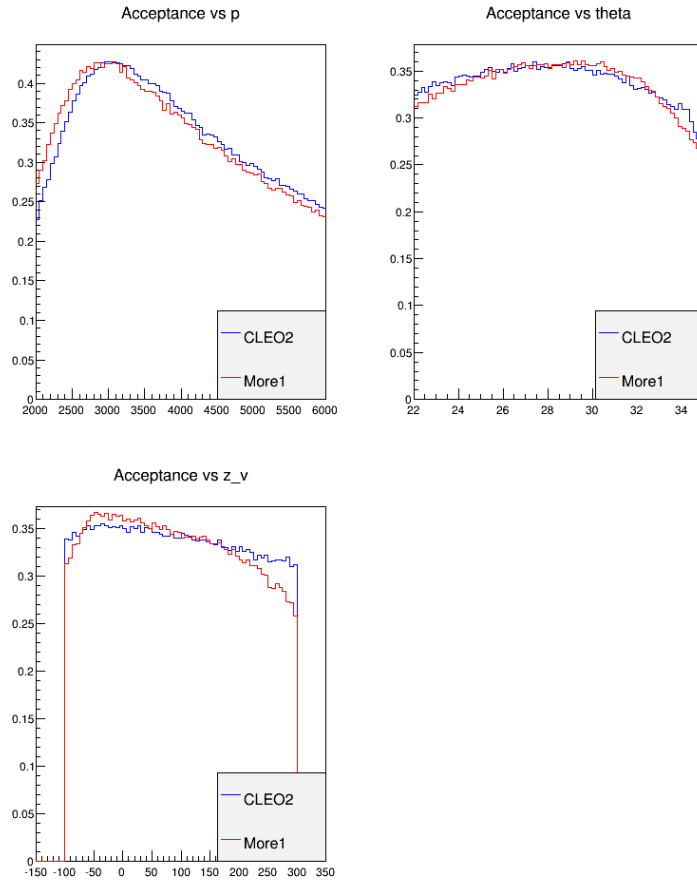


Figure 50: Geometric acceptance of the PVDIS baffles for DIS electrons with $Q^2 > 6 \text{ GeV}^2$, $W > 2 \text{ GeV}$, and $x_{bj} > 0.55$ versus momentum (top left), scattering angle (top right), and vertex position (bottom left). Blue (red) lines are acceptance for the optimized (previous) baffle design.

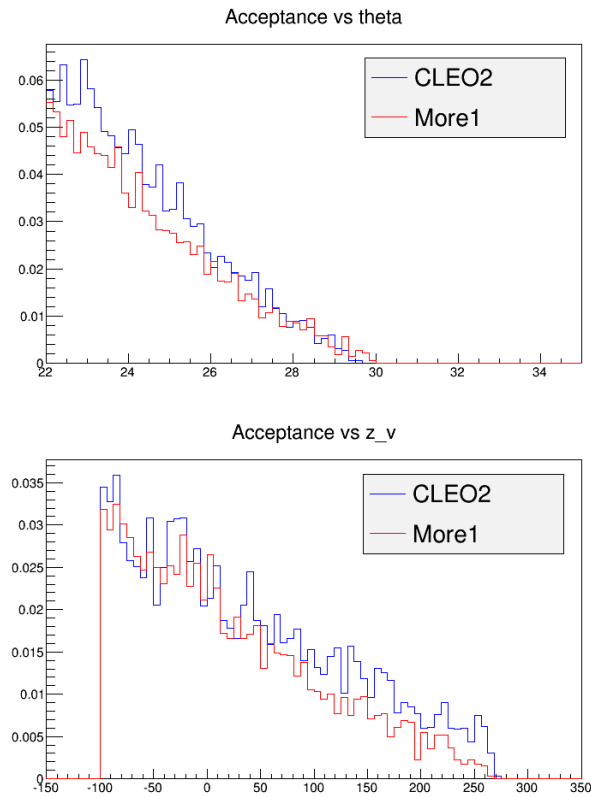


Figure 51: Geometric acceptance of the PVDIS baffles for photons versus scattering angle (top), and vertex position (bottom). Blue (red) lines are acceptance for the optimized (previous) baffle design.

1802 7 GEM Tracker

1803 7.1 Design

1804 The SoLID spectrometer requires high resolution track reconstruction under high rate conditions
1805 over a large area. A cost effective solution for such requirements is provided by the Gas Elec-
1806 tron Multiplier (GEM) technology invented by F. Sauli [207] in 1997. The GEM is based on gas
1807 avalanche multiplication within small holes (on a scale of $100\ \mu\text{m}$), etched in a Kapton foil with a
1808 thin layer of copper on both sides. The avalanche is confined in the hole resulting in fast (about 10
1809 ns rise time) signals. Several GEM foils (amplification stages) can be cascaded to achieve high gain
1810 and stability in operation. The relatively small transparency of GEM foils reduces the occurrence
1811 of secondary avalanches in cascaded GEM chambers. All these properties result in very high rate
1812 capabilities of up to $100\ \text{MHz per cm}^2$ and an excellent position resolution of $70\ \mu\text{m}$. Fig. 53 illus-
1813 trates the principle of operation of a triple (three foil) GEM chamber. Triple GEM chambers were
successfully used in the COMPASS experiment at CERN [208].

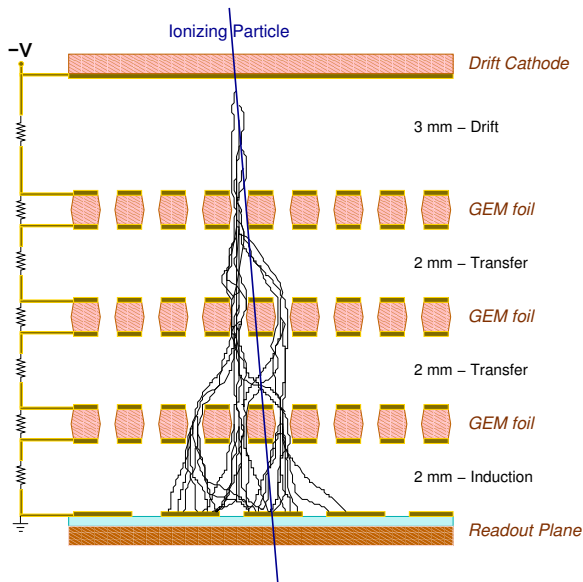


Figure 52: Principle of triple GEM operation.

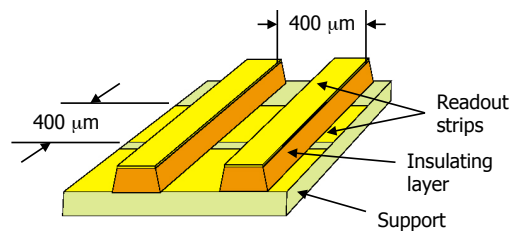


Figure 53: 3D view of the readout board.

1814 For the PVDIS configuration of SoLID, detector locations 1, 2, 3, 4, and 5 will be instrumented
1815 with GEM chambers. Table 10 summarizes the parameters of the SoLID PVDIS GEM chambers.
1816 At each detector location there will be 30 trapezoidal GEM chamber modules, one for each sector
1817 defined by the baffles. The GEM modules will have an angular width of 12° with the readout stripes
1818 parallel to the two edges of the sector, so that the stripes from the two readout layers are at a 12°
1819 stereo angle. The readout pitch for locations 1, 2 and 3 will be $0.4\ \text{mm}$ while the pitch for locations
1820 4 and 5 will be $0.6\ \text{mm}$. Figure 54 shows the GEM module arrangement for one of the detector
1821 locations of the PVDIS configuration. Figures 55 and 56 show the details of the GEM module
1822 edges and mounting at the inner and outer radii of the SoLID detector wheel.
1823

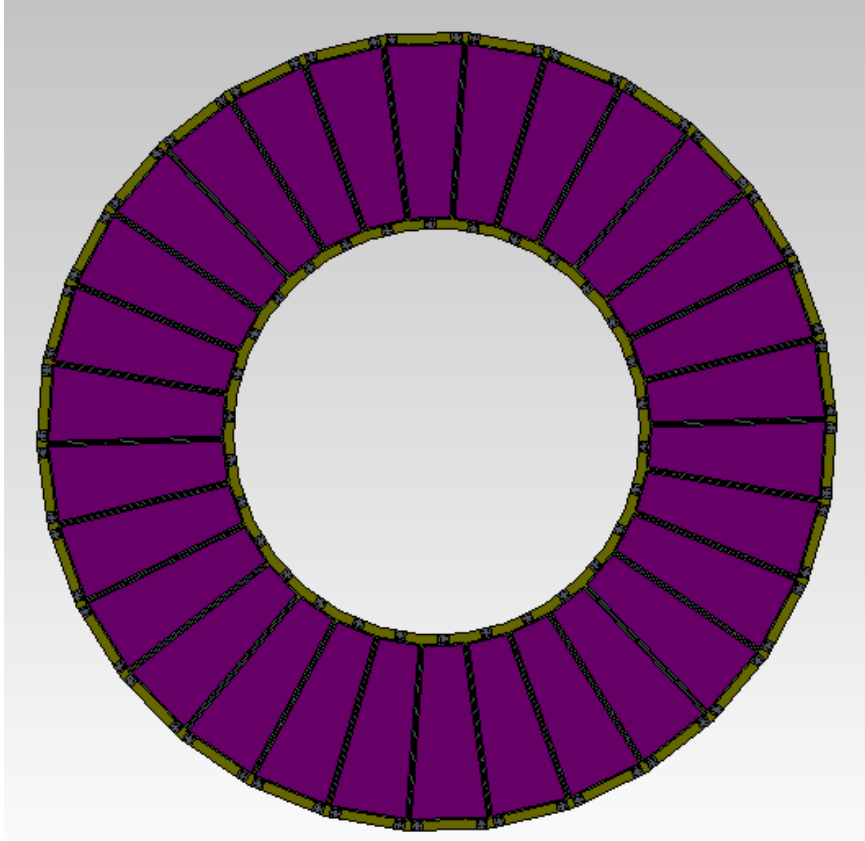


Figure 54: The GEM module arrangement at one of the detector locations of the SoLID PVDIS configuration

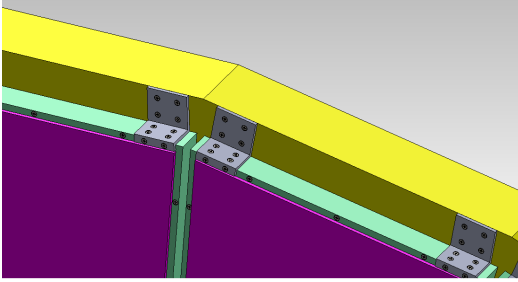


Figure 55: GEM module mounting at the outer edge of a GEM ring in the PVDIS configuration.

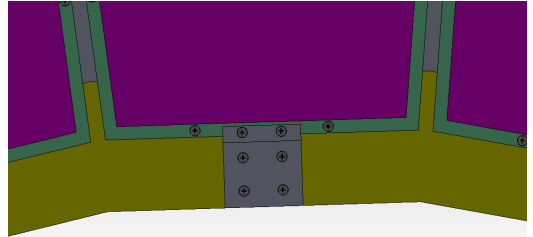


Figure 56: GEM module mounting at the inner edge.

Location	Z (cm)	R_{min} (cm)	R_{max} (cm)	Surface (m ²)	# chan
1	157.5	51	118	3.6	24 k
2	185.5	62	136	4.6	30 k
3	190	65	140	4.8	36 k
4	306	111	221	11.5	35 k
5	315	115	228	12.2	38 k
Total				≈ 36.6	≈ 164 k

Table 10: The locations, sizes and number of readout channels of GEM detectors for the SoLID PVDIS configuration

1824 The SIDIS configuration of SoLID calls for detector locations 1, 2, 3, 4, 5, and 6 instrumented
 1825 with GEM modules. Table 11 summarizes the parameters of the SIDIS GEM chambers. While
 1826 the number of detector stations is higher in the SIDIS configuration, the inner and outer radii of
 1827 the detector wheels are significantly smaller compared to the PVDIS configuration. Furthermore,
 1828 since there are no baffles in the SIDIS configuration, the active detection area has to cover the
 1829 the entire surface area of each detector wheel. In order to meet these requirements, the SIDIS
 1830 detector configuration will be set up by arranging the GEM modules from the PVDIS configuration
 1831 in an overlapping two-wheel arrangement at each detector station as indicated in Figure 57. In this
 1832 arrangement, 20 modules cover the entire active area of each detector station.

Location	Z (cm)	R_{min} (cm)	R_{max} (cm)	Surface (m ²)	# chan
1	-175	36	87	2.0	24 k
2	-150	21	98	2.9	30 k
3	-119	25	112	3.7	33 k
4	-68	32	135	5.4	28 k
5	5	42	100	2.6	20 k
6	92	55	123	3.8	26 k
Total				≈ 20.4	≈ 161 k

Table 11: The locations, sizes and number of readout channels of GEM detectors for the SoLID SIDIS configuration

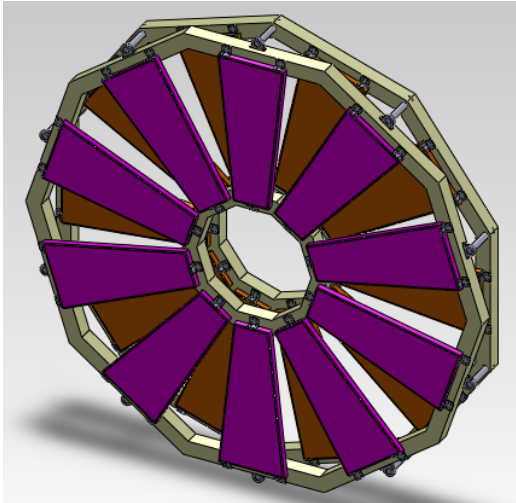


Figure 57: The GEM module arrangement at one of the detector locations of the SoLID SIDIS configuration

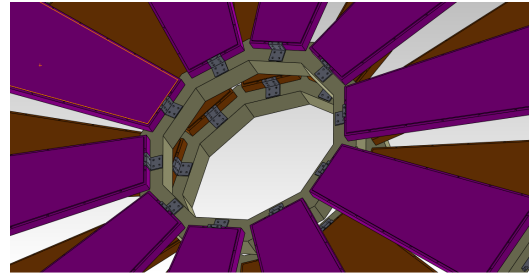


Figure 58: GEM module mounting at the inner edge of the ring in the SIDIS configuration

1833 Figure 59 shows the detailed design for a GEM module of the size proposed for SoLID. The
 1834 “wings” shown in the frames are to support the frames during chamber assembly; they will be
 1835 removed once the chamber is completed. The 2D readout plane will be glued on the bottom plate
 1836 (shown in cyan). This plate, made out of a 3 mm thick honeycomb structure material, also provides

1837 structural rigidity to the GEM chamber. All other frames are made out of Permaglass³ with 8 mm
 1838 wide sides. The spacers shown within the active area are for keeping the GEM foils from touching
 1839 each other; these spacers are approximately 300 μm wide and contribute only about 1% reduction
 1840 to the active area of the chamber. The GEM foils are mounted on the 3 light green frames, while the
 1841 drift cathode is glued on the red frame. A thin gas window is glued on the orange frame.

1842 Figure 60 shows the concept for the 2D readout frame. Strips for one direction (shown in blue)
 1843 continue across the readout plane, while the short segments of the strips for the other direc-
 1844 tion (shown in red) are connected via through holes to readout lines running along the back of the
 1845 plane. Large area readout planes of similar design have been tested in prototype GEM chambers for
 KLOE2 at Frascati.

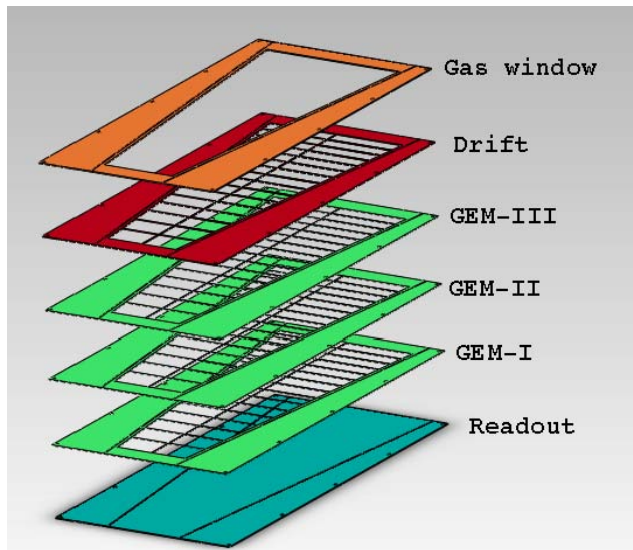


Figure 59: The frame assembly for a GEM module prototype of the size proposed for the largest SoLID GEMs

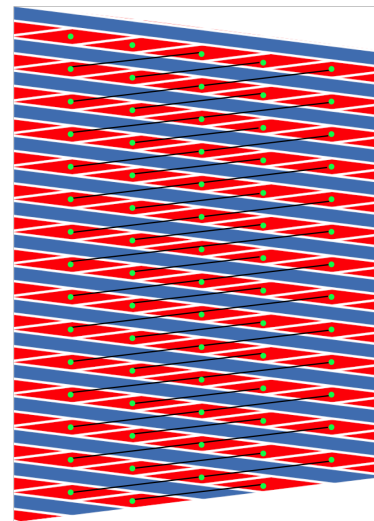


Figure 60: The schematics of the 2D readout plane proposed for SoLID

1846

1847 One challenge we are facing for the GEM trackers of SoLID is the large active area required;
 1848 the active area of the largest GEM modules needed will be approximately $113 \times (21-44) \text{ cm}^2$. Un-
 1849 til recently, the maximum GEM foil area had been limited to $45 \times 50 \text{ cm}^2$. However, over the last
 1850 few years the Micro Pattern Gas Detector (MPGD) group at CERN, in collaboration with INFN,
 1851 has perfected two techniques to produce large area GEM foils: single mask GEM etching and
 1852 GEM splicing [209, 210]. The single mask technique allows for the fabrication of foils as large
 1853 as $100 \times 200 \text{ cm}^2$. The splicing technique allows for two such foils to be combined with only a
 1854 3 mm wide dead zone between the two foils. Recently several large prototype GEM chambers
 1855 were constructed and tested at CERN using the large area GEM foils fabricated using the new tech-
 1856 niques [211]. These new prototype chambers, constructed under the CMS upgrade GEM project,
 1857 have trapezoidal shapes with an active areas of $99 \times (25-45.5) \text{ cm}^2$; these dimensions are close to
 1858 the dimensions of the largest GEM chamber modules planned for SoLID.

1859 Furthermore, there have been significant advances in the GEM chamber readout systems in the
 1860 recent years. The RD-51 collaboration funded Scalable Readout System (SRS) project at CERN

³Permaglass is a glass fiber material with randomly oriented fibers that can be machined with very high precision.

1861 has already developed and tested a low cost APV-25 based readout. The APV25-S1 analog readout
1862 chip [212] is currently in use for the COMPASS GEM trackers and the CMS silicon strip detec-
1863 tors. A mid-size prototype system consisting of 15,000 channels was successfully tested and was
1864 shown to work very well. The SRS group is continuing the development and is also working with
1865 a commercial vendor to fabricate the SRS modules. The cost of the APV-25 based SRS readout is
1866 expected to be approximately \$ 3 per channel.

1867 **7.2 GEM tracker R&D**

1868 Research and development towards the SoLID GEM tracker is currently being conducted in the
1869 United States at the University of Virginia (UVa) and in China at five institutions: China Institute of
1870 Atomic Energy (CIAE), Lanzhou University (LZU), Tsinghua University (THU), the University of
1871 Science and Technology of China (USTC) and the Institute of Modern Physics (IMP). According
1872 to the current plan, the UVa group, which has an ongoing large area GEM module production
1873 program, will do the initial designs and prototyping of the SoLID GEM chambers, while the Chinese
1874 institutions get their large area GEM production programs set up. At the same time CIAE has
1875 been working with CERN and Chinese manufacturers to develop large area GEM foil production
1876 capabilities in China.

1877 **7.2.1 GEM chamber R&D program in UVa**

1878 The Istituto Nazionale di Fisica Nucleare (INFN)-Roma group and the University of Virginia group
1879 are currently leading an aggressive R&D program to develop large area GEM chambers for the
1880 Hall A Super Bigbite apparatus (SBS). The active area of large tracking chambers of SBS will be
1881 $50 \times 200 \text{ cm}^2$. These large GEM trackers will be assembled by combining $40 \times 50 \text{ cm}^2$ and 50×50
1882 cm^2 “chamber modules” with narrow edges. The UVa group has already constructed several 40×50
1883 cm^2 and $50 \times 50 \text{ cm}^2$ GEM chamber modules. The expertise gained with these GEM modules will
1884 be applied to the design of GEM modules for SoLID.

1885 The UVa group operates a well-equipped GEM R&D facility that includes the following:

- 1886 • **UVa Detector development lab:** This $10 \times 10 \text{ m}^2$, well-equipped nuclear physics detector lab
1887 has been used for the development, construction and testing of many large detector systems.
1888 The detector lab consists of two $3 \times 3 \text{ m}^2$ level 1,000 clean rooms located within a $4 \times 10 \text{ m}^2$
1889 semi-clean area. So far seven large area GEM chambers have been successfully constructed in
1890 this clean room. The specialized GEM construction equipment in the lab includes large area
1891 GEM foil stretchers, GEM foil testing high-voltage boxes, a large volume ultra-sonic cleaner
1892 for GEM frame cleaning, a Keithley 6485 picoammeter for GEM foil testing, and a GEM foil
1893 storage dry N_2 box.
- 1894 • **GEM readout systems based on APV25-S1 electronics:** The UVa group has two APV25
1895 based readout systems: a 10,000 channel SRS system from CERN and a 3,500 channel system
1896 developed by the INFN group. Both systems are fully operational and are used for testing
1897 prototype GEM chambers.
- 1898 • **Wiener-Iseg multi-channel high voltage system** The UVa detector group owns a brand new
1899 Wiener-Iseg multi-channel high voltage system that is especially suited to provide high volt-
1900 age to sensitive tracking chambers. This system currently has 24 channels and can be ex-
1901 panded to 160 channels.

1902 The $50 \times 50 \text{ cm}^2$ GEM chambers built at UVa are currently being tested with radioactive sources
 1903 and cosmic rays. Figures 61 and 62 show results obtained from these test data. Figure 61 is the
 1904 absolute efficiency measured at several locations using electrons from a beta source, as a function
 1905 of the high voltage. An efficiency of $\approx 97\%$ is achieved. Figure 62 is the ratio of cluster charge for
 1906 x and y hits.

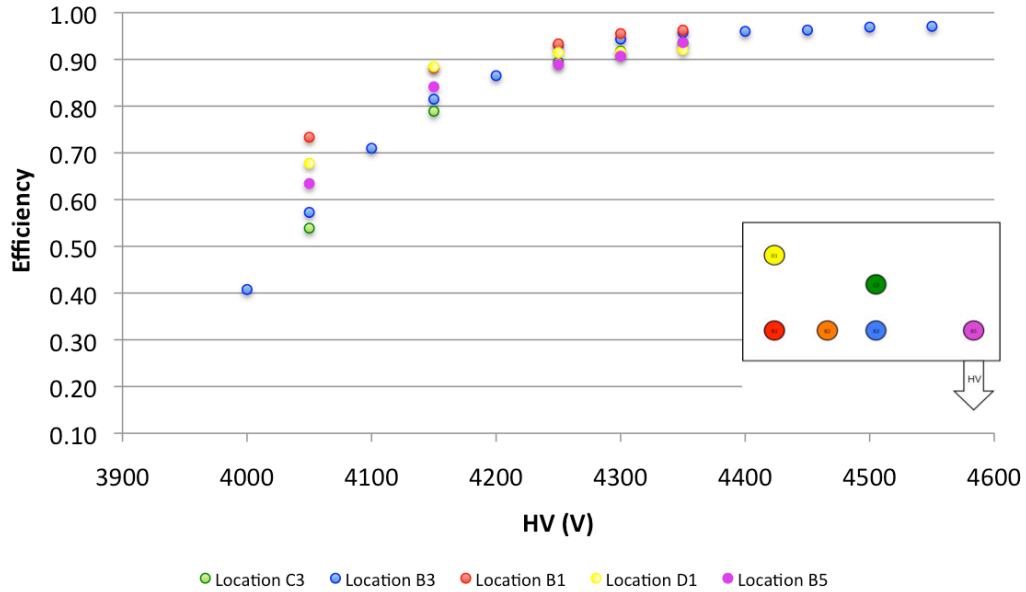


Figure 61: Efficiency of the $40 \times 50 \text{ cm}^2$ GEM chamber

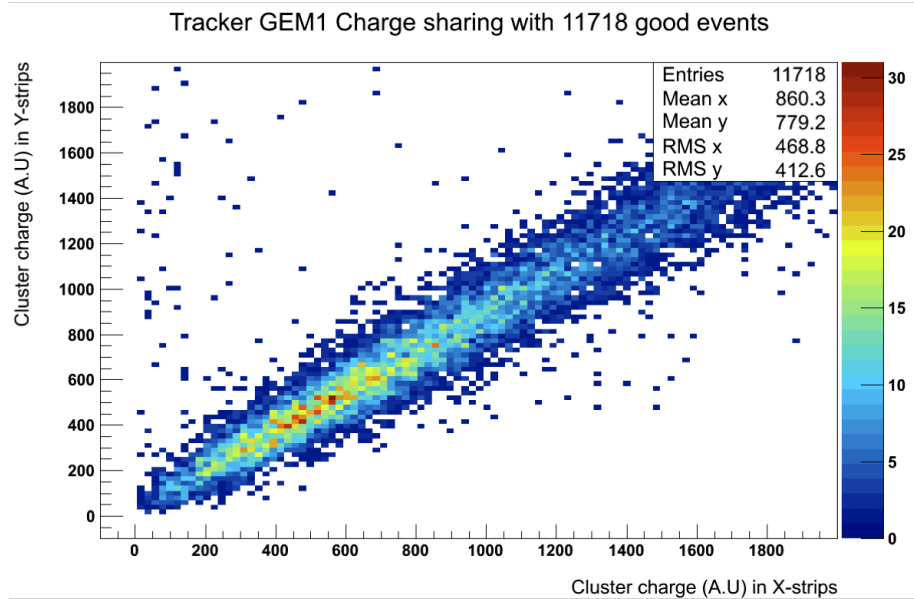


Figure 62: The charge division between x and y strips for the $40 \times 50 \text{ cm}^2$ GEM chamber.

1907 The UVa group recently completed the fabrication of a large prototype GEM module with di-
1908 mensions of $100 \times (21-38)$ cm², approaching the proposed size of the largest SoLID GEM sectors
1909 (Figure 63). This prototype was constructed under the Electron Ion Collider (EIC) detector R&D
1910 program. This chamber is the largest GEM chamber ever built with a 2-D readout. Its readout
1911 consists of stripes from the two readout layers at a 12° stereo angle. The chamber is currently pre-
1912 pared for a beam test at Fermilab scheduled for October 2013. The development and testing of this
1913 large prototype is used to gain expertise and understand the mechanical, electrical and electronic
properties of very large area GEM chambers.

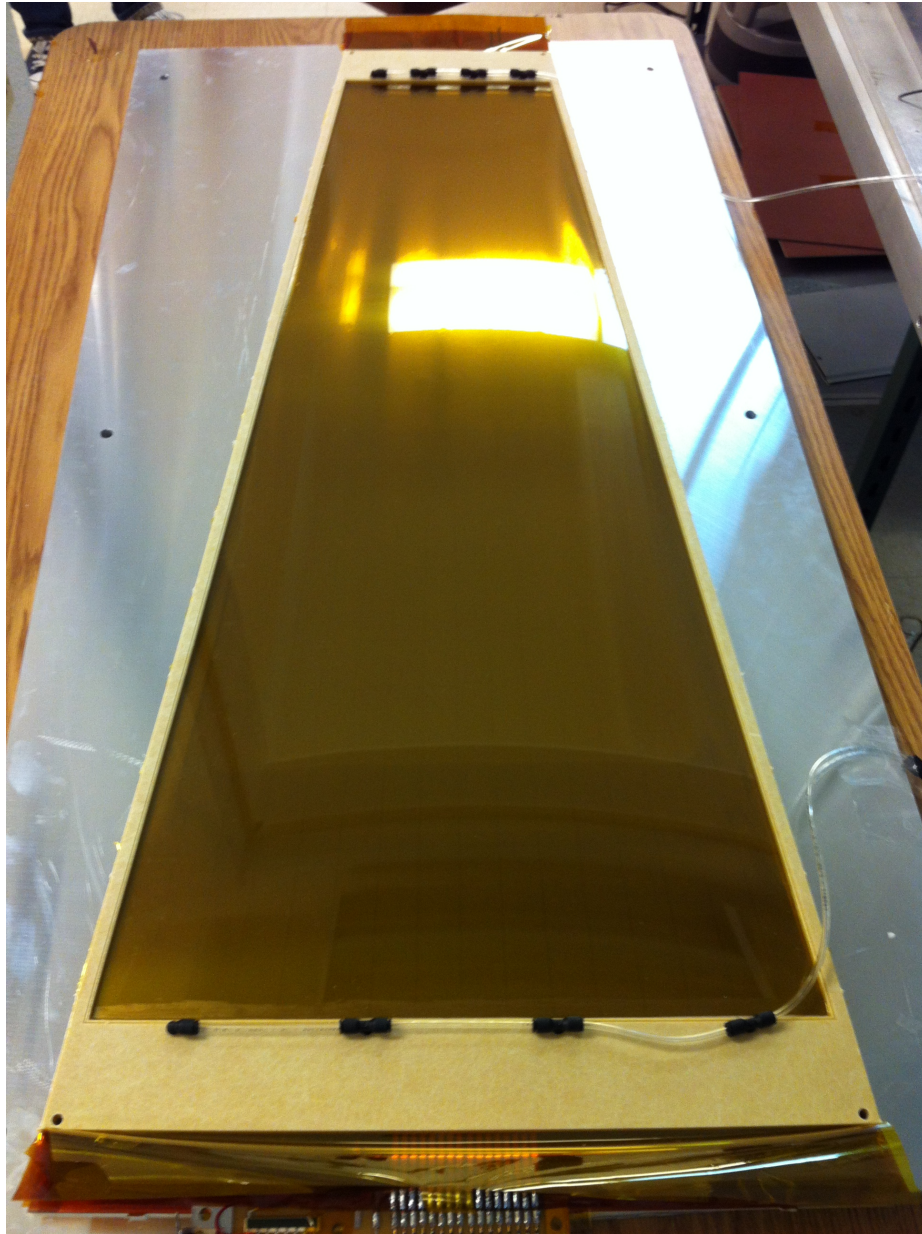


Figure 63: The 100 cm x (21 - 38) cm prototype GEM chamber at UVa being prepared for a beam test.

1915 **7.2.2 GEM chamber R&D programs in China**

1916 The five institutions of the Chinese collaboration for SoLID GEM detectors all have worked on gas
1917 detectors for many years, including R&D work on MWPC, MRPC, GEM, Micromegas, THGEM,
1918 and TPC, and applications of these detectors. These institutions have well-equipped GEM R&D
1919 facilities that include:

- 1920 • Clean rooms for GEM detector assembling
- 1921 • Front-end readout electronics based on APV25-S1 (developed by the INFN group)
- 1922 • Multi-channel HV power supply systems and DAQ systems

1923 CIAE, which has over 20 years of experience in nuclear pore foil production and Kapton etching,
1924 just signed a license agreement for manufacturing and commercialization of GEM foils and GEM
1925 based products with CERN, and received technical assistance from CERN. The base material of
1926 GEM foil is ultrathin, non-adhesive copper on a polyimide substrate, which can be purchased from
1927 CERN and other vendors. Several printed circuit board (PCB) technologies are applied during the
1928 manufacture of GEM foil. Recently, CIAE has started working on:

- 1929 • Production of photo-masks, a component for the manufacturing of PCBs which is transferred
1930 onto a light-sensitive chemical resist covering the surface of copper layer in the production of
1931 GEMs.
- 1932 • Lamination and exposure of dry film photoresist: Using a hot roll lamination (HRL) machine,
1933 both sides of the GEM substrate are laminated simultaneously by photoresist. The exposure
1934 system consists of an exposure unit, vacuum exposure frame, light source cooling, and an
1935 exposure control unit. This treatment transfers the photo-mask pattern onto the photoresist,
1936 forming an exact copy.
- 1937 • Copper etching.
- 1938 • Polyimide film etching.
- 1939 • Final cleaning and chrome coating.

1940 Figure 64 shows the film etching device at CIAE. In the beginning of 2013, a physicist from
1941 CIAE completed a training in GEM foil manufacturing at CERN.

1942 LZU has been building a Micromegas+AFTER chip system for fast neutron (14 MeV) imaging
1943 in the past few years. The experience gained from this R&D work is useful to their GEM project.
1944 For instance, several designs of neutron converters with different parameters were tried in a simu-
1945 lation based on MCNP4 and GEANT4 (for both Micromegas and GEM), and different conversion
1946 efficiencies were compared. Other studies based on Garfield to improve the spatial and time resolu-
1947 tion (as shown in Figure 65) were also performed and were proved to be helpful for the experimental
1948 study. The first version of the detector frame was designed and manufactured. 4 sets of GEM foils
1949 with the standard frame were purchased from CERN. Currently, a PhD student and a staff member
1950 are working together on the APV25-VME system. In the summer of 2013, an engineer visited JLab
1951 to gain experience about the SoLID DAQ.

1952 THU has experience with GEM detectors by developing the electronics, such as a GEM-based
1953 TPC readout, a 16-channel CSA and shaping amplifier for GEM. Recently, a planar GEM tracking
1954 detector prototype was assembled for a spatial resolution test. In this test, THU used the event rate



Figure 64: Film etching device at China Institute of Atomic Energy

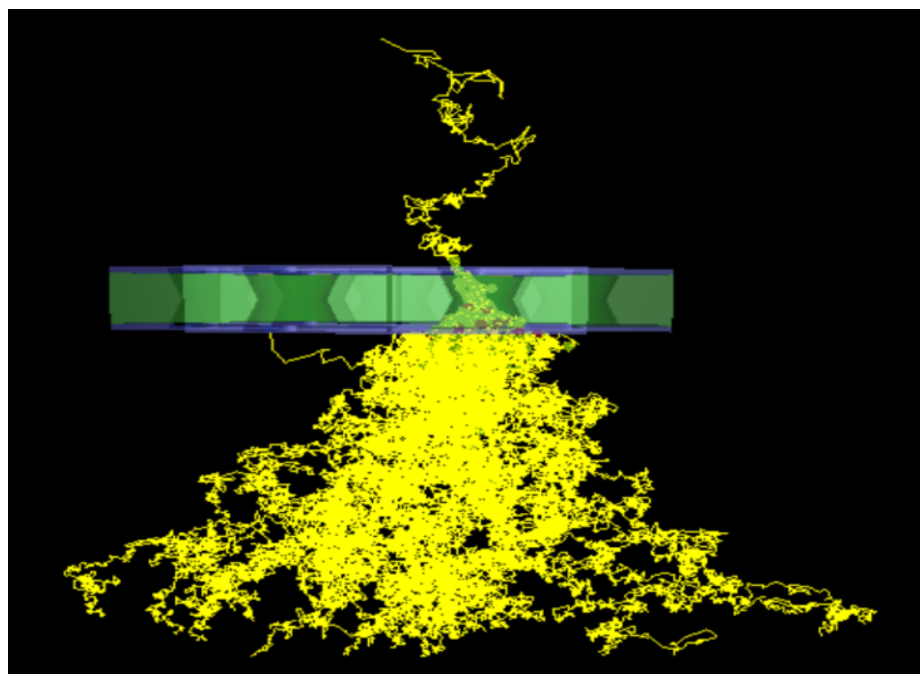


Figure 65: Avalanche process of an electron in a hole of GEM

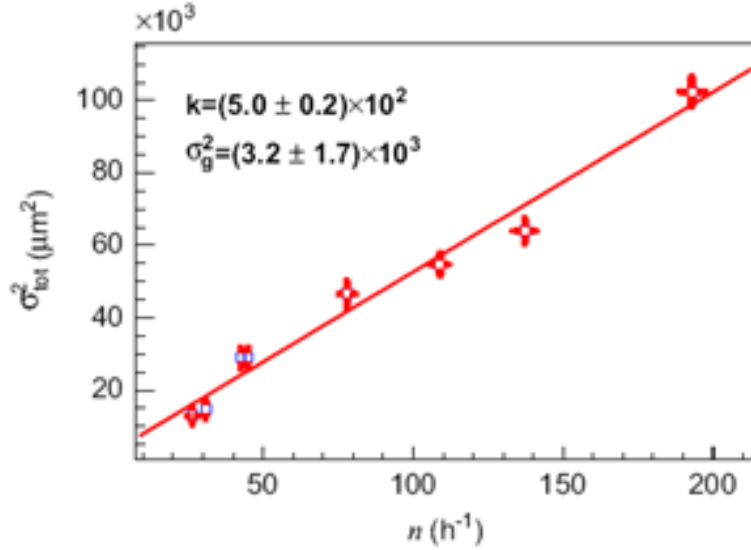


Figure 66: Linear fit of σ_{tot}^2 versus n

1955 to substitute for the square of the slit width to overcome the magnified uncertainty of the spatial
 1956 resolution which arises from the uncertainty of the slit width. The test demonstrated that the total
 1957 position variance of the incident particles exhibits a linear dependence on the event rate or square of
 1958 the slit width. The next step was to extend the measurement to zero slit width which is not directly
 1959 achievable, and it was practically implemented by a linear fit to data points on the $\sigma_{tot}^2 - n$ plane.
 1960 Figure 66 shows the linear fitting of σ_{tot}^2 versus n and the spatial resolution of the prototype is
 1961 $56 \pm 14 \mu m$. Currently, THU is focusing on the inter-foil and inter-strip distance effects of the GEM
 1962 detector. An APV based DAQ system will be built in the near future.

1963 USTC started the GEM R&D work in 2000. After working on the 3D electric field simulation of
 1964 GEM, USTC carried out a detailed gain performance test for the $10 \times 10 \text{ cm}^2$ triple GEM detector,
 1965 then made a GEM X-ray imaging prototype. Both Center-of-Gravity (COG) and delay-line readout
 1966 methods were used on this imaging prototype and a very good spatial resolution ($\sim 80 \mu m$) was
 1967 obtained. Currently, USTC is focusing on the R&D of the large area GEM detector. Due to the
 1968 fact that large area GEMs built by the glue technology have some disadvantages (e.g. very long
 1969 assembling period; parts of GEM detector are not replaceable; dead regions in the effective area;
 1970 aging problems of the glue and so on), USTC decided to use the NS2 (No Stretch, No Stress)
 1971 technology for the construction of a $30 \times 30 \text{ cm}^2$ GEM detector. NS2, which was developed at
 1972 CERN recently, is a totally new technology especially used for large area GEM detectors. The idea
 1973 of NS2 is to use screws and a stable main frame to achieve self-stretching of the GEM foils. The
 1974 advantages of NS2 are:

- 1975 • The whole construction process involves mainly tightening the screws, so it is easy and fast
 1976 and we can assemble a detector in half a day.
- 1977 • Because all the GEM foils are self-stretched, the detector does not need support frames. There
 1978 is no glue aging problem or dead area inside the detector.
- 1979 • All the screws can be loosened and tightened again, so that any part of the detector is replace-
 1980 able. This also means that the cost of the project can be greatly reduced.

1981 USTC just finished the design of the new $30 \times 30 \text{ cm}^2$ NS2 GEM and purchased six $30 \times 30 \text{ cm}^2$
1982 GEM foils from CERN. The HV dividers and screws are ready. The frames, drift electrode and
1983 readout PCB are in manufacturing. The readout electronics and instruments are ready. Figure 67
1984 shows a model of the $30 \text{ cm} \times 30 \text{ cm}$ NS2 GEM detector (without readout PCB). This detector has
1985 been assembled and tested in Summer 2013.

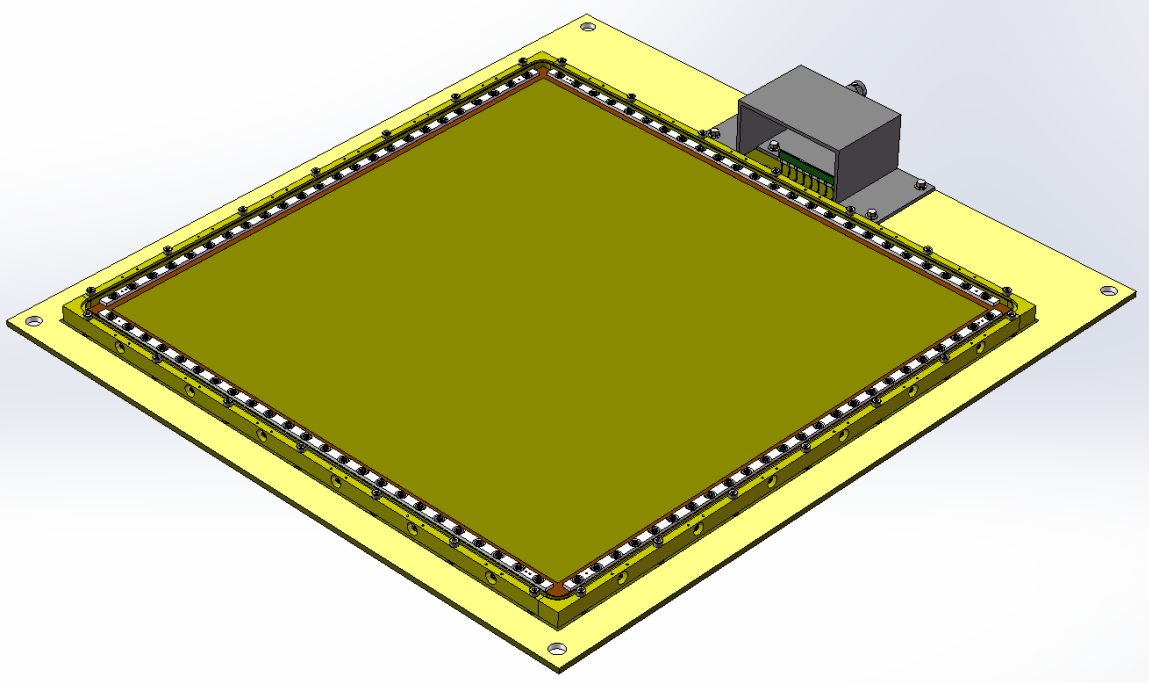


Figure 67: Design of the $30 \times 30 \text{ cm}^2$ NS2 GEM detector

1986 7.3 Collaboration Status and Construction Outlook

1987 The close collaboration between the CIAE group in China developing GEM foil fabrication capabil-
1988 ities and the US groups (UVa and Temple) is essential as the project moves forward. The ongoing
1989 China-USA SoLID GEM collaboration activities have included monthly phone meetings, discus-
1990 sion during SoLID collaboration meetings and hosting of Chinese visiting researchers at the GEM
1991 lab at UVa.

1992 A timetable is worked out with the CIAE group to lay out milestones for the fabrication of GEM
1993 foils with increasing active areas up to the full size of the largest SoLID modules. This timetable will
1994 also include goals for providing specific numbers of GEM foils produced in China to the Temple
1995 group for hole inspections and to the UVa and Temple groups for construction of test modules with
1996 these foils. The Chinese foils will be subjected to all acceptance criteria used for CERN GEM foils.
1997 The test modules will be evaluated under high luminosity conditions at the UVa x-ray test-stand
1998 as well as in beam tests at Jefferson lab. The two US groups will be closely interacting with the
1999 Chinese groups and giving them feedback during these evaluations. As part of the proposed SoLID
2000 pre-R&D program, funds have been requested for covering the cost of these Chinese GEM foils as
2001 well as for the fabrication of test modules.

2002 The current plan for SoLID calls for approximately 400 GEM foils. In the event the CIAE group
2003 is unable to meet the GEM foil production goals, the backup option is purchasing the required

2004 number of foils from CERN. The estimated cost of purchasing all 400 SoLID GEM foils from
2005 CERN will be approximately \$ 650 k

2006 The CERN workshop has demonstrated the capability to produce the largest size GEM foils
2007 (113 cm x 44 cm) needed for SoLID. In fact, the UVa group recently used 123 cm x 55 cm GEM
2008 foils produced at CERN to build two large area GEM detectors; these detectors were successfully
2009 used for Jefferson Lab PRad experiment. Furthermore, CERN has the production capacity to deliver
2010 large orders of GEM foils in a timely manner. Over the last two years the CERN workshop produced
2011 and delivered approximately 140 large area GEM foils to UVa for SBS and PRad GEM modules;
2012 these foils were of high quality with about 90% of the foils passing the acceptance criteria. The
2013 manager of the CERN GEM workshop, Rui De Oliveira, has indicated that they have the capacity
2014 to deliver the required number of GEM foils for SoLID and with an order to produce the required
2015 number of foils they will hire the needed technicians to deliver the order in a timely manner.

2016 While the R&D to produce large area single mask GEM foils has been suspended for the mo-
2017 ment at Tech-Etch due to lack of large orders for such foils, Tech-Etch has indicated that in the event
2018 they receive a firm order for a large GEM production, they will be able to commit the resources for
2019 the required R&D and production.

2020 Given these two backup options, the schedule risk due to a delay in Chinese GEM foils fabrica-
2021 tion schedule will be rather low.

2022 8 Light Gas Čerenkov

2023 8.1 Design

2024 The light gas Čerenkov detector for SoLID is divided into 30 identical sectors to match the 30 sector
2025 symmetry of the PVDIS baffle system. Many elements of the light gas Čerenkov remain identical
2026 between the PVDIS and SIDIS / J/Ψ experimental configurations, but some elements are adjusted
2027 or added / removed. Beyond the criteria dictated by the experimental physics requirements, the
2028 design of the Čerenkov detector was optimized with the goal of reducing the costs of construction
2029 and maintenance over the detector's lifetime including the switch over between experiments. The
2030 specifications of the tank and each major element per sector for each configuration are described
2031 below:

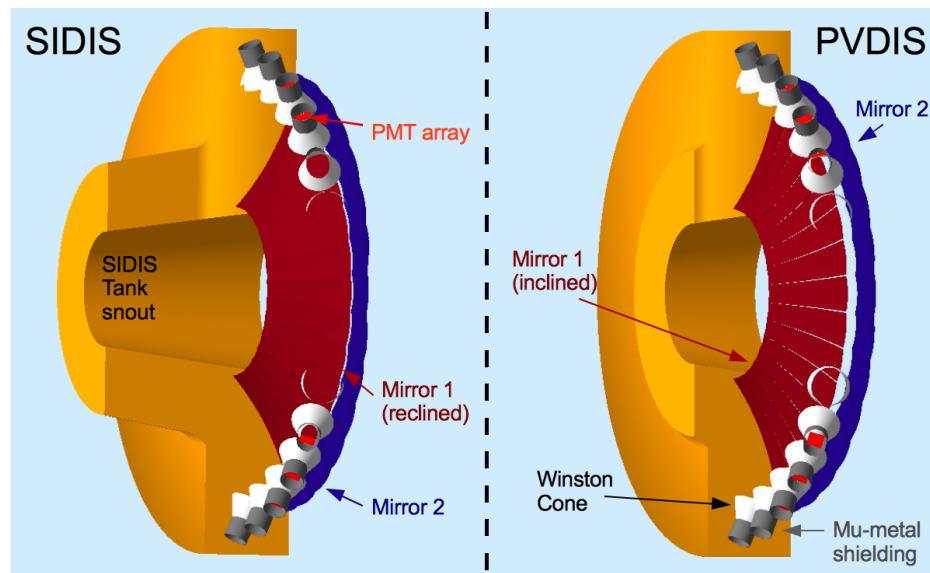


Figure 68: A side by side cross-section comparison of the light gas Čerenkov detector for both the SIDIS and PVDIS configuration with all major components labeled.

2032 8.1.1 Tank and Čerenkov Gas

2033 The main body of the tank remains identical between PVDIS and SIDIS configurations, and has a
2034 length roughly 105 cm with an inner radius of 71 to 85 cm, and an outer radius of 265 cm. With the
2035 PVDIS baffles removed for SIDIS, an additional tank ‘snout’ is attached upstream of the main tank
2036 inside the additional space evacuated by the baffle system. This tank snout adds an additional 107
2037 cm of length to the tank with an inner radius of 58 to 71 cm, and an outer radius of 127 to 144 cm.
2038 In both configurations, the windows will be constructed from polyvinyl fluoride (PVF or Tedlar) at
2039 a thickness of 0.05 mm and 0.1 mm for the entrance and exit windows respectively. PVF provides
2040 a strong and gas-tight seal at minimal density (1.45 g/cm^3). The radiator gas in both configurations
2041 will be CO_2 pressurized at slightly over atmospheric pressure to maintain gas purity.

2042 8.1.2 Mirrors

2043 Each sector will consist of two spherical mirror segments with dimensions listed in Tab. 12. Radially
2044 outward from the beam line, the inner most segment we will refer to as mirror 1 (red in Fig. 68) and

2045 the outermost segment as mirror 2 (blue in Fig. 68). In order to accommodate two different incident
 2046 particle angles between PVDIS (22° to 35° from a central Z-vertex 270 cm away) and SIDIS (8.0°
 2047 to 15.0° from a vertex 520 cm away), mirror 1 must be adjusted between experiments such that
 2048 the reflected Čerenkov light in both configurations falls into the PMT detector acceptance. This is
 2049 achieved by rotating mirror 1 by an angle of approximately 8° inward about the mirror’s inner-most
 2050 edge (or edge closest to the beam-line). In Fig. 68 we see a cross section of the light gas Čerenkov,
 2051 sliced along the beam or Z-direction, with the mirrors in both the reclined and inclined positions.
 2052 Mirror 2 is fixed in position and rotation and non-contributing to the SIDIS configuration; however,
 2053 mirror 2 is necessary to cover the larger angular range in the PVDIS configuration. The mirrors will
 2054 be crafted from carbon-fiber-reinforced polymer (CFRP) by Composite Mirror Applications (CMA)
 2055 [220] with an areal density no larger than 6 kg/m^2 . The surface smoothness and uniformity will
 2056 achieve a D0 spot size of $<2 \text{ mm}$ and be of similar quality to the mirror blanks CMA manufactured
 2057 for the RICH detectors at LHCb [221]. Mirror coating will be performed by our collaborators at
 2058 Stony Brook, and will consist of high reflectance ($\geq 85\%$ for $\lambda = 200 \text{ nm}$ to 620 nm) aluminum
 2059 with a protective coating of MgF_2 .

Mirror	inner-edge W (cm)	outer-edge W (cm)	L (cm)	R of curv. (cm)
Mirror 1	16.26	36.03	114.53	277.51
Mirror 2	37.06	45.95	59.26	157.99

Table 12: The dimensions of the two mirror segments in the light gas Čerenkov.

2060 8.1.3 PMTs

2061 The light gas Čerenkov will use Hamamatsu flat panel multianode photomultiplier tube assemblies:
 2062 H12700C [222]. These PMT assemblies are an 8×8 pixel square array with a total active surface
 2063 area of $49 \text{ mm} \times 49 \text{ mm}$ with a UV-glass window, Bialkali photocathode material producing an
 2064 average quantum efficiency around 15%, and a 12-stage dynode structure allowing resolution down
 2065 to a single photoelectron. A 3×3 array of these PMT assemblies will be mounted in each sector,
 2066 as shown in the PMT mounting prototype in Fig. 69. The position and orientation of the PMT ar-
 2067 ray will remain fixed between PVDIS and SIDIS configurations. The PMTs will be coated with a
 2068 wave-length shifting p-Terphenyl coating. This coating is a cost effective method to boost the PMT
 2069 response of Čerenkov radiation in the UV range. The expected effective increase in photoelectron
 2070 gain is shown in Fig. 70. Every pixel in the H12700C will be wired together to produce one signal
 2071 per PMT; a trigger will then be constructed by requiring two PMT assemblies in the same array to
 2072 fire in the same time window, with a minimum photoelectron discrimination. Simulations show a
 2073 $>90\%$ average electron detection efficiency, integrated over all angles and momenta, when requir-
 2074 ing 2 separate PMTs assemblies in an array to each generate 2 or more photoelectrons in either
 2075 the PVDIS or SIDIS configurations. This trigger configuration would result in 36 possible coinci-
 2076 dences per sector, consequently reducing the single photoelectron rate due to dark current or other
 2077 backgrounds by at least a factor of 10. Specific filtering of the PMT signals will be tested while
 2078 prototyping the PMT array and electronics. Additionally, we plan on improving the resolution of
 2079 the PMT sum signal through matrix gain balancing of the PMT pixel-array patented by Vladimir
 2080 Popov to Jefferson Lab.

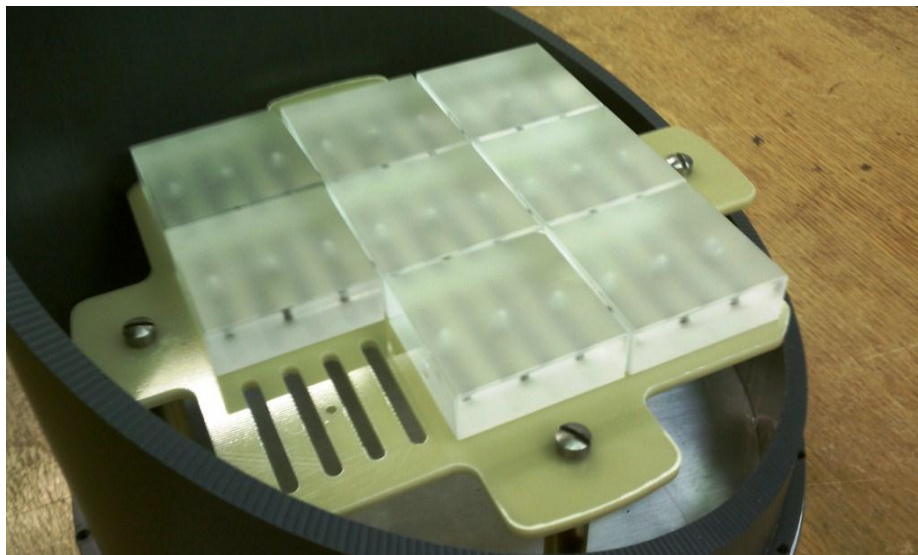


Figure 69: PMT assembly mounting prototype showing 3×3 array of dummy PMTs inside the space restricted by magnetic shielding.

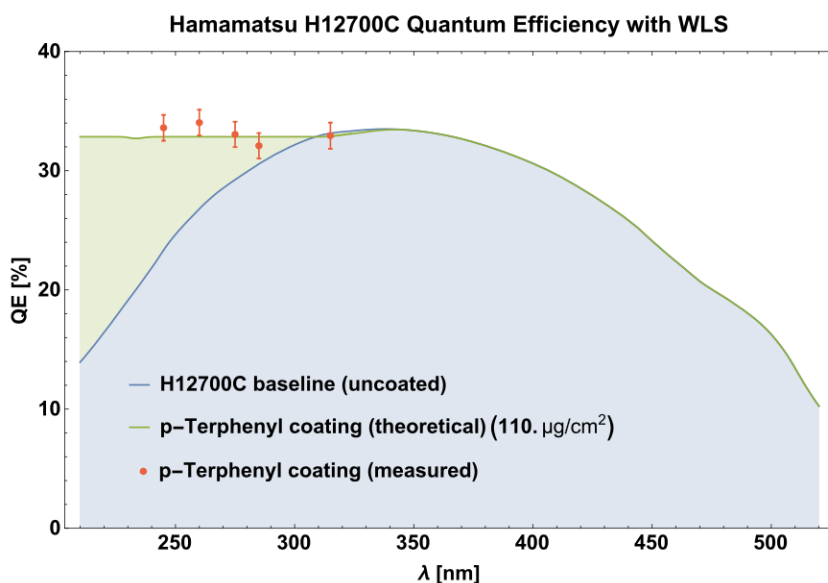


Figure 70: The increase in effective gain resulting from p-Terphenyl coating on H12700C PMTs. Red points are measurements done at Temple University. The curves show the current H12700C quantum efficiency, and the expected effective gain in the quantum efficiency from p-Terphenyl coating as a function of optical photon wavelength.

2081 **8.1.4 Magnetic Shielding and Winston Cones**

2082 The PMTs will be shielded by a mu-metal cylinder / cone construction that doubles as support for a
 2083 reflective aluminum inner glass cone to direct light onto the PMT array. The cylinders will measure
 2084 30 cm in length with an inner radius of 11.28 cm, the cone will have a height of 30 cm with an inner
 2085 radius of 7.8 cm at the narrow end and an inner radius of 21 cm at the wide end. The mu-metal

2086 shielding will be 0.04 inch thick reinforced by 0.125 inch thick 1008 carbon steel and manufactured
2087 by Amuneal Manufacturing Corp [223]. The PMTs are most sensitive to the magnitude of the
2088 magnetic field parallel to the photon collection face (transverse direction). We require a reduction
2089 of 95 gauss to <50 gauss in the transverse direction, and a reduction of 135 gauss to <50 gauss in
2090 the longitudinal direction, to where we expect an output loss <10% as seen in Figure 82

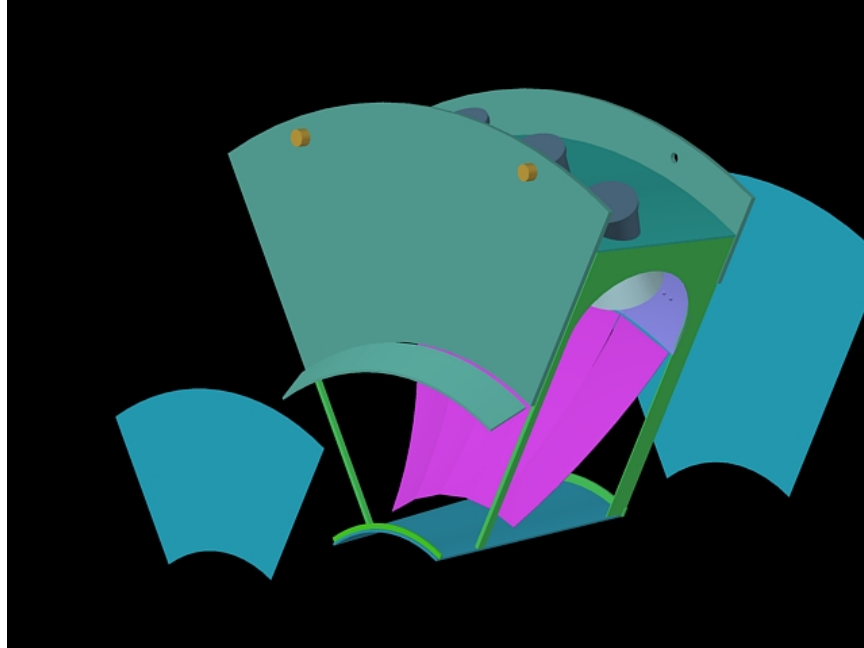


Figure 71: The support frame for one subsection of the light gas Čerenkov. The front and back acceptance windows (blue) are exploded to show the mirrors (pink and purple) and the support frame (green). The mounting points of the tank to the magnet housing are shown in orange.

2091 8.2 Tank Support

2092 The Čerenkov tank front and back windows will be divided into six radial sections. Between each
2093 pair of sections will be two thin rectangular aluminum support spokes, one to support and frame
2094 the upstream side of the tank and another to support and frame the downstream side (see Fig. 71).
2095 Both spokes are positioned and aligned to minimize the probability of tracks passing through the
2096 support material. Additionally, both spokes are interconnected at the outer radius of the tank, out-
2097 side of the desired physics acceptance, by a solid arc-shaped plane to increase the rigidity of the
2098 frame and provide additional support for mounting the focusing cones and PMT assemblies. The
2099 space between the upstream and downstream spokes will remain open to maximize Čerenkov light
2100 collection. The combined frame itself will be mounted to the back wall of the downstream mag-
2101 net housing, to support the full weight of the Čerenkov detector. This alleviates placing additional
2102 stress on the end-cap nose, which other additional downstream detectors will use to support their
2103 weight. Each PMT array will be accessible from the outer radial wall of the tank for alignment or
2104 maintenance purposes.

2105 **8.3 Simulations**

2106 All simulations were done with a slightly modified version of the GEMC [224] software developed
2107 at Jefferson Lab. GEMC uses a GEANT4.95 [225] backend to simulate all particle tracking through
2108 and interaction with materials and geometries. All plots shown in the light gas Čerenkov section
2109 of this document use the same simulation dataset. Event generation was performed by the eicRate
2110 DIS event generation tool authored by Seamus Riordan. The simulations also have the following
2111 features:

- 2112 • Acceptance through the PVDIS baffle system (PVDIS events only).
- 2113 • Čerenkov radiation process for creation of optical photons.
- 2114 • Expected delta ray and pair creation from e^- and π^- particles interacting with the Čerenkov
2115 front window using the standard and low energy EM packages for GEANT4.
- 2116 • Expanded mirror reflection properties in GEMC to be more in line with the latest functionality
2117 from GEANT4.
- 2118 • PMT photoelectron signal simulation which includes the PMT dead area, quantum efficiency
2119 pixel-by-pixel, and optical properties of the PMT UV glass window.

2120 **8.3.1 Collection Efficiencies**

2121 The collection efficiencies for electrons in both the PVDIS and SIDIS configuration can be seen
2122 in Figs. 72 and 73. The slight jump in photoelectrons around 32° in the PVDIS figure is a result
2123 of the inclined inner mirror, which moderately reduces the number of optical photons produced by
2124 reducing the particle's path length through the gas before crossing the mirror.

2125 **8.3.2 Background Rates**

2126 A low energy inclusive background simulation was performed using GEMC by generating an elec-
2127 tron beam on target, including all expected materials between the beam entrance to the Čerenkov
2128 back window. Secondaries produced anywhere in the SoLID detector and above the Čerenkov radi-
2129 ation momentum threshold while passing through the Čerenkov gas were considered as a possible
2130 source of background. For the PVDIS configuration, lepton production from initial π^0 production
2131 at small angle produced the majority of accidental backgrounds. This background was calculated
2132 using the same methodology as the modified Hall D generator, which uses a modified version of
2133 PYTHIA and SAID input to match known world data. More information on the pion generator can
2134 be found in Sec. 12.2.3. The combined background rate is estimated to be ≈ 0.8 MHz per sector for
2135 a trigger requiring at least 2 photoelectrons in 2 separate PMTs in the same sector. For the SIDIS
2136 configuration, the expected background rate is less than 100 KHz in the same trigger configuration
2137 above.

2138 **8.3.3 Pion Rejection**

2139 The expected pion rejection is shown in Figs. 74 through 77. All pion signal below the pion
2140 Čerenkov radiation threshold (3.2 GeV/c for the PVDIS gas) is produced by knock-ons or (e^+ , e^-)
2141 pair creation. The photoelectron signal itself is a poisson distribution convoluted with a gaussian
2142 to simulate the PMT 1 photoelectron resolution. The pion-electron photoelectron cut is determined
2143 by taking the intersection of the two signal distributions, simultaneously maximizing the electron

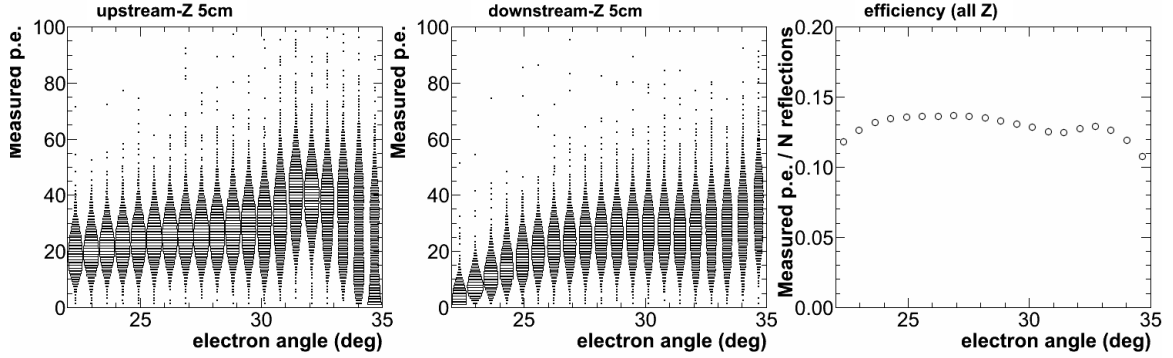


Figure 72: PVDIS configuration: The number of surviving photoelectrons versus theta after losses due to quantum efficiency of the PMTs, PMT dead area, or secondary reflections / absorptions off of the cones or PMT UV-glass window for events in the 5 cm of target most upstream (left) and 5 cm of target most downstream (middle). The right plot shows the corresponding collection efficiency versus theta for all 40 cm of the target Z-vertex.

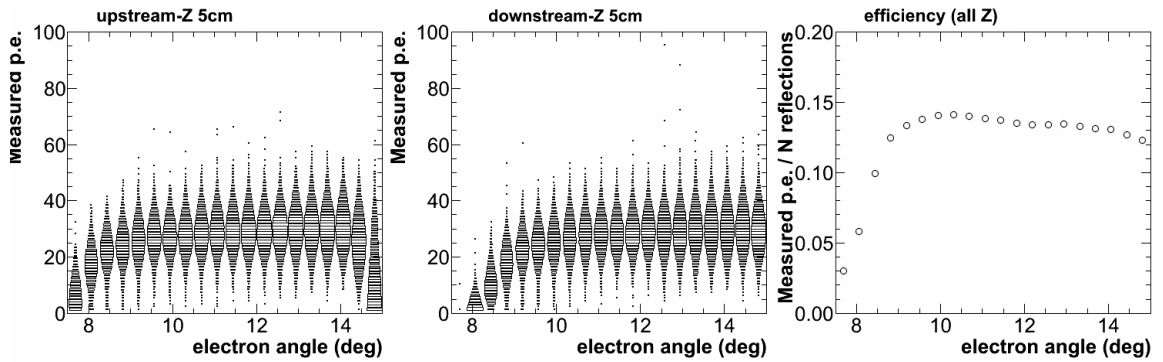


Figure 73: SIDIS configuration: Same as in Fig. 72 but with the SIDIS configuration.

2144 selection probability while maximizing the pion rejection probability. Additional calculations are
 2145 shown in Figs. 74 and 76 with a stricter cut on the pion signal, which consequently reduces the
 2146 electron efficiency (by 10% for the red points and 20% for the blue points). An example of these
 2147 photoelectron cuts are shown in table for one bin in momentum in the PVDIS configuration.

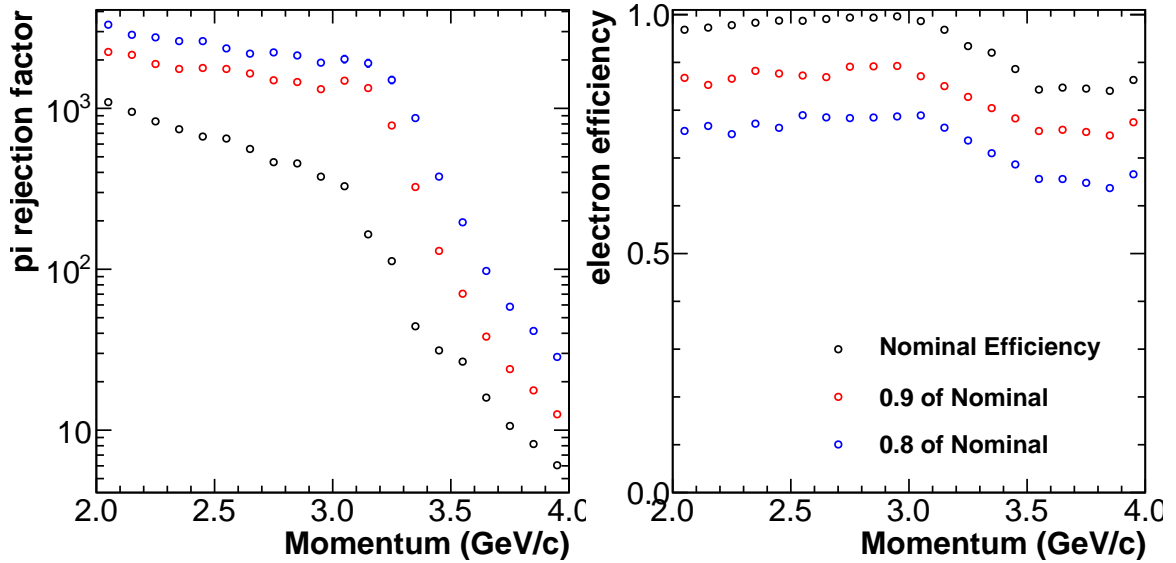


Figure 74: PVDIS configuration: The pion rejection factor versus momentum for 3 electron selection efficiencies: The nominal efficiency maximizes the pion rejection while minimizing loss of electrons, the red points correspond to a stricter pion cut with up to 10% additional loss of electrons, and the blue points allow an additional 20% loss of electrons.

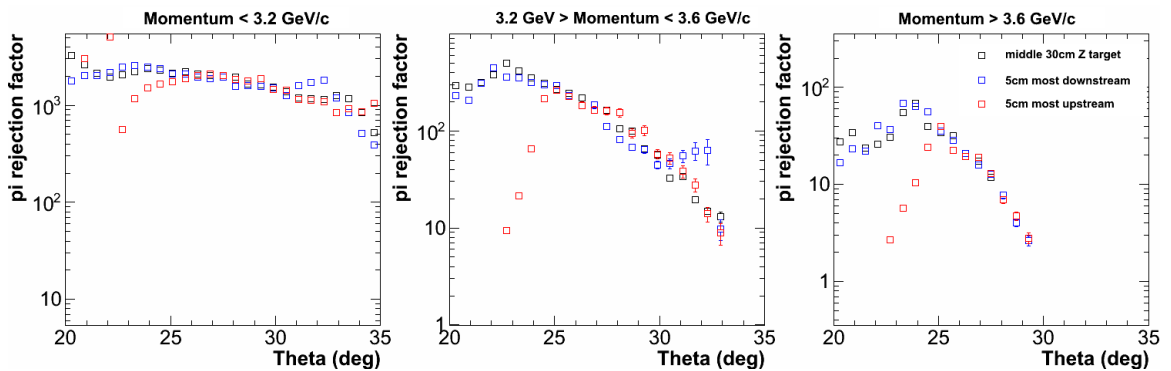


Figure 75: PVDIS configuration: The pion rejection factor versus the electron scattering angle theta over 3 momentum and Z-vertex ranges.

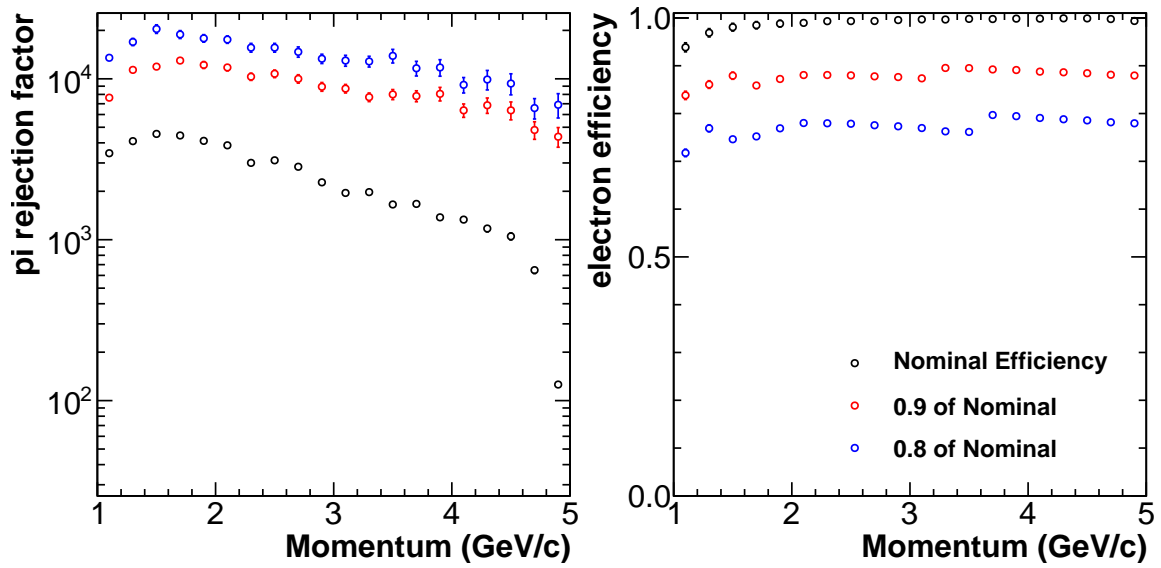


Figure 76: SIDIS configuration: Same as in Fig. 74 but with the SIDIS configuration.

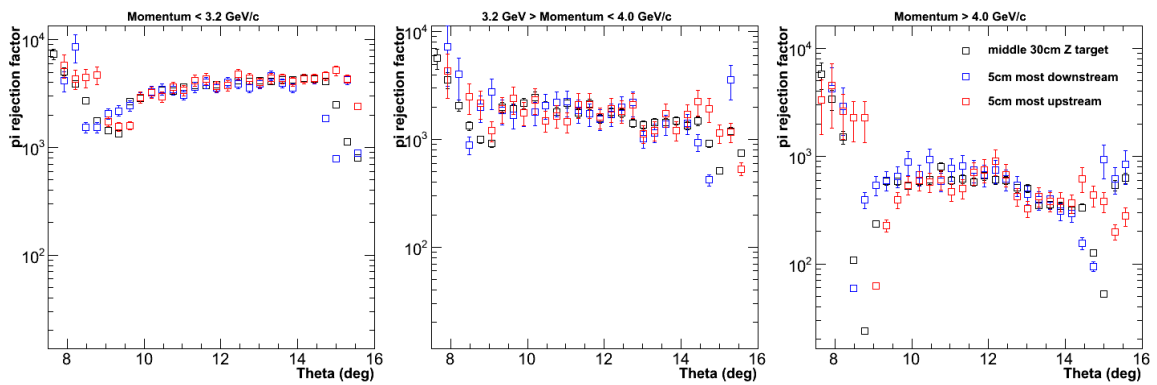


Figure 77: SIDIS configuration: Same as in Fig. 75 but with the SIDIS configuration.

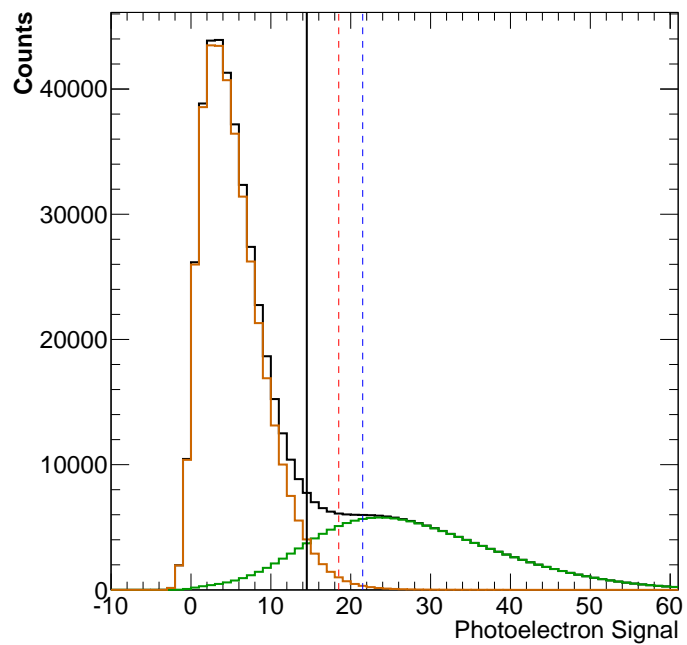


Figure 78: An example of the pion rejection cut made for one arbitrary bin in momentum for the PVDIS configuration. The pion signal is shown in orange and the electron signal is shown in green. The nominal efficiency cut is shown as a solid black line. The 90% and 80% electron efficiency cuts are shown as dashed red and blue lines respectively.

2148 9 Heavy Gas Čerenkov

2149 9.1 Optical System Design

2150 A hadron Čerenkov detector is required to help with the identification of both positive and negative
2151 pions. A clear distinction between pion and kaon Čerenkov signals is mostly required in the mid to
2152 high momentum range, namely from 2.5 to 7.5 GeV. The C_4F_8O/C_4F_{10} gas at 1.5 atm and a tem-
2153 perature of $20^\circ C$ gives a momentum threshold of 2.2 and 7.5 GeV for pions and kaons, respectively.
2154 Due to geometrical acceptance constraints the gas length available for Čerenkov light production
2155 is about 1 m. Requirements on the design are full azimuthal angular coverage and a good detec-
2156 tor performance in a magnetic field with strength as high as 200 Gauss. The optical system for
2157 the Čerenkov light collection has been optimized using a GEANT4 simulation package taking into
2158 account the expected SoLID magnetic field configuration with the CLEO-II magnet. The system
2159 consists of a ring of 30 spherical mirrors of 1.2 m length each and inner and outer widths of 0.2 and
2160 0.4 m, respectively. The mirrors will focus the light onto 30 photodetector as shown in Fig.79. The
2161 size of each photodetector could be reduced to 8x8 inches (i.e. 16 of 2-inch PMTs per array) by
2162 use of straight cones as an additional optical element to mirrors. The PMTs of choice are similar to
2163 those used for the light gas Čerenkov namely the multi-anode 2 inch H8500-03/H12700-03 devices
2164 from Hamamatsu: they perform well in relatively high magnetic field, are square shaped, and have
2165 good photocathode coverage (89% of total area), making them ideal for tiling.

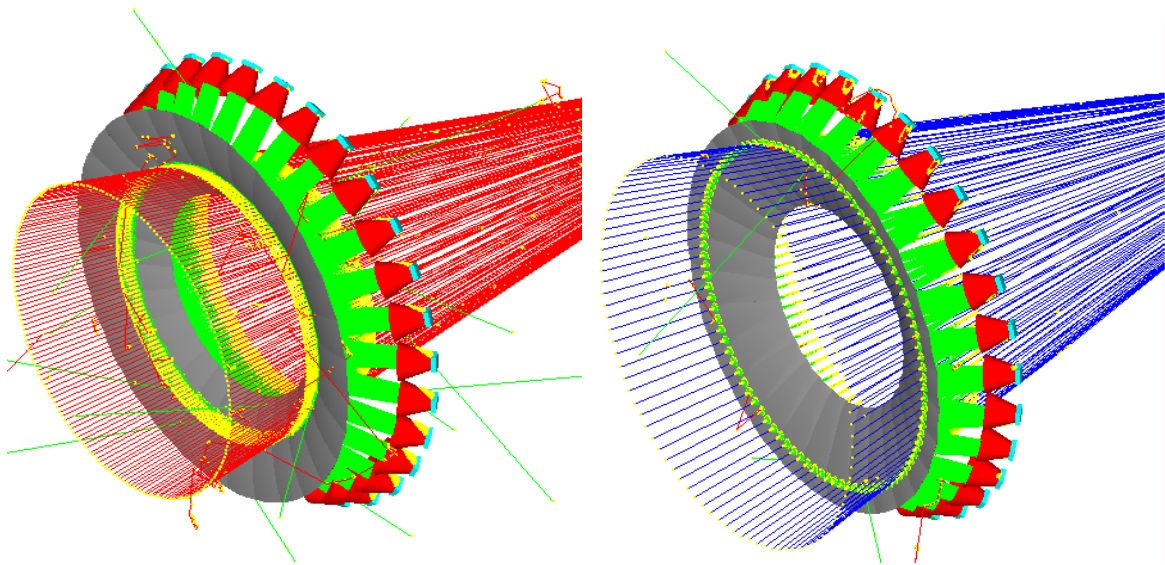


Figure 79: Optical system for the heavy-gas Čerenkov: a ring of 30 spherical mirrors (grey) will focus the Čerenkov photons created by the passage of negative (left panel) and positive (right panel) pions through the C_4F_8O radiator gas onto PMT (cyan) arrays with the aid of straight cones (red).

2166 9.2 Simulation

2167 9.2.1 Photoelectron Yield

2168 Due to the SoLID geometrical acceptance with respect to the target and to the constraints on the
2169 photon detector positioning inside the Čerenkov tank, the particles with large polar angle entering

2170 the detector will travel a larger gas length compared to those with a low polar angle. Thus, the
2171 optimization was done favoring the low angle kinematics whenever possible and by keeping the
2172 number of maximum reflections to 2: one on the mirrors and one possibly on the cones (not all
2173 photons need the extra bounce on the cones to be collected by the PMT arrays). As a consequence,
2174 the loss of photons through absorption on the reflective surfaces is kept to a minimum.

2175 Our simulation of the expected number of photoelectrons shown in Fig.80, takes into account
2176 realistic parameters for the gas index of refraction, gas transparency, mirror and cone reflectivities
2177 and the quantum efficiency of the H8500-03 PMTs to account for the photon to photoelectron con-
2178 version. We scaled down the number of photoelectrons obtained from the GEANT4 simulation by
2179 a conservative factor of 0.5 mostly to account for the dead zones on the PMT tiles due to incom-
2180 plete photocathode coverage. The index of refraction of C_4F_8O has been measured at Syracuse
2181 University [226] between 400 and 650 nm, while below 400 nm we used an extrapolation based
2182 on a parametrization from HERA/DELPHI of this index[227]. We studied the impact on the ex-
2183 pected number of photoelectrons on the large uncertainty in the C_4F_8O refractivity by assuming a
2184 refractivity 20% smaller than the nominal value extracted from the Syracuse and HERA/DELPHI
2185 measurements. We found that the yield of photoelectrons would still be sufficient, though marginal,
2186 at the lowest momentum of 2.5 GeV. The C_4F_8O transmittance has been measured at Jefferson Lab
2187 in Hall B with great accuracy in a photon wavelength range of 200 to 500 nm. We used these data
2188 in our simulation to account for Čerenkov photon absorption in the gas. For mirror, the Carbon
2189 Fiber Reinforced Polymer (CFRP) mirror base is preferred, which is a more rigid, lighter mate-
2190 rial as a suitable choice for large size mirrors. We contacted the USA company Composite Mirror
2191 Applications (CMA) that manufactured CFRP mirrors for the LHCb program at CERN [228] and
2192 we received a favorable response regarding the feasibility of such mirrors for our detector. CMA
2193 supplied us with data on CFRP mirror reflectivity as measured on the LHCb mirrors they manufac-
2194 tured. We used these parameters in our simulation to account for the Čerenkov photon absorption
2195 on the reflective surface of mirrors and cones. For the reflection cone, we plan to use the Aluminum
2196 coated Lexan film and attach it its base which sever as the magnetic fielding cone also. The film
2197 is also used by CLAS12 Low Threshold Cerenkov as their mirror reflection surface and has good
2198 performance.

2199 The photoelectron yield dependence on polar angle and momentum is shown in Fig.80. For a
2200 fixed polar angle the number of photoelectrons increases with increasing momentum as we move
2201 away from the pion firing threshold of 2.2 GeV and then saturates. There is also an increase of yield
2202 with increasing polar angle due to the detector geometry which allows pions with larger angle to
2203 traverse more gas than those with low polar angle.

2204 9.2.2 Pion Detection Efficiency and Kaon Rejection Factor

2205 The expected performance of the detector has been further studied by estimating the pion detection
2206 efficiency and kaon rejection factor for a given cut on the number of photoelectrons with no input
2207 from other particle identification detectors. Background studies have shown [229] that the expected
2208 pion to kaon ratio is 10 to 1. The pion and kaon photoelectron distributions are simulated as con-
2209 volutions of Poisson and Gauss distributions. The resolution of the PMT enters as the standard
2210 deviation of the Gauss distribution while the mean of the Poisson distribution is the output of the
2211 GEANT4 simulation shown in Fig.80. We measured the resolution of H8500C-03 to be 1 photoelec-
2212 tron. We mapped the pion detection efficiency and kaon rejection factor for few kinematics where
2213 we expect the smallest number of photoelectrons, namely at 8.0 degrees and momentum between
2214 2.5 and 4.5 GeV and our results are shown in Fig.81. Assuming that kaons would produce at most
2215 1 photoelectron below the Čerenkov threshold, for a cut on the number of photoelectrons of 3, the a

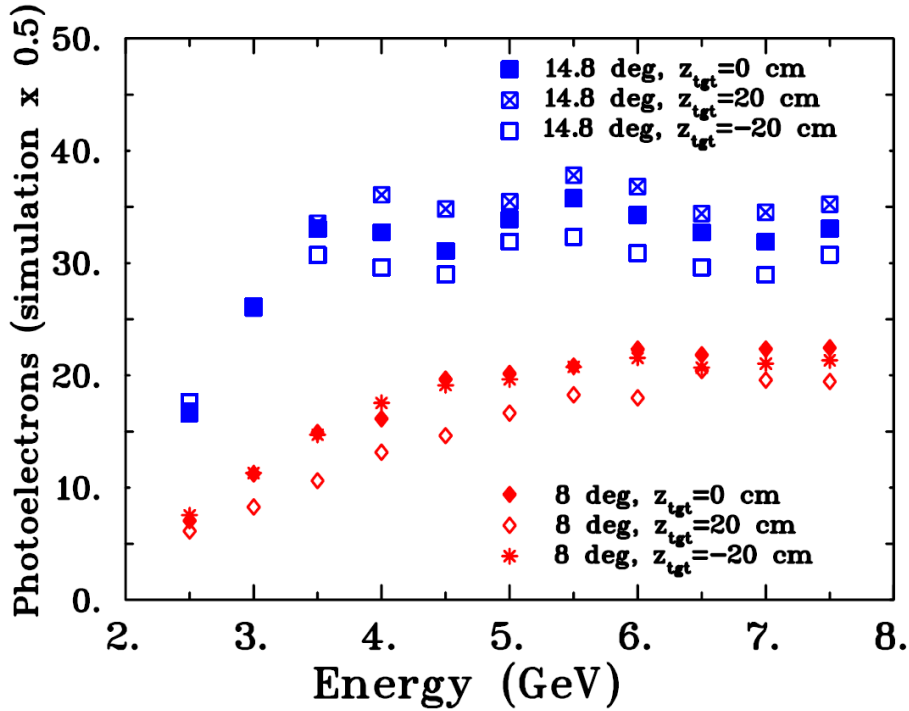


Figure 80: Simulated number of photoelectrons as a function of the pion polar angle and momentum. The results are shown for positive pions. A very similar output is obtained for negative pions.

2216 pion detection efficiency is 99.0% (99.6%) at 2.7 GeV (3.0 GeV) with the same kaon contamination
 2217 as small as 0.8%. At 8 degrees and below 2.7 GeV, the pion efficiency starts to drop below 99%.
 2218 For larger momenta, a cut placed at 4 photoelectrons would result in a pion detection efficiency
 2219 larger than 99.7% with a kaon contamination below 0.3%. This would meet the requirements of the
 2220 approved experiments with SoLID.

2221 9.3 Performance of the PMTs in Magnetic Field

2222 We performed extensive bench tests of the H8500-03 and H12700-03 PMT at Jefferson Lab to map
 2223 its performance in a magnetic field and assessed its capability of resolving single photoelectron
 2224 signals[230]. The single photoelectron resolution was measured to be 1 photoelectron or better.
 2225 The magnetic field test results are summarized in Fig.82. The longitudinal field is perpendicular
 2226 to the face of the PMT and is labeled as B_z . The transverse field orientations, perpendicular to the
 2227 sides of the PMT are shown as B_x and B_y . The PMT relative output is reduced by at most 30% when
 2228 exposed to a longitudinal magnetic field up to 400 Gauss. Our studies of the single photoelectron
 2229 response in field indicated that these losses happen mostly at the amplification stage on the dynode
 2230 chain making it possible to compensate for this effect with external amplification. These results are
 2231 very encouraging as it suggests that the effect of the field component which is hardest to shield,
 2232 the longitudinal one, could be compensated for by superficial shielding and additional external
 2233 amplification. The degradation of the PMT output in transverse magnetic field is more pronounced,
 2234 up to 90% at 180 Gauss but this field component is easier to shield.

2235 The magnetic field shield that would incorporate the cones used for focusing and that would
 2236 reduce the SoLID field at the PMT location to a few tens Gauss in the longitudinal direction and to
 2237 a few Gauss in the transverse one. Suggestion from the USA company Amuneal is that a 2-layer
 2238 shield with a thin inner layer of Amumetal and a thin outer layer of carbon steel with mylar in

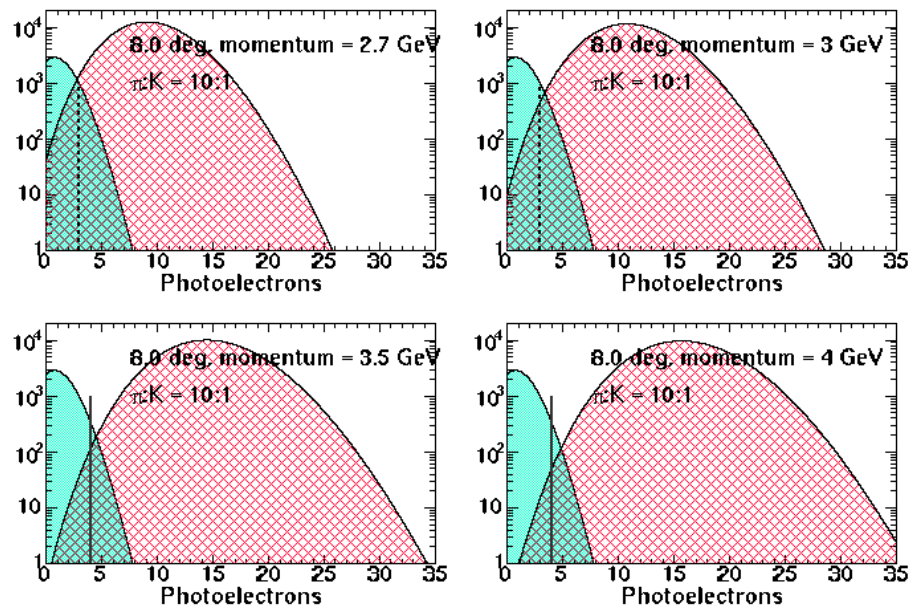


Figure 81: Simulated distributions of pions (red) and kaons (green) at with a polar angle of 8.0 degrees taking into account the photon detector resolution and the expected pion to kaon ratio.

2239 between would meet our requirements.

2240 9.4 Engineering Design

2241 The detector is separated into two halves and total 10 (36 deg) segments to facilitate fabrication
 2242 and handling. An engineering design of one half of the pressure tank is given in Fig.83. The
 2243 structure is mostly made of Aluminum. The outer shell parts are formed into an arc, welded and
 2244 then precision machined. One segment with PMTs, cones, and mirrors are shown in Fig.84. The
 2245 PMT arrays are inserted from outside the tank, into tubes arrayed on the outer shell; they seal with
 2246 an o-ring on a male gland. The cones are mounted inside the outer shell, with the possibility of fine
 2247 position adjustment (from outside) through the PMT mount tube. The CFRP spherical mirrors are
 2248 fixed with mounts at each end of the mirror and attached to the tank's outer shell and inner cone,
 2249 respectively. The detector is positioned, in the magnet pole extension assembly, on large 1.5 inch
 2250 diameter precision stainless steel rods (they could be shared with the adjacent detectors). The rods
 2251 are mounted on the magnet extension black plate and insert into the magnet rear pole upon magnet
 2252 assembly. Each detector segment will slide over them and are held in place (in Z) with shaft collars.
 2253 The tank's inner cone is secured to the magnet inner cone.

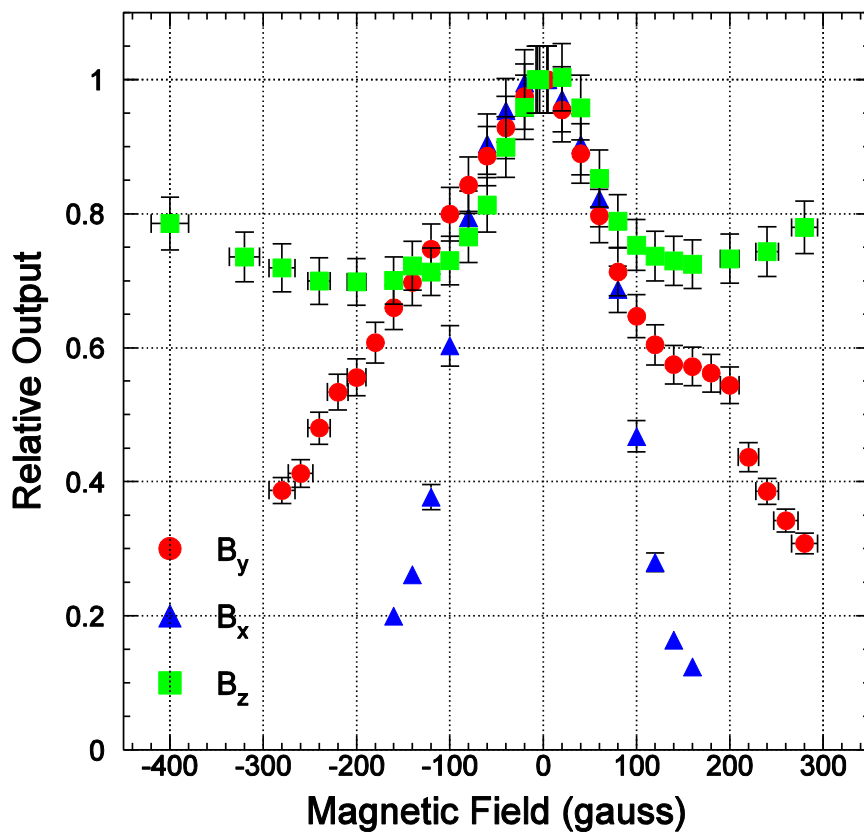


Figure 82: Relative output of the H8500-03 PMT in magnetic field. The PMT output normalized to the zero magnetic field configuration is shown for a longitudinal field orientation (i.e. perpendicular to the face of the PMT) in squares and for the transverse orientations (i.e. perpendicular to the sides of the PMT) in circles and triangles.

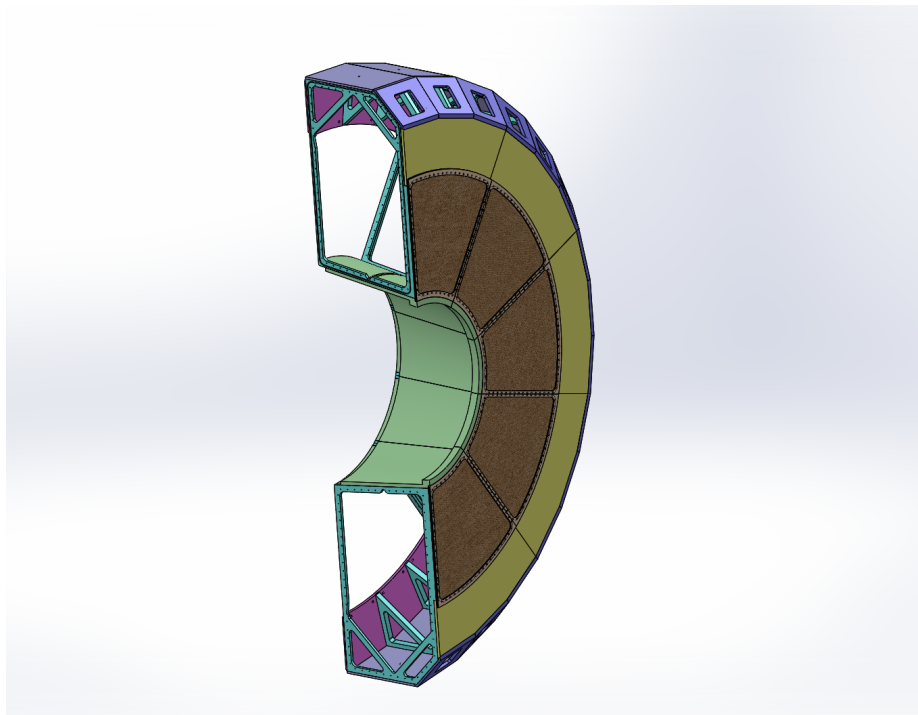


Figure 83: Conceptual design of the heavy gas Čerenkov detector

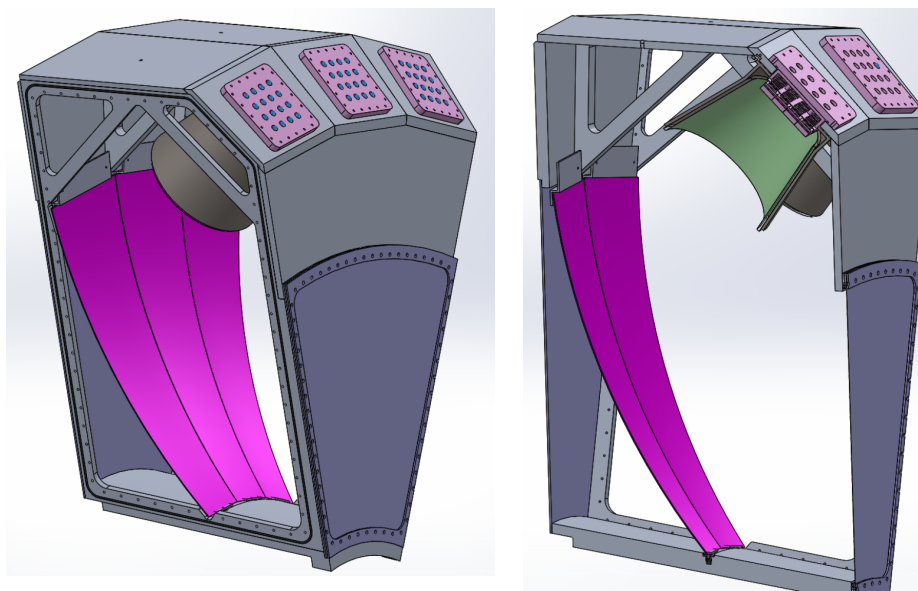


Figure 84: Conceptual design of the heavy gas Čerenkov detector (left) and PMT assembly (right)

2254 10 Electromagnetic Calorimeter

2255 10.1 Overview

2256 Electromagnetic calorimeters (EC) are used in the PVDIS, SIDIS and J/ψ experiments to mea-
 2257 sure the energy deposition of electrons and hadrons, and to provide particle identification (PID).
 2258 The SIDIS and J/ψ experiments share similar configurations and will be referred to as the SIDIS
 2259 configuration hereafter. There are three calorimeters: the PVDIS experiment uses a forward an-
 2260 gle calorimeter (FAEC) to detect the scattered electrons; the SIDIS experiments use a forward angle
 2261 calorimeter (FAEC) and a large angle calorimeter (LAEC). Both detect the scattered electrons while
 2262 the FAEC also provides MIP triggers for pions. For electron detection, the dominant background
 2263 comes from electro- and photo-produced pions. The desired performance is summarized in Table 13
 2264 and the EC geometry in Table 14. Please note that the EC geometrical coverage is slightly larger
 2265 than other detectors because the edges of the EC are expected to have degraded performance due to
 2266 shower spreading. The total coverage area of the SIDIS FAEC and LAEC is less than that of the
 2267 PVDIS FAEC. The plan is to share modules between the two configurations. Thus all modules need
 2268 to be rearranged when we switch between the PVDIS and SIDIS configurations.

	Desired performance
π^- rejection	$\gtrsim[50:1]$ for above Cerenkov threshold
e^- efficiency	$\gtrsim 95\%$
Energy resolution	$< 10\%/\sqrt{E}$
Radiation resistance	$\gtrsim 400$ kRad
Position resolution	$\lesssim 1$ cm

Table 13: Overview of the SoLID calorimeter desired performance.

	PVDIS FAEC	SIDIS FAEC	SIDIS LAEC
z (cm)	(320, 380)	(415, 475)	(-65, -5)
Polar angle (degrees)	(22,35)	(7.5,14.85)	(16.3, 24)
Azimuthal angle	Full coverage		
Radius (cm)	(110, 265)	(98, 230)	(83, 140)
Coverage area (m ²)	18.3	13.6	4.0

Table 14: Geometrical coverage for the SoLID electromagnetic calorimeters. The z direction is along the electron beam and the origin is at the solenoid center.

2269 The design of the SoLID ECs is determined by both the physics goal and the expected running
 2270 conditions. The design is challenging due to our unique constraints including high radiation back-
 2271 ground (≈ 400 kRad, as in Table 13), strong magnetic field (1.5 T on SIDIS LAEC), large coverage
 2272 area, and the budget. These factors prevent the use of many traditional calorimeter technologies,
 2273 including NaI (TI), CSI, BGO and lead glass because of the low radiation resistance; PbWO_4 , LSO
 2274 and PbF_2 because of their high cost; and lead/scintillator fiber calorimeter because of the high cost
 2275 and the large amount of light readout required.

2276 Due to the PID requirement, it is necessary to segment the EC longitudinally into a preshower
 2277 and a shower detector. The following design that meets the experimental requirements was chosen:
 2278 the shower calorimeter modules are based on the so-called Shashlyk design [231], a sampling-

2279 type design consisting of alternating layers of scintillator and lead (as an absorber); the preshower
 2280 detector is made of a layer of lead as a passive radiator followed by scintillator pads [232, 233].
 Details of the design are summarized in Tables 15 and 16.

Type	passive radiator + sensitive layer
Passive radiator	$2X_0$, Pb
Sensitive layer	2 cm, plastic scintillator 100 cm ² hexagon tile
Light transportation	WLS fiber embedded in the scintillator

Table 15: SoLID electromagnetic calorimeter, preshower design.

2281

Type	Shashlyk sampling calorimeter	
Each layer	Absorber	0.5 mm Pb
	Scintillator	1.5 mm STYRON 637 plastic scintillator
	Gap	Paper, 0.12 mm × 2 sheets
	Radiation Length	$0.093X_0$
Overall	Radiation length (X_0)	24 cm
	Molire radius	5 cm
	Length	$18 X_0$, 43.4 cm
	Total number of layers	194
	Lateral granularity	100 cm ² hexagon
	Light transportation	WLS fiber, 100 per module, penetrating layers longitudinally

Table 16: SoLID electromagnetic calorimeter, shower design.

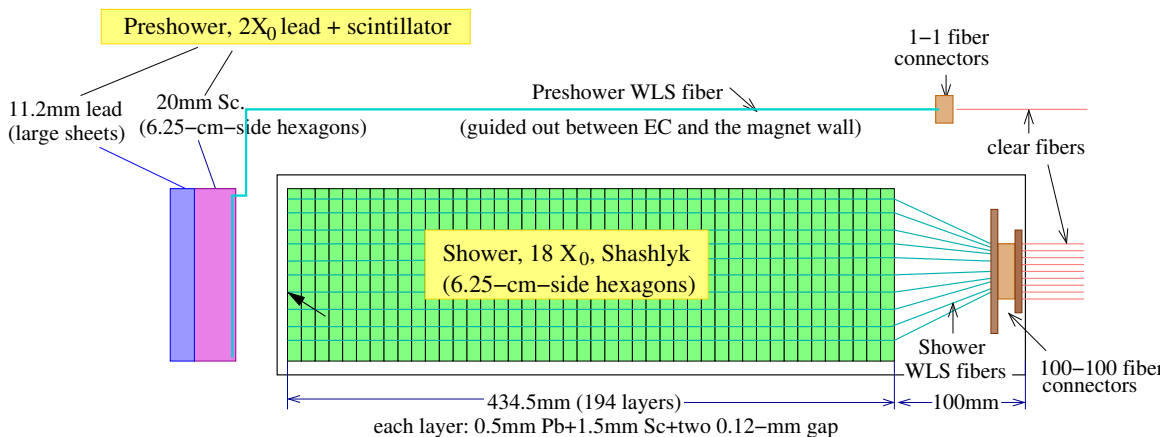


Figure 85: Design diagram of the SoLID electromagnetic calorimeter module. Spacing between the preshower and the shower detectors, and the spacing between the shower module and the 100-100 fiber connectors, need to be kept as small as possible yet still allow safe routing of the WLS fibers and positioning of the support structure.

2282 The structure of both the preshower and the shower detector is illustrated in Fig. 85. In the
 2283 experiment, particles are incident close to perpendicular to the scintillator-lead layers. Scintillation

2284 light is absorbed, re-emitted and transported to the photon detector by wave-length shifting (WLS)
 2285 optical fibers penetrating through the shower modules longitudinally, along the incident particle
 2286 direction. The cross sectional area of the shower modules was optimized to be 100 cm^2 (see Sec-
 2287 tion 10.2.3), with a hexagon shape determined for the convenience of the support structure design.
 2288 The scintillator tile of preshower modules has the same 100 cm^2 hexagon shape to match the shower
 2289 modules, which maximizes PID efficiencies, facilitates the design, and allows fast switch-over be-
 2290 tween SIDIS and PVDIS. The lead absorber of the preshower can be made of large sheets.

2291 Geant4-based simulations are used to study the performance and optimize the design of the
 2292 key specifications while minimizing the cost. Figure 86 shows the simulated shower of a 3 GeV
 electron incident on the PVDIS EC. In the following we will present details of the shower and the

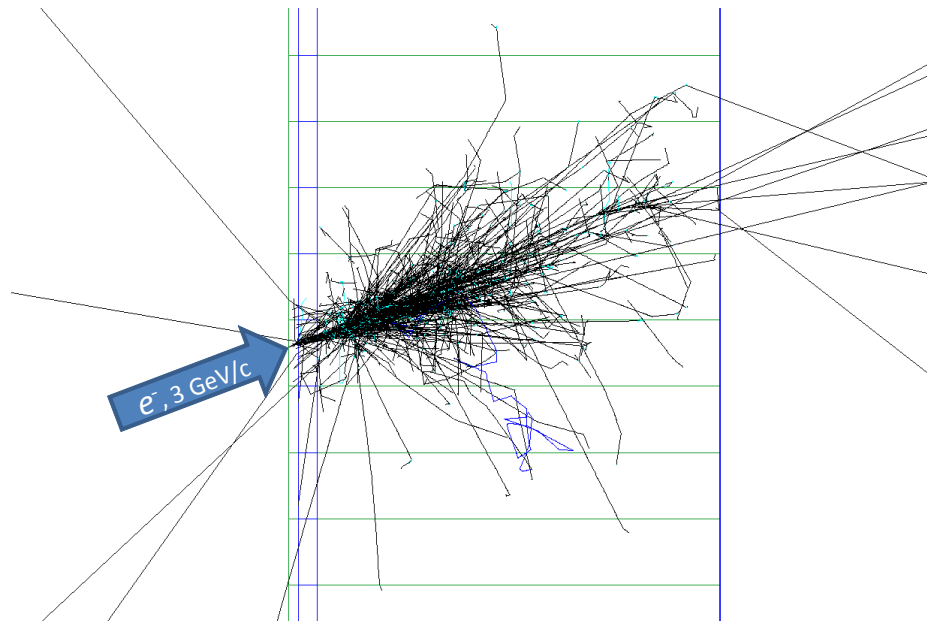


Figure 86: GEANT4 simulation of the shower generated by a 3-GeV electron incident on the PVDIS calorimeter. The black and green tracks are secondary photons and electrons respectively. The green horizontal lines are edges of calorimeter modules. The first two layers of materials are the preshower detector, consisting of $2X_0$ of lead and 2 cm thick of scintillator.

2293
 2294 preshower design, general layout and the support system, light readout, expected radiation dose,
 2295 PID and trigger performance, and a cost estimate.

2296 10.2 Shower Detector Design Considerations

2297 10.2.1 Total Length of the Calorimeter

2298 The overall length of calorimeter should be long enough to enclose most of the electromagnetic
 2299 shower and short enough to maximize the difference in energy deposition between electrons and
 2300 pions. The fraction of energy leak out for electron showers, averaged inside the acceptance of
 2301 the SIDIS-Forward calorimeter, was studied for different total lengths of calorimeter. As shown
 2302 in Fig.87, a total length of 20 radiation lengths was found to be a good balance. Considering the
 2303 2-radiation-length thickness of preshower, this leads to a shower detector length of 18 radiation
 2304 lengths or 43.4 cm.

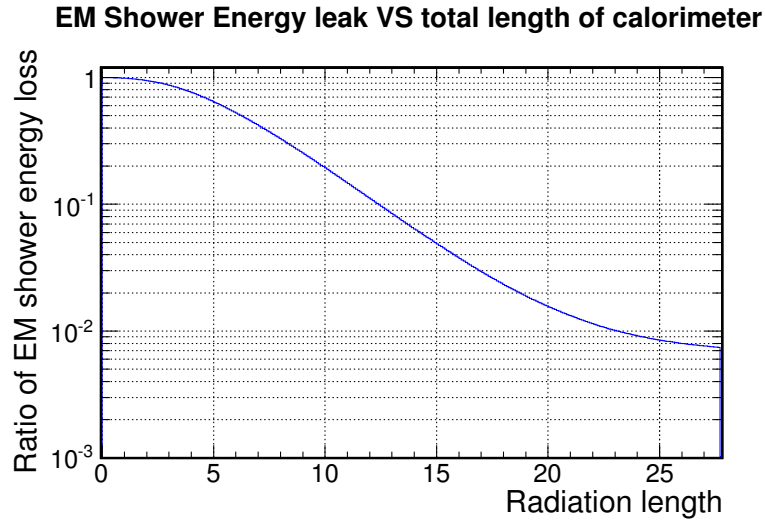


Figure 87: Fractional energy leak for an average SIDIS-Forward electron shower vs. different total length of the calorimeter.

2305 **10.2.2 Sampling Ratio of the Shower Detector**

2306 Each layer of the shower module consists of a 1.5 mm-thick scintillator plate and a 0.5-mm absorber
 2307 plate made of lead. The Pb absorber thickness of 0.5 mm or less is favored to provide a fine sampling
 2308 and therefore better energy resolution. The thickness of the scintillator plate should be thin enough
 2309 to ensure fine longitudinal sampling, while thick enough to reduce light attenuation in the lateral
 2310 direction. A thickness of 1.5 mm was chosen following the experience of previous Shashlyk designs
 2311 used by the KOPIO experiment [231, 234], the PANDA experiment [235], and the COMPASS-II
 2312 experiment. The COMPASS module is shown in Fig. 88. A gap of 120 μm is kept between the lead
 2313 and scintillator plates to accommodate a sheet of high-reflectivity paper, which reduces the loss of
 2314 scintillation light.

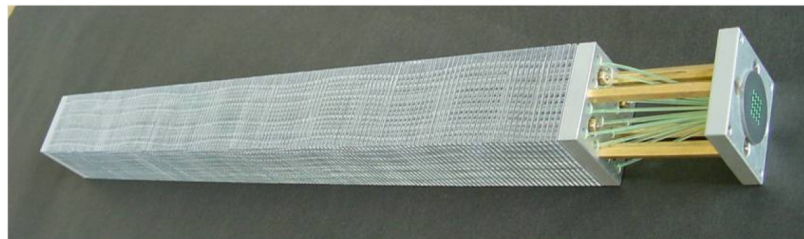


Figure 88: COMPASS-II Shashlyk calorimeter module. This illustrates the basic design of shashlyk modules: each module consists of alternating scintillator and lead (or other absorber material) layers, with WLS fibers penetrating across all layers to guide out the scintillation light signal. Four stainless steel rods are used to fix all layers together and support the whole module.

2315 Figure 89 shows the simulated energy resolution using the chosen configuration of 1.5 mm
 2316 scintillator and 0.5 mm lead. A resolution of about $4\%/\sqrt{E}$ is achieved.

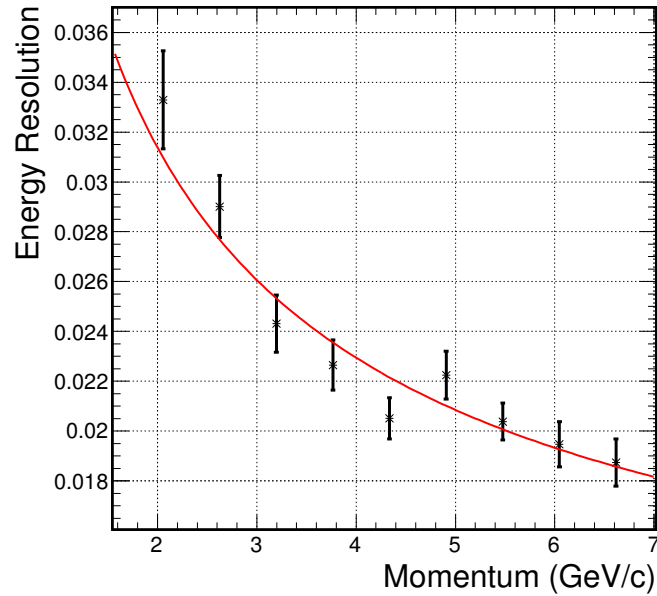


Figure 89: Simulated energy resolution of the SoLID calorimeter using both the Preshower and the Shower. The error bars are statistical error of the simulation. This simulation was performed without background to demonstrate the intrinsic PID performance of the EC. Simulation results including the background will be presented in section 10.7.

2317 10.2.3 Lateral Size of the Calorimeter Module

2318 A smaller lateral size for calorimeter modules leads to better position resolution and lower back-
 2319 ground. However, it will also increase the total number of modules and readout channels, leading to
 2320 higher overall cost. The study shows that a lateral size of about 100 cm^2 will provide a good balance
 2321 between position resolution, background and the overall cost as shown in Fig. 90. A hexagon lateral
 2322 shape is favored by the layout and the support design.

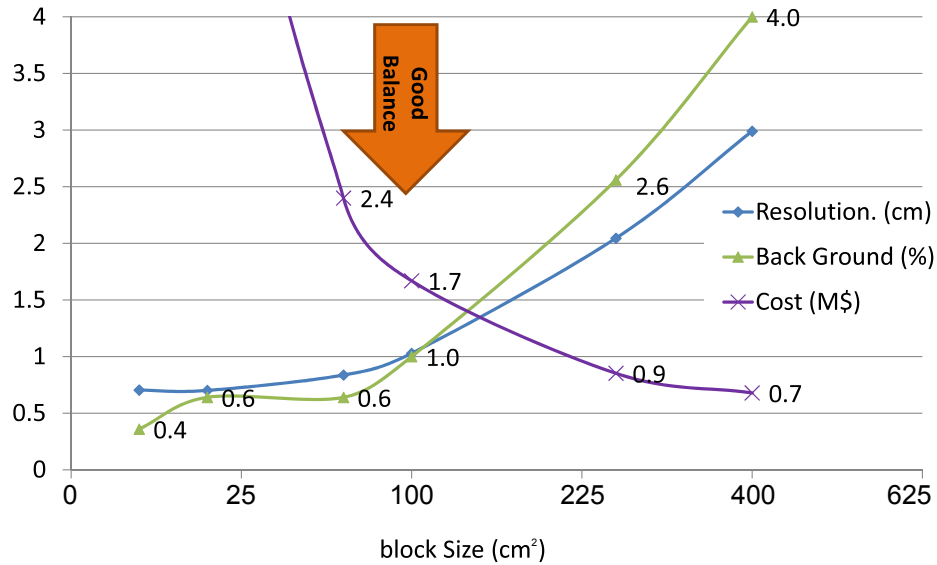


Figure 90: Position resolution and background level from simulation and the cost of the shower detector vs. lateral block size of the module.

2323 10.3 Preshower Detector

2324 Segmenting the EC longitudinally into a preshower and a shower part is essential to reaching the re-
 2325 quired pion rejection. Two designs were considered for the preshower detector: a full Shashlyk-type
 2326 design that is optically isolated from the shower detector, and a passive radiator/scintillator pad de-
 2327 sign as used in the HERMES [232] and LHCb [233] experiments. Comparing to a Shashlyk-type
 2328 preshower, the passive radiator/scintillator pad design has several advantages including increased
 2329 radiation hardness, simplicity in construction, and fewer WLS fibers to read out. For a passive
 2330 radiator of $2X_0$, the impact on overall energy resolution is less than $0.5\%/\sqrt{E}$ for electrons with
 2331 momentum larger than $2 \text{ GeV}/c$. Therefore, the passive radiator/scintillator pad design was adopted
 2332 for the preshower detector. Details of the design are as follows:

- 2333 • The thickness of the preshower radiator was determined by optimizing the overall pion rejec-
 2334 tion at the desired electron efficiency. As shown in Fig. 91 (top), the preshower-alone pion
 2335 rejection improves as the radiator thickens up to $3.5X_0$ due to immediate development of the
 2336 electromagnetic shower. However, the impact on the overall energy resolution degrades with
 2337 increased thickness of the absorber. A thickness of $2X_0$ for the radiator was found to be an
 2338 optimal choice for the SoLID application.
- 2339 • The scintillator and readout design is similar to that of the LHCb experiment [233]: WLS
 2340 fibers are embedded in one 2 cm-thick scintillator pad to absorb, re-emit and conduct the
 2341 photons for readout.

2342 With the above configuration and assuming a response of 100 photoelectrons per MIP (see next
 2343 paragraph), the relation between pion rejection and electron efficiency for preshower alone can be
 2344 plotted as a function of scintillator energy cuts, as shown in Fig. 91 (bottom right). One can see a
 2345 pion rejection of better than 5 : 1 can be achieved at an electron efficiency of $> 94\%$.

2346 Figure 92 shows pictures of the LHCb preshower tile (left) compared to a SoLID preshower
 2347 prototype made by IHEP (right). Preliminary cosmic tests show that we can achieve up to 50 photo-
 2348 electrons per MIP by embedding two 1.5-m long, 1-mm diameter Kuraray Y11(200)S WLS fibers

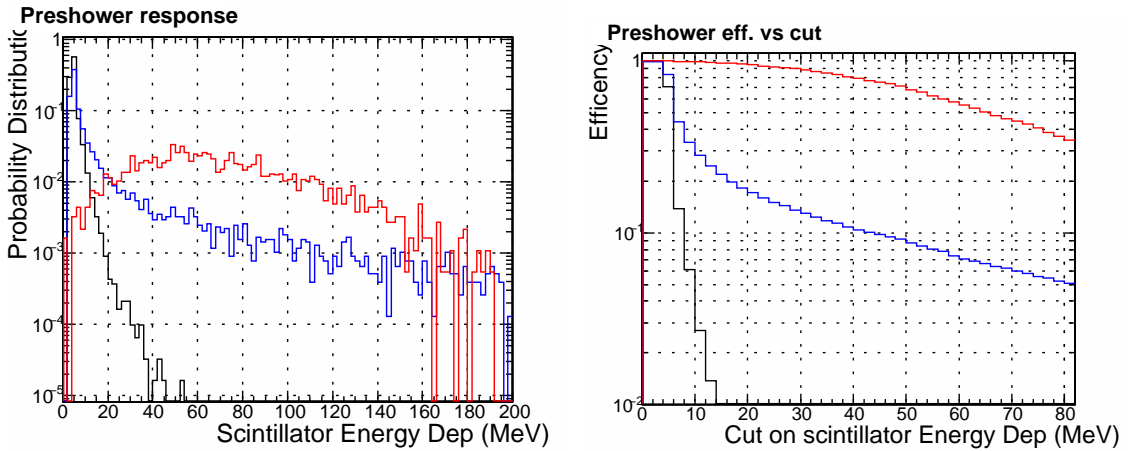
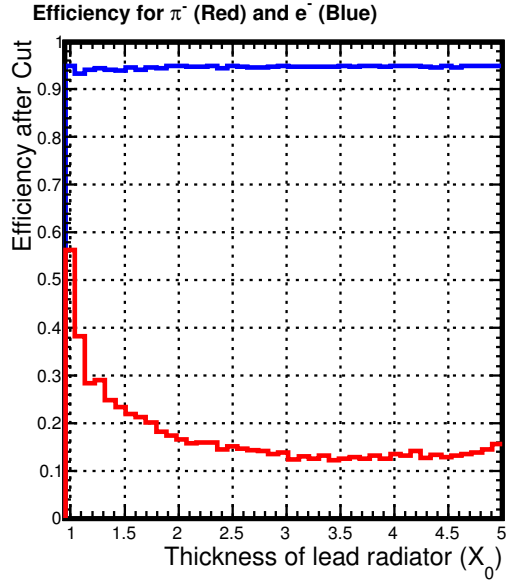


Figure 91: Simulated performance for the preshower detector. Top: $1/(\pi^-$ rejection) (red curve) at a 95% electron efficiency (blue curve) vs. different thickness of the lead radiator. Bottom: Energy deposition in the scintillator (left) and detector efficiency vs. energy deposition cut (right), for electrons (red), π^- (blue) and μ^- (black), for a preshower consisting of $2X_0$ of lead radiator and 2 cm of scintillator.

2349 in the circular groove on the preshower scintillator. The use of multiple fibers allows minimizing
 2350 the attenuation due to WLS fiber length. The final number of photoelectrons that reaches the PMT
 2351 will depend further on loss in the fiber connector and the attenuation in the clear fiber. Current
 2352 simulation assumes a preshower response of 100 photoelectrons per MIP, and studies of how the
 2353 number of photoelectrons affects the PID performance are ongoing.

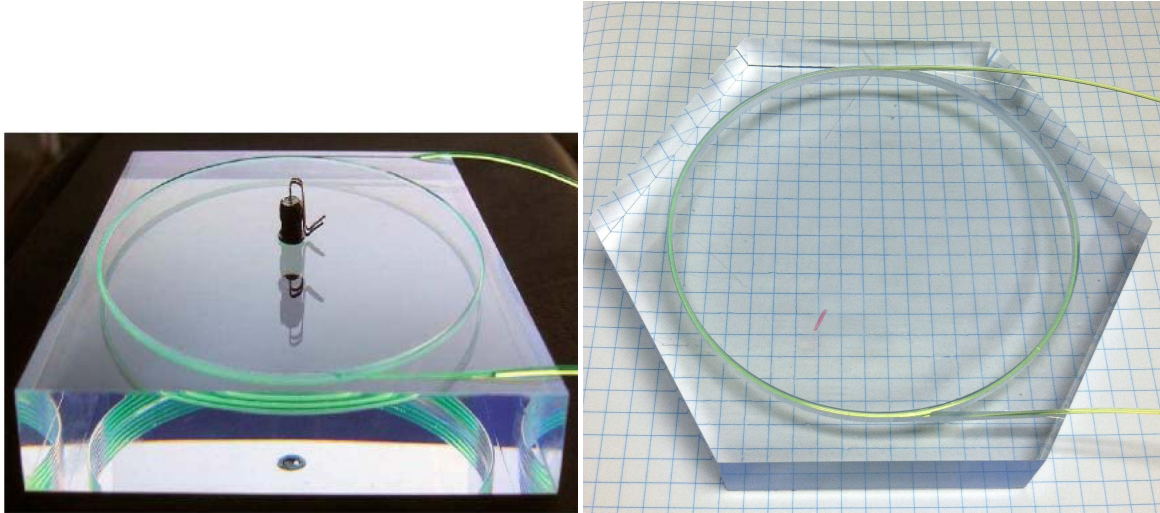


Figure 92: Preshower scintillators. Left: LHCb preshower tile ($12 \times 12 \times 1.5$ cm) [233]. A single WLS fiber is embedded in a circular groove for 3.5 turns. In the middle of the tile is an LED for testing purposes. Right: SoLID preshower prototype made by IHEP. The SoLID prototype has a geometry of 6.25-cm-side hexagon and is 2 cm thick. Shown here are two 1-mm diameter WLS fibers embedded in a 9-cm diameter circular groove, each 2.5 turns.

2354 10.4 Layout and Support

2355 The total area of the PVDIS EC is slightly larger than that of the SIDIS ECs. The modules will
 2356 be re-arranged between the two configurations, where modules from the PVDIS FAEC will be split
 2357 and re-arranged into the SIDIS FAEC and LAEC. The SIDIS EC layout must preserve the 2-fold
 2358 rotation symmetry in the spectrometer, and it is convenient to have the same symmetry for the
 2359 PVDIS configuration as well. The design layout that meets these requirements is shown in Fig.93
 2360 for the PVDIS configuration. The forward angle support system is shared by PVDIS and SIDIS
 2361 FAEC, and the SIDIS LAEC will have a separate support system.

2362 The scintillator tiles of the preshower modules will be mounted on a aluminum plate that simul-
 2363 taneously supports also the $2X_0$ lead. For shower modules, the lead and the scintillator layers in
 2364 each Shashlyk module are held together by six stainless steel rods penetrating longitudinally through
 2365 the module. The modules are terminated by two aluminum endplates. The six rods protrude from
 2366 the endplates and are supported by two aluminum support structures, one 2 cm thick plate between
 2367 preshower and shower, and one 4 cm thick plate behind the shower. The support structure also holds
 2368 the optical fiber connectors (see next section).

2369 10.5 Light Readout

2370 For both preshower and shower, the blue light from scintillators is converted into green light by
 2371 WLS fibers embedded in or penetrating through the modules. Each preshower tile will use two
 2372 WLS fibers with 1 mm diameter, each fiber arranged for two turns and embedded in a groove on
 2373 the surface of the tile. The preshower WLS fibers will be routed using the space between preshower
 2374 and shower to the space between EC and the solenoid wall. Each shower module will use 100
 2375 1 mm diameter WLS fibers arranged along the direction of the particle trajectory, and the fibers
 2376 will be guided directly towards the back of EC. To avoid light loss over long distances, WLS fibers
 2377 will be connected immediately to clear fibers using one-to-one connectors for readout by PMTs.

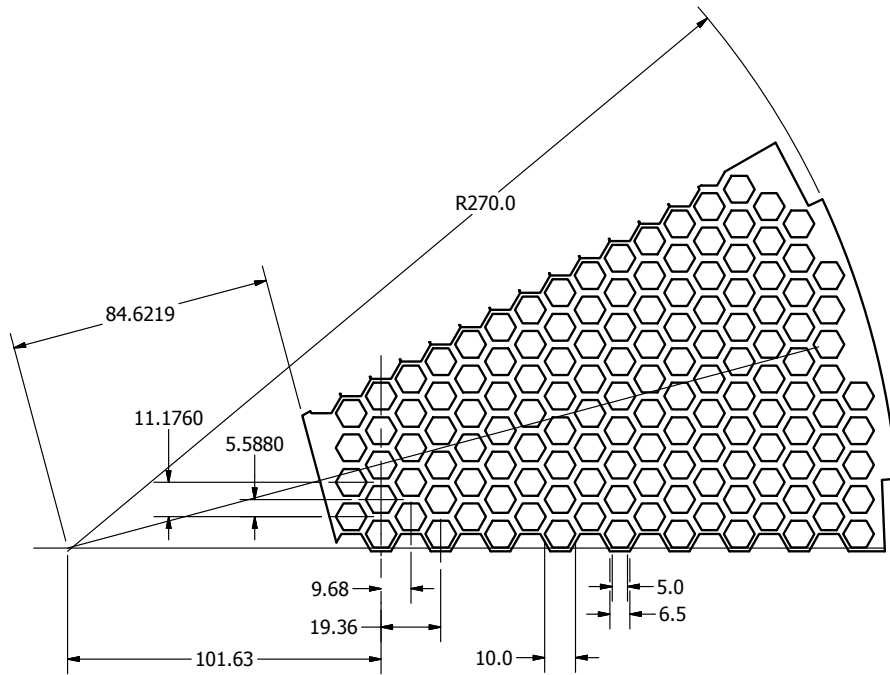


Figure 93: Layout of the hexagon-shaped modules with their support for a 30-degree wedge of the FAEC for the PVDIS configuration. The number of modules is 138 full modules plus 9 half-modules along the horizontal line. If counting 147 modules per 30-degree wedge, the total number of modules needed is 1764. We use 1800 modules for planning purposes at this stage.

2378 LHCb used homemade fiber connectors. For SoLID, homemade connectors is an option but we
 2379 have tested fiber connectors from the Japanese Fujikura company and found they work well. The
 2380 Fujikura connectors were used by the Minerva experiment and their tests indicate the light loss in
 2381 the connector is in an acceptable range of (10-20)% [237].

2382 For the preshower it is essential to achieve a high photoelectron yield such that the best PID
 2383 performance can be reached. We chose the Kuraray Y11(200) fiber because it has better mechanical
 2384 properties and further a small minimal bending radius, as shown by the ATLAS Collaboration [236],
 2385 which is crucial for us because our preshower fiber groove has a bending radius of 4.5cm. Our tests
 2386 show the Bicon BCF91A fiber has similar light loss to Y11 but the light output is reduced by a factor
 2387 of two when it is embedded in the preshower groove (compared to nearly zero loss for the Y11). The
 2388 Y11 fiber has also been tested to higher radiation dose than Bicon BCF91A fibers by ATLAS [238].
 2389 For shower modules, the fibers are straight and hence the Bicon BCF91A WLS fiber becomes a
 2390 more economical choice while still satisfying the requirement on radiation hardness. Bicon BCF92
 2391 fiber has faster decay time but gives less yield than BCF91A, and is not being considered for the
 2392 SoLID ECs.

2393 The magnetic field reaches about 1.5 T behind the SIDIS LAEC and a few hundred gauss behind
 2394 both the PVDIS and SIDIS FAECs. For other experiments such as those at JLab Hall D or at LHC,
 2395 silicon photomultipliers (SiPMs) are used. However, our simulation shows the radiation background
 2396 behind the calorimeter is at the level of 10^{13} cm^{-2} 1 MeV equivalent neutrons. Studies done by the
 2397 LHCb on their tracker upgrade [239] reported cooling the SiPM can overcome the radiation damage
 2398 from a high neutron background. Still, projecting from the LHCb study tells us for SiPM to work

2399 for the shower detector, we need to cool to -70 or -80 ° C . The space limitation alone imposed
2400 by the SoLID magnet makes such cooling nearly impossible, let alone the necessary electronics for
2401 temperature control. Therefore, our current default design is to use PMTs. Long clear fibers (about
2402 1.5 m for the SIDIS FAEC and 3.5 m for the SIDIS LAEC) will be used to guide the light from the
2403 WLS fibers to PMTs located outside the solenoid region.

2404 We will use one PMT per shower module to read out the 100 fibers. We plan to design custom
2405 PMT bases so that preamplifiers with a $\times(2-5)$ gain can be used and to minimize the aging of the
2406 PMTs. For preshower modules we plan to use multi-anode PMT (MAPMTs), with all four fiber
2407 ends from each module read out by one pixel of the MAPMT. For MAPMT, the high background of
2408 the SoLID running condition constrains us to a relatively low gain in the range of $5E3-2E4$, due to
2409 the fact that the total anode current needs to be kept at only a fraction of the maximum specification
2410 to reduce the aging of the MAPMT. We plan to design pre-amplifiers with gain up to 50 and 16-
2411 channel MAPMTs. Pre-R&D of MAPMT and its preamplification board is currently underway.
2412 Note that LHCb used 64-ch MAPMTs at a gain of $5E3$ combined with a front-end electronic board
2413 that provided an intrinsic gain of about 10, and our current design is based on and is consistent with
2414 the LHCb readout method.

2415 **10.6 Radiation Effects**

2416 The ECs for the SoLID spectrometer are designed for high luminosity experiments. The expected
2417 luminosity and run time are 169 PAC-days at $10^{39} N \cdot \text{cm}^{-2} \text{s}^{-1}$ in the PVDIS configuration, 245
2418 PAC-days at $10^{37} N \cdot \text{cm}^{-2} \text{s}^{-1}$ for the SIDIS experiments and 60 PAC-days for the J/Ψ experiment.
2419 In the current design, the maximum radiation dose on the active material — scintillator and WLS
2420 fibers — in the calorimeter is significantly reduced by the use of the $2X_0$ lead plate in the preshower,
2421 and the lead blocks described in section 6 for the PVDIS configuration. Because of the use of lead
2422 blocks, the PVDIS configuration has been divided into higher and lower photon flux regions; each
2423 consists of thirty 6-degree azimuthal regions.

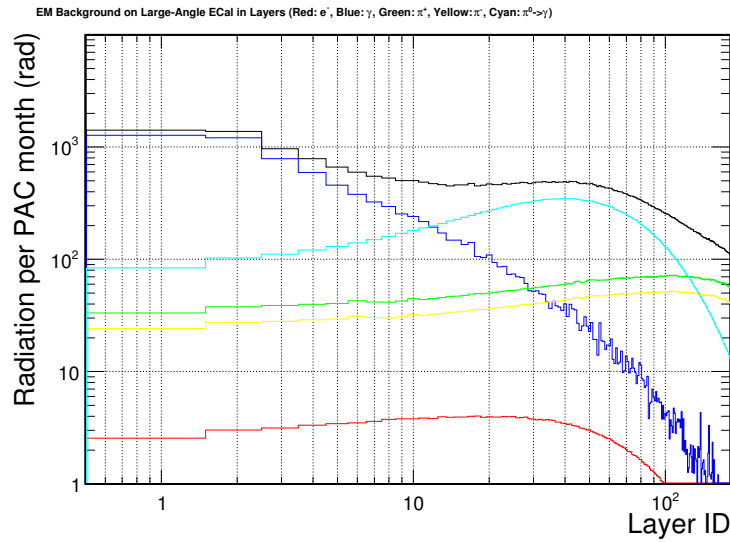
2424 The radiation dose inside the calorimeter was simulated using GEANT4 based simulations con-
2425 sidering a wide range of energy and species for the background particles. The dose rates for the
2426 active material (scintillators and fibers) are shown in Figs. 94 and 95. The highest radiation region
2427 is at the front part of the calorimeter, including the preshower scintillator pad and the front scintil-
2428 lators of the Shashlyk calorimeter modules. The maximum integrated radiation level for the active
2429 material reaches 100 kRad for the PVDIS experiment and 20 kRad in the SIDIS and J/Ψ exper-
2430 iments, which leads to a total radiation dose of less than 200 kRad for all approved experiments.
2431 This dose level can be safely handled by the choice of scintillator and WLS fibers.

2432 **10.7 Performance**

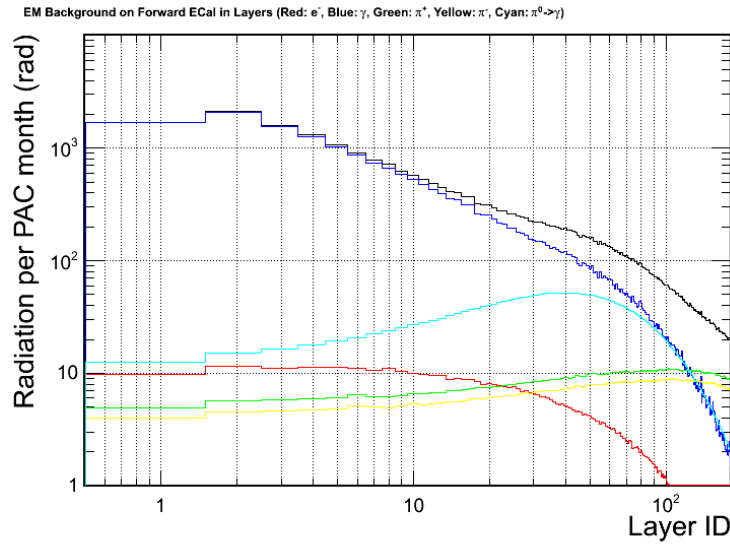
2433 The EC system plays multiple roles in the SoLID spectrometer. Its performance was evaluated in
2434 the GEANT4 based simulation and discussed in this section, including PID performance, trigger
2435 capability and shower position resolution. A realistic background simulation was set up to evaluate
2436 the calorimeter considering a wide range of species and momenta of the background particles.

2437 **10.7.1 Intrinsic electron-pion separation**

2438 As a baseline, the PID performance was first evaluated without the background. The primary track
2439 is propagated through the SoLID magnetic field in GEANT4, then enters the calorimeter. A lo-
2440 cal cluster which consists of the central calorimeter module and six neighboring hexagon-shaped

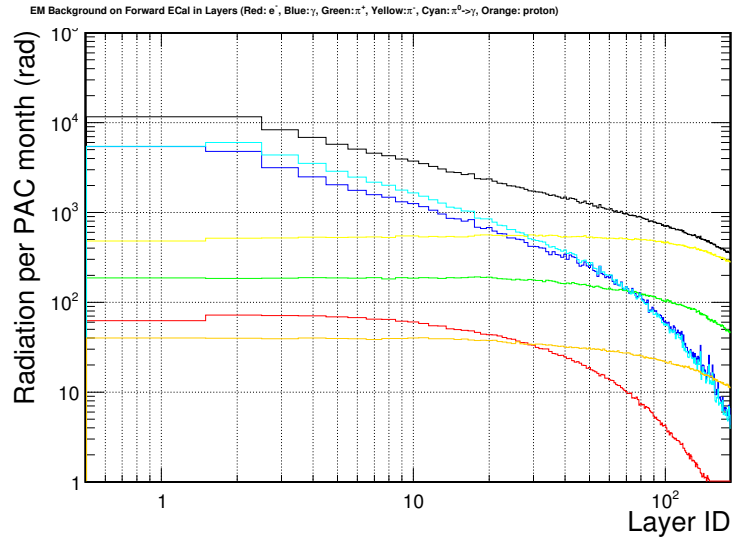


(a) SIDIS large-angle calorimeter

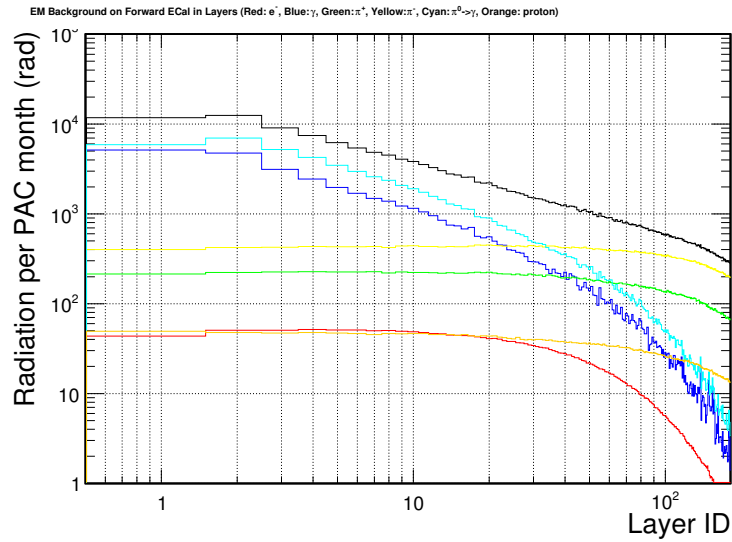


(b) SIDIS forward-angle calorimeter

Figure 94: SIDIS radiation dose rates per PAC month in each layer of the scintillator tiles in the calorimeter. Layer ID 1 is the preshower scintillator. The rest of IDs are assigned for each scintillator layer in the Shashlyk calorimeter in the order of increasing z . The color code stands for different contributions of various particle species at the front surface of the preshower: electrons (red), photons (blue), EM total (magenta), π^+ (green), π^- (yellow). The overall dose is shown by the black curve.



(a) PVDIS calorimeter in higher-photon flux region



(b) PVDIS calorimeter in lower-photon flux region

Figure 95: PVDIS radiation dose rates per PAC month in each layer of the scintillator tiles in the calorimeter. Layer ID 1 is the preshower scintillator. The rest of IDs are assigned for each scintillator layer in the Shashlyk calorimeter in the order of increasing z . The color code stands for different contributions of various particle species at the front surface of the preshower: electrons (red), photons (blue), EM total (magenta), π^+ (green), π^- (yellow), and protons (brown). The overall dose is shown by the black curve.

2441 modules is formed. With a multidimensional cut of the preshower and shower response within the
 2442 cluster (see Sec. 10.7.5), the overall pion rejection averaged over the acceptance of each calorimeter
 2443 is shown in Fig. 96. A 100 : 1 pion rejection at 95% electron efficiency is achieved for momentum
 2444 bins of $p > 2 \text{ GeV}/c$. For the lowest momentum bin $1 < p < 2 \text{ GeV}/c$, which is only needed for
 2445 the SIDIS FAEC, a better than 50 : 1 pion rejection at 90% electron efficiency is obtained.

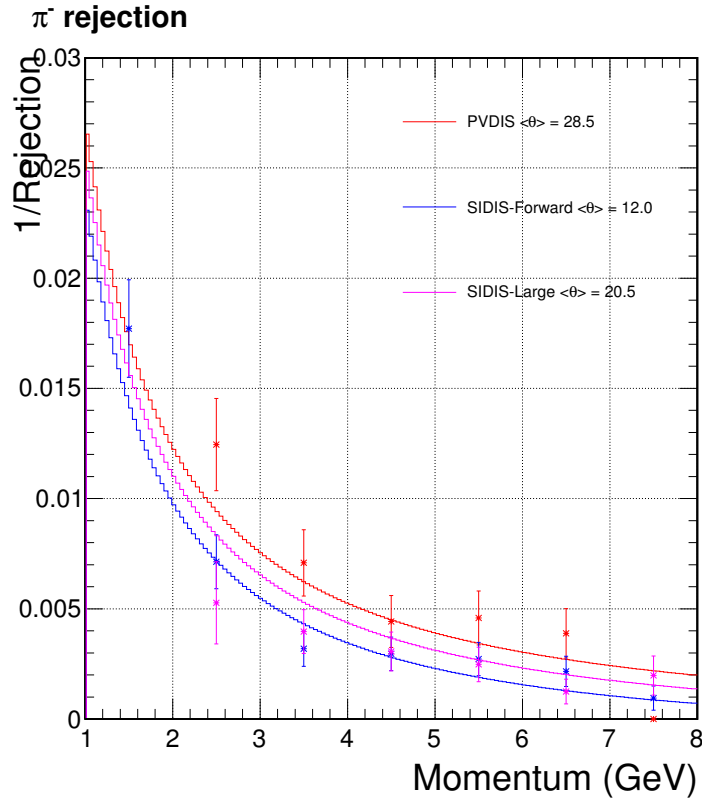


Figure 96: SoLID EC intrinsic (without background) π^- efficiency (1/rejection). From top to bottom: PVDIS with average track polar angle $\langle\theta\rangle = 28.5^\circ$ (red), SIDIS LAEC with $\langle\theta\rangle = 20.5^\circ$ (magenta) and SIDIS FAEC with $\langle\theta\rangle = 12.0^\circ$ (blue). A constant 95% electron detector efficiency is maintained for $p > 2 \text{ GeV}/c$. A 90% electron efficiency is maintained for the lowest momentum bin $1 < p < 2 \text{ GeV}/c$, which is only required for the SIDIS FAEC. The $\langle\theta\rangle$ value is different for the three calorimeter configurations, which leads to slight differences in the pion rejection curves.

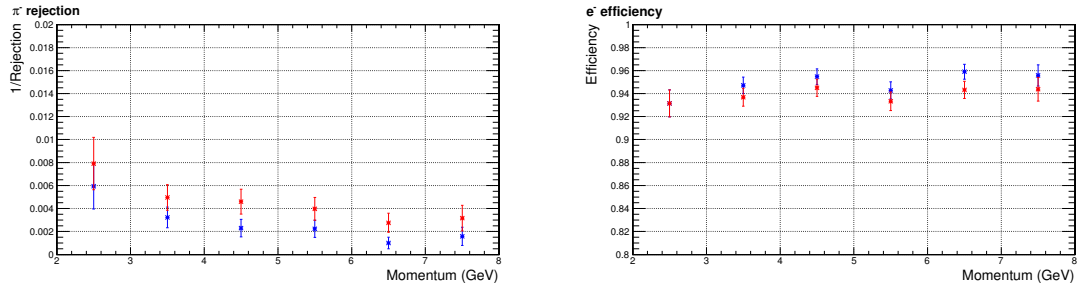
2446 10.7.2 PID performance under realistic background simulation

2447 For a large intensity device, background particles and their influence on the calorimeter perfor-
 2448 mance have to be considered. A full background simulation was implemented to study calorimeter
 2449 performance. The background simulation procedure is as follows:

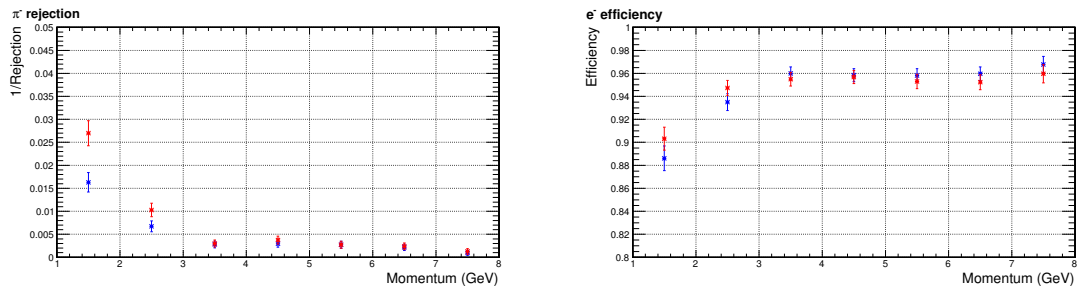
- 2450 1. Particles are generated at the target including photons and electrons from the low energy
 2451 EM processes (based on physics in GEANT4), DIS electrons (based on CTEQ6 PDF), and
 2452 hadrons (based on the Wiser fit);

- 2453 2. Particles are propagated through a SoLID GEANT4 simulation to the front surface of the
 2454 calorimeter;
- 2455 3. The EC response is simulated for a wide range of background particles — electrons, photons,
 2456 pions, and protons — within the momentum range $10 \text{ keV} < p < 11 \text{ GeV}$. A statistical model
 2457 is used for the correlation between preshower and shower responses;
- 2458 4. The background contribution to each event is produced by combining the background rate
 2459 at the EC front surface and the EC response described above for a region of interest on the
 2460 calorimeter, usually defined by a radius-azimuthal angular bin. A conservative 30 ns coinci-
 2461 dence window between background particles and the primary event is assumed.
- 2462 5. The background contribution is embedded into the raw signal from the simulated primary
 2463 particles (high energy electrons and pions). The background-embedded data are then analyzed
 2464 as raw ADC signals. The energy response is calibrated and PID and trigger performance are
 2465 analyzed.

2466 Typically, background rate is the highest in the inner radius region and drops by approximately
 2467 one order of magnitude in the outer radius region. Figure 97 shows the EC performance for the
 2468 SIDIS configuration in the inner radius region. For SIDIS experiments, effects from background
 2469 particles are visible but not significant: for large-angle EC, the pion rejection remains better than
 2470 100:1 for all momentum bins; for forward-angle EC, there is no noticeable change in the PID per-
 2471 formance other than for the lowest momentum bin $1 < p < 2 \text{ GeV}/c$ where the pion rejection is a
 2472 half of the no-background case. However, the Cherenkov detector provides high PID performance
 2473 in the low momentum range and the overall pion rejection is sufficient for the experiment.



(a) SIDIS large-angle calorimeter



(b) SIDIS forward calorimeter

Figure 97: Calorimeter pion and electron efficiency without (blue) and with (red) the consideration of background particles for the inner radius region (highest background) for the SIDIS configuration.

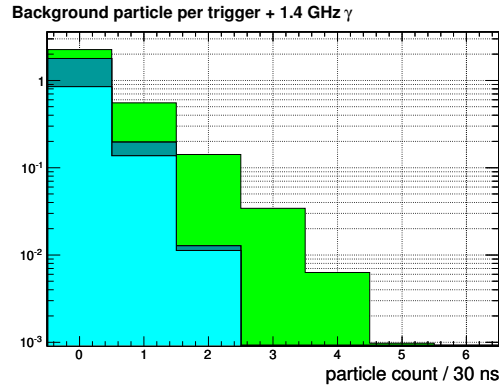
2474 In the PVDIS configuration, the background rate is significantly higher and the performance
 2475 is affected. The 30-fold structure of the baffle system for the PVDIS experiment causes the back-
 2476 ground to alternate between high- and low-rate 30 times in the azimuthal direction. Therefore,
 2477 calorimeter performance is studied for the high- and the low-rate “slices” separately, with each fan-
 2478 shaped slice covering 6 degrees. Background structure for the inner-radius, high-rate slice is shown
 2479 in Fig. 98. The PID performance with the background is evaluated for different radius, see Fig. 99.
 2480 Comparing to the intrinsic performance of Fig. 96, the pion rejection is up to 8 times worse: the pion
 2481 rejection varies from 25–50 at $p = 2.5 \text{ GeV}/c$ to 50–100 at $p = 6 \text{ GeV}/c$, while keeping the electron
 2482 efficiency to be in the range (90–95)%. Particle identification for the experiment will need to rely
 2483 on a full-waveform analysis of the EC, combined with information from the Cherenkov detector.

2484 10.7.3 Trigger capability

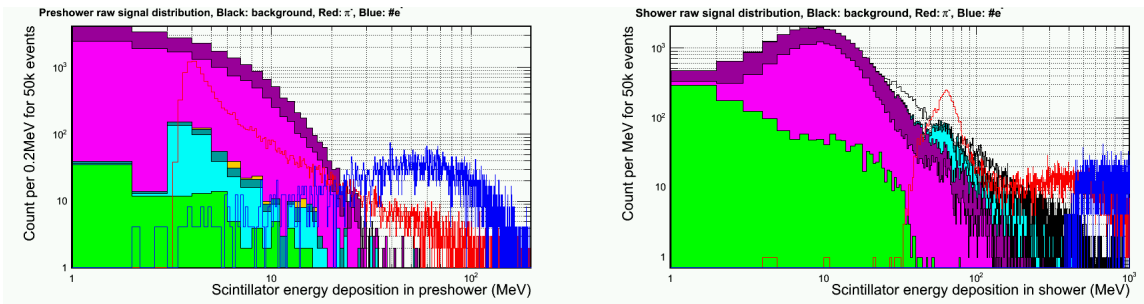
2485 Trigger capability is an important function of the EC. The calorimeter shower energy deposition
 2486 in all combinations of local 6+1 clusters (central block plus six neighboring hexagon blocks) is
 2487 first summed after digitization, forming local shower sums. Triggers are then formed by passing
 2488 the local shower sums through a threshold cut. Electron triggers are formed with a targeted electron
 2489 threshold, and the efficiency curves for both pions and electrons are studied with the full-background
 2490 simulation. The following triggering specifications have been studied:

- 2491 • SIDIS large angle calorimeter: electron triggers of 3 GeV are formed by cutting on local
 2492 shower sum larger than 2.6 GeV. The trigger turn-on curve is shown in Fig. 100. High elec-
 2493 tron efficiency is observed for electrons above the threshold. The rejection on few-GeV pion
 2494 background is high, in the range (20-100):1, which satisfies requirement of the SIDIS experi-
 2495 ments.
- 2496 • SIDIS forward calorimeter: position dependent electron triggers provide high trigger effi-
 2497 ciency for electrons of $Q^2 > 1 \text{ GeV}^2$. The pion rejections with 1 GeV threshold is shown on
 2498 the left plot of Fig. 101. With higher thresholds, pion rejections are better.
- 2499 • SIDIS forward calorimeter: MIP triggers allow the calorimeter to trigger on hadrons for the
 2500 SIDIS measurement. The threshold is determined by MIP peak - two sigma of the Landau
 2501 fit of the distribution, which lead to a calibrated local shower sum energy of 220 MeV. The
 2502 trigger efficiency for pions is high, as shown on the right plot of Fig. 101.
- 2503 • PVDIS forward calorimeter: electron triggers are formed with radius-dependent trigger thresh-
 2504 olds. As shown in Fig. 102, the targeted electron threshold varies from 1.5 GeV at outer radius
 2505 to 3.8 GeV at inner radius on the calorimeter, which produces high trigger efficiency for DIS
 2506 electrons with $x > 0.35$. The trigger turn-on curves are evaluated for several regions on the
 2507 calorimeter as shown in Fig. 102. The efficiency for both electrons and pions are lower for
 2508 inner radius regions due to the use of high thresholds for background-suppression. Overall
 2509 the pion rejection at the trigger level is > 2 and varies with the radius.

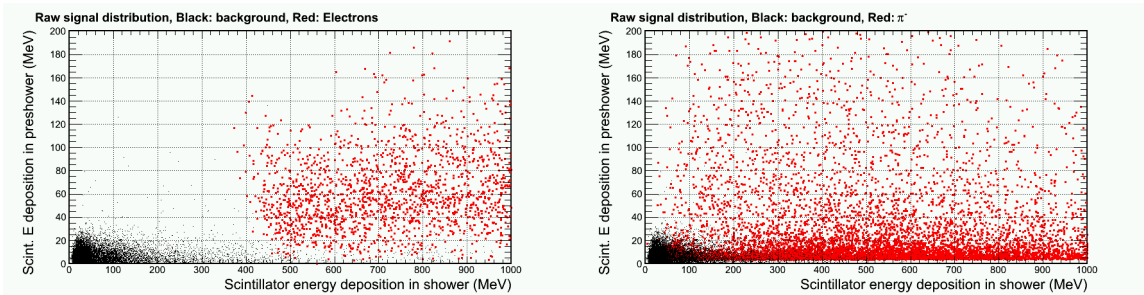
2510 The PVDIS experiment will run with a luminosity up to $10^{39} \text{ cm}^{-2}\text{s}^{-1}$. A baffle system is
 2511 used to reduce the very high background rate expected at this luminosity. To further reduce the rate
 2512 from high energy photons from neutron pions and low energy backgrounds, fan-shape lead blocks,
 2513 each covering 2.5 degrees azimuthally, will be placed in front of the EC. The trigger of PVDIS will
 2514 be formed by taking the coincidence between the EC and the gas Cherenkov detector. Estimation
 2515 of the trigger rate from EC can be performed using the realistic background simulation (described



(a) Stacked probability to find the number of background π^- (light blue), π^+ (dark blue) and electrons (green) at the front of the preshower. The photon rate is as high as ~ 1.4 GHz, thus the photon count is off-scale and not shown in this figure.

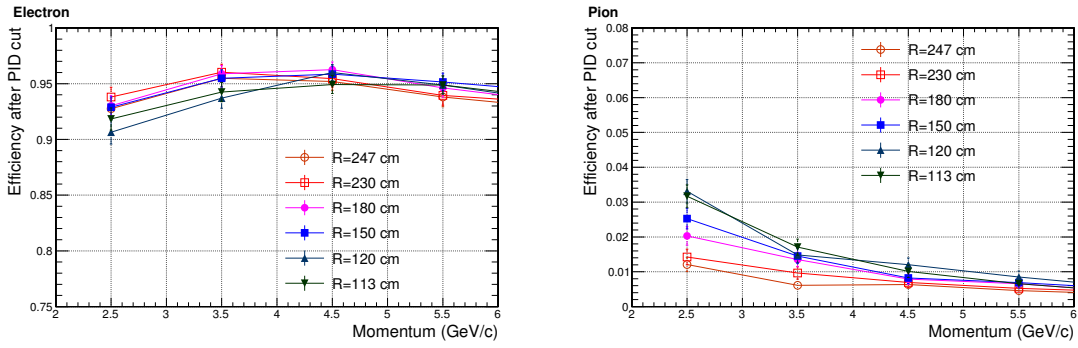


(b) Stacked probability (count per 50k events) vs. Preshower (left) and Shower (right) scintillator energy deposition for incoming background electrons (green), π^- (light blue), π^+ (dark blue), protons (yellow), EM process-originated photons (magenta) and π^0 -originated photons (dark magenta). For comparisons, energy deposition for high energy pion (red) and electrons (blue) are shown as non-filled curves.

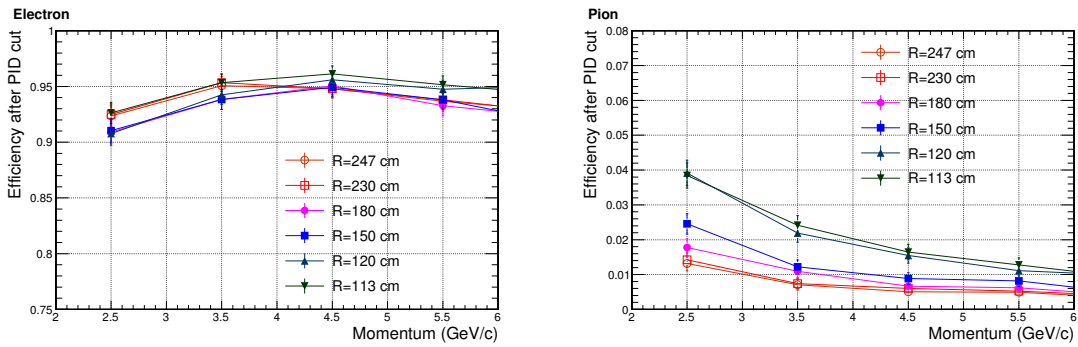


(c) Preshower-shower scintillator energy correlation for background particles (black), compared with high energy electrons (left, red) and pions (right, red)

Figure 98: Background distribution for the PVDIS forward calorimeter at the production luminosity of a liquid deuteron target. Background for the inner radius ($R \sim 1.2$ m) and higher-radiation azimuthal region is shown. The energy deposition originated from background is compatible to that of high energy pions.

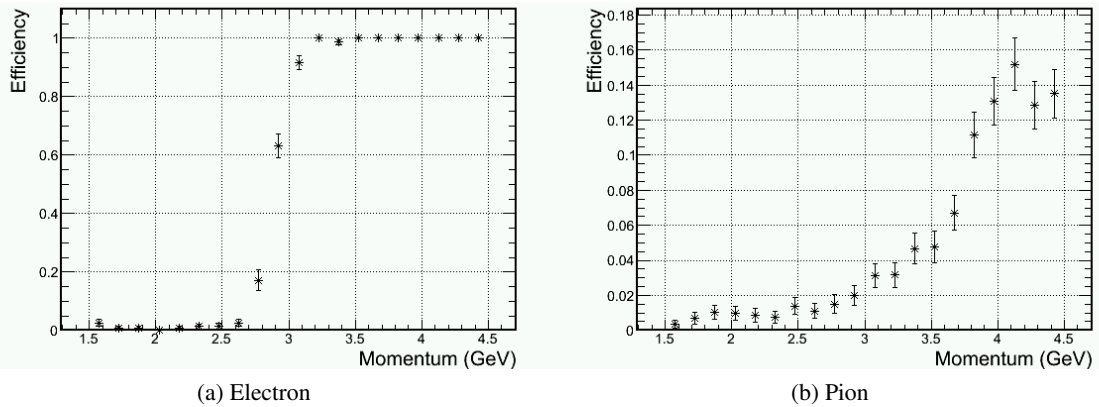


(a) lower-radiation azimuthal region



(b) higher-radiation azimuthal region

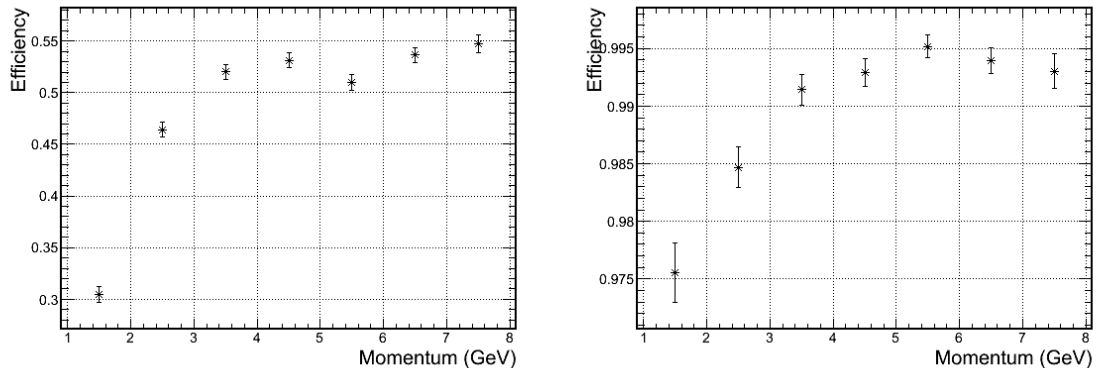
Figure 99: Calorimeter pion and electron efficiency for the PVDIS experiment, evaluated with the presence of background at eight typical regions on the calorimeter.



(a) Electron

(b) Pion

Figure 100: Trigger efficiency for electrons (a) and pions (b) for the SIDIS large angle calorimeter. The target trigger threshold is approximately $P_e = 3 \text{ GeV}/c$. Only the (high-background) inner-radius region is shown here.



(a) Pion efficiency in electron trigger with a target trigger threshold of ($P_e = 1 \text{ GeV}/c$)

(b) Pion efficiency in the MIP trigger

Figure 101: Trigger efficiency for pions in the SIDIS forward calorimeter for electron triggers (a) and MIP triggers (b). Only the (high-background) inner-radius region is shown here.

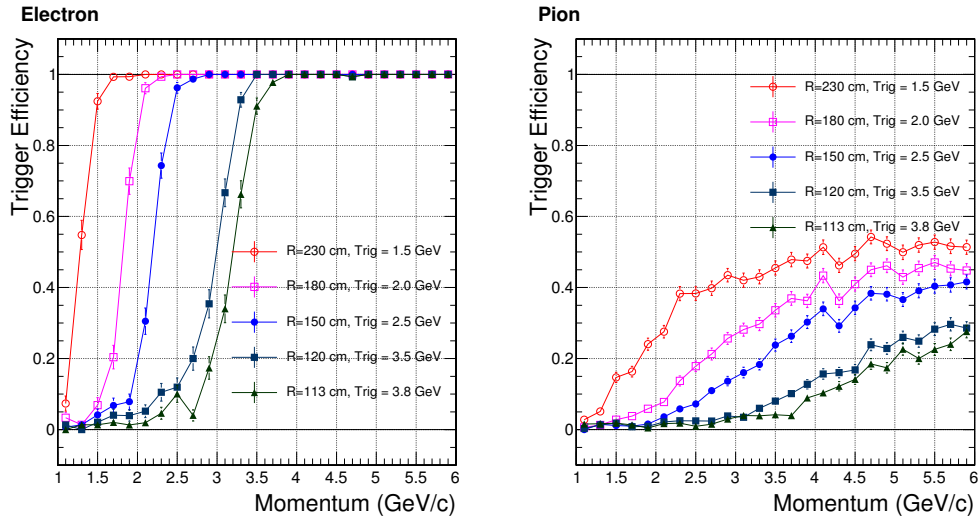
2516 previously in Section 10.7.2) combined with EC trigger capability results described above. The
 2517 EC trigger rate will then be combined with gas Cherenkov trigger rate to obtain the expected DAQ
 2518 trigger rates and to make sure they can be handled by the DAQ system. For SIDIS experiments
 2519 on ^3He , the luminosity will be up to $3 \times 10^{36} \text{ cm}^{-2}\text{s}^{-1}$ on ^3He target and additional about $3.7 \times$
 2520 $10^{36} \text{ cm}^{-2}\text{s}^{-1}$ on target glass windows. Target collimators (described previously in Section 10.7.2)
 2521 will be used to reduce backgrounds from the glass windows. The SIDIS triggers are formed from
 2522 EC in combination with Cherenkov, MRPC and SPD. The FAEC will also provide MIP trigger for
 2523 hadron detection. Trigger rate estimation for SIDIS is carried out similar to the PVDIS case. Results
 2524 for both PVDIS and SIDIS trigger rates will be presented in Section 14.

2525 10.7.4 Shower Position Measurement

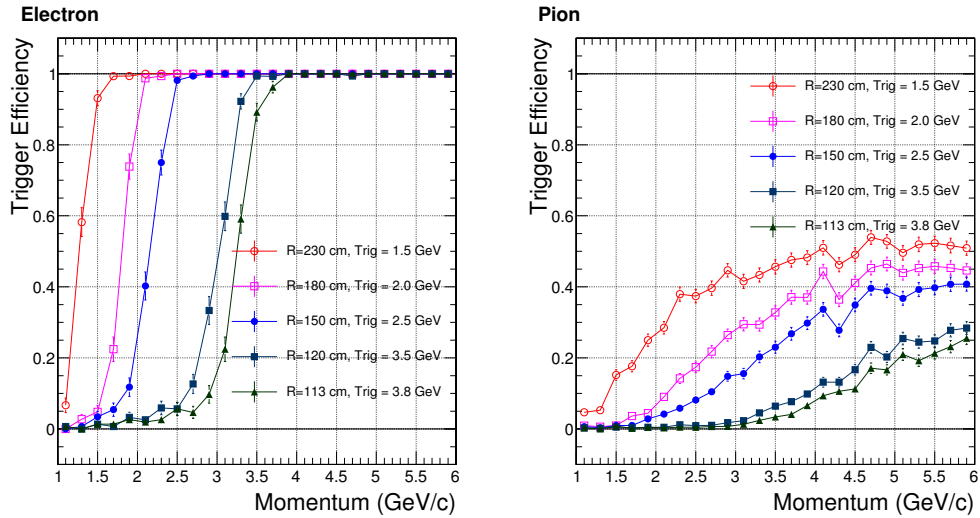
2526 Position resolution of the shower center was studied for different lateral sizes of the calorimeter
 2527 modules, as shown in Fig. 103. The radial resolution is in general worse than the azimuthal resolu-
 2528 tion because the tracks are not perpendicular to the radial direction. As can be seen from Fig. 103,
 2529 with the use of proper algorithm, a position resolution of better than 1 cm is achieved for both
 2530 directions at the designed lateral granularity of 100 cm^2 .

2531 10.7.5 Supplemental Information: PID Selection Cuts

2532 A three dimensional PID cut was used to select the best electron samples with maximal π^- rejection
 2533 as illustrated in Fig. 104. For each given momentum bin, the cut on E/P and preshower energy
 2534 roughly follows the contour lines of the ratio of π^- efficiency to e^- efficiency, which is the optimal
 2535 cut for the π^-/e^- separation. A momentum dependence is then introduced to the cut to maintain a
 2536 constant 95% electron efficiency for most of the bins. Events passing the cut are highlighted in red
 2537 in the plots.

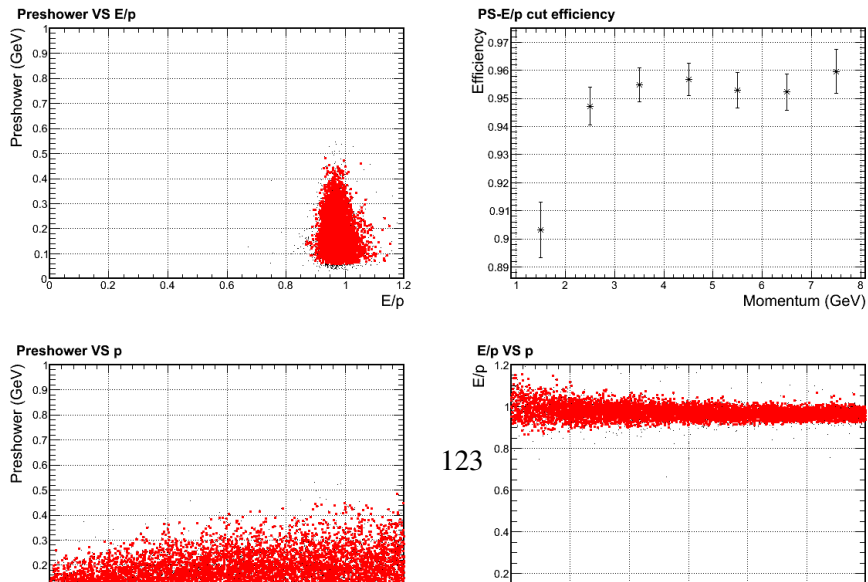


(a) Higher-radiation azimuthal region



(b) Lower-radiation azimuthal region

Figure 102: Trigger efficiency curves for the PVDIS configuration.



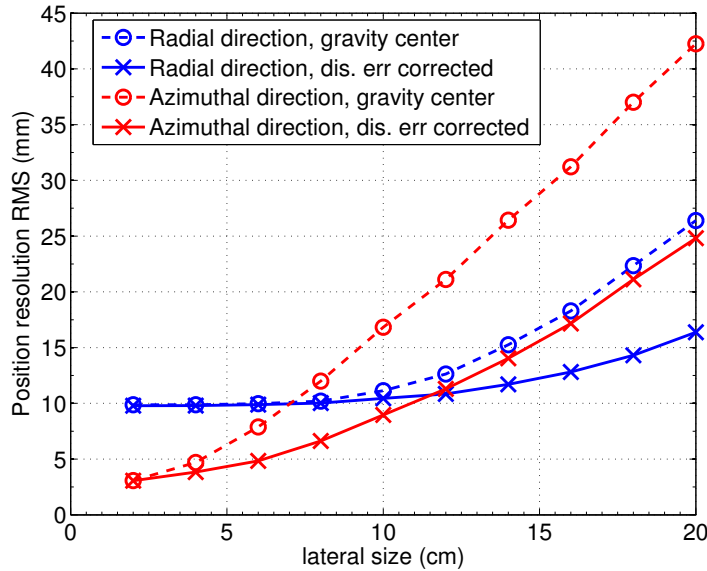


Figure 103: Position resolution for electron showers vs. different lateral size of the calorimeter module. Both azimuthal (red) and radial (blue) resolutions are shown, with the shower center calculated from a simple energy-weighted geometrical center (dashed curves), and those calculated with further corrections using the energy deposition distribution among neighboring modules (solid curves).

2538 10.8 Scintillator Pad Detector for SIDIS Experiments

2539 The main purpose of the scintillator pad detector (SPD) is to reduce calorimeter-based trigger rates
 2540 for high-energy charged particles (see Section 10.7.3 for calorimeter trigger capability) by rejecting
 2541 photons through the coincidence between the SPD and the calorimeter. Two SPDs will be used: one
 2542 in the forward direction between the heavy gas Cherenkov detector and the MRPC, and the other
 2543 in the large-angle direction immediately before the large-angle calorimeter. Both SPDs consist of
 2544 fan-shaped scintillator pads arranged perpendicular to the beam direction. The LASPD will also
 2545 provide time-of-flight for particle identification with a timing resolution goal of 150 ps.

2546 The performance for the scintillator was studied in the GEANT4 simulation. For FASPD, we
 2547 plan to use 5 mm thickness scintillators based on a balance between the light yield and the radiation
 2548 length. The 5-mm thickness corresponds to a radiation length of $\approx 0.013X_0$ which directly affect
 2549 the photon conversion rate. Typical responses of the FASPD to photons and charged particles are
 2550 shown in Fig. 105. Approximately 20% of the photon background leave energy in the scintillator
 2551 due to back splashing from the calorimeter front face. The trigger threshold was set at two standard
 2552 deviations below the MIP peak to ensure a high efficiency for charged particles. Pile up effects
 2553 were studied for fixed ADC timing windows of 30 and 50 ns. The photon rejection depends not
 2554 only on the trigger rate per scintillator, but also the scintillator segmentation, see Fig. 106. In
 2555 addition, photons attenuates significantly in long scintillators and thus the length of the individual
 2556 segmentation needs to be minimized. The segmentation of FASPD is chosen to be 240 based on
 2557 Fig. 106 and a desired 5:1 photon rejection at the large angle, and is further divided into 60 in
 2558 the azimuthal direction and 4 in the radial direction. The readout of FASPD is by using WLS
 2559 fibers embedded on the surface of the scintillator, then connected to clear fibers and are readout by
 2560 MAPMTs. This is similar to the preshower. Because the threshold is below MIP and is much lower

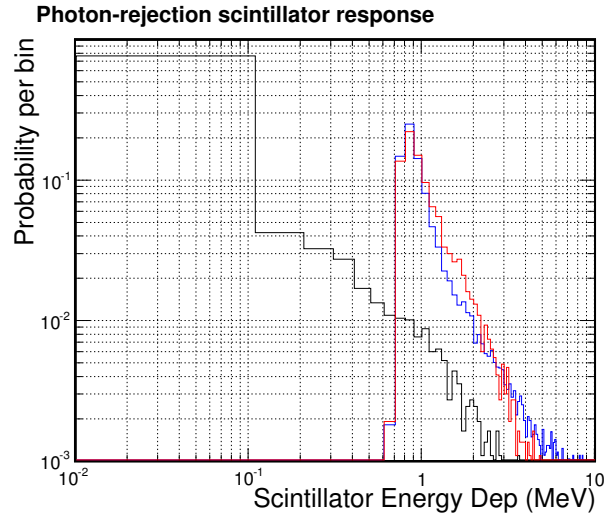


Figure 105: Typical probability for scintillator energy depositions in the SPD, for electron (blue), pion (red) and high energy photons (black).

2561 than for preshower, a higher combined gain of PMT and the preamplifier is needed. We currently
 2562 plan to use preamplifiers with gain ≈ 50 because it's the maximum comfortable gain that can be
 2563 achieved on a pre-amplifier board. This will allow us to place the threshold around 20 mV, the
 2564 minimal threshold that is above the noise level.

2565 For the LASPD, a 10:1 photon rejection is desired to bring the photon-induced calorimeter trig-
 2566 ger rate down to below the electron-induced rate. Figure 107 shows the simulated photon rejection
 2567 factor vs. segmentation. The 10:1 rejection can be achieved by 60 azimuthal segments. Because
 2568 the radial coverage of the LASPD is small and because of the requirement of high photoelectron
 2569 statistics to reach the TOF requirement, the LASPD has only azimuthal segmentation, with each
 2570 covering 6 degrees. For readout, the use of WLS fiber is impossible, again because of high pho-
 2571 toelectron statistics. We plan to use field-resistant fine-mesh PMTs on the outer radial edge of the
 2572 LASPD to readout the scintillating light.

2573 10.9 EC Collaboration Status and Construction Outlook

2574 The shashlyk sampling technique used by the SoLID EC has been used by many experiments at the
 2575 LHC, including LHCb, ALICE and ATLAS. The CMS experiment's calorimeter upgrade will use
 2576 a similar technique. In the R&D for SoLID EC, we studied extensively the calorimeter design and
 2577 technical details from these experiments. We also learned many useful facts from other experiments
 2578 and/or collaborations, including for example Minerva, MINOS, and JLab Hall D.

2579 Our general design for the SPD, the preshower, and the shashlyk shower modules is based heav-
 2580 ily on the LHCb's SPD and ECal design. The LHCb and other LHC experiment's detector TDR
 2581 and associated technical notes provide tremendous knowledge. This includes: readout design for
 2582 the preshower and the SPD (WLS fiber embedding in grooves on the scintillator surface and the
 2583 use of MAPMTs) (LHCb); wrapping of the scintillator (LHCb, ATLAS), relative light yield be-
 2584 tween different scintillator material and WLS fiber types (LHCb); the use of optical grease or glue
 2585 (LHCb); side treatment and painting of shashlyk modules (LHCb); adding mirror ends to WLS
 2586 fiber (LHCb); coupling between WLS fiber and MAPMTs (LHCb); Tests of light yield uniformity

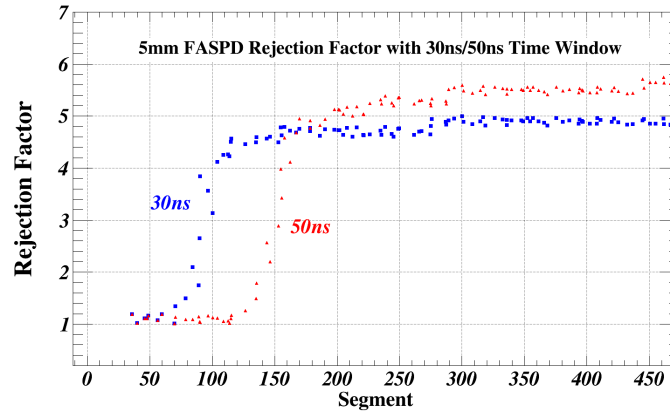


Figure 106: Photon rejection factor for 5-mm thick FASPD as a function of the segmentation, for DAQ windows of 30ns (blue) and 50ns (red), respectively. For the 30-ns timing window, a 240 segmentation is appropriate to reach a photon rejection of 5:1.

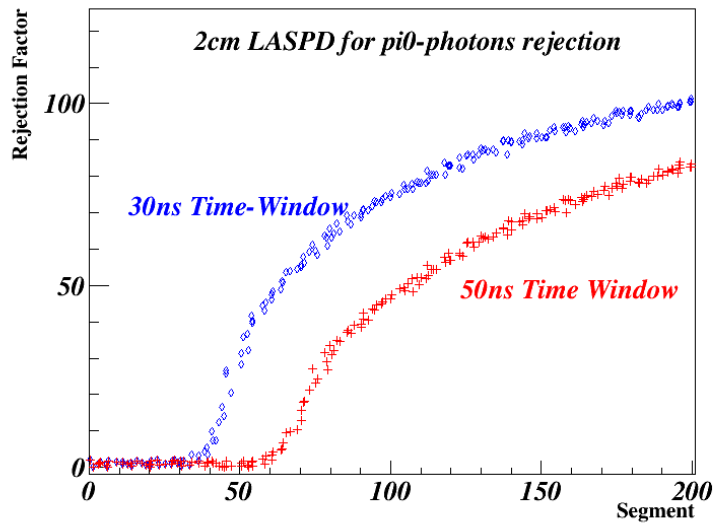


Figure 107: Photon rejection factor for 20-mm thick LASPD as a function of the segmentation, for DAQ windows of 30ns (blue) and 50ns (red), respectively. For the 30-ns timing window, a 60 segmentation is appropriate to reach a photon rejection above 10:1.

2587 (LHCb); radiation hardness of the preshower and shashlyk modules (LHCb ECal and HCal) and
 2588 plastic scintillating fibers (LHCb tracker upgrade, JLab Hall D GlueX barrel EMCAL); LED moni-
 2589 toring system (LHCb); WLS fiber bending light loss (simulation by LHCb; direct data from ATLAS
 2590 Tile ECal TDR); performance of SiPM under high neutron radiation background (mainly LHCb
 2591 tracker upgrade, but also JLab Hall D and CMS); EC commissioning and calibration procedure
 2592 (LHCb ECal and HCal); tolerance/quality control for the scintillators and fibers (LHCb).

2593 Once prototype modules are constructed, the light yield can be compared with that of LHCb,
 2594 ALICE, KOPIO, PHENIX, COMPASS, and COMPASS-II.

2595 For ECal construction, most of previous experiments that utilized the sampling-type design

2596 made use of the Russian IHEP for the scintillator production. On the other hand, assembling of
2597 the modules can be performed either by IHEP, or by other institutions. For example, Wayne State
2598 University (WSU) and China Central Normal University (CCNU) both assembled modules for the
2599 ALICE experiment (for CCNU, threading WLS fiber was done in Italy, separately from the initial
2600 assembling). The collaboration is in close contact with the WSU group but their module assembly
2601 lab has been dismantled a long time ago. We are also in contact with the U. of Iowa group (Prof.
2602 Onel) who is participating in the CMS ECal upgrade, but the CMS Ecal utilizes crystal layers and is
2603 very different from SoLID EC in the choice of material and thus the construction process. Currently
2604 the SoLID collaboration is pursuing the possibility of manufacturing the scintillators in China. Two
2605 groups, Shandong University (SDU) and Tsinghua University (THU), are participating in the SoLID
2606 EC R&D, and they have developed local contact with the CCNU group to learn their experience in
2607 module assembly. The SDU group has extensive experience with scintillator production in China
2608 and cosmic ray testing of the scintillator's light yield, and is in a good position to lead the prototype
2609 R&D for SoLID EC.

2610 11 MRPC

2611 11.1 Overview

2612 The Multi-gap Resistive Plate Chamber (MRPC), which will be used as the time of flight (TOF)
2613 system, is located in front of the forward-angle calorimeter. Several MRPCs have been recently used
2614 in RHIC STAR and LHC ALICE as their TOF systems [240–243] and the typical time resolution for
2615 these detectors is better than 80 ps. Most importantly, as a gas chamber, the MRPC does not need
2616 PMTs for readout so it can work inside a magnetic field. For the SoLID-SIDIS configuration, the
2617 total path length is around 8 meters from the target and the flight time is calculated by comparing the
2618 timing signal to the beam RF signal. With a time resolution of 100 ps, we can identify pions from
2619 kaons at a rejection factor of 20:1 with momenta up to 2.5 GeV/c. Compared with the MRPCs used
2620 at STAR and ALICE, the MRPC for SoLID receives a higher flux rate, approximately 10 kHz/cm².
2621 Tsinghua University has developed a new type of low resistivity glass with a bulk resistivity on the
2622 order of 10 Ωcm. The rate capability of the high rate MRPC assembled with this type of glass can
2623 reach 50 kHz/cm² [244, 245]. We propose to construct the high rate SoLID-MRPCs with this low
2624 resistive glass.

2625 11.2 Structure of the MRPC Prototype

2626 The layout of the MRPC is shown in Fig. 108. The inner diameter of the detector plane is about
2627 1 meter and the outer diameter is 2 meters. The area of the disk is about 10 m². The whole detector
2628 consists of 50 super modules and each super module consists of 3 MRPC modules. There is overlap
2629 between MRPC modules and super modules to avoid blind areas.

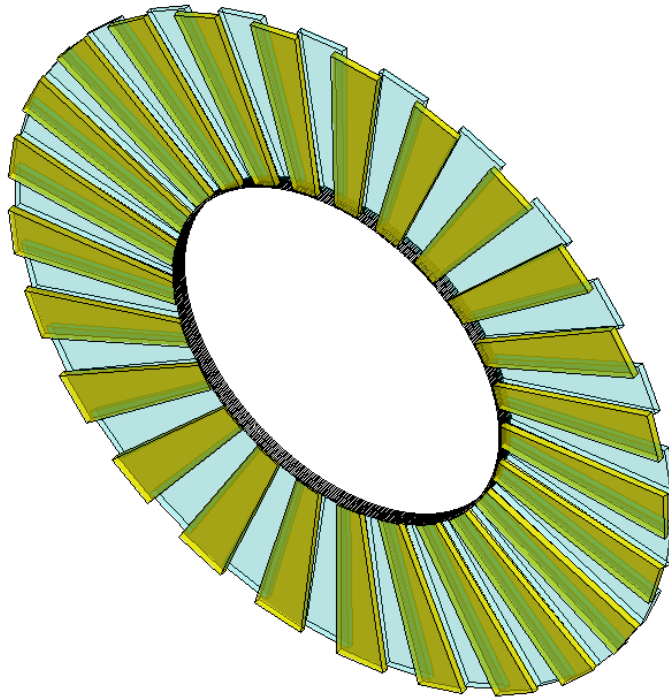


Figure 108: The layout of MRPC TOF

2630 A prototype of the MRPC has been assembled and its structure is shown in Fig. 109. This

2631 trapezoidal module is assembled with our low-resistivity glass. The module has ten gas gaps and
 2632 the width of each gap is $250\ \mu\text{m}$. The outer glass is 1.1 mm thick and the inner glass is 0.7 mm
 2633 thick. Colloidal graphite is sprayed on the surface of the outer glass and the surface resistivity is
 2634 about $5\text{M}\Omega\text{cm}$. Fig. 110 shows the structure of the readout strips. Each module consists of 11 strips
 2635 and the width of each strip is 25 mm with a 3 mm gap. The shortest strip is 13 cm and the longest
 2636 is 17 cm. This prototype will be similar to the smallest module of the three modules in one super
 2637 module. With this design, the whole detector will consist of 1650 strips, and the total number of
 2638 readout channels is 3300 since each strip has readouts on both ends.

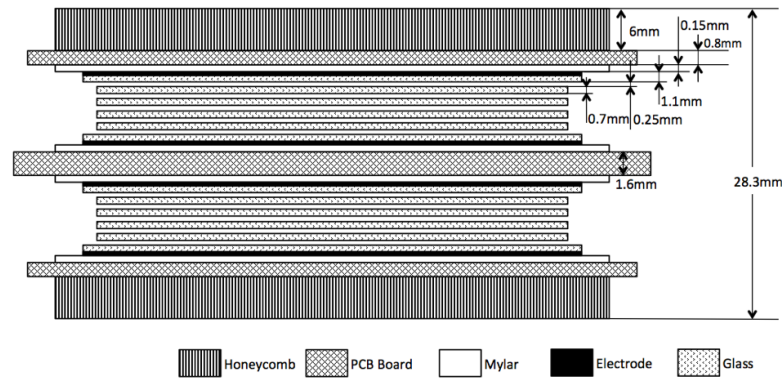


Figure 109: The structure of the MRPC prototype

2639 11.3 Cosmic Ray Test

2640 The cosmic ray test system for the MRPC prototype consists of a cosmic ray telescope and a VME
 2641 based DAQ system. The telescope consists of three $20\ \text{cm} \times 5\ \text{cm} \times 5\ \text{cm}$ scintillators and two
 2642 $4\ \text{cm} \times 2\ \text{cm} \times 1\ \text{cm}$ scintillators. These five scintillators were used to trigger on cosmic rays.
 2643 The layout of the cosmic ray telescope and the prototype is shown in Fig. 111. Two of the larger
 2644 scintillators and one of the smaller scintillators are above the module, and the rest are below the
 2645 module. PMT0 through PMT4 were used for basic coincidence triggering and to provide the refer-
 2646 ence time. The two small scintillators are used to measure the efficiency of the module. The width
 2647 of the area subtended by the small scintillators is smaller than the width of a MRPC strip. Since
 2648 this module would be tested with an electron beam at JLab (see later discussion), the cosmic test is
 2649 only for checking primary performance parameters, such as dark current, noise, efficiency and time
 2650 resolution. With a high voltage setting of 13.2 kV, the dark current is less than 10 nA and the noise
 2651 rate is a few Hz/cm^2 . Fig. 112 shows the efficiency plateau. It can be seen that the efficiency can
 2652 reach 98% and the plateau region is larger than 600 V. Fig. 113 shows the relation between charge
 2653 and time after slewing correction. The time spectrum after correction is shown in Fig. 114. The
 2654 time jitter of four PMTs is 87 ps, so the resolution of the MRPC can reach 50 ps. All of these show
 2655 that the MRPC module has good performance.

2656 11.4 Beam Test at Hall A

2657 The setup of the beam test is shown in Fig. 115. The beam was mainly for the JLab g2p exper-
 2658 iment [246]. Our test setup stood about 10 m to the side. There was an electron beam passing
 2659 through our trigger system and the backgrounds were mainly soft photons, electrons and neutrons.

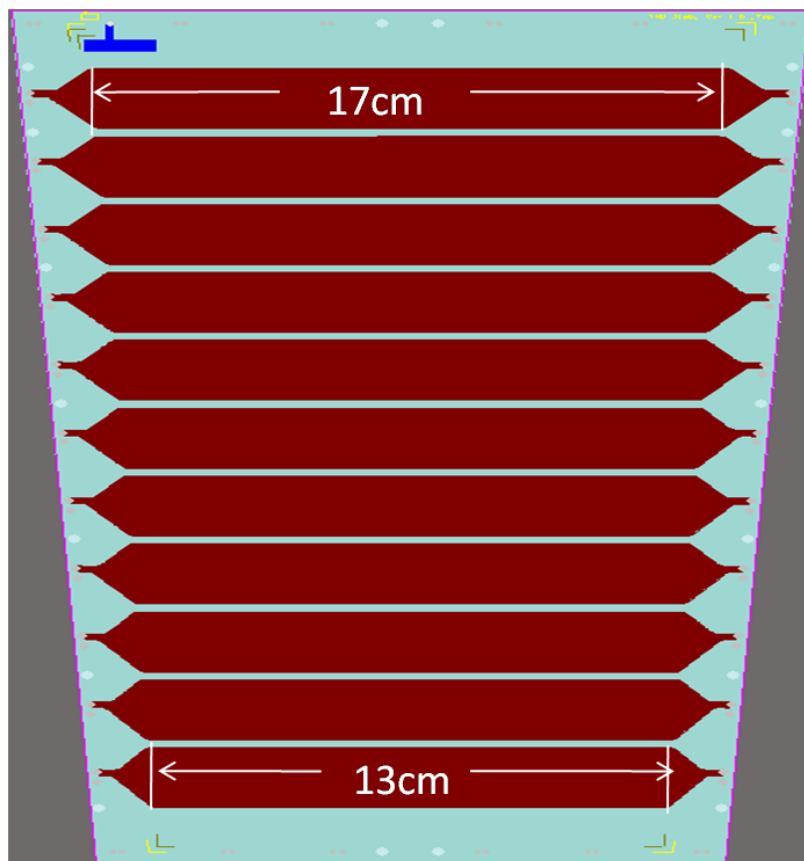


Figure 110: The structure of the readout strips

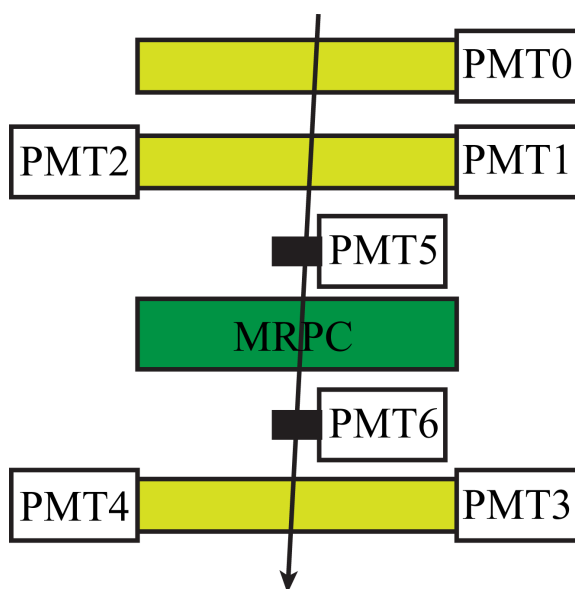


Figure 111: Layout of the test setup

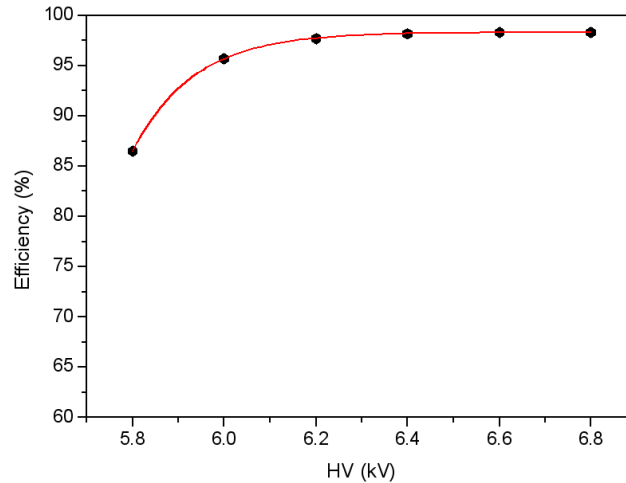


Figure 112: Efficiency plateau of the MRPC

2660 The background intensity was stronger than the main electron beam. A thick concrete shield was
 2661 used to suppress background particles striking the MRPC. A diagram of the DAQ is shown in
 2662 Fig. 116. The trigger system was very similar to that of the cosmic test system. One small scintillator
 2663 ($5\text{ cm} \times 5\text{ cm} \times 1\text{ cm}$) was read out by PMT 0 and each of two long scintillators ($10\text{ cm} \times 5\text{ cm} \times 1\text{ cm}$)
 2664 was read out on both ends (by PMTs 1–4). The coincidence of PMT0 and PMT4 provided the trig-
 2665 ger signal of the system. The delayed coincident signal also acted as the gate signal of the flash
 2666 ADC and the stop signal of the TDC. PMT1~PMT4 provided the reference time of the system.
 2667 A CAEN V775 TDC was used to record the time signal and a flash ADC, JLAB FADC 250, was
 2668 used to record the charge signals. A VME scaler was used to record the time interval between two
 2669 triggers. From this time interval we can get the signal rate to study the rate capability of the detector.

2670 11.5 Beam Test Results

2671 11.5.1 HV Scan

2672 MRPCs were conditioned under high voltage for a few hours in order to reach a stable, low dark rate
 2673 working region. The electronics threshold was set to 30 mV. The dark current was less than 8 nA
 2674 and the rate of the module was less than 10 Hz/cm^2 at 108 kV/cm. The coincidence of PMT1–PMT4
 2675 provided the T0 of the test system, with a time jitter of about 100 ps. In order to find the optimum
 2676 working voltage of the counters, the efficiency and time resolution were scanned as a function of
 2677 the applied voltage for a ‘low’ flux of $\bar{\phi} \sim 1\text{--}4\text{ kHz/cm}^2$. The results are summarized in Fig. 117.
 2678 The counters showed large efficiency plateaus above 600 V, and time resolutions were as good as
 2679 75 ps. It can be seen that the time resolution obtained from cosmic rays is better than that from the
 2680 electron beam test, because the time jitter of T0 in the beam test was larger than that in the cosmic
 2681 test.

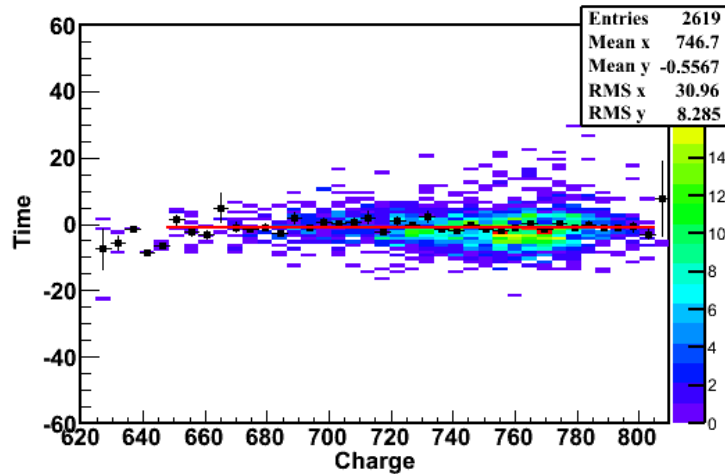


Figure 113: The relation between charge and time after slewing correction

2682 11.5.2 Rate Scan

2683 The rate depended on background intensity. From the scaler we can get the signal rate of the MRPC.
 2684 Fig. 118 shows the signal rate change with time in runs 188 and 193 respectively. The rate was not
 2685 stable in each run. From these runs, we obtained different rates from 1 to 16 kHz/cm². These two
 2686 runs were combined to analyze the rate performance. The results are shown in Fig. 119. It can be
 2687 seen even when the flux rate reaches 16 kHz/cm², the efficiency is still higher than 94% and the
 2688 time resolution is close to 80 ps. So this module meets the requirement of the SoLID TOF system.

2689 The evolution of the charge distribution can be seen in Fig. 120 for this MRPC. The charge is
 2690 obtained from the sum of its two ends. It can be seen that, with increasing flux, the average charge
 2691 decreases and the spectrum shifts down to lower charges as expected.

2692 11.6 Conclusions

2693 A high rate MRPC was proposed to construct the time of flight system for the SoLID-SIDIS pro-
 2694 gram, and a prototype has been designed and constructed. The trapezoidal prototype module as-
 2695 sembled with low resistivity glass has 10×0.25 mm gas gaps and 11 readout strips. The width of
 2696 the strips is 2.5 cm with an interval of 3 mm. This module was tested using cosmic rays and also
 2697 tested using electron beams in Hall A of JLab. The results show its rate capability of larger than
 2698 16 kHz/cm². This module has a very promising time resolution. The time resolution can reach 50 ps
 2699 in cosmic test and is about 75 ps in the beam test. The chambers behaved very stably during the
 2700 experiment. This performance meets the requirement of the SoLID-TOF system. A detailed aging
 2701 study has to be performed to assure the stability over a long running time.

2702 11.7 R&D Plan for Better Time Resolution

2703 A joint Chinese collaboration for RHIC, SoLID and EIC for the next generation MRPC aims at
 2704 20 ps. Tsinghua University is planning to develop a prototype in the next coming year. Beam test
 2705 and finalization of detector and electronics will be done the following year.

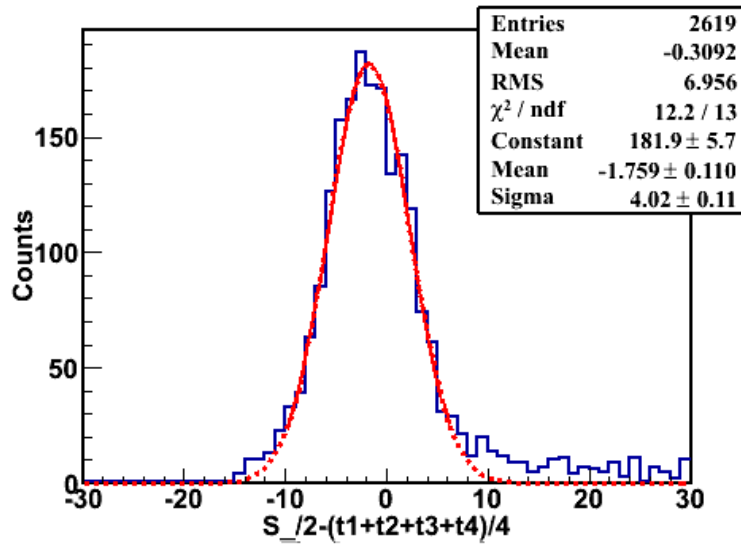


Figure 114: Time spectrum after correction

Chip	Sample Frequency GHz	Bandwidth GHz	Samples	Channels	Readout MHz	Resolution ps
PSEC4	4 to 15	1.5	256	6	40 to 60	9
SAMPIC	3 to 8.2	1.6	64	16 or 8	80	5
DRS4	0.7 to 5 GHz	0.950	1024	9	33	1
DRS5	10	3	4096	32	300 ?	5 ?
PSEC5	5 to 15	1.5 to 2	32768	4	500?	5?

Table 17: Table summarizing the characteristics of different sampling chips available and future generation ones for DRS5 and PSEC5

2706 Obtaining good timing resolution also depends on the electronics, both preamplification of sig-
 2707 nals and digitization:

2708 EIC R&D at BNL is using 7 GHz bandwidth TI LMH5401 [180] amplifiers for preamplifiers.
 2709 Tsinghua University will also develop its own amplifier chip which could drive lower costs and give
 2710 a more compact footprint for the electronics with a multichannel amplifier chip.

2711 New sampling electronics, development of which is being motivated by MCP PMTs, can reach
 2712 picosecond level timing resolution for multi-photons. The system is based on Switched Capacitor
 2713 Arrays (SCAs), which continuously sample the detector signal on a circular array of capacitors.
 2714 Sampling frequencies up to 10 GSamples/s have been reached. With a good calibration, a timing
 2715 resolution of 1 ps has been achieved. The following Table 17 summarizes the different available
 2716 chips.

2717 One of the main drawbacks of the SCA is the inherent dead time to allow readout of all the
 2718 samples for each trigger. A multi level array design will be implemented in the next generation of
 2719 DRS5 or PSEC5 chips. There is a joint effort from HEP/NP and a commercial company to offer a
 2720 commercial modular system based on the future PSEC5. This is currently the best option with costs

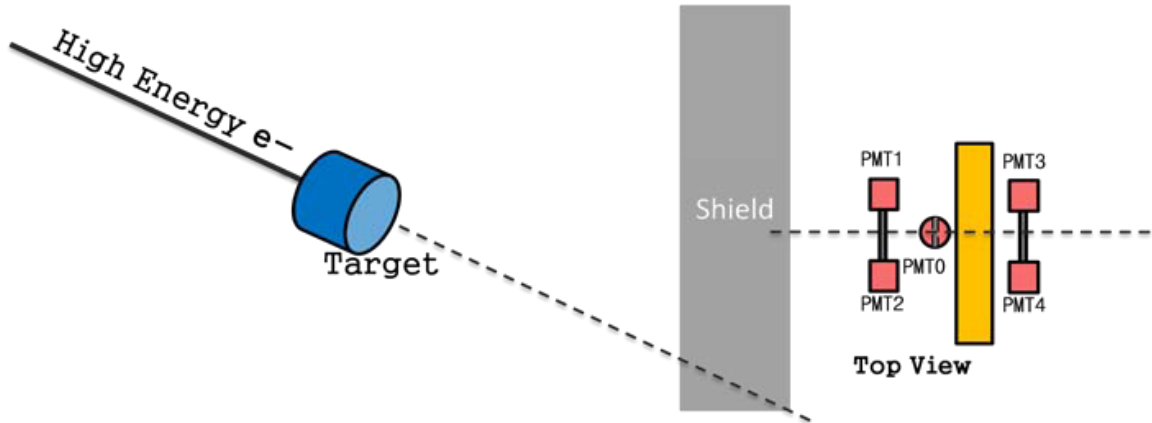


Figure 115: Setup of beam test in Hall A

2721 which could go as low as \$15 per channel.

2722 Assuming a cost similar to SAMPIC (about \$4K for 32 channels) the additional cost for sam-
 2723 pling electronics readout for 3,300 channels will be approximately an additional \$500K. This would
 2724 allow for electronics that can perform at a resolution of 20 ps or better and have the ability to record
 2725 the whole waveform of the detectors.

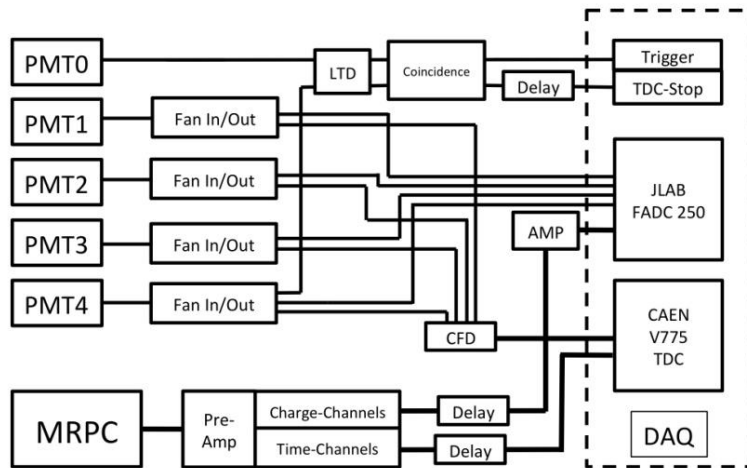


Figure 116: Diagram of the DAQ system

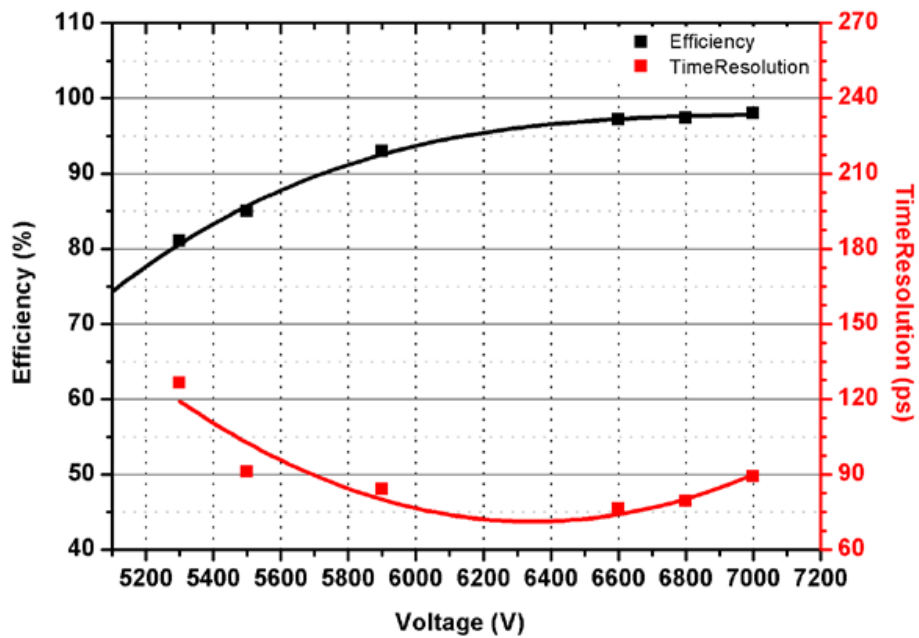


Figure 117: Time resolution and efficiency change versus applied voltage

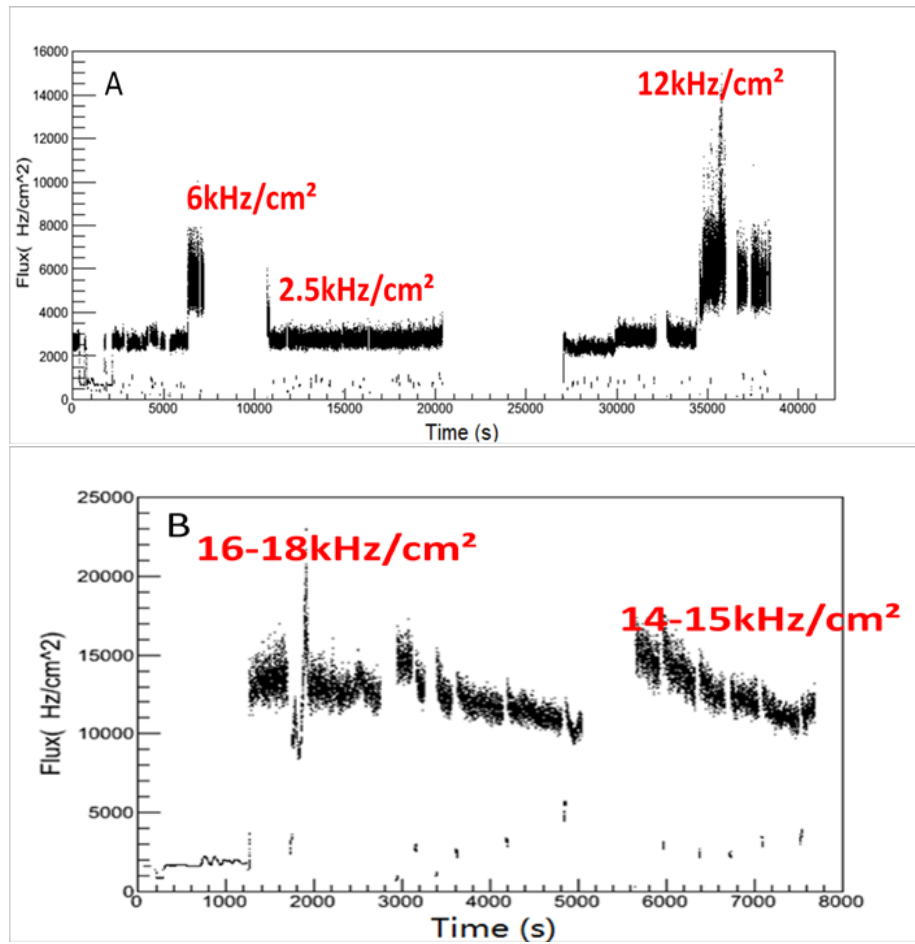


Figure 118: Signal rate changes with time. (A) shows run 188 and (B) shows run 193. The MRPC was located 5 meters from the target. There is shielding in front of the detector in (A), no shielding in front of the detector in (B).

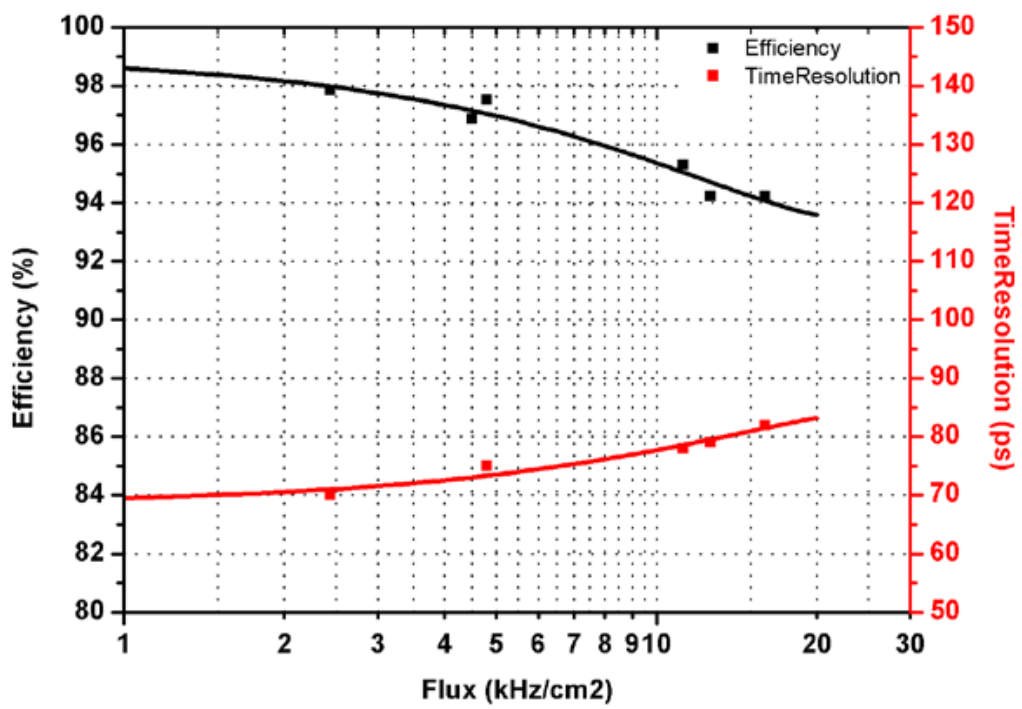


Figure 119: Measured efficiencies and time resolutions as a function of the particle flux.

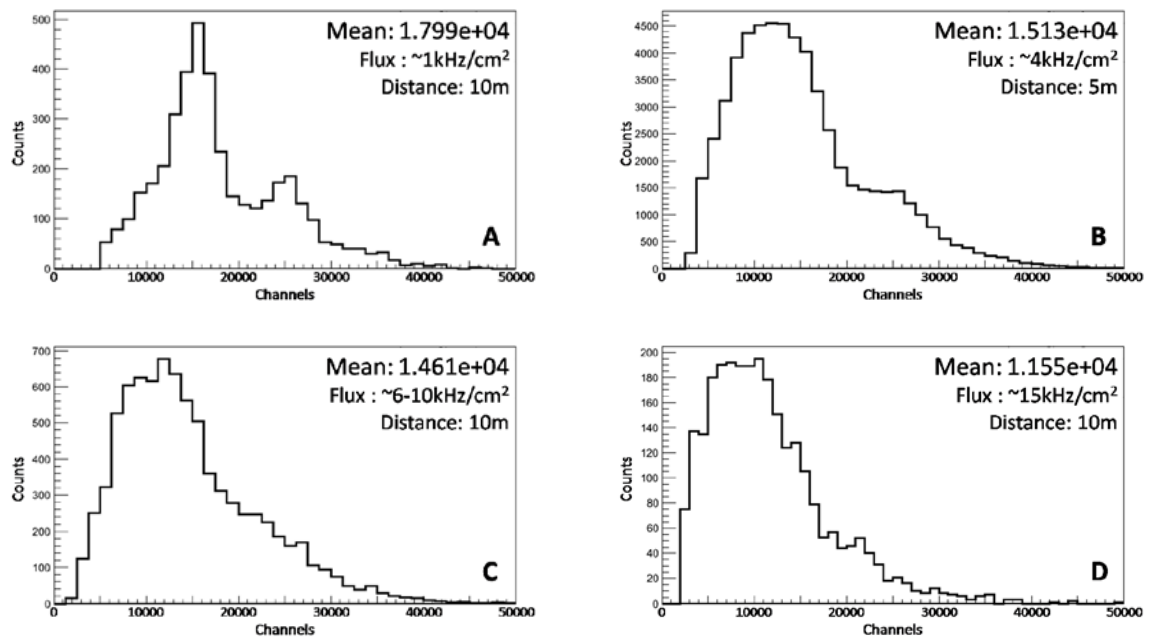


Figure 120: Charge distribution at various fluxes over one readout strip. Flux increases from figure A to D.

2726 12 Simulation and Reconstruction

2727 12.1 End-to-End Software Framework

2728 At the time of this writing, research is underway to identify a comprehensive software framework
2729 for SoLID. A framework should be chosen early in the software development cycle, where SoLID
2730 is now, to provide a common programming interface (API) for all software components. If chosen
2731 well, the API will stay constant, or at least backward compatible, throughout the project’s life-
2732 time so that early investments in code development will continue to pay off. Additionally, it is
2733 important at this stage to identify software features and capabilities that will be needed for SoLID
2734 data analysis, to the extent foreseeable now. Such feature requirements should be well matched to
2735 the specifics of the SoLID experiments, such as data volumes, detector types and configurations,
2736 and analysis methods. Retrofitting capabilities that were initially overlooked is often difficult and
2737 wasteful because doing so may invalidate original design assumptions, requiring large parts of the
2738 first-generation software to be re-written. Conversely, choosing a framework with too many fea-
2739 tures typically results in overly complex, bloated software that is difficult to learn and faces user
2740 resistance.

2741 With these goals in mind, we have developed the following requirements for the SoLID software
2742 framework; it should

- 2743 1. support all major components of the physics data processing chain, *viz.* simulation, digi-
2744 tization, reconstruction and physics analysis, within a *consistent* development and run-time
2745 environment (“end-to-end framework”);
- 2746 2. allow multi-pass data processing, where the output of one analysis pass can be used as the
2747 input for the next pass—an essential capability to minimize the need for reprocessing large
2748 data sets;⁴
- 2749 3. allow multiple processing chains in a single job, for example to run different track fitting, PID
2750 or physics analysis algorithms on the same data in a single processing pass;
- 2751 4. support interactive analysis of reconstructed quantities with ROOT, since ROOT will most
2752 likely be the data analysis package best known to and preferred by future SoLID collaborators;
- 2753 5. save extensive metadata to its output, for example database parameters used in previous anal-
2754 ysis stages (if practical) and detailed information about data provenance;
- 2755 6. support parallel computing, *i.e.* multi-threading and/or distributed processing;
- 2756 7. be written in C++, as most SoLID collaborators are well-versed in that language; and
- 2757 8. be readily available at this time, so that development can start without delay;

2758 Given limited manpower, the effort needed to develop a new framework from scratch that sat-
2759 isfies the above set of requirements would be prohibitive. As experience in other collaborations
2760 shows [247–250], frameworks with comparable capabilities are invariably complex and may take
2761 the better part of a decade to mature. Therefore, it is practically unavoidable, and certainly wise, to
2762 build the analysis software for a specific experiment on already existing packages, unless truly un-
2763 usual or novel requirements arise. Of course, we are not the first to discover this. Motivated by the

⁴This is typically achieved in physics frameworks by a clear separation of data and algorithms, where the data objects are persistable and saved to intermediate files. Regarding object persistence, the ROOT streamer model represents the state of the art in the field.

2764 increasing complexity of software in the field, various collaborations worldwide have, over the past
2765 decade or two, put considerable effort into developing high-quality, general-purpose frameworks
2766 aimed at processing the event-type data prevalent in nuclear and particle physics experiments. The
2767 present trend in HEP is a collaborative approach toward software, where already-developed, widely
2768 tested frameworks are increasingly shared by similar experiments and re-used for new ones [251].
2769 Practically no modern software in the field does without ROOT [252] in regard to interactive anal-
2770 ysis, visualization and object persistency, while a number of choices exist for event processing
2771 frameworks that support simulation and reconstruction.

2772 Obviously, we do not expect to find a perfect framework that satisfies all our criteria fully.
2773 Generally, however, a good event processing framework should stand out by a superior technical
2774 design and reliance on widely adopted, state-of-the-art technologies (*e.g.* support for C++11/14,
2775 ROOT object persistency). To minimize development time and maximize user adoption, the right
2776 mix of features, excellent documentation and a large body of available example code would clearly
2777 be beneficial.

2778 At present, we are evaluating a number of different NP and HEP data analysis frameworks
2779 that are popular and readily available. Specifically, we have been studying Podd (JLab Hall A/C)
2780 [253], Clara (JLab Hall B) [247], JANA (JLab Hall D) [248], Fun4All (PHENIX/sPHENIX at BNL)
2781 [254], FairRoot (GSI) [249], and *art* (FNAL) [250]. Of these, FairRoot, a package developed for the
2782 heavy-ion program at the future FAIR facility at GSI in Darmstadt, Germany, and *art*, the framework
2783 developed for and adopted by the Intensity Frontier experiments at Fermilab, appear to be the most
2784 promising candidates for long-term use by SoLID. Both frameworks satisfy the majority of the
2785 SoLID requirements listed above, are mature, sufficiently rich in features, sufficiently flexible for
2786 general-purpose simulation and analysis tasks, well supported, and serve a large user community
2787 that is unlikely to dissolve over the next decade.

2788 Both the FairRoot and *art* collaborations participate in the monthly ROOT planning meetings;
2789 as stakeholders, they provide direct input to the ROOT team to help improve compatibility of the
2790 respective frameworks with ROOT. We interpret this as an additional encouraging sign for the ex-
2791 pected longevity of these two frameworks in particular.

2792 Currently, neither FairRoot nor *art* are multi-threaded, but as of 2017 a major effort is underway
2793 by the core development team at Fermilab to implement multi-threading in *art* [255]. This feature
2794 is expected to become available in 2018. The heavy dependence of FairRoot on ROOT, with its
2795 many global variables, on the other hand, effectively rules out a future multi-threaded version of
2796 FairRoot. Instead, the GSI FAIR experiments are considering moving to a new, concurrent and
2797 distributed framework, ALFA [256], which will presumably be in the upgrade path of FairRoot.
2798 This option may or may not materialize in time for SoLID. ALFA could also form the basis of an
2799 extension of SoLID software to distributed computing.

2800 We are in the process of prototyping and testing simulation and analysis routines with several
2801 frameworks to gain experience with the frameworks' relative benefits. A decision as to which
2802 framework to adopt for SoLID, if any, will be made at an appropriate time.

2803 An estimate of the manpower required for implementing the complete SoLID simulation and
2804 reconstruction software can be found in Appendix C.

2805 **12.2 Simulation**

2806 **12.2.1 Simulation Software**

2807 Development of the SoLID spectrometer requires the detailed evaluation of different solenoidal
2808 fields, optics from those fields, backgrounds from multiple sources, possible detector and baffle

2809 geometries, detector responses, and tracking. Overall, a figure-of-merit must be calculated for dif-
2810 ferent configurations for quantitative comparison. It is also necessary that such simulations be done
2811 in a coherent fashion and validated as well as possible. Because details of the design have not been
2812 finalized, it must also be flexible enough to be quickly adapted to different configurations.

2813 Initial simulations for SoLID were done using a combination of GEANT3 and COMGEANT.
2814 However, these are FORTRAN based and GEANT3 is no longer actively maintained. The deci-
2815 sion was made to offer a modern design based on Geant4 [258] to handle particle propagation and
2816 interactions. This is a well-supported framework and offers a variety of physics packages, such
2817 as simulation of low-energy electromagnetic backgrounds. However, the detector geometries, how
2818 magnetic field maps are specified, input parameters, and output formats must all be developed on
2819 top of this framework. Because this is being done with a new simulation package, it is necessary to
2820 also compare and reconcile the output between GEANT3 and Geant4.

2821 To accomplish all these goals, we have adopted a simulation suite, GEMC, which was suc-
2822 cessfully developed and employed for similar CLAS12 simulations [259]. It utilizes Geant4 and
2823 includes facilities for external event generators, output to a compact style similar to that utilized by
2824 JLab data acquisition systems, and a flexible framework to specify arbitrary detector geometries.
2825 A framework for specifying sensitive detectors, processing particle hits, and generating output is
2826 also included. The geometry and sensitive detector types are read in at run time allowing for easy
2827 modification of designs. Advanced visualization abilities are available, which provides a useful
2828 debugging tool.

2829 As described in Sec. 4, magnetic field maps for GEMC can be produced using the Poisson
2830 Superfish package [260] developed at LANL or TOSCA [261]. The POISSON package allows for
2831 the calculation of azimuthally symmetric magnetic fields (relevant for the solenoidal spectrometer).
2832 Because both the optics and the fields in the detector regions are relevant, accurate optimization of
2833 the iron yoke is important. More detailed field maps produced by TOSCA will be used for the next
2834 stage of design.

2835 The overall software design is based on a modular philosophy which is general enough to allow
2836 many different software components to interact with each other. This needs to encompass ideas
2837 such as external event generators, ROOT analysis scripts, raw hit digitization, and tracking analysis.
2838 A schematic is given in Fig. 121. Detailed discussions of the individual components follow in later
2839 subsections and Sec. 12.1.

2840 GEMC and generally Geant4 provide the predominant simulation component in modeling sec-
2841 ondary physics processes (such as multiple scattering) and propagation through a magnetic field.
2842 Physics generators provide information on the initial particle type, position, and momentum to the
2843 simulation for each event and are described in Sec. 12.2.3. These can take more than one form and
2844 we allow for general text file input and internal generators within GEMC. Magnetic field maps are
2845 described over a grid using text files. GEMC allows for various coordinate systems to be used in
2846 the grids and handles all interpolation and lookup.

2847 Detector Description including geometries and materials are defined in a tabular structure which
2848 can be store in text files or SQL database. GEMC is built as a library and linked to a code called
2849 "solid_gemc" to have detector responses and output file formats customized for SoLID simulation.
2850 This gives access to all of the functionality within GEMC, but allows us to modify and add compo-
2851 nents as we need them.

2852 Output from GEMC is through EVIO, which is a binary format developed at Jefferson Lab.
2853 Libraries are available to provide decoding. These files can be converted to ROOT files through
2854 available tools or used by higher level analysis packages, such as the detector digitization.

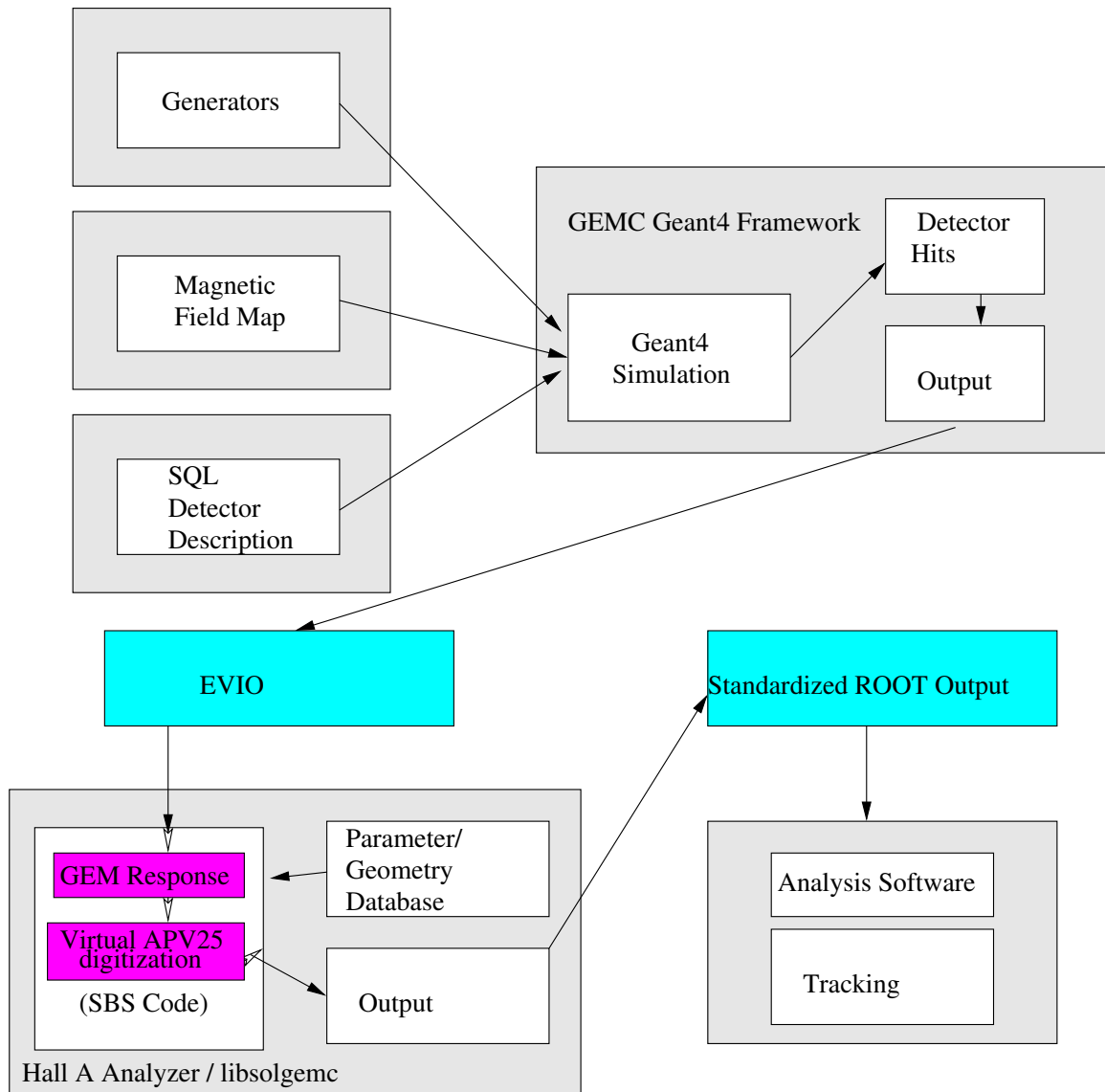


Figure 121: Schematic of the simulation and software framework.

2855 **12.2.2 Simulation Status**

2856 Significant progress has been made with the SoLID simulation, which has allowed realistic perfor-
 2857 mance studies of the core measurements and other important issues. The SoLID simulation has been
 2858 taking advantage of the new GEMC development. The simulation of each individual subsystem has
 2859 been developed by different groups using the same framework, and then all subsystems are com-
 2860 bined into the whole SoLID simulation without any code change at run time. We can also choose
 2861 to turn off a subsystem or replace it with a different version in the whole simulation for testing. The
 2862 entire code, including the production and development version, is kept in a version control system.

2863 The materials in non-detector subsystems have been implemented. Detector subsystems have
 2864 materials and responses tailored to themselves. In addition to studies done by different groups for
 2865 subsystems, we also produce the whole simulation output for various overall studies of characteris-
 2866 tics such as acceptance, background rates and trigger performance to ensure consistent results.

2867 The simulation output is stored in ROOT trees. Each detector has a standalone tree, and different
2868 trees are linked by the same tree index for one event. Then each tree is analyzed by a standalone
2869 ROOT script. Combining the set of ROOT scripts, we can analyze all SoLID sub-detectors and
2870 perform the overall studies mentioned above.

2871 In general, the SoLID simulation is an effort which will last the entire SoLID lifetime. We are
2872 still at its early stage. The simulation code will evolve with the Geant4 and GEMC development.
2873 SoLID's detector and engineering design will also evolve and they can be easily transferred into the
2874 simulation by a CAD model. Detector prototyping and tests will give direct input to the simulations
2875 and in turn improve the overall SoLID design.

2876 The SoLID collaboration may adopt the *art* event-processing framework as its software frame-
2877 work. *art* currently uses generic Geant4 as its simulation engine and allows a flexible middle layer.
2878 We are exploring the possibility of using GEMC for the simulation layer of *art*.

2879 12.2.3 Physics Event Generators

2880 Beyond the physics included in Geant4, several generators have been implemented to study specific
2881 processes. The interface between the generator and GEMC is the LUND format (or an extension of
2882 it), which is a text-based file containing event-by-event information of the initial particle configu-
2883 ration. These generators allow for an extended target and randomly sampled position to simulate a
2884 fast-rastering system. The generators implemented presently are

- 2885 • Deep inelastic scattering cross sections from the CTEQ6 parton distribution fits [263].
- 2886 • Charged and neutral pion production based on empirical fits to SLAC data [264] using the
2887 Weizsäcker-Williams approximation.
- 2888 • Charged and neutral pion production based on the modified Hall D background generator
- 2889 • Elastic scattering from protons and neutrons based on dipole parameterizations.

2890 The modified Hall D background generator gives better pion background results matching exist-
2891 ing data. The original Hall D photo-production generator uses various experimental data to generate
2892 photo-production cross sections on a proton target for photon energies below 3 GeV [267, 268]. It
2893 uses a modified version of PYTHIA to generate cross sections of photo-production for photon en-
2894 ergies above 3 GeV [267, 268]. The Hall D generator is only a photo-production event generator.
2895 SoLID requires an electro-production generator. Hadron production in electron scattering on a nu-
2896 cleon target can originate either from real bremsstrahlung photons radiated in the target or from
2897 the interaction of the virtual photon with the nucleons. The virtual contribution is calculated in
2898 the Equivalent Photon Approximation [269]. The bremsstrahlung contribution is implemented fol-
2899 lowing PDG-2012 [270, 271]. A more detailed overview of the hadron generators used for SoLID
2900 simulation is available from [266].

2901 Additional generators are planned, which includes extending the present generators to include
2902 initial radiative and multiple-scattering effects. Additionally, self-analyzing hyperon decay pro-
2903 cesses are a potential systematic and must be evaluated as well. Background rates for processes
2904 included in Geant4 can be evaluated by simulating sufficient numbers of individual electrons pass-
2905 ing through the target.

2906 **12.2.4 GEM Digitization**

2907 GEM digitization is a crucial aspect in evaluating hit tracking under realistic conditions. The method
 2908 implemented is based on an approach by the Super-BigBite collaboration, which takes the individual
 2909 ionization events in the GEM drift region, and produces a charge signal across several readout strips
 2910 based on a realistic model with parameters tuned to real data.

2911 A track passing through a GEM in Geant4 will record energy deposition events caused by ion-
 2912 ization which are then amplified through the GEM foils, resulting in a detectable signal over several
 2913 readout strips, Fig. 122. Within the simulation, the individual ionization events are written into the
 2914 output and are post-processed through an independent library built upon the Hall A analyzer analy-
 2915 sis software [253]. The digitization and track reconstruction can then be developed within a single
 2916 framework similar to what could be used for analysis of real data.

2917 A full description of the digitization process can be found in Ref [274]. To summarize, from
 2918 the individual ionization hits, an average number of hole/electron pairs are determined by sampling
 2919 a Poisson distribution based on the ionization energy W , such that $n_{\text{ion}} = \Delta E/W$. The physical
 2920 spread of the resulting charge cloud is described by a simple diffusion model assuming a constant
 2921 drift velocity, where the Gaussian width of the cloud is given by

$$\sigma_s(t) = \sqrt{2Dt} \quad (13)$$

2922 where D is the diffusion constant and t is the time from ionization. Variation in the amplification of
 2923 the GEM signal is described by a Furry distribution

$$f_{\text{Furry}} = \frac{1}{\bar{n}} \exp\left(-\frac{n}{\bar{n}}\right) \quad (14)$$

2924 where \bar{n} is the average number of ionization pairs. The previous formalism provides a realistic
 2925 (unnormalized) charge distribution over an area which can then be associated with a set of GEM
 2926 readout strips.

2927 The final component of the digitization is to reproduce the time-shaping of the electronics com-
 2928 ponents. For this application, we have assumed the use of APV25 electronics developed at CERN
 2929 (see Sec. 7). The time-dependent digitized signal $S(t)$ is produced by convoluting the charge signal
 2930 with the form

$$S(t) = A \frac{t}{T_p} \exp(-t/T_p) \quad (15)$$

2931 which provides a good parameterization of real data, Fig. 123. The parameters are chosen to repre-
 2932 sent real data and the time constant T_p is roughly 50 ns, providing a full-width half-max of about
 2933 100 ns.

2934 The advantage to using such a shaping signal is that three samples can be used to deconvolute
 2935 the longer, shaped signal to suppress out-of-time background hits. Assuming the form given in
 2936 Eq. 15, the signal in time sample k is given by

$$s_k = w_1 v_k + w_2 v_{k-1} + w_3 v_{k-2} \quad (16)$$

2937 where weights w_i are proportional to

$$w_1 \sim e^x/x, w_2 \sim 2/x, w_3 \sim e^{-x}/x. \quad (17)$$

2938 To obtain a more reliable result from the track reconstruction, it is crucial to simulate the res-
 2939 sponses of GEM detectors and related electronics to a highly realistic level. Such an effort was

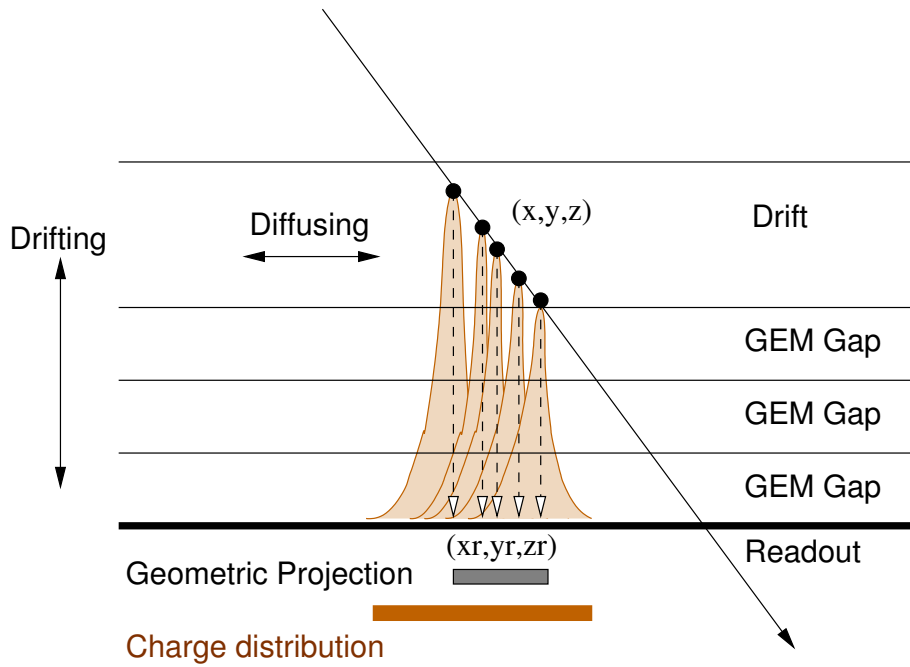


Figure 122: Diagram of the concept behind GEMs using electron avalanching and detection through a set of readout strips.

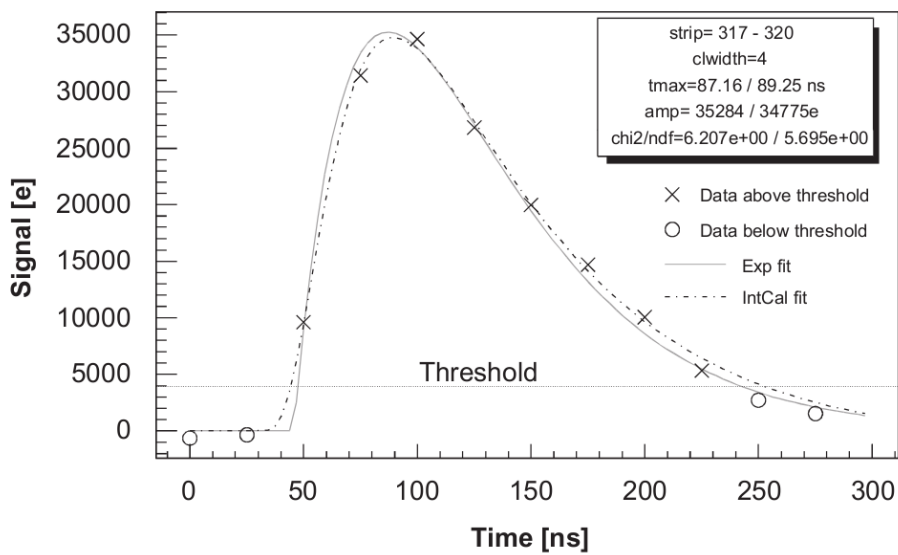


Figure 123: Representation of the signal vs. time response for an APV25 module.

PVDIS GEM occupancies			
Plane	Total strip number (u+v) per sector	Raw Occupancy (%)	Noise filtered Occupancy (%)
1	1156	21.17	9.97
2	1374	10.35	5.11
3	1374	8.81	4.42
4	2287	3.07	1.64
5	2350	2.79	1.50

Table 18: PVDIS GEM average occupancies with LD2 target estimated by digitizing its whole simulation data. The raw occupancy with only pedestal cut and the noise filtered occupancy with 3 samples are shown.

SIDIS ^3He GEM occupancies		
Plane	Total strip number (u+v) per sector	Raw Occupancy (%)
1	906	2.37
2	1020	7.98
3	1166	3.40
4	1404	2.24
5	1040	2.03
6	1280	1.52

Table 19: SIDIS ^3He GEM average occupancies estimated by digitizing its whole simulation data. The raw occupancy with only pedestal cut is shown, Because only 1 sample is used, there is no noise filtering from multiple samples.

2940 recently carried out, based on the existing SoLID GEM digitization program, by comparing simu-
 2941 lated results with actual GEM detector experimental data from beam tests and highly ionizing x-ray
 2942 test at UVa. The digitization parameters were fine tuned based on this study to work for both highly
 2943 ionizing low energy photon signals and for MIP signals. This is critical for a reliable simulation of
 2944 SoLID conditions as much of the background hits in SoLID GEM detectors are due to low energy
 2945 photons.

2946 By using the tuned digitization code, we digitized the whole simulation for PVDIS setup with
 2947 LD2 target, SIDIS setup with $^3\text{H3}$ target, and the J/ϕ setup with LH2 target. The same set of
 2948 simulation data are used for acceptance and trigger study including all detector response. The GEM
 2949 geometry and material are modeled carefully in simulation the according to the latest design and
 2950 prototype. The things missing are dead areas by spacers and frames, and the possible overlap over
 2951 different sectors, which we plan to add in the next round of simulation. Both the simulation and our
 2952 test have shown that the dominant GEM background is caused by low energy photons which have
 2953 only a few percents probability to deposition energy and fire GEM, but a huge rate. The occupancy
 2954 is obtained as the average number of readout strips fired within 275 ns time window divided by total
 2955 number of strips in the readout plane in one of 30 sectors. Both u and v strips are counted. The
 2956 results are shown in Table 18, 19 and 20. The noise filtering from 3 samples is applied where it's
 2957 available.

J/ψ GEM occupancies			
Plane	Total strip number (u+v) per sector	Raw Occupancy (%)	Noise filtered Occupancy (%)
1	906	7.68	4.65
2	1020	14.4	9.28
3	1166	8.82	5.49
4	1404	7.00	4.30
5	1040	5.92	3.78
6	1280	4.58	2.95

Table 20: J/ψ GEM average occupancies estimated by digitizing its whole simulation data. The raw occupancy with only pedestal cut and the noise filtered occupancy with 3 samples are shown.

2958 12.3 Reconstruction

2959 12.3.1 Tracking

2960 SoLID track reconstruction requires an accurate and efficient track finder able to identify signal
2961 tracks in a high-noise environment and sufficiently fast for the level-3 trigger. In addition, an ac-
2962 curate and robust track fitter is required in order to optimize the resolutions for the vertex variables
2963 and other track-related variables.

2964 In order to satisfy the requirements, a Kalman Filter (KF)-based track finding and track fitting
2965 algorithm is being developed and tested with digitized GEM simulation data. A Kalman Filter is a
2966 recursive fitting algorithm [272]. In contrast to the well-known least-squares fit that provides only
2967 one set of parameters after fitting, the track parameters of the KF can evolve along the trajectory.
2968 There are three basic steps for the KF. First, it predicts the measurement on the next measurement
2969 site by propagating the current track parameters. Second, the covariance matrices of current track
2970 parameters are propagated along the trajectory. And last, it filters the next measurement in order to
2971 improve the track parameters at the next measurement site. The local field information and errors
2972 due to multiple scattering can be collected during the first two steps of the algorithm. Thus, given
2973 that particle tracks in the SoLID detector will cross both fringe and uniform field regions, it is
2974 expected to perform better than other algorithms that explicitly require a globally uniform magnetic
2975 field.

2976 The KF can be easily extended into acting as a track finder as well, achieving concurrent track
2977 finding and fitting. This is done by adding two steps to the standard KF algorithm. First, an algo-
2978 rithm is needed to search for seeds, which are track segments that provide initial estimated track
2979 parameters. These seeds are used to initialize the KF. Second, a set of arbitration rules need to be
2980 applied before filtering to identify hits belonging to the track. A straightforward rule is to require
2981 that the hit on the next measurement site fall within a window around the prediction. An alternative
2982 rule is to cut on the χ^2 increment when a candidate hit is added [273].

2983 The whole simulation including all SoLID subsystems in their different respective configura-
2984 tions is used for the tracking studies. Both signal tracks from various event generators and back-
2985 ground produced by low energy particles, mostly photons, are included in the simulation data.

2986 At present, the track finding algorithm is being developed and tested for the different SoLID
2987 configurations. For the SIDIS ^3He configuration, using only one time-sample from the APV25
2988 and GEM digitization, both the efficiency of the track finder and the probability of identifying all
2989 correct hits of a track typically exceeds 90% for electron tracks in both the forward angle and the
2990 large angle regions. For the PVDIS and J/ψ configurations, using three time-samples from the

2991 APV25 and GEM digitization, the efficiency is about 85% for electron tracks. The track finder
 2992 also achieves a reasonable execution speed. We will study the possibility of using the current track
 2993 finding algorithm with looser conditions to improve the reconstruction speed for the planned level-3
 2994 data reduction farm.

2995 The track fitting algorithm is also being developed and tested for different SoLID configurations.
 2996 The kinematic dependence of the reconstruction resolution of the track parameters for the SIDIS ^3He
 2997 configuration is shown in Figure 124 as an example. Resolution values averaged over the kinematic
 2998 ranges, obtained for the SIDIS ^3He and PVDIS configurations, are summarized in Table 21. J/ψ
 2999 results are similar to SIDIS ^3He results. In these studies, energy loss is included for all materials,
 3000 except for materials in the dead areas of the GEM planes. Low energy photon background in the
 3001 GEMs is also not included. Both of them could worsen the resolution. To make our current results
 3002 conservative, we multiply all values by a safety factor of 1.5 when applying them to various physics
 3003 studies. We will update the results with all effects included in near future.

3004 All SoLID physics programs are using these track resolutions in their studies by directly apply-
 3005 ing the full kinematic dependent results.

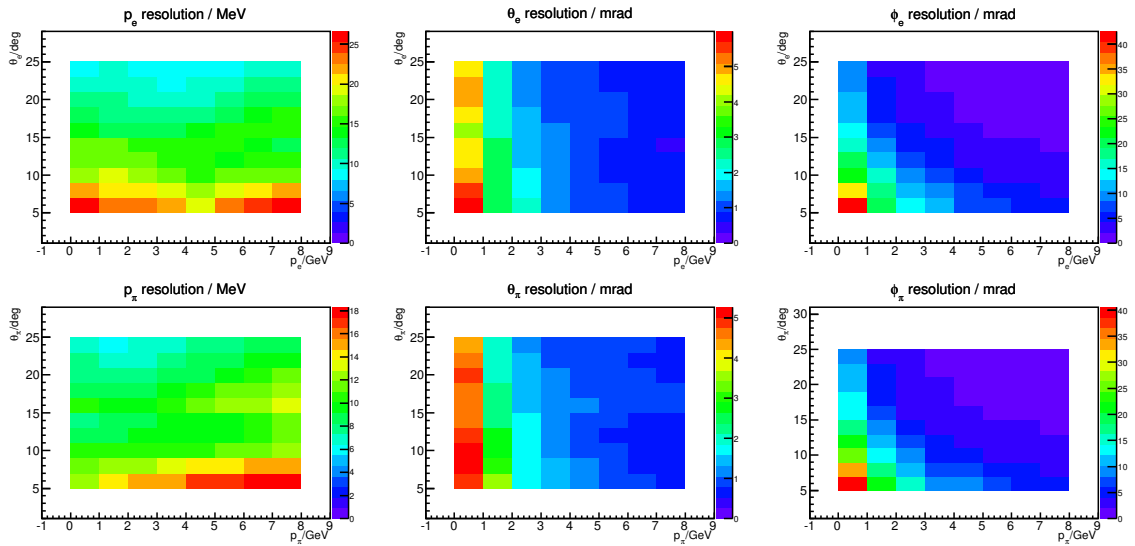


Figure 124: SIDIS ^3He resolutions by track fitting studies with most of material energy loss and without background. The upper panels are the resolution of the electron kinematics. The lower panels are those of the pion kinematics. The variables are defined in lab frame with beam line as the z -axis.

	θ angle (mrad)	ϕ angle (mrad)	Vertex z (cm)	p (%)
SIDIS ^3He fwd angle (e)	1.3	5.7	0.9	1.7
SIDIS ^3He fwd angle (π)	1.2	5.2	0.9	1.1
SIDIS ^3He large angle (e)	1.0	1.7	0.5	1.2
PVDIS (e)	0.8	1.7	0.3	1.2

Table 21: Averaged resolutions by track fitting with most of material energy loss and without background

3006 **12.3.2 Additional Reconstruction Algorithms**

3007 Many existing detector reconstruction algorithms available in the Hall A analyzer [253] or in other
3008 packages should be reusable for SoLID, for instance the Cherenkov photoelectron yield analysis and
3009 the calorimeter clustering algorithm. While the basic physics algorithms can be adopted without
3010 much change, code will have to be developed to support the cylindrical geometry of SoLID as well
3011 as the individual local detector geometries. Furthermore, a likelihood-based particle identification
3012 scheme or similar should be written. Development of calibration software tuned to the SoLID
3013 detectors will be necessary as well.

3014 A high-level overview of the necessary algorithm development tasks can be found in Appendix
3015 C, specifically in the spreadsheet referenced in that section [348].

3016 **13 Integration and Expected Performance**

3017 **13.1 Overview**

3018 System integration incorporates several tasks : 1) Quality control of the engineering of the appa-
3019 ratus so that all the pieces fit and so that the system satisfies *all* of the experimental program with
3020 minimal turnover between experiments; 2) Integration of the detectors so that they work together
3021 and form efficient triggers, and so that we can predict the combined PID performance; 3) Control
3022 of calibrations and systematic errors; and 4) Commissioning plans.

3023 In a preliminary engineering study done at Argonne National Lab by Paul Reimer, scenarios
3024 for assembling and disassembling of the apparatus have been developed which allow for switching
3025 rapidly between PVDIS and SIDIS, as well as for allowing other experiments to share Hall A during
3026 the SoLID running era. We believe we can switch between running setups in approximately three
3027 months.

3028 For the second topic, we have made a study of the combined particle ID using the gas Cherenkov
3029 and the calorimeters, see Figure 125 where the resulting π/e ratios are shown. A similar PID perfor-
3030 mance was achieved by the Hermes spectrometer [275]. Our study was performed by using the pion
3031 rejection factor and electron efficiency as a function of the scattered angle and momentum for both
3032 detectors for both the PVDIS and SIDIS configurations based on Geant simulations of the current
3033 detector designs. The results here, shown for PVDIS, are preliminary since the detector designs
3034 and the analysis strategies are still evolving. Nevertheless, the preliminary results are encouraging
3035 and show that we can likely meet the requirements for the error in the pion contamination, which is
3036 10^{-3} for entire experimental program. We believe it may be possible to combine some information
3037 with the shower shape in a multi-variable analysis to further improve the pion rejection. We are also
3038 still considering the issues of rate dependence and pileup on the pion rejection factor.

3039 In the following sections, we will present the study of the acceptance, efficiency, systematics,
3040 and calibration for various experiments.

3041 **13.2 SIDIS Program**

3042 The acceptance and efficiencies of the SIDIS configuration with a 40 cm long polarized ^3He target
3043 was studied using the whole simulation. The particles detected by the detectors were compared to
3044 those of the original particles from a full-length target. We have good electron detection efficiency
3045 from all sub-detectors. They vary slightly across the phase space and the average efficiency values
3046 are shown in Table 22. The acceptance is ~ 0.7 due to the two target window collimators. Fig-
3047 ure 126 shows the combined effect of acceptance and efficiency (except tracking). We will continue
3048 to fine-tune the design and the reconstruction algorithm to improve the efficiency.

Table 22: Average electron detection efficiencies of all SoLID sub-detectors and the total SoLID efficiency.

Detector	EC	Cerenkov	Scintillator pad and MRPC	GEM tracking	Total
average efficiency	95%	95%	98%	90%	80%

3049 We have conducted a careful study of the systematic uncertainties of the SIDIS experiments and
3050 the results are presented below.

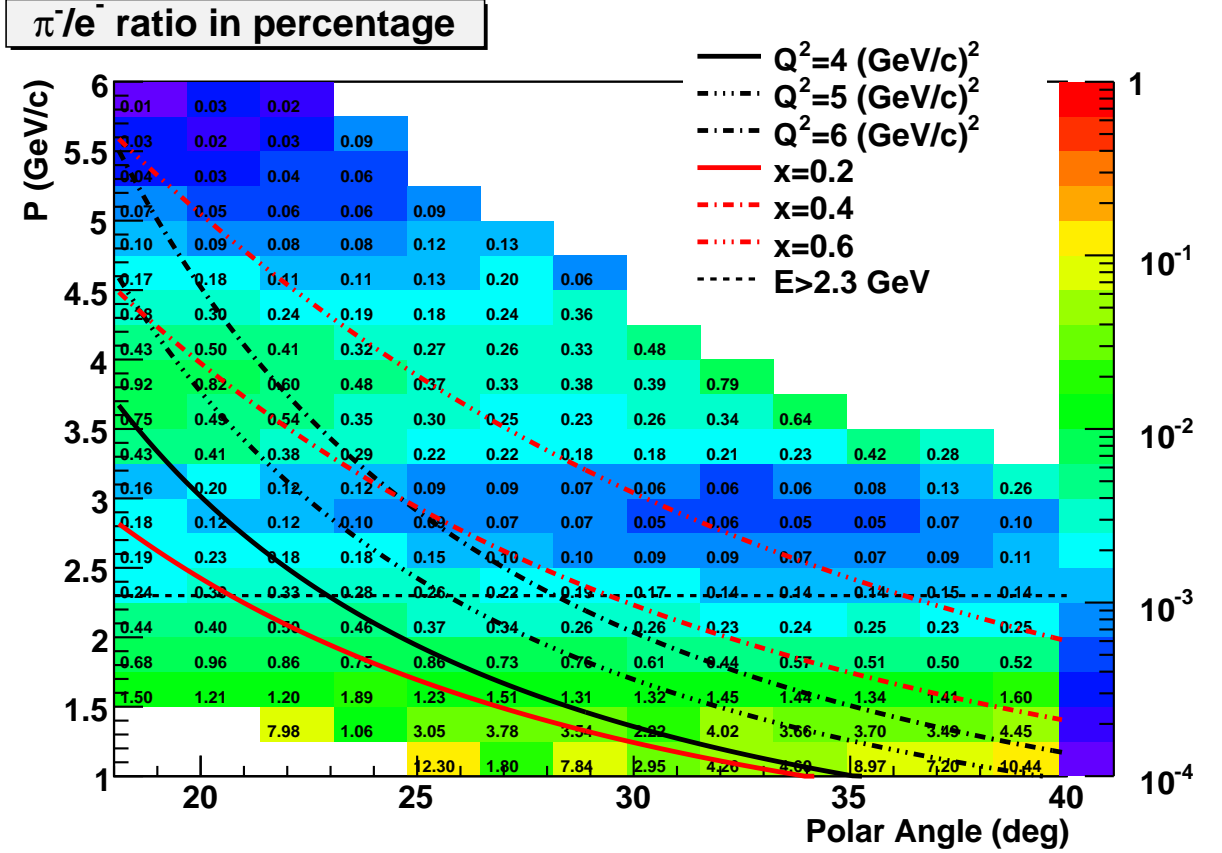


Figure 125: The π/e ratio from combined Cherenkov and Calorimeter detector performance as a function of the scattered momentum P and polar angle θ . The numerical values are the ratios corresponding to that cell in (P, θ) . The curves indicate various regions of Q^2 x or scattered energy E .

The SIDIS cross section is in general expressed as [276]

$$\frac{d\sigma}{dx dy dz dP_{h\perp}^2 d\phi_h d\phi_S} = \frac{\alpha^2}{xyQ^2} \frac{y^2}{2(1-\varepsilon)} \left(1 + \frac{\gamma^2}{2x}\right) [F_{UU}(x, z, Q^2, P_{h\perp}) + \text{asymmetric terms}]. \quad (18)$$

3051 In the simulation, we model the SIDIS cross section by assuming factorization to express the struc-
3052 ture function as a convolution of TMD distribution and fragmentation functions

$$F_{UU}(x, z, Q^2, P_{h\perp}) = x \sum_a e_a^2 \int d^2k_{\perp} d^2p_{\perp} \delta^{(2)}(P_{h\perp} - p_{\perp} - zk_{\perp}) f_1^a(x, k_{\perp}) D_1^a(z, p_{\perp}). \quad (19)$$

The unpolarized TMD distribution function $f_1(x, k_{\perp})$ and fragmentation function $D_1(z, p_{\perp})$ are parameterized as

$$f_1(x, k_{\perp}) = f_1(x, Q^2) \frac{e^{-k_{\perp}^2/\langle k_{\perp}^2 \rangle}}{\pi \langle k_{\perp}^2 \rangle}, \quad (20)$$

$$D_1(z, p_{\perp}) = D_1(z, Q^2) \frac{e^{-p_{\perp}^2/\langle p_{\perp}^2 \rangle}}{\pi \langle p_{\perp}^2 \rangle}, \quad (21)$$

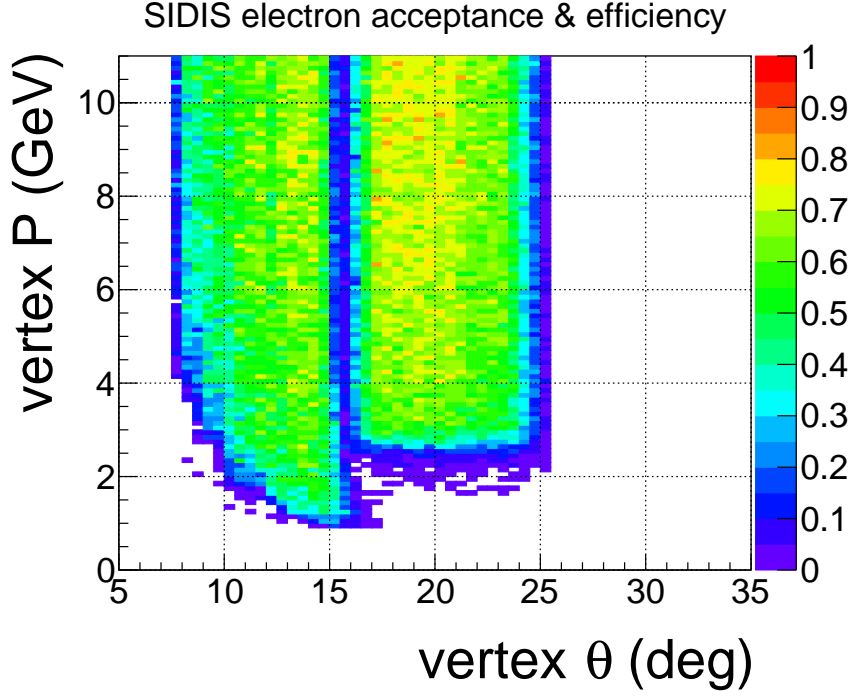


Figure 126: Electron acceptance and efficiency (except tracking) of SoLID SIDIS with the 40 cm ^3He target and two target window collimators. The result for J/ψ has a similar shape, but higher values because it has a 15 cm long target and no collimator.

3053 where $f_1(x, Q^2)$ and $D_1(z, Q^2)$ are collinear distribution and fragmentation functions. In our sim-
 3054 ulation, we use CT14 leading order collinear PDF parameterization [277] and DSS leading order
 3055 collinear FF parameterization [278]. The two parameters describing the transverse momentum de-
 3056 pendence are chosen as $\langle k_{\perp}^2 \rangle = 0.25$ and $\langle p_{\perp}^2 \rangle = 0.20$ [279]. For the three leading twist single spin
 3057 asymmetry (SSA) terms, the Sivers, the Collins, and the pretzelosity, we use the phenomenological
 3058 models [280–282] as inputs to the simulation. To take into account the detector efficiency effect,
 3059 we use 85% of the statistics for the estimation of the uncertainties.

Taking the advantage of the 2π azimuthal coverage, we are able to reduce the systematic un-
 certainties associated with luminosity and detection efficiencies by defining the target single spin
 asymmetry as

$$A_{UT}(\phi_h, \phi_S) = \frac{2}{P_1 + P_2} \frac{\sqrt{N_1(\phi_h, \phi_S)N_2(\phi_h, \phi_S + \pi)} - \sqrt{N_1(\phi_h, \phi_S + \pi)N_2(\phi_h, \phi_S)}}{\sqrt{N_1(\phi_h, \phi_S)N_2(\phi_h, \phi_S + \pi)} + \sqrt{N_1(\phi_h, \phi_S + \pi)N_2(\phi_h, \phi_S)}}, \quad (22)$$

3060 where the subscripts 1, 2 represents a target spin flip pair. $N_1(\phi_h, \phi_S)$ and $N_1(\phi_h, \phi_S + \pi)$
 3061 are taken at the same time with target polarization P_1 , while $N_2(\phi_h, \phi_S)$ and $N_2(\phi_h, \phi_S + \pi)$
 3062 are taken at the same time with target polarization P_2 . Thus, the luminosity at different times will
 3063 cancel. Since $N_1(\phi_h, \phi_S)$ and $N_2(\phi_h, \phi_S + \pi)$, $N_1(\phi_h, \phi_S + \pi)$ and $N_2(\phi_h, \phi_S)$
 3064 are taken in the same detector region, the acceptance and detector efficiency will also cancel to first order. The
 3065 time-dependent detector efficiencies will be monitored with single electron and pion rates. With
 3066 a ^3He target spin flip rate of 1/(10 minutes) (20 minutes for each pair), we expect to control the
 3067 time-dependent detector efficiency uncertainty to better than 1%. In 48 days with 11 GeV beam,

3068 we will have 3456 pairs, and in 21 days with 8.8 GeV beam, we will have 1512 pairs. Then, the
 3069 systematic uncertainty of the raw asymmetry is estimated as $1.0\%/\sqrt{3456} = 1.7 \times 10^{-4}$ for 11 GeV
 3070 data, and $1.0\%/\sqrt{1512} = 2.6 \times 10^{-4}$ for 8.8 GeV data. With a proton (ammonia) target spin flip
 3071 rate of 1/hour (2 hours for each pair), we expect to control the time-dependent detector efficiency
 3072 uncertainty to under 2%. In 55 days with 11 GeV beam, we will have 660 pairs giving an estimated
 3073 systematic uncertainty of $2.0\%/\sqrt{660} = 7.8 \times 10^{-4}$. In 27.5 days with 8.8 GeV beam, will have
 3074 330 pairs, and the systematic uncertainty is estimated as $2.0\%/\sqrt{330} = 1.1 \times 10^{-3}$. The derived
 3075 absolute systematic uncertainties of the SSA data associated with the raw asymmetry are obtained
 3076 by dividing these numbers by the target polarization and the dilution factor in each bin.

3077 The knowledge of the target polarization is at the 3% level. This translates to a 3% relative
 3078 systematic uncertainty of the SSA data. The knowledge of the target polarization direction is about
 3079 0.2 degree. The corresponding uncertainty of the target polar angle translates into 6×10^{-6} relative
 3080 uncertainty of the SSA. The uncertainty of the target azimuthal angle is included in the uncertainty
 3081 of the azimuthal angle ϕ_S together with the detector resolution effect.

3082 The systematic uncertainties associated with detector resolutions are estimated based on the
 3083 track fitting studies. The resolutions of the kinematic variables in the Trento convention for each
 3084 bin are obtained by Monte Carlo sampling according to the resolutions of the lab frame variables
 3085 shown in Figure 124. The resolutions of the kinematical variables in the Trento convention are
 3086 summarized in Table 23. The systematic uncertainty associated with the resolution mostly come
 3087 from the uncertainties of the azimuthal angles ϕ_h and ϕ_S which affect the separation of the SSA
 3088 terms. It is estimated by smearing the pseudo-data according to the resolution, separating the SSA
 3089 term with the smeared pseudo-data, and then comparing them to the model input of the simulation.
 3090 The absolute systematic uncertainty of the SSA due to the resolution is less than 1×10^{-4} , which
 3091 is negligible compared to the other uncertainties.

E_{beam} (GeV)	x	z	Q^2 (GeV ²)	$P_{h\perp}$ (GeV)	ϕ_h (rad)	ϕ_S (rad)
11	0.002	0.003	0.02	0.006	0.015	0.006
8.8	0.002	0.004	0.02	0.006	0.018	0.006

Table 23: Resolution of kinematical variables (in the Trento convention) with the ³He target setup.

Nuclear effects contribute to the systematic uncertainty when we extract the SSA of the neutron from ³He data. We derive the SSA of the neutron from that of ³He as

$$A_n = \frac{A_{^3\text{He}} - 2P_p f_p A_p}{P_n f_n}, \quad (23)$$

3092 where the SSA of proton A_p will also be measured with SoLID in the same kinematic region. We
 3093 assign 10% relative uncertainty of the knowledge of the proton SSA. The $f_{p/n}$ are the dilution fac-
 3094 tors associated with the hydrogen and the ³He target, respectively. The light-front spectral function
 3095 of ³He including the final state interaction effect was recently developed [283]. With a theoret-
 3096 ical calculation of the nuclear effect of the SSAs in the SoLID kinematic region [284], we estimate
 3097 that the relative uncertainty in the extraction of the neutron SSAs due to the nuclear effect is about
 3098 4~5%.

3099 The random coincidence background is estimated using single electron and single pion rates.
 3100 By assuming a 1 ns time resolution, we choose a plus-minus three-sigma time window of 6 ns.
 3101 For the ³He target, we also apply a three-sigma vertex cut according to the track fitting results. As
 3102 the SIDIS signal rate drops with increasing $P_{h\perp}$, we summarize the signal background ratio with

3103 respect to $P_{h\perp}$ in Table 24. The relative systematic uncertainties due to the random coincidence
 3104 background are estimated by varying the background rate by 20% for each bin.

$P_{h\perp}$ (GeV/c)	[0.0, 0.2]	[0.2, 0.4]	[0.4, 0.6]	[0.6, 0.8]	[0.8, 1.0]	[1.0, 1.2]
11 GeV beam (π^+)	110	160	150	105	75	40
11 GeV beam (π^-)	120	160	140	90	70	50
8.8 GeV beam (π^+)	75	95	80	50	45	
8.8 GeV beam (π^-)	65	95	75	50	45	

Table 24: The ratio of SIDIS signal and random coincidence background within 6 ns. These values are estimated with the ^3He target. Similar results are obtained for the proton target.

3105 The radiative correction effect of SIDIS is simulated with HAPRAD, which was developed
 3106 based on the QED calculation to one-loop level [285, 286]. The systematic uncertainties from the
 3107 radiative corrections are estimated by varying the model parameters $\langle k_{\perp}^2 \rangle$ and $\langle p_{\perp}^2 \rangle$ of the SIDIS
 3108 model in our simulation by a factor of 2 (multiplied and divided). This gives relative uncertainties
 3109 of about 2.5% for the 11 GeV data and about 2% for the 8.8 GeV data. A summary of the systematic
 3110 uncertainties is in table 25.

Table 25: The systematic uncertainties on the asymmetry measurements of SIDIS.

Systematic (abs.)		Systematic (rel.)	
Raw asymmetry	0.0014	Target polarization	3%
Detector resolution	< 0.0001	Nuclear effect	(4 – 5)%
		Random coincidence	0.2%
		Radiative correction	(2 – 3)%
		Diffraction meson	3%
Total	0.0014	Total	(6 – 7)%

3111 13.3 PVDIS Program

3112 13.3.1 Acceptances, efficiencies, and systematic uncertainties for PVDIS

3113 We now have a full Monte Carlo simulation that includes all elements of the PVDIS apparatus, layer
 3114 by layer energy deposition in the electromagnetic calorimeter (EC) and optical physics in the light
 3115 gas Cherenkov (LGC). At present we have preliminary GEM responses and tracking under realistic
 3116 backgrounds, both of which are under continued development. We now also have recent data from
 3117 newly constructed GEMs which are being employed at Jefferson Lab to refine our simulations. For
 3118 the present results, true values of track hit positions in the GEMs are used. Neither the GEMs nor
 3119 the calorimeter are segmented in the simulation. However, since the GEM sector boundaries will be
 3120 far from the baffle-defined signal regions and the tracks entering the EC will not be parallel to the
 3121 module boundaries, the effects of GEM and EC segmentation on our acceptance are expected to be
 3122 negligible.

3123 Input events to the Monte Carlo are electrons from a DIS generator using cross sections from
 3124 CTEQ6 parton distribution fits [287]. Our analysis integrates primary electrons which reach the
 3125 active area of the EC after passing through the active areas of all five GEMs and the front window
 3126 of the LGC. The acceptance is shown in Figure 127 as a function of p and θ (left panel) and as a

3127 function of Q^2 and x_{bj} (right panel). Lines on these plots show the boundaries of the kinematic
 3128 region of interest: $Q^2 > 6 \text{ GeV}^2$, $W > 2 \text{ GeV}$, and $x_{bj} > 0.55$. Our acceptance in this region is
 3129 typically 40%.

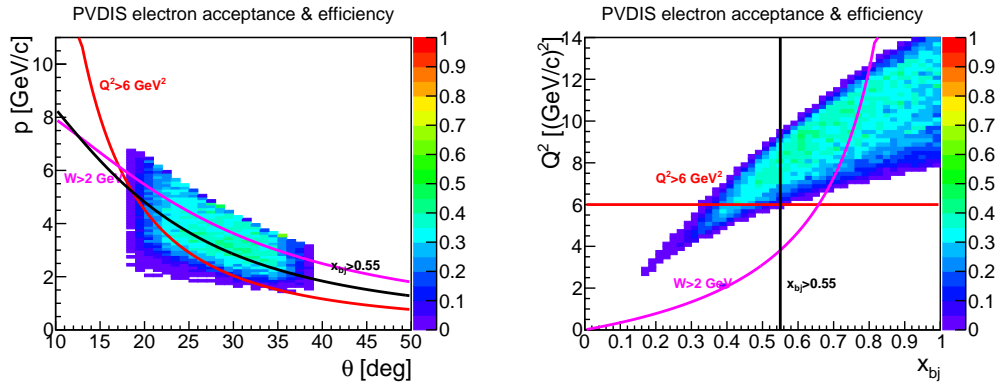


Figure 127: Left: PVDIS acceptance and efficiency as a function of p and θ . Right: PVDIS acceptance and efficiency as a function of Q^2 and x_{bj} . Curves show bounds of the kinematic range with $Q^2 > 6 \text{ GeV}^2$, $W > 2 \text{ GeV}$, and $x_{bj} > 0.55$.

3130 Contributions to the efficiency are as follows:

3131 *Calorimeter:* Efficiency of $\sim 95\%$ as reported in subsection 10.7.

3132 *LGC:* With the changes of the radiator gas and PMT quantum efficiency, new studies of the
 3133 LGC efficiency need to be undertaken. Requiring ≥ 2 photoelectrons in each of ≥ 2 PMTs in the
 3134 sector matching the EC yields 96% efficiency.

3135 *Tracking:* The GEM detection efficiency is 97% per plane. From our studies using a tree search
 3136 algorithm with realistic and correlated superimposed backgrounds and our current model of digi-
 3137 tization, a track finding efficiency of $\sim 90\%$ appears to be achievable. Development of the track
 3138 finding software is continuing.

3139 Combining the above contributions yields an estimate of 82% for our overall efficiency.

3140 The systematic errors on our measurement of the parity violating asymmetry are summarized in
 3141 Table 26.

3142 The systematic error on the polarization of the beam $\Delta P/P$ is required to be better than 0.4%
 3143 [288]. The best achievable precision of such measurements is 0.6% at present, but 0.4% are consid-
 3144 ered to be within reach [289]. The dominant systematic error in [288] is the laser polarization, which
 3145 was estimated to be 0.3% but is given in [289] to be below 0.2%. The higher analyzing power and
 3146 large-angle characteristics of the 11 GeV beam relative to the Qweak 1 GeV beam result in a better
 3147 precision for SoLID. We also expect better to understand the systematic errors of the polarimetry
 3148 by building on the experience of the MOLLER experiment, where polarimetry plays a particularly
 3149 important role.

3150 The radiative corrections are similar to those computed for the HERA experiments [290]. Many
 3151 of the important radiative corrections come from tails of events at larger x , which are small for the
 3152 SoLID high- x kinematics. We have assembled a team including A. Aleksejevs, S. Barkanova and
 3153 W. Melnitchouk, who will assist in performing the necessary calculations. We estimate an error of
 3154 0.2% from radiative corrections.

3155 Finally, systematics on the asymmetry due to reconstruction errors, including DAQ issues and
 3156 particle identification, will be kept to the 0.2% level. The pion contamination is expected to be

3157 below 1% for most bins and the required corrections should be valid to at least 10% of that. Work
 3158 on the DAQ is in progress to demonstrate that the pile-up and dead-time corrections can be kept to
 3159 below 0.15%.

3160 The total systematic error is 0.6%, unchanged from the proposal value, allowing sufficient sen-
 3161 sitivity to meet our physics goals.

Polarimetry	0.4
Q^2	0.2
Radiative corrections	0.2
Reconstruction errors	0.2
Total	0.6

Table 26: Summary of PVDIS systematic errors, in percent.

3162 13.3.2 Kinematics, Resolution and Calibration for PVDIS

3163 In this section, we describe the general method of measuring the momentum p and the scattering
 3164 angle θ of each track. In addition, we discuss the resolution of x , and Q^2 , the relevant variables
 3165 for the analysis. Finally, we discuss the calibration of the average value of Q^2 . The most critical
 3166 requirements are the the x resolution is on the order of 0.01 to avoid kinematic smearing and that
 3167 the average Q^2 , which is proportional to the asymmetry, is calibrated to 0.1%.

3168 The method that we use to reconstruct the tracks, determining the scattering angle and momen-
 3169 tum, is easiest to understand in the approximation of a uniform field. Based on this method, we can
 3170 explain our alignment tolerances and systematic errors. We then show how to make the corrections
 3171 for the realistic case. These corrections do not alter most of the tolerances.

3172 First, we look at the track in the x - y plane. This is given in Figure 128. All we require is hits
 3173 in two GEM detectors. The one closest to the target is labeled GEM _{i} and the other is GEM _{j} . Since
 3174 the beam is small (300 μm by 250 μm), it provides a third point which is sufficient to determine the
 3175 radius of curvature ρ of the helix. The transverse momentum of the electron is then κ/ρ , where κ
 3176 is a constant proportional to the magnetic field. The transverse distance between the beam and the
 3177 first GEM is R and between the two GEM's is D . The angle between the line segments R and D is
 3178 $(\psi + \delta)/2$. From the diagram, we have

$$\frac{1}{\rho} = \frac{2(\sin(\psi/2) + \sin(\delta/2))}{(R + D)} \approx \frac{\psi + \delta}{R + D}, \quad (24)$$

3179 where the approximation is for small angles. Since

$$\frac{\sin(\psi/2)}{\sin(\delta/2)} = \frac{R}{D}$$

3180 and $(\psi + \delta)/2$ is measured, Eq. 24 can be evaluated exactly.

3181 For the helix, the angle θ between the trajectory and the z -direction is constant, and thus is the
 3182 scattering angle. If Δz is the difference in the z -coordinates of the GEM's, then

$$\tan \theta = \frac{\rho}{\Delta z} \sin^{-1} \frac{D}{\rho} \approx \frac{D}{\Delta z}. \quad (25)$$

3183 From the approximation, we see that the error in ρ contributes little to the error in θ .

3184

Finally, we note that

$$Q^2 = 4E^{\frac{\kappa}{\rho}} \tan(\theta/2).$$

3185

Thus the fractional error in Q^2 is the sum in quadrature of the fractional errors in ρ and θ .

3186

Thus with two GEM points and a narrow beam, we can reconstruct the important variables

3187

for DIS. In addition, the distance r from the first GEM to the beam line in the x - y plane and

3188

the azimuthal angle of the first GEM hit are measured. The first can be used to determine the z -

3189

coordinate of the interaction, which can be used as a check that the track is valid and also determine

3190

if it came from the front or rear target windows.

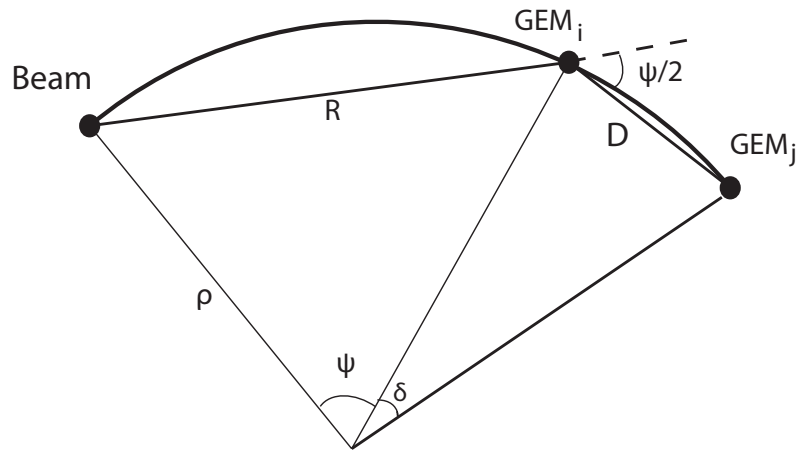


Figure 128: Projection of the track in the $x - y$ plane. The projected radius of curvature is ρ .

3191

For realistic magnetic fields, we generated with our Monte Carlo many trajectories and deter-

3192

mined the discrepancies with Eqs. 24 and 25. These discrepancies could be parameterized in terms

3193

of the measured variables $\psi + \delta$, D , R , and r and used as corrections. With the corrections, ρ and

3194

θ can be determined from the GEM hits with a precision better than 0.1%.

3195

Rather than $\psi + \delta$, we used the angle α between the line segment R and the line joining the

3196

beam with the hit in GEM_j . Then

$$\alpha \approx \frac{\psi + \delta}{2} \frac{D}{R + D},$$

3197

and

$$\frac{1}{\rho} = \frac{2\alpha}{D}.$$

3198

Thus our precise and realistic equation for ρ is

$$\frac{1}{\alpha\rho} = \frac{2}{D} + F_\rho(R, D, r, \Delta z). \quad (26)$$

3199 An important feature is that the angle α only appears in the left side. This feature is useful for our
 3200 momentum calibration method shown below. For θ ,

$$\tan \theta = \frac{D}{\Delta z} + F_\theta(R, D, r, \Delta z, \alpha). \quad (27)$$

3201 There are two effects that contribute to F_θ . The first is the approximation in Eq. 25. The second is
 3202 the fact that radial components of the magnetic field change the angle that the trajectory makes with
 3203 the z -axis. Thus F_θ depends slightly on α .

3204 Since F_ρ and F_θ are small, the errors in their arguments do not contribute significantly to the
 3205 errors in ρ or θ . The requirements for calibration can be obtained from the leading approximations.

3206 The momentum resolution, which is dominated by multiple scattering, mostly in the air, is about
 3207 1%, independent of momentum. The angular resolution, dominated by GEM resolution, is about
 3208 0.5%. The resolution in Q^2 is 1.5% and in x is 1%. The z -resolution is 7 mm. These numbers are
 3209 obtained with our simulation with realistic GEM signals.

3210 The first step in momentum calibration is alignment of the GEM trackers. To make estimates
 3211 of the systematic errors in track momentum reconstruction we use artificial displacements of GEM
 3212 hits in our simulation. In the simple case of a uniform field and a thin target the minimum distance
 3213 between the beam axis and the line through two GEM hits is linearly related to $1/p$. That distance
 3214 is of order 10 cm, implying a need to calibrate the GEM transverse positions to $\sim 100 \mu\text{m}$ in order
 3215 to achieve a systematic error on the relative momentum $\Delta p/p$ of order 10^{-3} .

3216 For a more realistic estimate we use a Monte Carlo simulation incorporating a realistic field
 3217 and a long target to study the effects on our momentum and angle reconstruction of all elementary
 3218 displacements: lateral and transverse position shifts, and rotations in and perpendicular to the de-
 3219 tector plane, of one or both GEMs. Results are shown in Table 27. Due to the symmetry of the
 3220 apparatus, Q^2 is insensitive to all these misalignments to first order except for single GEM angular
 3221 displacement in-plane. We find that we need to understand transverse GEM positions relative to
 3222 straight tracks to within about $200 \mu\text{m}$, and absolute positions parallel to the beam axis at the level
 3223 of about 3 mm.

1/p and θ residuals for GEMs 1, 4					
transform	GEM(s)	$\delta p(\text{mean})$	$\delta p(\text{width})$	$\delta \theta(\text{mean})$	$\delta \theta(\text{width})$
transverse displacement	1, 4	-0.01%/mm	0.77%/mm	0.00%/mm	0.00%/mm
	4	0.00%/mm	0.76%/mm	0.00%/mm	0.08%/mm
longitudinal displacement	1, 4	0.05%/mm	0.00%/mm	0.00%/mm	0.00%/mm
	4	0.08%/mm	0.01%/mm	0.06%/mm	0.00%/mm
in-plane rotation	1, 4	0.00%/mrad	0.00%/mrad	0.00%/mm	0.00%/mm
	4	1.61%/mrad	0.15%/mrad	0.01%/mm	0.01%/mm
out-of-plane rotation	1, 4	0.00%/mrad	0.08%/mrad	0.00%/mm	0.03%/mm
	4	0.00%/mrad	0.09%/mrad	0.00%/mm	0.06%/mm

Table 27: Momentum and angle reconstruction sensitivities to various displacements of GEMs 1 and 4: transverse, longitudinal, and rotational (in and perpendicular to the detector plane) displacements of both GEMs or of GEM 4 only. “ $\delta p(\text{mean})$ ” and “ $\delta \theta(\text{mean})$ ” are the changes in the mean of the $1/p$ and θ residuals and “ $\delta p(\text{width})$ ” and “ $\delta \theta(\text{width})$ ” are the changes in those residuals’ width per unit displacement. Due to detector symmetry, the displacement to which we are most sensitive is single GEM in-plane rotation.

3224 Within a GEM, strip positions relative to one another will be known to within $25 \mu\text{m}$. With
 3225 standard surveys, relative strip positions within a full GEM plane can be established to better than
 3226 $500 \mu\text{m}$. To achieve our resolution goal and to monitor possible motion of the tracking chambers,
 3227 straight-through electrons with the magnetic field off and low energy photons with the field off and
 3228 on will be used to calibrate the relative transverse positions of the GEMs with the required precision.
 3229 A thin carbon target about 10 cm upstream of the LD₂ target has lines of sight to most of the area
 3230 of the GEMs, as shown in Figure 129. For x-ray studies, an absorber ring with holes, or conversely
 3231 a set of absorbing beads mounted on a ring of light material, will provide the fiducials.

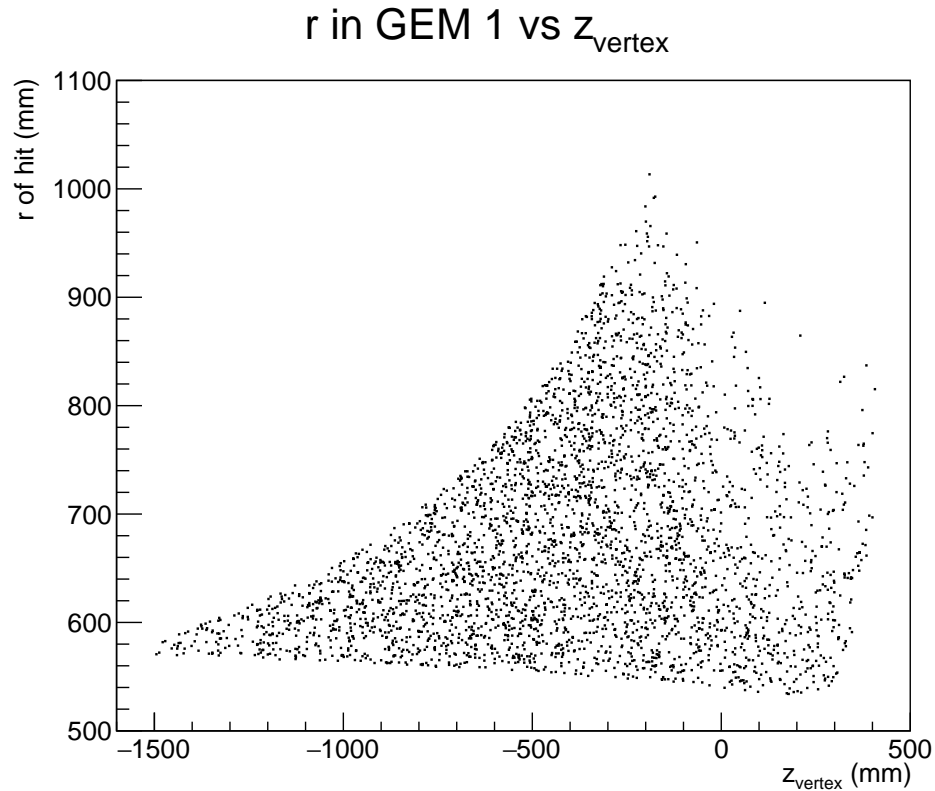


Figure 129: Radial coordinates of photon hits in GEM 1 versus vertex z position. Most of the detector area is covered for vertex at $z = -200$ mm, corresponding to a position about 10 cm upstream of the LD₂ target. Similar results are seen in the other GEMs.

3232 Once the positions of the GEMs are known, the magnetic field is calibrated as follows. First
 3233 a map is obtained with a precision of about 1%. With this map the radial fields are known well
 3234 enough so that F_θ can be precisely determined. To improve the calibration of the momentum to the
 3235 0.1% level, we use electron hydrogen elastic scattering data at beam energies of 4.4 and 6.6 GeV as
 3236 well as at different magnetic field settings. Since the beam energy is known to better than 0.1% and
 3237 the angle can be measured to that precision, the location of the elastic peak provides a calibration
 3238 of the magnetic field. One issue is that for one beam energy, there is only one track energy at each
 3239 angle, whereas for DIS, the angle and energy are much less correlated. However, the correction F_ρ
 3240 in Eq. 26 is independent of α , so a single momentum at each angle is sufficient. In other words, the
 3241 importance difference between two similar fields is the value of $\int B_z ds_\perp$ which is a scale factor for
 3242 all momenta. Hence a single momentum from the elastic scattering is sufficient to make a precise

3243 correction.

3244 Clean separation of the elastic peak will be required. Figure 130 shows results from simulations
3245 where the green histograms are elastics and the blue histograms are the inelastic background from a
3246 Christy-Bosted parameterization [291]. Target and detector materials were included and momenta
3247 were smeared by 1% to simulate detector resolution. At both energies the elastic peaks are cleanly
3248 resolved. Rates are ample for calibration; see Figure 131. At 6.6 GeV, the integrated rate is about
3249 150 Hz per μA of beam current. At 50 μA , sufficient data can be collected in only a few minutes.

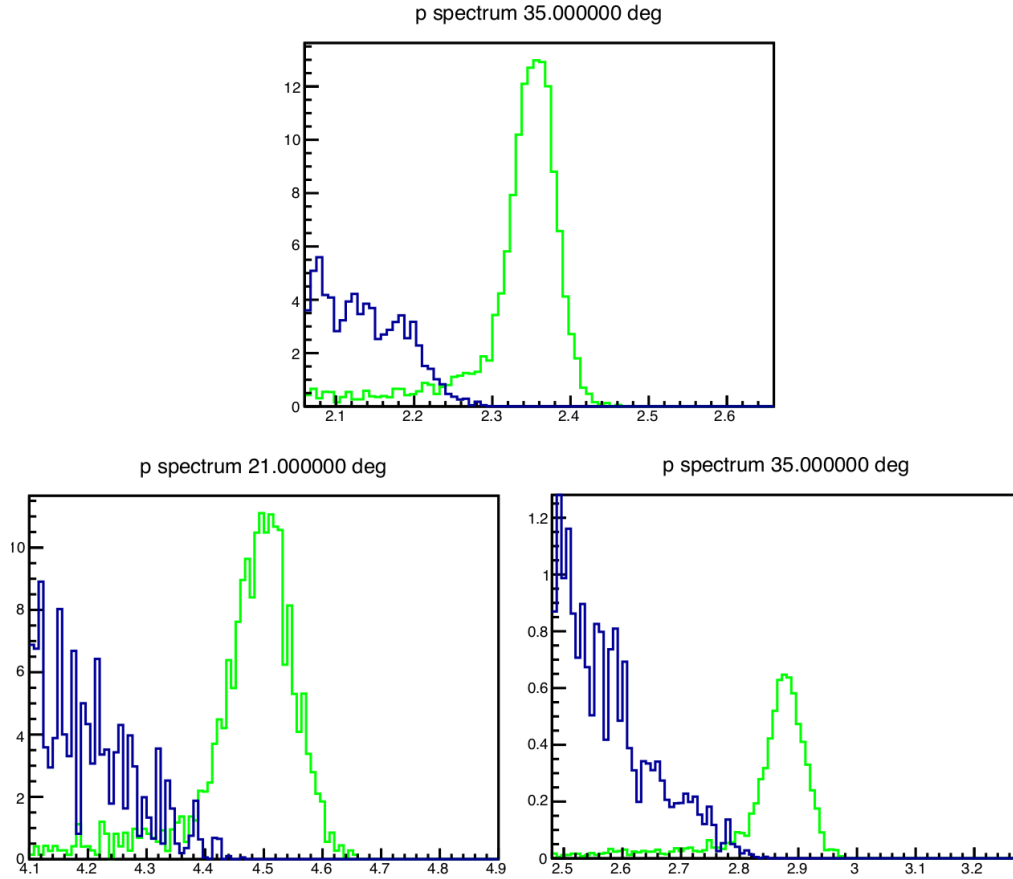


Figure 130: Elastic (green) and inelastic (blue) spectra for 4.4 GeV (top) and 6.6 GeV (bottom) electrons on a hydrogen target, at scattering angles of 21° (bottom left) and 35° (top and bottom right).

3250 13.4 J/ψ Program

3251 Recent simulation studies of J/ψ production have been performed including approximate radiative
3252 effects. External bremsstrahlung was applied to both the incident and scattered electrons. The inci-
3253 dent electron radiation loss is calculated with the peaking approximation through the target material
3254 up to the reaction vertex. The external radiative loss for the scattered electron is calculated within
3255 the framework of Geant4/GEMC and folded into the total resolution smearing of the track. Internal
3256 bremsstrahlung is calculated according to the Q^2 dependent equivalent radiator method, and applied

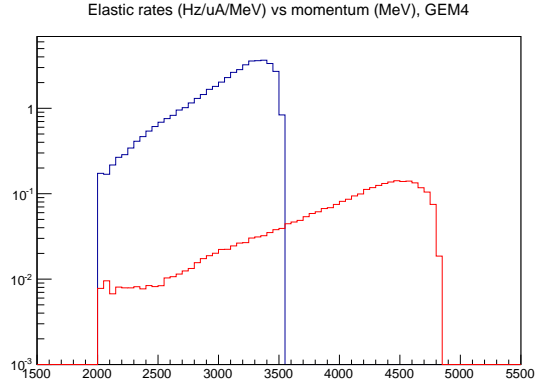


Figure 131: Elastic rates at GEM 4 for 4.4 GeV/c (blue line) and 6.6 GeV/c (red line) electrons on LH2, as a function of momentum in MeV/c. Rates are in Hz per μA per MeV/c. Target and detector materials are included.

3257 to both the incident and scattered electrons. These radiative calculations are well known and widely
 3258 used and have historically described radiative losses with reasonable precision. A more robust and
 3259 explicit calculation would allow for a more precise unfolding of the radiative losses, however such
 3260 an endeavor is non-trivial and would require a significant investment of manpower. For the approxi-
 3261 mate calculations, one can see in Figure 132 the effects of bin-migration along W , and the estimated
 3262 correction needed to recover the unradiated cross-section. The plotted calculations were simulated
 3263 with a 4-fold coincidence; the 3-fold coincidence has identical radiative losses (incident electron,
 3264 scattered electron). Additionally, the internal radiative corrections in the equivalent radiator method
 3265 are near zero when in the quasi-real photon kinematics of the 2-fold coincidence measurement. We
 3266 plan to continue developing our radiative corrections procedure with exact calculations, accurate
 3267 unfolding, and tests of model dependence.

3268 A physics generator which includes acceptance effects was developed for the experiment pro-
 3269 posal and has since been extended to include resolution effects and the radiation effect approxima-
 3270 tions outlined above.

3271 Because the J/ψ experimental configuration is very similar to the SIDIS setup: a target position
 3272 offset by 35 cm being the only difference. the acceptance and efficiencies are in-line with the SIDIS
 3273 ^3He program shown in Figure 126 and Table 22. The only difference is that the J/ψ setup has
 3274 higher acceptance because its 15 cm long LH2 target requires no collimators as SIDIS ^3He

3275 As stated in the original proposal, we expect the systematic uncertainty to be dominated by the
 3276 acceptance ($<10\%$), with an additional contribution of a few percent from sub-detectors, luminosity,
 3277 target windows and background contaminations. We take the total systematic uncertainty to be 11%.
 3278 Without radiative corrections of the data, systematics due to bin migration can be estimated from
 3279 Figure 132. However, much of these systematics can be corrected by accurately simulating and
 3280 properly unfolding the radiative effects (see section above).

3281 An updated analysis of the J/ψ experiment's di-lepton trigger from the decay lepton pairs and
 3282 triple lepton trigger with additional scattered electron were preformed, similar to what the PVDIS
 3283 and SIDIS ^3He programs have done. This simulated trigger study included the signal and combi-
 3284 natorial background from leptons, pions, and additional hadrons over both forward and large angle
 3285 acceptance including the most up-to-date EC, LGC, and SPD response. The resulting di-lepton
 3286 trigger and triple lepton trigger are calculated to have a coincidence rate about 60 kHz and 30 kHz

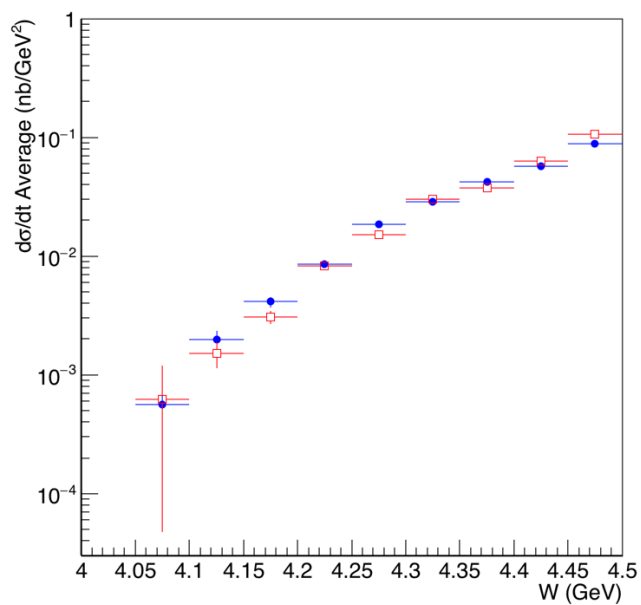


Figure 132: Simulation of cross-section including acceptance effects but no additional radiative losses (blue circles) for comparison with the expected cross-section measurement including acceptance smearing and all radiative effects listed in the text (red squares).

3287 respectively. The triple lepton trigger will be our main trigger and it's also possible to take some
 3288 pre-scaled di-lepton trigger to preserve photoproduction data. We are working on improving the
 3289 trigger rate estimation and fine tuning the trigger design to see what's the best way to maximize the
 3290 physics program under reasonable trigger limit.

3291 14 Data Acquisition

3292 14.1 Introduction and Requirements

3293 The SoLID detector is a large acceptance detector designed to run at high luminosity. The detector
 3294 will operate in two basic configurations: the parity-violating electron scattering (PVDIS) config-
 3295 uration and the semi-inclusive deep inelastic scattering (SIDIS) configuration. The experiments
 3296 planned under these configurations have in common a large number of channels (over 160,000
 3297 GEM tracking channels and over 4,000 trigger/particle ID channels), high background rates, and
 3298 high trigger rates.

3299 We use the whole detector simulation with various experimental setups to study trigger as men-
 3300 tioned in Section 12.2. The high energy primary particles are from event generators like single
 3301 electron generator, pion SIDIS generator and the modified HallD hadron generators. All secondary
 3302 particles are generated by Geant4. The low energy particles mostly from electromagnet processes
 3303 are produced by Geant4 directly when shooting beam electrons into target. The response in various
 3304 detectors are examined even by event according to trigger setup. low energy background and pile
 3305 up effect are taken into account. The expected trigger rates are shown in Table 28 for different
 3306 experimental setups. (Upon the improvement of our software tool, the ongoing DAQ test, and the
 3307 availability of JLab 12 GeV data, our trigger simulation will be further improved.)

3308 The SIDIS configuration, with an expected trigger (coincidences and accidentals) rate of ~ 100
 3309 kHz and total data rate of over 3 GB/s represents the greatest challenge for SoLID data acquisition.
 3310 For PVDIS, the DAQ requirement is more modest as the ~ 450 kHz rate is divided among 30 parallel
 3311 DAQ systems, following the segmentation provided by the baffle system. However, there are addi-
 3312 tional challenges as the DAQ systems for adjacent sectors must communicate trigger information
 3313 and data for events where calorimeter showers extend into adjacent sectors.

3314 We present here a conceptual design for a DAQ system based on modest evolution of current
 3315 technology, much of which has been developed at JLab. Considering the large number of channels,
 3316 the rate requirements and the availability of new electronics developed for the Hall D GlueX de-
 3317 tector, a pipelined electronics approach has been chosen. These electronics continuously digitize
 3318 the detector signals, keeping the data in several microsecond deep buffers which can be retrieved
 3319 after a trigger is received. With these electronics, the First Level Trigger (L1) is generated primarily
 3320 from prompt data streams from Flash Analog to Digital Converters (FADC). This gives the ability
 3321 to reprogram trigger algorithms without the need for re-cabling.

Experiment	PVDIS	SIDIS ^3He	J/ψ
Trigger rate (expected) (kHz)	15×30	100	30
Data rate (GB/s)	0.2×30	3.2	2.5
Running time (days)	169	125	60
Total data (PB)	175	70	25

Table 28: Rates, run times and data total estimates for the PVDIS, SIDIS ^3He and J/ψ experiments. For PVDIS, there are 30 sectors each of which has a separate DAQ.

3322 14.1.1 SIDIS Trigger and Rate Estimate

3323 Three experiments, E12-10-006 [292], E12-11-007 [293], and E12-11-108 [294], have been ap-
 3324 proved to measure single and double asymmetries of semi-inclusive deep-inelastic scattering (SIDIS)

3325 ($e, e'\pi^\pm$) with SoLID. As these experiments have similar reaction channels, they can share the
3326 same DAQ system design. The required overall luminosity of E12-10-006 and E12-11-007 is
3327 $10^{37}/\text{cm}^2/\text{s}$, which is an order of magnitude higher than that of E12-11-108. Therefore, we will use
3328 E12-10-006 as an example to illustrate the requirements of the SIDIS DAQ. The goal of the SIDIS
3329 DAQ is to satisfy the requirement of ~ 100 kHz trigger rate, see Section 14.2.1 for more information
3330 about the limit.

3331 The SIDIS process requires the detection of both the scattered electron and the leading pion.
3332 Therefore, a single electron trigger or a coincidence trigger of the electron and the hadron would
3333 satisfy this need. The electron trigger for the large angle detector will be provided by the E&M
3334 calorimeter at a threshold of about 3 GeV. Such a trigger is sensitive to both high energy electrons
3335 and high energy photons (mostly from the π^0 decay). A set of scintillator paddles, added in front of
3336 the calorimeter, are incorporated into the trigger in coincidence, significantly suppressing triggers
3337 from high energy photons.

3338 The electron trigger at the forward angle detectors will be formed by a coincidence of the Gas
3339 Cerenkov detector, the E&M calorimeter, the scintillator paddle detector (SPD) and the Multigap
3340 Resistive Plate Chamber (MRPC). Considering the kinematics information of the scattered electrons
3341 from the DIS process (e.g. $Q^2 > 1 \text{ GeV}^2$), a position dependent energy threshold with a lower limit
3342 of 1 GeV in the E&M calorimeter will be used.

3343 The single electron trigger rate was estimated from simulation to be 116 kHz for the forward
3344 angle calorimeter in coincidence with the Gas Cerenkov, SPD and MRPC. And it is 32 kHz for the
3345 large angle calorimeter in coincidence with the SPD giving a total single electron rate of 148 kHz.
3346 In order to keep the Level-1 trigger rate below the 100 kHz limit, we plan to form a coincidence
3347 trigger between the electron trigger and the charged hadron trigger with a 20 ns time window. The
3348 charged hadron trigger using the calorimeter with the SPD and the MRPC is 20 MHz. The SIDIS
3349 processes including charge pions, neutral pion and proton have coincidence trigger rate of 27 kHz.
3350 Other multiple hadron process can also contribute to coincidence rate of 12 kHz. Excluding the true
3351 coincidence from SIDIS and multiple hadron process, we estimate the accidental coincidence rate
3352 46 kHz with a 20 ns time window. Some single electron trigger will also be acquired. These will be
3353 prescaled to about 15 kHz such that the total trigger rate remains below 100 kHz.

3354 14.1.2 J/ψ Trigger and Rate Estimate

3355 The E12-12-006 experiment is designed to measure the cross section of the $p(e, e'J/\psi)p$ reaction
3356 at an unpolarized luminosity of $1.2 \times 10^{37} N/\text{cm}^2/\text{s}$ with a proton target. A double coincidence
3357 trigger between the electron/positron pair from J/ψ decay will allow both the electroproduction
3358 and photoproduction reactions recorded. By using similar electron trigger setup, except a different
3359 radial dependent EC trigger threshold, we obtain a rate of 60 kHz. Adding the scattered electron
3360 into trigger to form a triple coincidence could reduce the trigger rate by a factor of 2 to be 30 kHz,
3361 but this will limit the data taking to electroproduction only. It's also possible to take some pre-
3362 scaled double coincidence trigger to preserve photoproduction data, We are working on improving
3363 the trigger rate estimation and fine tuning the trigger design to see what's the best way to maximize
3364 the physics program under reasonable trigger limit.

3365 14.1.3 PVDIS Trigger and Rate Estimate

3366 The PVDIS measurement is based on the asymmetry of inclusive electron scattering between inci-
3367 dent electrons of opposite helicity states. To achieve the needed statistical accuracy of this parity
3368 violating asymmetry, high rates will be required in the detector. The rate over the whole detector

3369 is expected to be of the order of 500 kHz, above the trigger rates that can be handled by the JLAB
3370 electronics. As the measurement is of singles inclusive electrons, the detector can be divided into
3371 30 sectors each with a separate trigger, giving an acceptable rate for each sector. For each sector, the
3372 trigger will be a coincidence between the gas Cerenkov and electromagnetic calorimeter. Based
3373 on our simulations of the inclusive electron rate and accidentals (with a 30 ns coincidence window)
3374 between singles in the electromagnetic calorimeter and the Cerenkov counter the estimated trigger
3375 rate is 15 kHz per sector.

3376 **14.2 DAQ Hardware and Trigger**

3377 The DAQ system for SoLID will use modules recently developed by the Physics Division Fast
3378 Electronics and Data Acquisition groups of Jefferson Laboratory for Hall D. These include flash
3379 ADCs (FADC250), VXS Trigger Processors (VTP) and Global Trigger Processors (GTP), Sub-
3380 System Processors (SSP), Trigger Supervisors (TS), Trigger Interface (TI), and Signal Distribution
3381 (SD) modules.

3382 Analog signals are digitized by the JLab FADC250, a 16-channel 12-bit flash analog to digital
3383 converter sampling at 250 MHz. The input signals are continuously recorded into a memory with a
3384 depth of up to 8 μ s with event data latched by a trigger. The system is dead-timeless as long as the
3385 latched data can be readout as fast as it is generated.

3386 In addition to making data available for readout when triggered, the FADC250 is capable of
3387 sending continuous data over high speed VME switched Serial (VXS) lanes on the backplane con-
3388 nector. This data, a 16 bit word per module every 4 ns, could be a digital sum of the 16 channels of
3389 the ADC or more complex information.

3390 Each crate will have a VXS Trigger Processor (VTP) which receives a 16 bit word from each
3391 FADC250 every 4 ns. The VTP processes the data stream from each module in the crate to generate
3392 a 32-bit word every 4 ns. This word, which could be, for example, a sum of all the channels in the
3393 crate or a bit pattern, is sent upstream via a 10 Gbps optical link to a Sub-System Processor (SSP)
3394 board which gathers trigger data from multiple crates. All the SSP boards send their information to
3395 the Global Trigger Processor (GTP) which generates the level one (L1) trigger.

3396 The GTP sends the trigger to the Trigger Supervisor (TS) which makes sure the system is ready
3397 to accept a trigger and sends the accepted signal to the Trigger Distribution boards which are linked
3398 to the Trigger Interface (TI) boards in each crate via optical links as represented in Fig.133. The
3399 trigger and synchronization clock signals will then be sent back to individual crates and payload
3400 modules through Trigger Distribution (TD) boards and Signal Distribution (SD) boards which dis-
3401 tributes the signals to the electronics such as the FADC. Once a trigger is generated, the full resolu-
3402 tion data which is still in the pipeline, is readout out using a serial VXS link at a data rate of 8 Gbit/s
3403 correspond to 1 GB/s. As this is a point to point connection, the aggregate full crate bandwidth is
3404 16 GB/s giving plenty of headroom for FADC readout.

3405 **14.2.1 GEM readout**

The plan for readout of the GEM detectors is to use the CERN Scalable Readout System (SRS)
[295] which is based on the APV25 [296] front end chip. The APV25 chip is a shaper amplifier
circuit that samples 128 channels at 40 MHz, storing the most recent 192 samples of amplifier output
in a switched capacitor analog memory array. When a trigger is issued the corresponding slice in
time is frozen, allowing a look back in time of up to 4 μ s. With such a pipeline design, the system is
deadtimeless as long as the trigger rate is well under the 40 MHz sample rate. Readout of the chip
by the front end electronics is also done at 40 MHz. For each trigger 128 channels are readout with

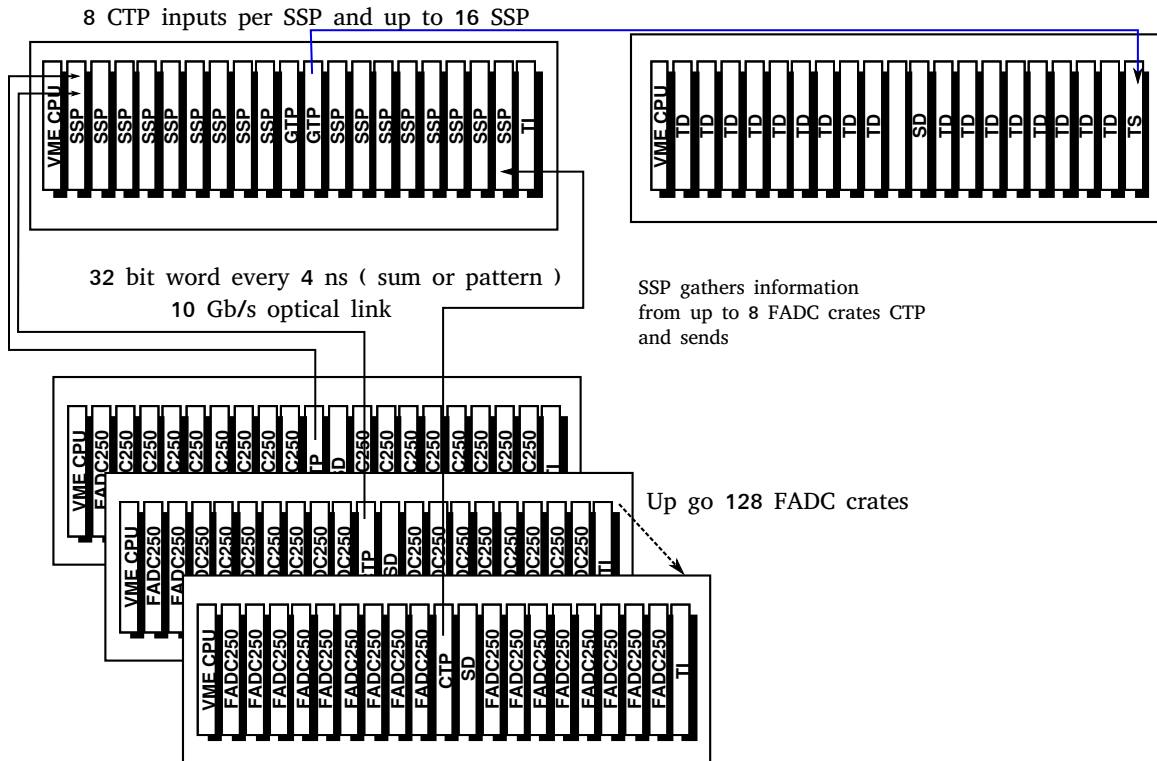


Figure 133: Standard Triggering scheme using the JLAB pipeline electronics

additional control signals making a total of 141 signals to be transferred. The chip has the ability to record 1 sample per trigger or 3 samples in case of high background. The signal is transferred in an analog form to the front end card where it is digitized by a flash ADC. In the case of one sample it will take :

$$141 * 25 = 3.6\mu s$$

3406 to transfer the data from the chip. This time is tripled to 10.6 us for 3 sample readout. This data
 3407 transfer rate is ultimately limiting the trigger rate capability of the chip to 91 kHz in 3 sample mode
 3408 and 280 kHz in single sample mode. All the data is digitized on the front end board with pedestal
 3409 subtraction and zero suppression.

3410 The SRS system, developed by the RD51 collaboration, gathers all the common high level
 3411 digital functions of a typical readout system : triggering, buffering, data transfer and event building.
 3412 To use the APV25, a chip specific adapter is needed. Such an adapter card is available which links to
 3413 the the hybrid board that holds the APV25 using HDMI cables. This card has 8 FADCs reading out
 3414 8 APVs chips, digitizing 2048 channels of detectors per board. These boards interface with the SRS
 3415 Front-End Card (FEC). The FEC card process the digitized data and can transfer the data directly to
 3416 a computer through Gigabit Ethernet. These FECs are mounted in Eurocrates which each can hold
 3417 up to 8 FECs. For larger systems, a Scalable Readout Unit (SRU) can be used to gather data from
 3418 multiple FECs. In this case data is transferred from the FEC to the SRU using a custom protocol
 3419 over standard CAT6 ethernet cables. The data gathered by the SRU is sent to a computer over 10
 3420 Gigabit Ethernet. As each FEC can communicate individually to a computer or a SRU, the system
 3421 is highly scalable and modular. As many FECs can be added as need to readout all the detector
 3422 channels.

3423 GEM readout systems based on the APV25 are currently in use at JLab (Heavy Photon Search,

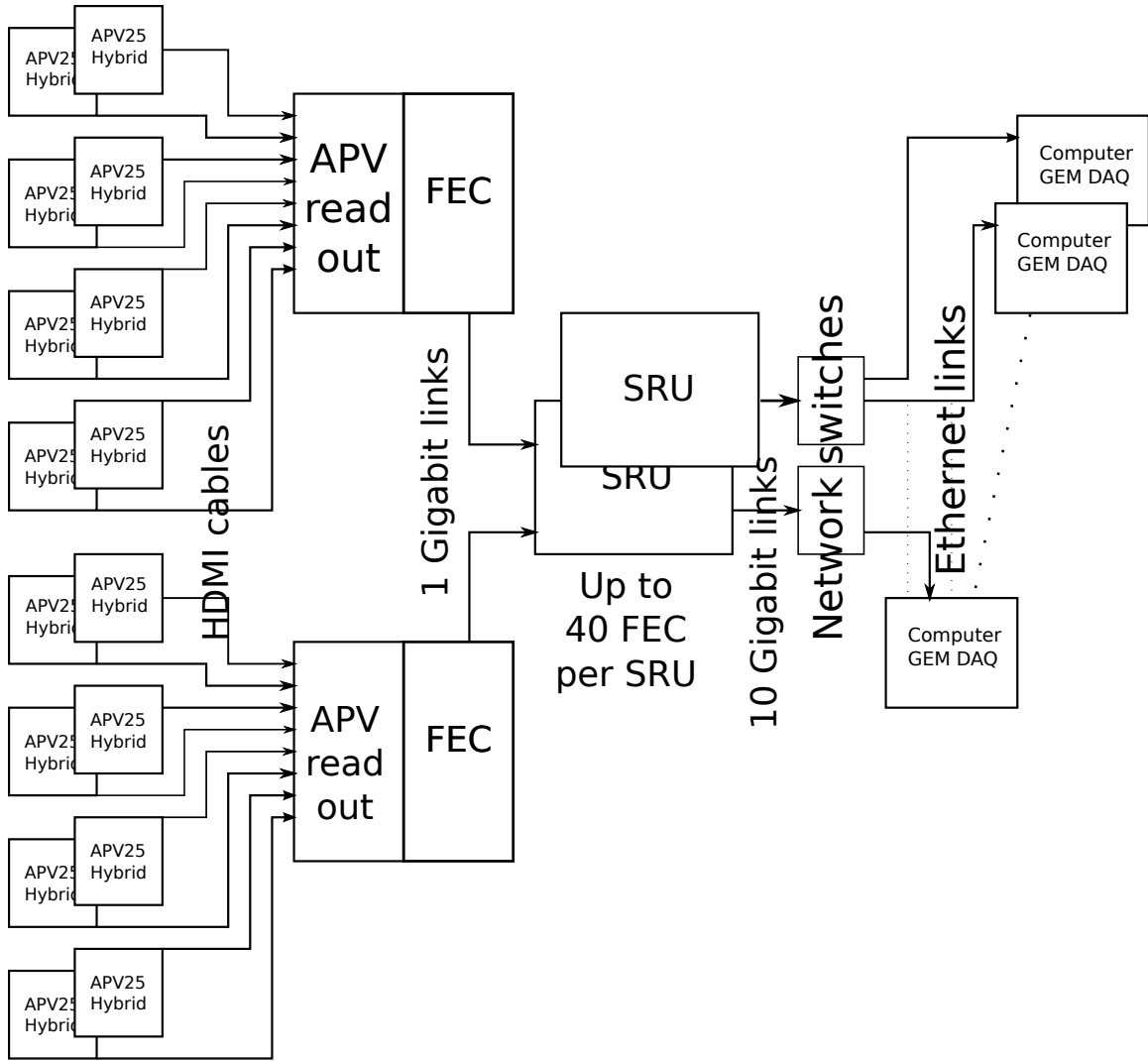


Figure 134: Standard SRS architecture which will be used for SIDIS experiment

3424 Proton Radius Experiment and the Super Bigbite Spectrometer). The experience with these exper-
 3425 iments indicates that a readout system based on the APV25 can be built that supports the trigger
 3426 and data rates required by SoLID. A variety of other GEM readout front end chips are under devel-
 3427 opment. The collaboration will monitor these developments for improvements in cost, performance
 3428 and DAQ rate.

3429 14.2.2 SIDIS Configuration

3430 The SIDIS experiment will use a similar detector setup as the PVDIS experiment with the addition
 3431 of more detectors. Scintillator planes will be used to reduce the photon background as the PVDIS
 3432 baffles will be removed. A Heavy Gas Cerenkov and a MRPC will be added for π/K separation.
 3433 The PVDIS crates will serve as the basis of the SIDIS DAQ, but the signals from the VTP will
 3434 be sent to the SSP and GTP in an additional crate to make a coincidence trigger. The additional
 3435 detectors will be instrumented with FADCs for the Heavy Gas Cerenkov and TDCs for the MRPC.

3436 Based on our current simulation, the size of each event is expected to be about 3.1 kByte includ-

Detector	Channel
EC Shower	1800
EC Preshower	1800
SPD	300
Light Gas Cerenkov	270
Heavy Gas Cerenkov	480
MRPC	3300

Table 29: Detector channel counts for the SIDIS and J/Ψ experiments, excluding the GEMs.

3437 ing signals from all detectors. So the 155.5 kHz singles rate and 68 kHz coincidence rate for SIDIS
 3438 ^3He will correspond to 482 MB/s and 210 MB/s aggregate DAQ rates over the 30 sub-crates.
 3439 The SIDIS experiment trigger formula is

3440 **forward angle electron trigger** Forward Angle Calorimeter *AND* Light Gas Cherenkov *AND* SPD
 3441 *AND* MRPC

3442 **large angle electron trigger** Large Angle Calorimeter *AND* SPD

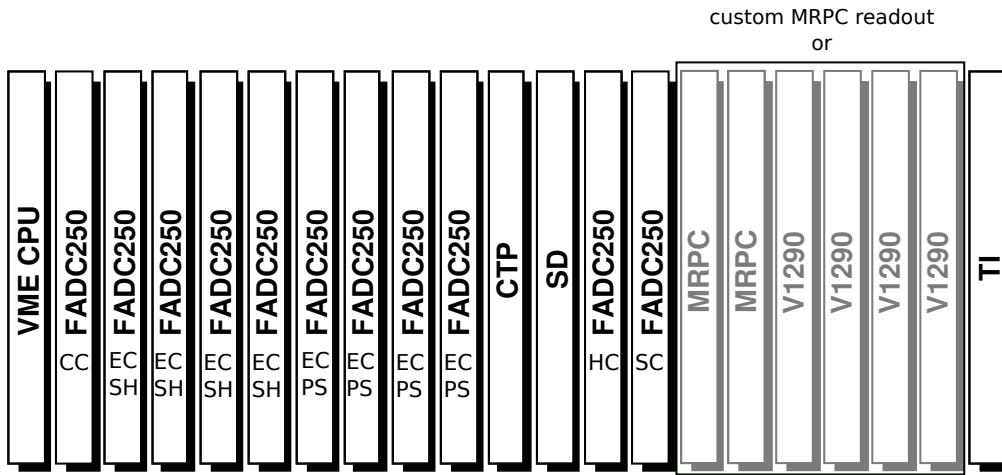
3443 **forward angle charged particle trigger** Forward Angle Calorimeter *AND* SPD *AND* MRPC

3444 **coincidence** electron trigger (large *OR* forward) *AND* forward angle charged particle trigger

3445 The SIDIS experiment and J/Ψ will use the same detector configuration, cabling, DAQ and
 3446 trigger hardware. The only difference is that the DAQ will be configured to trigger on a high energy
 3447 electron and a pion for SIDIS while for J/Ψ it will trigger on 3 high energy leptons.

3448 **MRPC readout** The current plan for MRPC readout is to develop a custom electronics module for
 3449 the readout of the 1550 MRPC strips. It will be a custom designed TDC that digitizes 3300 channels
 3450 of MRPC. (Strips are readout at both ends.) The baseline solution will be to use a chip similar to the
 3451 NINO chip which is an amplifier discriminator chip. This chip generates a discriminated signal with
 3452 a time resolution on the order of 10 ps with a logic output width proportional to the time the pulse
 3453 is above threshold which allows amplitude information for time walk correction. In order to include
 3454 the MRPC in the trigger, a new module, VETROC board, was developed by the JLAB electronics
 3455 group.

3456 **SIDIS GEM rates** As the DAQ for the SIDIS experiments can not be segmented in to a separate
 3457 DAQ chain for each sector, the event size is an important factor in keeping the DAQ throughput
 3458 below limits to the overall data rate that can be recorded. The occupancy of the detector is fairly low
 3459 when using the on-board deconvolution which is the default running mode for SIDIS. By reading in
 3460 one sample mode with deconvolution, we expect the allowed trigger rate to be about 200 kHz which
 3461 is very close to the theoretical limit of 270 kHz. But in trigger design for the SIDIS experiment, we
 3462 put an additional safety factor of 0.5 to further reduce the allowed trigger rate to 100 kHz to tolerate
 3463 any uncertainties in our rate estimation. We are planning to use a SRU to concentrate the signal
 3464 from the SRS FEC, this module gathers all the FEC signals and send the data to a 10 Gbit Ethernet
 3465 port which means around 1.2 GB/s. To have a safety margin a second SRU will be added for an
 3466 additional \$4000 in case occupancies happen to be much higher than expected from Simulation.



Optical link 10 Gbps
1250 MB/s

Figure 135: SIDIS FADC crate layout

Chamber	Hits	Hits > 200	Hits with deconvolution
0	510	150	30
1	1890	450	60
2	1020	270	30
3	870	240	30
4	810	180	30
Total hits	5880	1470	210
Naive occupancy(%)	4.1	1.04	0.1
Event size 1 sample (Kbytes)	34.32	8.88	1.2
Data rates 100 kHz (Mb/s)	3432	888	120

Table 30: SIDIS GEM occupancies and event size for GEM

Table 31: Channel counts of individual detectors for PVDIS for one sector

Detector	Module Type	Number of Channels	Number of Modules
Electromagnetic Calorimeter (EC)	FADC	122	8
Light Gas Cherenkov (GC)	FADC	9	1
GEM	SRS	4700	1

3467 14.2.3 PVDIS Configuration

3468 **Calorimeter trigger for PVDIS** There are currently two options to generate a Level-1 (L1) trig-
3469 ger from the calorimeter. The standard option is to use the sum of the 16 FADC channels which is
3470 computed and sent to the VTP every 4 ns. The VTP can add all the FADC sums, generating a global
3471 sum for each crate and generating a trigger when that sum exceeds a threshold. Another scheme
3472 was devised for the Heavy Photon Search experiment in Hall B. In this scheme 16 bits of data for
3473 each of the 16 FADC channels is sent every 32 ns as in Fig. 138. These data contains both the signal
3474 amplitude, and the timing (to a 4 ns resolution) of any threshold crossing. With the VTP receiving a
3475 signal from all the calorimeter element, it can compute the signal sum, in parallel, of every possible
3476 3×3 cluster of one central and 6 surrounding blocks. This approach of triggering on the cluster
3477 sum can reduce the number of triggers coming from background and improve online pion rejection.

3478 Particles near the edge of a sector will likely shower into calorimeter blocks in the adjacent
3479 sector. In order to avoid inefficiencies near the edges of sectors, VTPs for neighboring sectors will
3480 share information through bidirectional optical links as shown in Fig. 137. Once the VTP receives
3481 all the FADC data from its own crate and the two adjacent crates, it either computes the total sum or
3482 performs cluster searching to generate trigger. If the cluster trigger method is used, a 64 bit pattern
3483 containing the FADC channels to be readout will be generated by the VTP and transferred to the
3484 Flash ADC using the trigger data path. A new firmware for the FADC will be developed to take this
3485 pattern into account allowing each FADC to only read the channels that are part of a cluster in order
3486 reduce event sizes.

3487 **Gas Cerenkov trigger** Both Cerenkov detectors are divided into 30 sectors. The most straightfor-
3488 ward way to generate a Cerenkov trigger is to put all the channels of a given sector (9 for the light
3489 gas and 16 for the heavy gas) into one FADC board and generate the trigger in the VTP by putting
3490 a threshold on the sum of the PMT signals. To improve efficiency at interface between two sectors
3491 one can put the threshold on the sum of two adjacent sectors. If the combinatory background is too
3492 large, a clustering scheme similar to that discussed for calorimeter could be used. The efficiency
3493 and background of the different schemes has been evaluated in the full simulation of the digitized
3494 background. This simulation shows that a simple trigger based on PMTs sums works and has a
3495 sufficient efficiency.

3496 In order to estimate the per event size of data from the GEMs, the GEM signal and the APV25
3497 digitization process were modeled in a simulation. This simulation is detailed in the simulation
3498 section 12.2.4 of this document. The total number of GEM strips firing in a 25 ns window was
3499 computed in three different ways: one way included all hits having non zero energy, another used
3500 an arbitrary ADC threshold of 200, while the third was obtained by simulating the on chip deconvo-
3501 lution algorithm 12.2.4 in addition to the threshold of 200. The last column are the results coming
3502 from the GEM digitization Section 18. An optimization of the threshold with the background level
3503 and tracking efficiency will be done once the full simulation including background and tracking
3504 analyzing framework is ready.

3505 **PVDIS GEM rates** For PVDIS, we are interested in the data rate per sector. The numbers will
3506 be evaluated for 30 kHz (20 kHz rate + 50% safety margin). One can conclude that even if the
3507 occupancy is high, the data rates are manageable for PVDIS. The deconvolution and filtering are
3508 able to significantly reduce the occupancy and event size. We will plan to read out 3 samples to be
3509 able to do more treatment of the data offline in case the on chip deconvolution is affected by the
3510 high level of background. Using the SRS system, each FEC can transfer 1Gbps through its Ethernet
3511 link. Each sector has about 4700 strips so will need at least 3 FEC, by using an additional FEC, one

Chamber	Hits	Hits>200	Hits with deconvolution	Offline treatment
0	316	199	23	160
1	303	147	12	116
2	283	107	9.4	104
3	280	102	8.9	72
Total hits	1182	555	53.3	452
Naive occupancy(%)	25.2	11.8	1.2	9.6
Event size 1 samples (Kbytes)	9.47	4.44	0.432	1.5
Event size 3 samples (Kbytes)	28.39	13.32	1.296	6.1
Data rates 20 kHz 3 samples (Mb/s)	567.84	266.4	25.92	30.6

Table 32: PVDIS GEM occupancies and event size for GEM

3512 can insure a 500 MB/s transfer rate. Each dedicated computer to will have 4 Gigabit Ethernet port
3513 and one 10 GigE Ethernet port to send the data to the L3 farm allowing transfers up to 500 MB/s
3514 which should be sufficient. We expect the combination of shower and PID cut in association with
3515 crude tracking to give us the factor of 4 data reduction needed. Testing of online data reduction will
3516 be studied using the simulation data we generated.

3517 14.3 Event size from FADC

3518 The FADC samples are 12 bit at 250 MHz. In the case of PVDIS, since pile up is going to be
3519 significant, we plan to record all the waveform. The pulse signal is 40 ns wide, so we will be
3520 recording 10 samples for each detector channel. The event size per channels is per FADC : 4 bytes
3521 for block header, 4 bytes block trailer, 4 bytes for event header and two samples are packed in a 4
3522 bytes word. For 10 samples each event is then $(12 + n * 10 / 2 * 4)$ bytes with n the number of
3523 channels firing.

3524 The FADC simulation with digitization is still being developed. Given the size of a sector,
3525 the event size will be estimated with a maximum of 2 clusters of 7 for shower and 2 clusters of 3
3526 preshower and assuming all 9 PMTs of the Cerenkov fire all the time. With this assumption the
3527 event size is 1160 bytes per event.

3528 With the trigger rate of 20 kHz, this gives 23.2 MB/s data rate. As far as data rate are concerned
3529 VME320 backplane can transfer up to 200 MB/s.

3530 In the case of SIDIS, the occupancy on the detector is small enough to only record the integral
3531 of the pulses, the estimated event size using the occupancies from the simulation is 1.9 KBytes,
3532 which gives an aggregated data rate of 187 MB/s at 100 kHz for all 30 crate.

3533 14.4 Data rates,event size and L3 Farm

Experiment	Event Size (kBytes)	L1 trig Rate (kHz)	L3 Data in Rate MByte/sec
PVDIS	47.76	20	955.2
SIDIS	3.1	100	310
JPsi	2.58	3	7.74

3535 The L3 Farm will provide data reduction before putting it on tape since the amount of data generated
3536 by the electronics can be very large especially for the PVDIS experiment where the full waveform
3537 is recorded.

3538 The trigger rate per sector in coincidence will be about 20 kHz per sector so L3 farm will be
3539 designed to handle 30 kHz to have a safety margin.

3540 In addition to L1 trigger which is based on the FADC information, the L3 Farm will do crude
3541 and quick reconstruction giving access to momentum.

3542 The data reduction strategy will be based on regions of interest by correlating GEM information
3543 with calorimeter position and doing crude tracking. This should significantly reduce the GEM data
3544 by discarding random hits. The timing will be refined by computing the time walk effect and taking
3545 into account path length and momentum corrections. One can expect a resolution of the order of
3546 one nanosecond but to be conservative we will assume 10 ns for the data reduction estimates which
3547 giving a factor of 3 reduction which already satisfies the limit of 250 MBytes/s put on tape.

3548 The Flash ADC data will be further reduced by clustering on the calorimeter, considering the
3549 energy sharing between blocks we can expect a factor of 2 of reduction.

3550 The simulation is being developed to generate digitized data including background. Once the
3551 full simulation is complete the different algorithm speed will be evaluated.

3552 In order to have a first estimate of the processing, we will use the Hall D estimate for the
3553 L3 tracking. The Hall D forward detector has 24 detectors layers with 96 wires per plane and 3
3554 readout channels per plane for a total of 6912 channels of tracker and 2800 channels of lead glass
3555 calorimeter. With wire based tracking, the speed of reconstruction is 27 Hz per CPU. Without
3556 tracking, the L3 trigger speed triples to 77 Hz. Each sector for PVDIS has about 4700 GEMs strips
3557 for 61 calorimeter blocks. Given the higher background and 3 samples treatment, a slightly lower
3558 speed for tracking of 20 Hz is assumed. Given the fewer number of blocks, the non tracking speed
3559 should be faster but 77 Hz will be assumed for now.

3560 Assuming a rate of 30 kHz per sector for PVDIS, we would require 1500 CPUs with tracking
3561 and 390 CPUs without wired base tracking.

3562

3563 **14.5 Hall DAQ installation**

3564 The DAQ for both the SIDIS and PVDIS configurations will be located in the hall. As is typically
3565 done, a shielded bunker will be constructed to house the data acquisition electronics, protecting it
3566 from beam induced radiation. This bunker will contain ~ 15 racks containing 32 VXS crates and
3567 the crates containing the GEM front-end cards.

3568 Approximately 4500 coaxial cables (RG58) will connect the PMT based detectors to the ADCs
3569 in the bunker. Additionally, ~ 200 ribbon cables will connect the MRPC discriminators to also in
3570 the bunker and HDMI cables will connect the detector mounted GEM chips to the front end cards.

3571 **14.5.1 Experiment switch over**

3572 Switch over of the DAQ electronics between the PVDIS and SIDIS setups will be relatively straight-
3573 forward. Changing to the PVDIS setup, the VTP module in each sector's crate will connect directly
3574 to the TI module in that crate to give an L1 trigger signal for that crate and the corresponding GEM
3575 electronics. The unused SSP, TD and TS, and GTP modules as well as ADC and TDC modules for
3576 detectors not in PVDIS will be removed from the hall to avoid extra radiation dose.

3577 **14.6 Managing data rates**

3578 Managing total data rates for SoLID will require careful system design to avoid bottlenecks. While
3579 the PVDIS configuration has the highest overall trigger and data rate, the segmentation of SoLID

3580 into 30 nearly independent sectors allows for natural parallelization. The data rate per sector is a few
3581 hundred MB/s. The parallel data paths can be preserved through the event builder (that combines
3582 VME and GEM data), to temporary disk storage, through parallel network paths, and through an L3
3583 farm before merging into a smaller number of paths for storage on tape.

3584 The SIDIS configuration is more challenging as the data for each event which is spread over
3585 30 VME systems and 30 sectors of GEMs must be combined to build events. It is presently not
3586 feasible to build and events from these 60 sources into single data stream of over 3 GB/s. This can
3587 be overcome with the option in CODA of multiplexing events to multiple event builders. A possible
3588 architecture would have up to 60 ROCs pushing data to several primary event builders so that each
3589 event builder handles a more modest data rate. (One event builder for the VME crates and several
3590 event builders for the GEM data.) Each of these primary event builders, which contain a fraction of
3591 each event, would feed, in round robin fashion, several secondary event builders. Each secondary
3592 event builder would build complete events, but only have a fraction of a given runs events saved
3593 to its disk cache. This architecture is scalable such that bottlenecks can be mitigated by using a
3594 sufficient number of primary and secondary event builders.

3595 **14.7 Summary and Pre R&D plans**

3596 The conceptual design of the SoLID data acquisition system is based on hardware that has all ready
3597 seen use with beam at JLab. While SoLID's trigger rate and total data rate exceed what has been
3598 achieved by detectors such as GlueX and HPS, it expected that it is feasible to meet the requirements
3599 with careful system design, hardware firmware improvements and upgrades to the CODA software.
3600 The DAQ component of the SoLID Pre R&D will serve to understand the capability and limitations
3601 of the conceptually designed system. Some of the specific items to address in Pre R&D include:

- 3602 • Test single VXS crate to acquire data at 100 kHz.
- 3603 • Test acquisition of GEM data from one sector at 100 kHz with data rate of 100 MB/sec.
- 3604 • Mockup 60 ROC system and multiple event builders and establish ability to handle throughput
3605 of 4GB/sec at 100 kHz trigger rate.
- 3606 • Provide prototype small scale DAQ system for detector beam tests.
- 3607 • Test trigger and data sharing scheme between adjacent sector PVDIS DAQ systems.

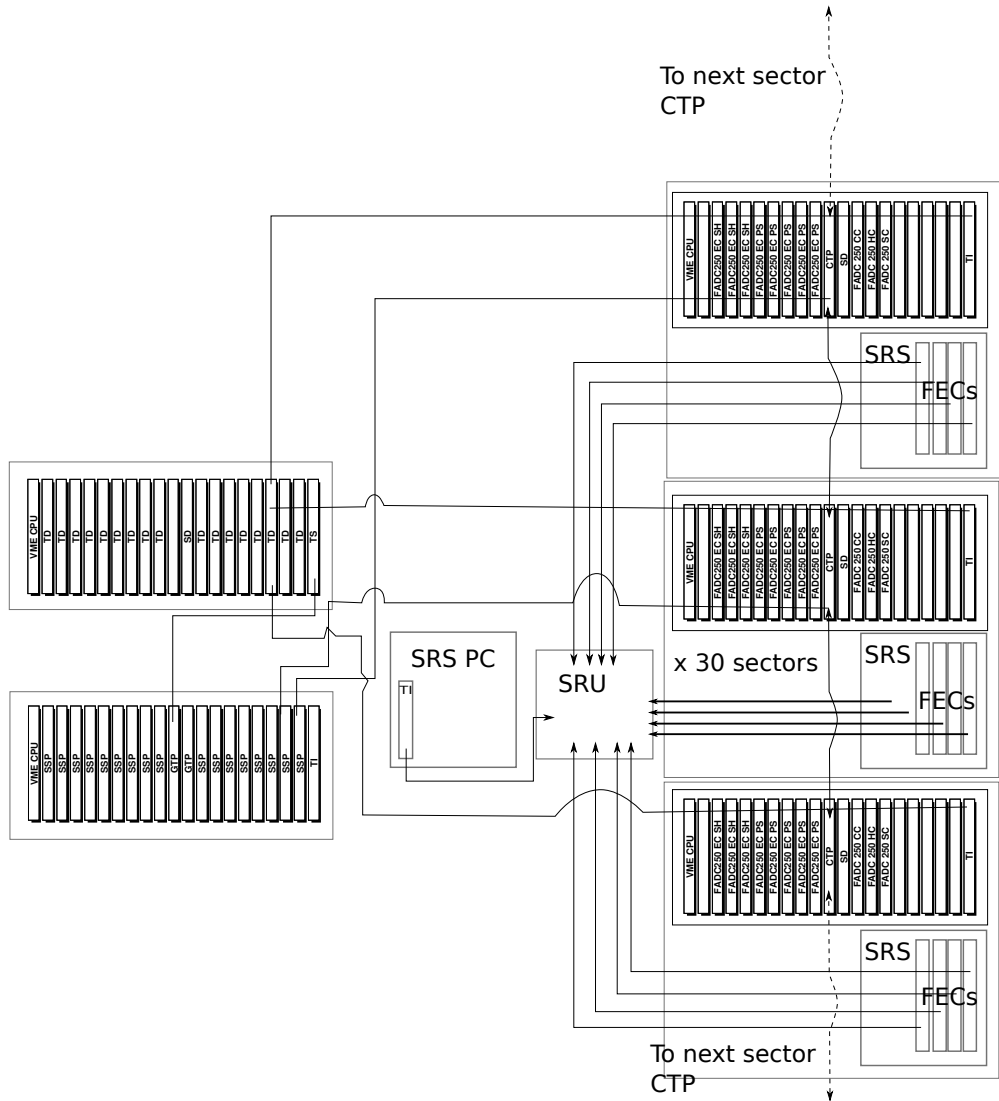


Figure 136: SIDIS DAQ overview

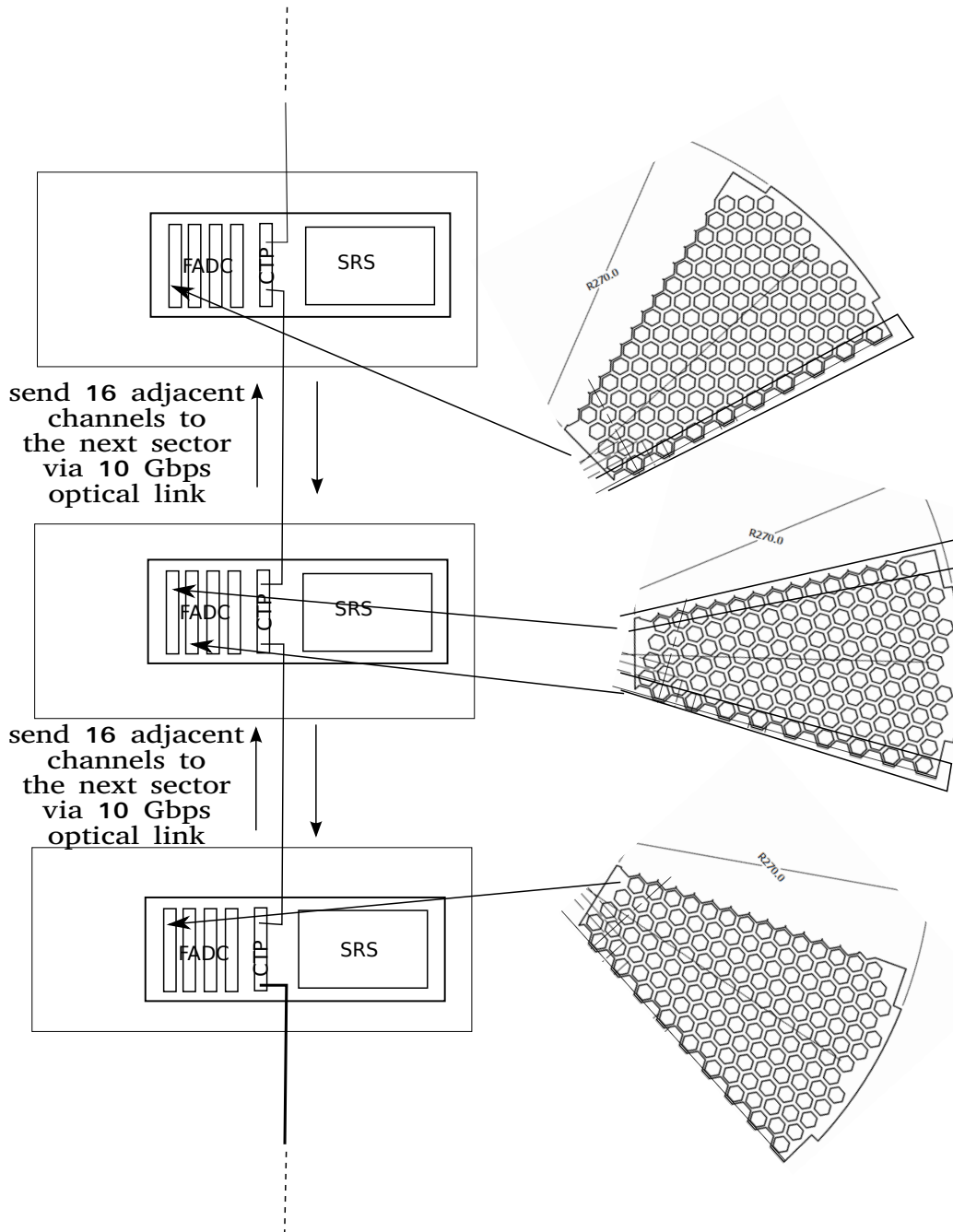


Figure 137: PVDIS specific electron trigger

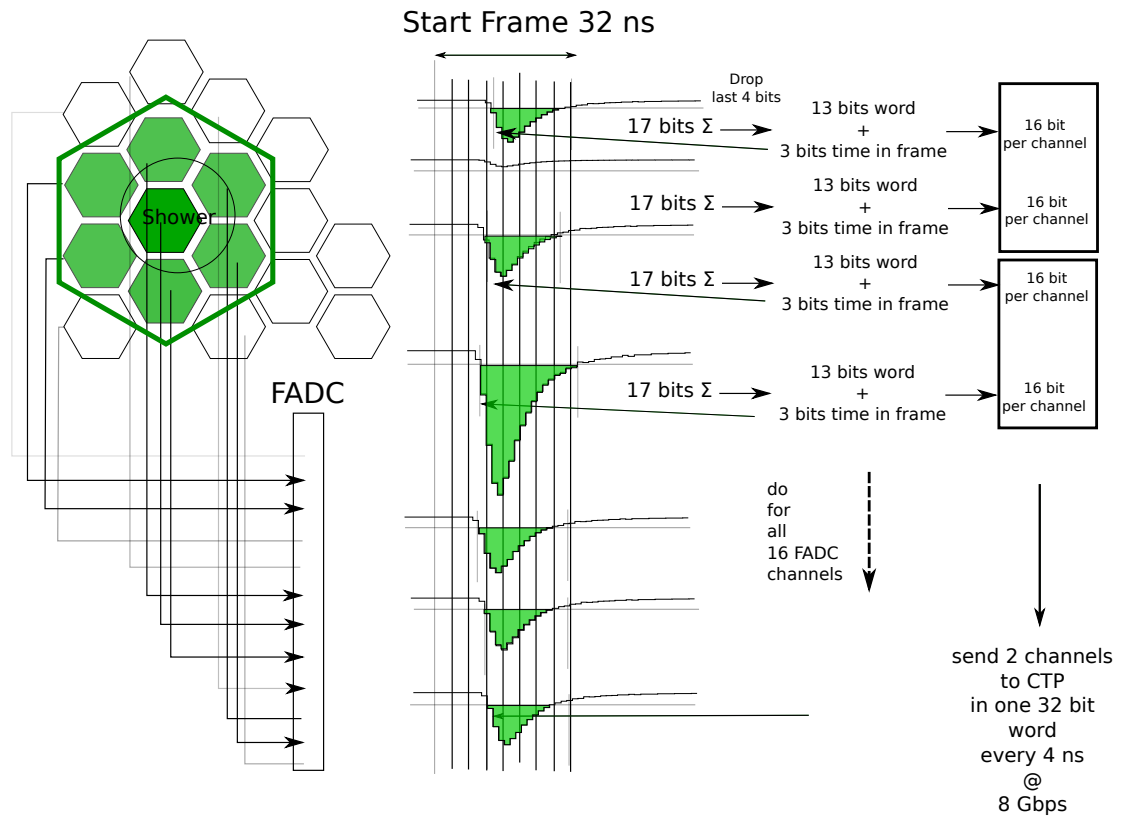


Figure 138: Calorimeter clustering scheme using the HPS algorithm. All calorimeter signals are sent to the FADC.

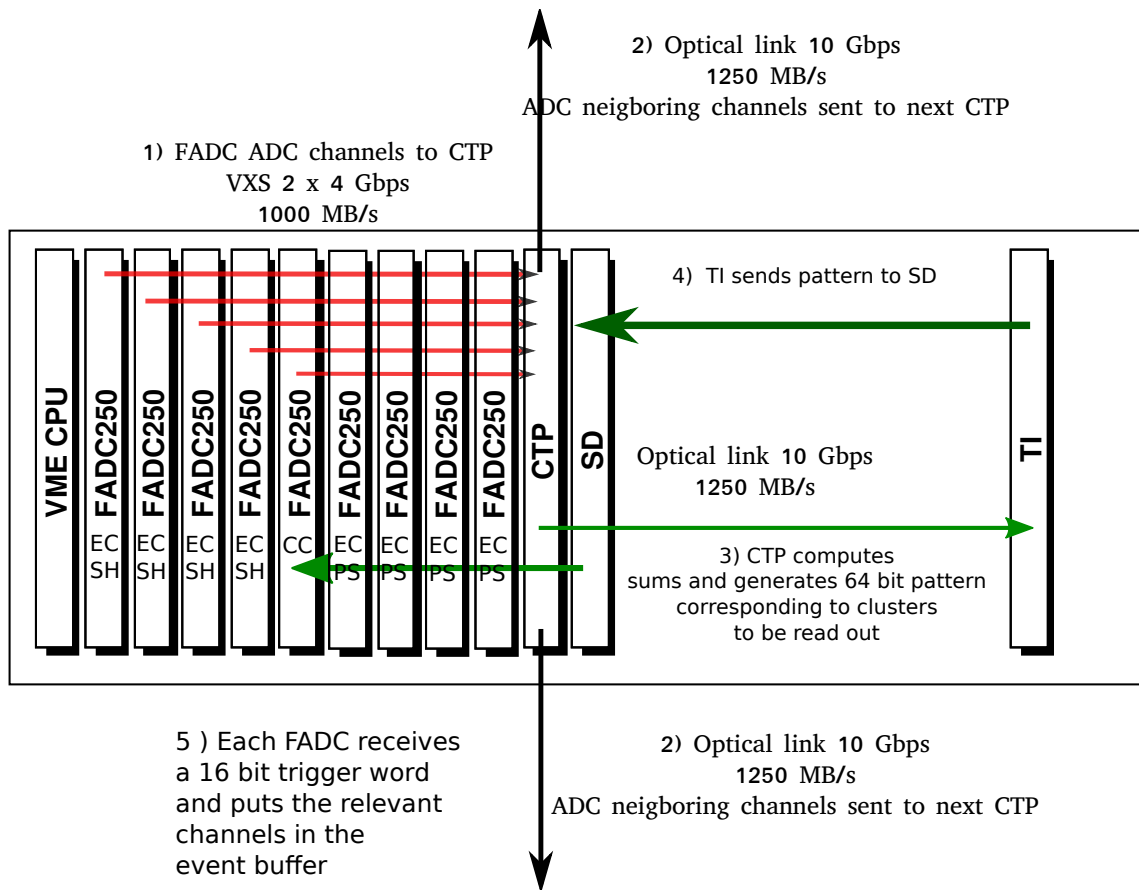
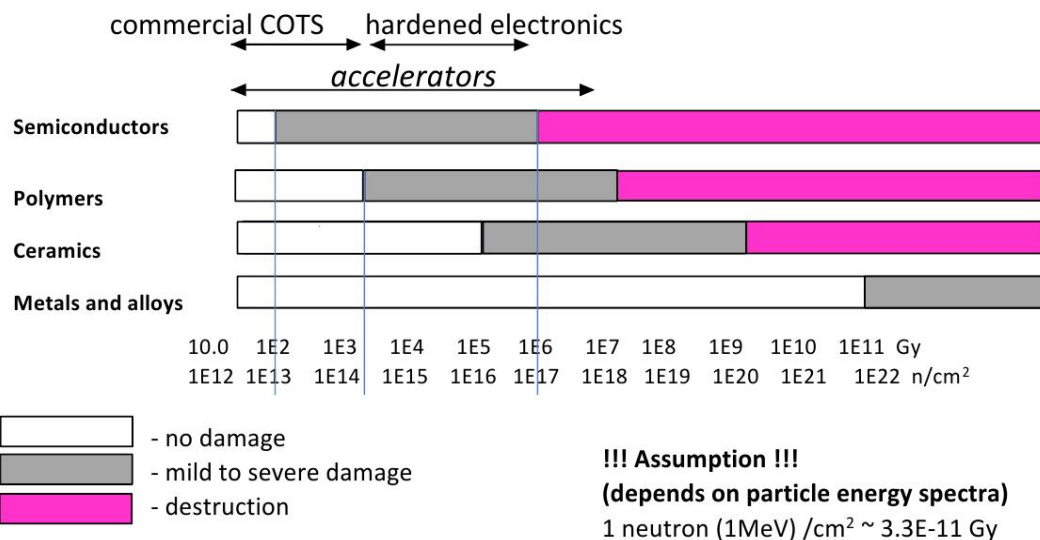


Figure 139: PVDIS FADC crate layout

3608 **15 Radiation damage estimates and Activation**

3609 The simulation and background calculation software for SoLID is using the two simulation packages
 3610 with independent code base (Geant4 and FLUKA [299] [300]). This allows independent cross
 3611 checks both in geometry and in physics modeling. At the same time the two codes each provide
 3612 unique capabilities expanding the overall reach. FLUKA provides useful tools that simplify the
 3613 study of radiation damage and estimates but the physics processes present in the simulation lack
 3614 of direct electro-nuclear dissociation and fragmentation models. Such electro-nuclear reactions are
 3615 dominant in the neutron production from the Liq.D target at high energies (see figure 145). If one
 3616 just considers the neutron photo-production, both codes (GEANT4 and FLUKA) have really good
 3617 agreement with experimental cross section, as shown in figure 143 and 144. A full simulation and
 3618 tests are underway in order to construct a better and common target background generator for both
 3619 simulation packages (see figure 145). To have a first idea of the tolerance of different material to
 radiation damage, see figure 140. As a weighting factor to estimate the effect of radiation damage on



© Lockheed Martin

Figure 140: Estimate of the tolerance of different material to different level of radiation exposure given in Gy and $\frac{neutron(1MeV)}{cm^2}$. This is just a first order approximation and a detailed analysis of each equipment is needed in order to establish the correct radiation tolerance of each detector/material

3620 electronics I used, in parallel to the calculation of full Dose estimates, the Displacement damage in
 3621 silicon, on-line compilation curves by A. Vasilescu (INPE Bucharest) and G. Lindstroem (University
 3622 of Hamburg). This curves assume that the damage effects by energetic particles in the bulk of any
 3623 material can be described as being proportional to the so called Non Ionizing Energy Loss and
 3624 normalize the damage in Silicon to the one caused by a 1 MeV neutron (more details can be found
 3625 here [302]).
 3626

3627 **15.1 Radiation damage to GEM electronics**

3628 A simulation in order to test the radiation level on the GEM foils has been done. Comparison to
 3629 estimated radiation level of the CMS experiment, which shares the part of the electronics most sus-

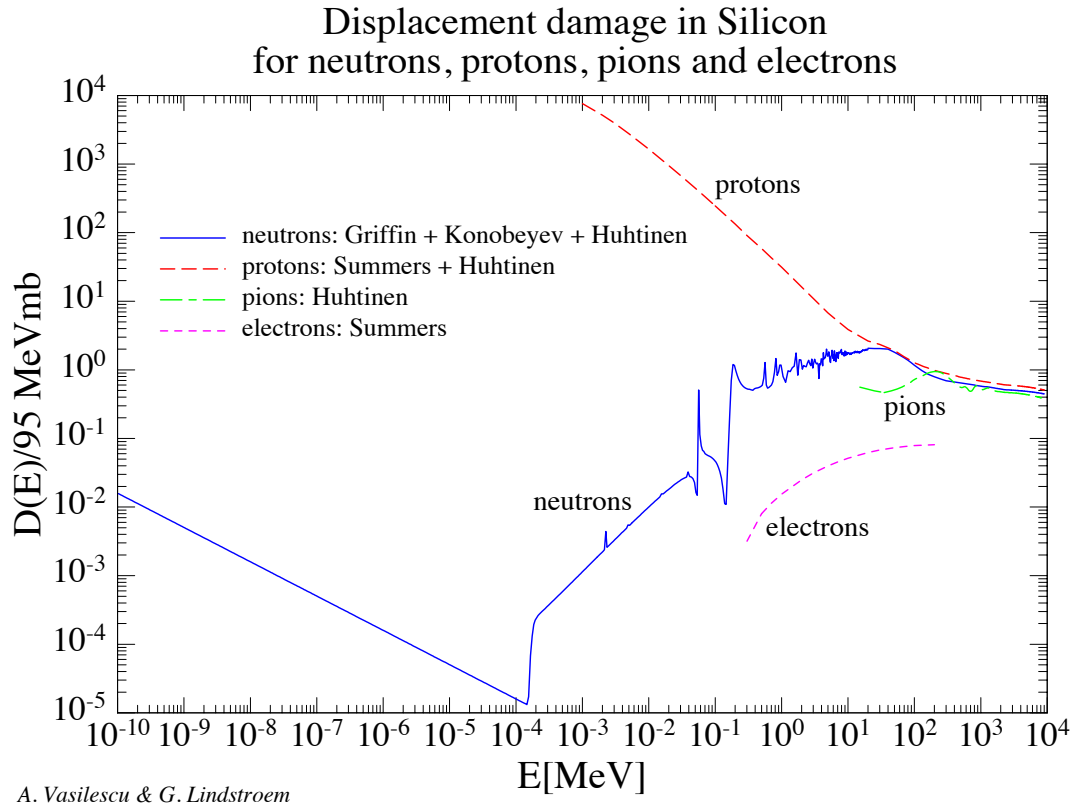


Figure 141: Not Ionizing Energy Loss curves to 1MeV equivalent damage in Silicon for electrons, pions, neutrons and protons

3630 ceptible to radiation damage for the GEM chambers detectors, permitted us to establish a radiation
 3631 limit flux for our expected running time. Already with our first conceptual design of the shielding
 3632 we are able to reach tolerable radiation levels also in the first layer of the GEM chambers (the one
 3633 that is supposed to sustain the higher radiation fluxes). This result is show in figure 146

3634 15.2 Power deposited

3635 A detailed study of the power deposited in the SoLID spectrometer has been done in order to detect
 3636 areas of possible activation. In these areas, in order to define possible activations, the FLUKA sim-
 3637 ulation has been used as a tool, and particle fluxes were provided by GEANT4 for areas where was
 3638 the particle fluxes estimated by FLUKA were known to be incorrect. FLUKA in fact provides many
 3639 good tools for activation and radiation estimates, but lacks in direct electro-nuclear dissociation-
 3640 fragmentation models and has limitations in producing more complex geometry, like the Baffle
 3641 design for the PVDIS experiment in SoLID. In the following study of activation, GEANT4 has
 3642 been used as a common input for an estimate of the background radiation in areas where direct
 3643 electro-nuclear dissociation-fragmentation models are important.

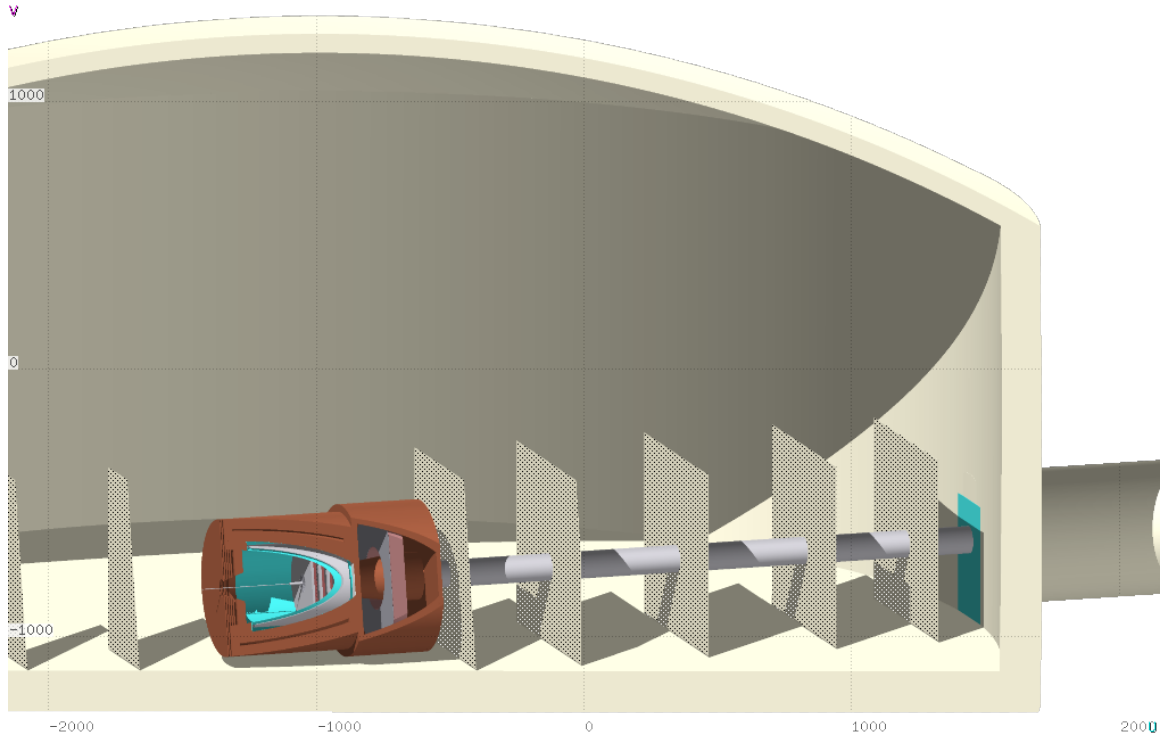


Figure 142: FLUKA simulation for the PVDIS experiment with SoLID.

3644 **15.2.1 Power in 1st baffle (due to Möllers), (Cooling, activation)**

3645 The first baffle, due to his proximity to the Deuterium target in the PVDIS configuration for SoLID,
 3646 has a power deposition of $\sim 8W$ for a beam current of $50\mu A$ and an energy of $6.6GeV$. The high
 3647 production of neutrons from the Deuterium target can be an ulterior source for activation in the
 3648 baffle. For this reason an investigation of the possible activation has been done. In this study has
 3649 been considered at the same time the radiation coming from the target and from the baffle itself
 3650 that “self-irradiate” different parts of its structure. The impact of Activation due to the utilization
 3651 of different materials have been directly studied (see 147 for the first baffle: In order to optimize
 3652 the computing time and avoid issues of pixelization due to the detailed shape of the baffle, a single
 3653 block of material was used in this study. Since the solid angle coverage seen by the main source of
 3654 radiation (the target) of the baffle used in this study is not the same, the radiation calculated should
 3655 be scaled accordingly or used as an extra safety factor due to our relying just on simulations.

3656 These results (see show the Dose equivalent radiation spatial distribution for 3 different cooling
 3657 times. This study (see figure 147) shows, for example, that, in order to survey the area in proximity
 3658 of the first baffle, one should wait around 1 day of cooling, in order to reach level of radiation
 3659 tolerable. The Residual nuclei activated in the Lead baffle are shown for the same cooling time in
 3660 the bottom plots of figure 148.

3661 **15.2.2 Power in exit hole in magnet (elastics) (Cooling, activation)**

3662 Another spot for possible activation will be the part close to the exit hole of the magnet. Further
 3663 investigation will need to be done, after a final design of the magnet will be reached, but it is
 3664 expected to be less important than the activation on the first baffle, due to the not proximity to the
 3665 target and to the less intense and less localize radiation. This situation has been investigated and

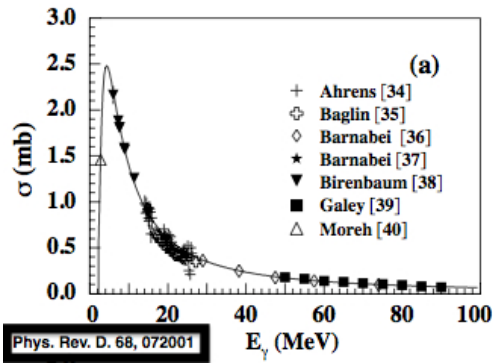


Figure 143: Neutron cross section for photo-production [301]

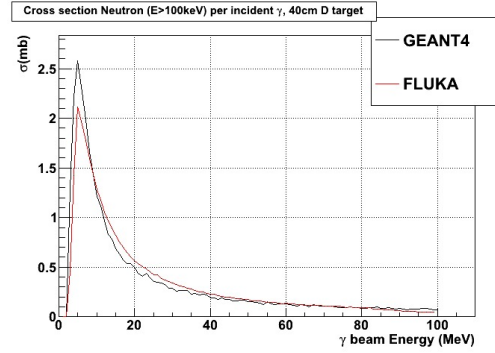


Figure 144: Test for Neutron cross section for photo-production with FLUKA and GEANT4

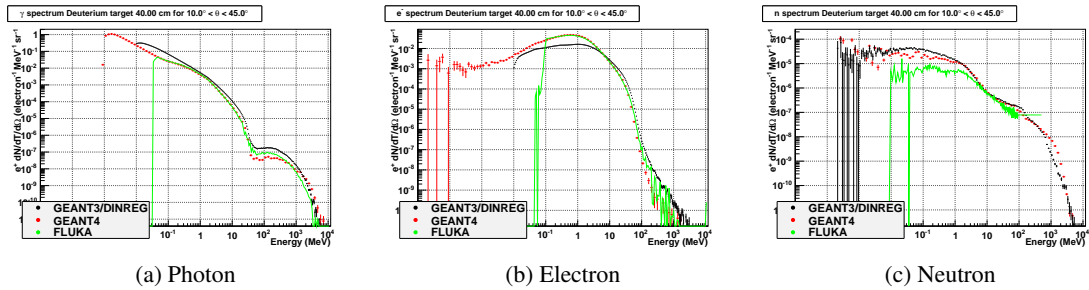
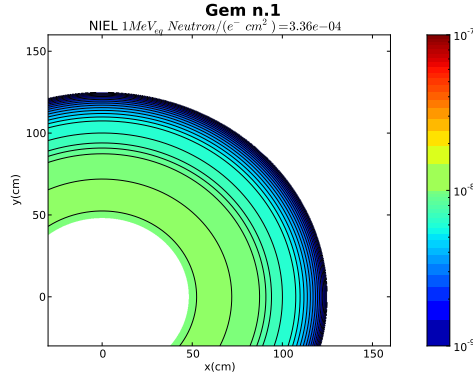


Figure 145: Background comparison produced from GEANT3(DINREG), GEANT4 and FLUKA with 40cm of Liquid Deuterium. Here is plotted the $\frac{d^2N}{dTd\Omega}$ per incoming electron in the angle range of $10^\circ < \theta < 45^\circ$ for γ (a), e^- (b) and n (c)

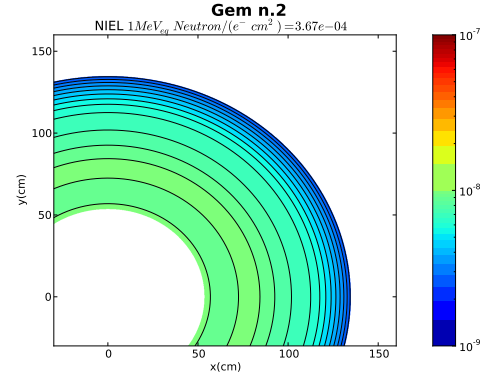
3666 compared to the PVDIS design, because it is the one with the expected higher activation of all the
 3667 configuration with SoLID, with the proximity of the lead baffles to the target (see this section at
 3668 page 180). This has been done in order to compare power deposition to have a first idea of possible
 3669 activation areas. The levels of power deposited in the exit hole of the magnet are at least lower
 3670 by one order of magnitude respect to the one expected in the first baffle, as shown in figure 149a
 3671 and 149b. The integrated value (using the cylindrical symmetry) over the higher area of power
 3672 deposition in the exit hole of the magnet has a maximum of $\sim 0.9W$ per cm in the z direction
 3673 over the full internal section of the exit hole with $r_{xy} < 40cm$ (color scale of $\sim 3E - 04$ in figure
 3674 149a). This compares to a full power deposition on the first baffle of $\sim 20W$, running in the same
 3675 conditions. A power deposition estimate for the beam-line downstream is shown in figure 149b.
 3676 As one can see in 150c, is considerably smaller the impact of the configurations like SIDIS to the
 3677 activation in this area.

3678 15.2.3 Power in the entrance surface of the magnet (Cooling, activation) (external target 3679 configurations)

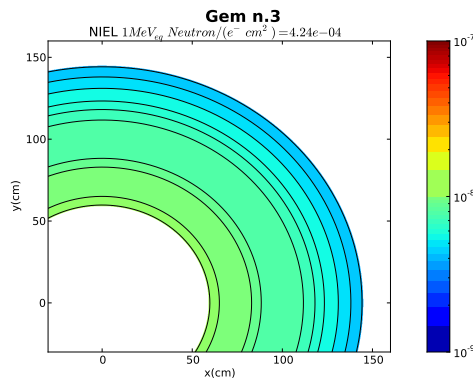
3680 With configuration like SIDIS that have the target positioned outside the magnet, there is a consistent
 3681 power deposition in the front part of the magnet. Some simulation has been done in order to estimate
 3682 the possible activation in this area. The results of these studies are presented in figure 150 and show
 3683 the areas of power deposition in the magnet and in the front surface of the magnet. As expected



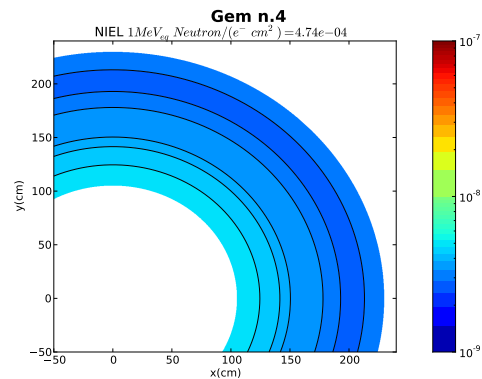
(a) NIEL weighted 1MeV equivalent neutron flux per cm^2 per incident electron on the 1st GEM foil



(c) NIEL weighted 1MeV equivalent neutron flux per cm^2 per incident electron on the 2nd GEM foil



(b) NIEL weighted 1MeV neutron equivalent neutron flux per cm^2 per incident electron on the 3rd GEM foil



(d) NIEL weighted 1MeV equivalent neutron flux per cm^2 per incident electron on the 4th GEM foil

Figure 146: The CMS experiment dose rates are expected to be of the order of 10 MRad(SiO_2) ($5 \times 10^{13} \frac{n}{cm^2}$). This translate for us, assuming 2000 hours of beam at $100\mu A$, in a flux of $\sim 1.1 \times 10^{-8} \frac{1MeVeqn}{e^-cm^2}$. This put us on the same level of radiation that the APV25 chip was built to tolerate

3684 the areas of possible activation is the area more exposed to the target radiation and the collimator
3685 positioned in front of the nose-cone of the magnet.

3686 15.2.4 Heat load in magnet cryostat

3687 A detailed design of the Cryogens and coils of the CLEO II solenoid has been obtained and was
3688 constructed a detailed model that replicates key components of the magnet (see Fig.151). Particular
3689 attention was put in well represent:

- 3690 1. the 3-5 mm of stainless steel which is the inner bore of the cryostat
- 3691 2. the 3-5 mm of aluminum thermal shield 3-5 cm beyond (1)
- 3692 3. the 6+ mm of stainless steel which is the helium vessel
- 3693 4. any winding forms left at the inner diameter of the coils

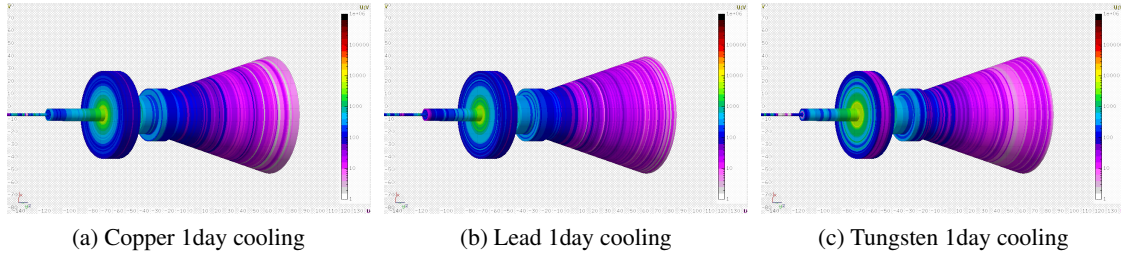


Figure 147: First Baffle: Activation study has been calculated for 3 different Cooling times (here is just shown after 1day), after an assumed exposure to the beam of 3 separate full weeks interleaved by a down time of 4 days. (147a, 147b,147c) The dose is expressed in $mrem/h$ and here is shown their spatial distribution.

3694 5. the copper matrix in which the Nb-Ti is embedded. Typical conductors of the era were 66-
3695 80% copper with balance Nb-Ti (2:1 to 4:1 Cu:SC).

3696 After updating the design, a detailed calculation was done with the PVDIS configuration with Deu-
3697 terium as its target: This configuration, with the Deuterium target inside the magnet, is the one be-
3698 tween the different SoLID configurations which presents the highest flux of neutrons on the Coils.
3699 An integrated dose was calculated and determined using the cylindrical symmetry of the system
3700 and the flux calculated per cm^2 on the more susceptible parts of the magnet. An integrated dose
3701 of $10^{17} \frac{1MeV_{neutron}}{cm^2}$ is needed in order to start to see some modification on the Critical Current (I_c)
3702 of the magnet. A map of the integrated dose for the PVDIS and D_2 case was created and presents
3703 peaks for the integrated fluxes around $10^{14} \frac{1MeV_{neutron}}{cm^2}$, well below the tolerance level of the mag-
3704 net. As a consequence, also if it is not known what is the current level of exposure reached by the
3705 CLEO-II solenoid, the full scientific outreach that is planned at this moment with SoLID does not
3706 seem to be going to affect considerably the lifetime of the coils of the magnet (see Fig. 152).

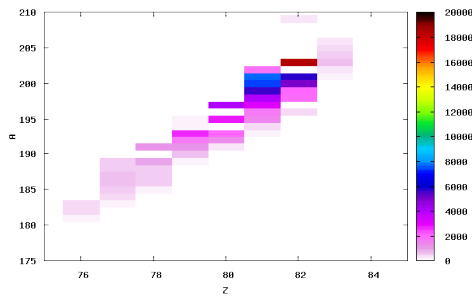
3707 15.3 Estimates for radiation damage in the Hall

3708 A study has been done in order to address possible radiation damage areas with the current SoLID
3709 design with no further shielding in place. This work has been done in order to address and pinpoint
3710 areas that will need to be further investigated when a final design for the magnet and electronics will
3711 be reached.

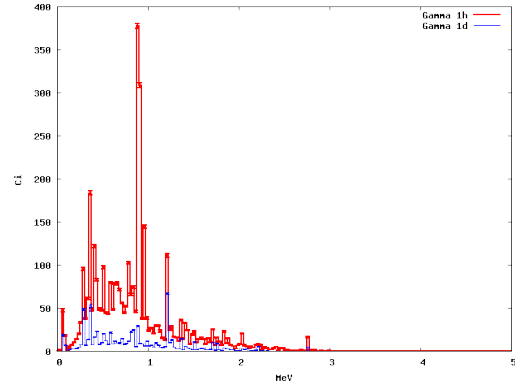
3712 15.3.1 Radiation damage to electronics in Hall

3713 The results of the different simulations run suggest that the design of a shielding structure to min-
3714 imize the radiation in the Hall seems not to be a priority. With the current different layouts of the
3715 multiple configuration possible with the SoLID spectrometer. In this study the magnet has been
3716 placed in a dome structure of concrete that mimics the presence of the Hall (It is important to con-
3717 sider that the SoLID spectrometer will not be placed in an open environment, but in an Hall full
3718 of equipments, with relative reflectivity that could cause an enhancement of the radiation present
3719 in the Hall). Different features of these results are in common with the different configurations for
3720 SoLID:

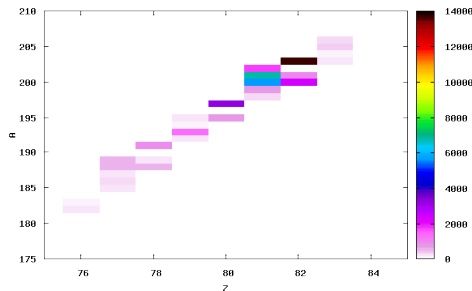
- 3721 • The radiation damage estimated with the simulation is, as expected, consistently lower in the
3722 area outside the SoLID spectrometer respect to the one inside the magnet.



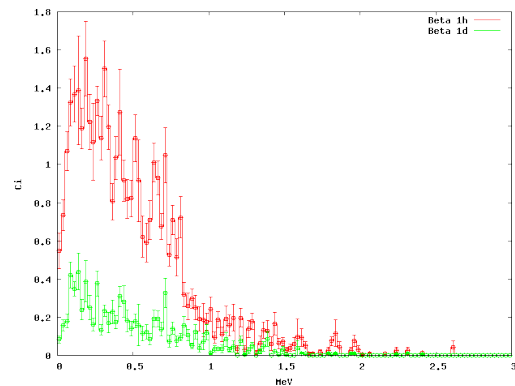
(a) Residual Nuclei for Lead Target after 1hour cooling (Z vs A)



(c) Photon Energy spectrum in Curie due to activation at 2 different cooling times



(b) Residual Nuclei for Lead Target after 1day cooling (Z vs A)



(d) Electron Energy spectrum in Curie due to activation at 2 different cooling time

Figure 148: (148a, 148b) The Residual decaying Nuclei are shown as a function of Z,A in the first baffle assumed constructed on Lead. The Gamma and Beta activity is also shown for the same decaying time (148c, 148d). Determining the activity permits in establishing different needs for shielding at different times of the experimental running (repair or decommissioning)

- 3723 • In the downstream part of the Hall, the predominant part of the radiation that escape the
- 3724 magnet is present in the last part of the beam-line, enhancing the choice of keeping in the
- 3725 upstream section of the Hall the existing left and right arm spectrometers existing in Hall-A.
- 3726 • The configurations that have the target area external to the solenoid have also an high radiation
- 3727 area in the proximity of the target

3728 The configuration that gives the higher radiation estimates in this simulation study, is the PVDIS
 3729 configuration with Deuterium target. The radiation damage estimate in this configuration is investi-
 3730 gated in detail in the next section.

3731 15.3.2 Radiation from beam pipe

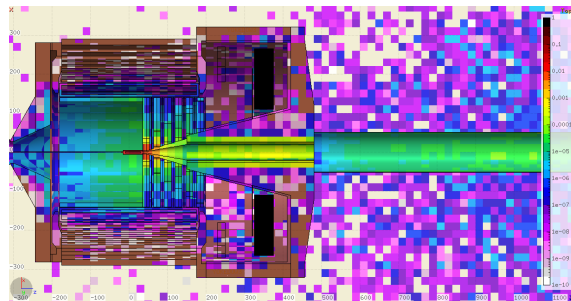
3732 The main source of radiation leaking from the magnet to the Hall is from the beam pipe downstream.
 3733 In order to quantify the leaking with the different layouts with SoLID, different simulation have been
 3734 carried out. The one that presents the biggest impact on possible damage to electronics is the PVDIS

3735 configuration with 40cm Liquid Deuterium target, but the localization of the leakage (close to the
3736 beam-line, see figures [153b](#) ,[153c](#) and [153d](#)), and the low level of radiation present, suggest that a
3737 shielding construction is not needed. A further factor of 10 reduction, if needed, can probably be
3738 reached placing shielding material on the hot areas, around the beam-line, if this area, will be used
3739 during the experiment, reaching levels of radiation compatible also to commercial electronics.

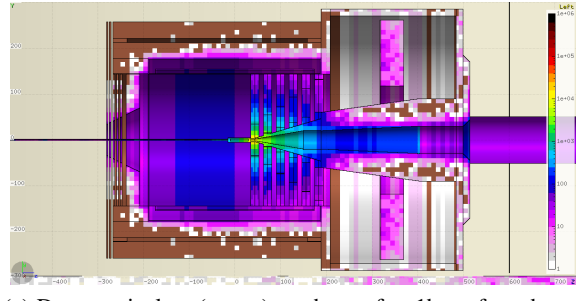
3740 **15.3.3 Radiation with external targets**

3741 Some of the configuration with the SoLID spectrometer, position their target in the proximity of
3742 the entrance of the magnet. Simulations have been done in order to evaluate possible high radiation
3743 areas for electronics. An example for the possible areas of high radiation with these layouts for
3744 the experiments is shown in figure [154](#) (SIDIS configuration with ${}^3\text{He}$ target) and figure [155](#) (J/Ψ
3745 configuration with H_2 target).

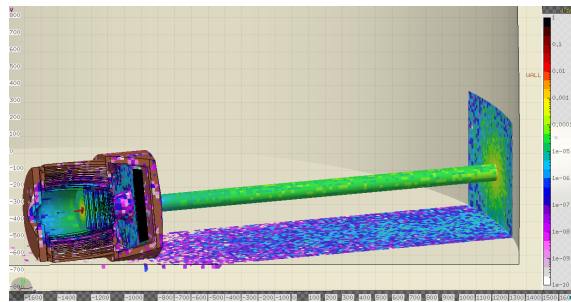
3746 More details and plots on the studies can be found in [[303](#)].



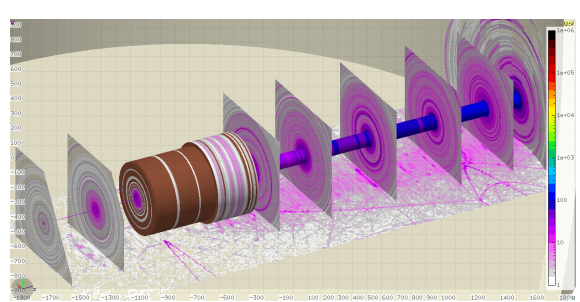
(a) Energy deposited (W) per cm^3 for PVDIS configuration and Liquid Deuterium target



(c) Dose equivalent (mrem) per hour after 1 hour from beam exposure for PVDIS configuration and Liquid Deuterium target

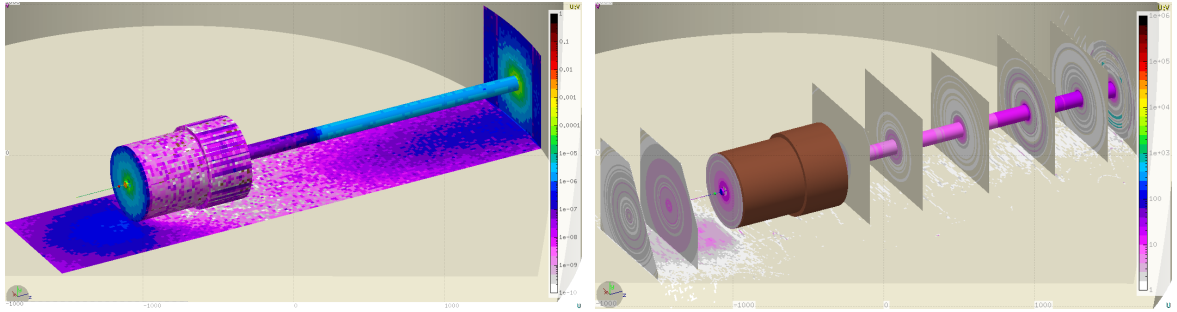


(b) Energy deposited (W) per cm^3 for PVDIS configuration and Liquid Deuterium target (Hall view)

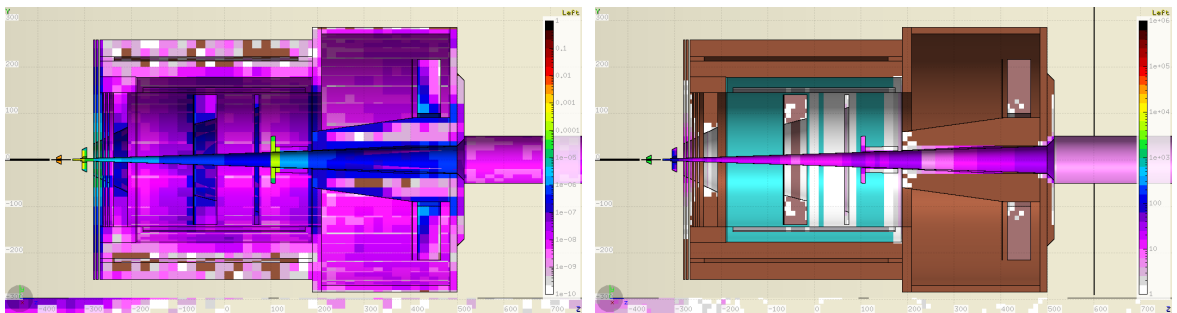


(d) Dose equivalent (mrem) per hour after 1 hour from beam exposure for PVDIS configuration and Liquid Deuterium target (Hall view)

Figure 149: Energy deposited (W) per cm^3 (149a and 149b) considering running condition with Liquid Deuterium target and electron beam current of $100\mu A$. The spectrum is averaged in blocks of size of $20cm \times 20cm \times 20cm$ in order to boost statistics, since this simulation with the complex SoLID design is very high demanding in CPU time. One can see how the power deposited in the first baffle region is considerably higher respect to the one expected in the exit hole of the magnet. In order to obtain the integrated power deposition for the expected beam time for the PVDIS configuration (2000h), multiply the values of the plots by $7.2E+06$. Activation dose equivalent (mrem) rate per hour (149c and 149d) expected with the same configuration after 1 hour from beam exposure ($100\mu A$ for a month). This study has been done in order to simulate condition in the Hall during running time. For a more accurate description of the activation expected in the baffle area, see figure 147



(a) Energy deposited (W) per cm^3 considering SIDIS running (b) Dose equivalent (mrem) per hour after 1 hour from beam exposure for SIDIS configuration and 3He target (Hall view) (Hall view)



(c) Energy deposited (W) per cm^3 considering SIDIS running (d) Dose equivalent (mrem) per hour after 1 hour from beam exposure for SIDIS configuration and 3He target (Inside the magnet) (Inside the magnet)

Figure 150: Energy deposited (W) per cm^3 (150a 150c) considering running condition with 3He target and electron beam current of $15\mu A$. In order to obtain the integrated power deposition for the expected beam time for the SIDIS configuration (3000h), multiply the values of the plots by $1.08E+07$. The main part of the energy is deposited, as expected, in the target area and in the collimator positioned in front of the nose-cone part of the magnet. The energy deposited in the exit hole of the magnet is considerably lower than with the PVDIS configuration. Activation dose equivalent (mrem) rate per hour (150b and 150d) expected with the same configuration after 1 hour from beam exposure ($15\mu A$ for a month). This study has been done in order to simulate condition in the Hall during running time.

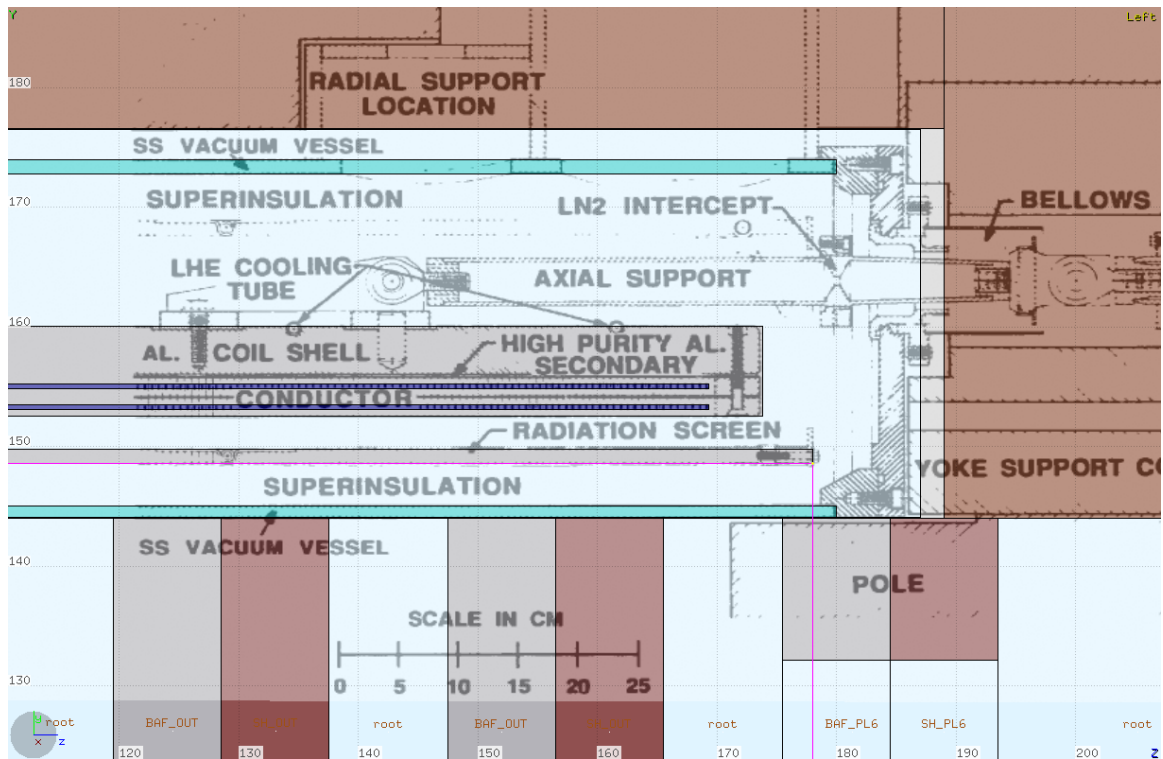


Figure 151: Existing engineering design for the CLEO magnet are put in comparison with the simulation design used for this study.

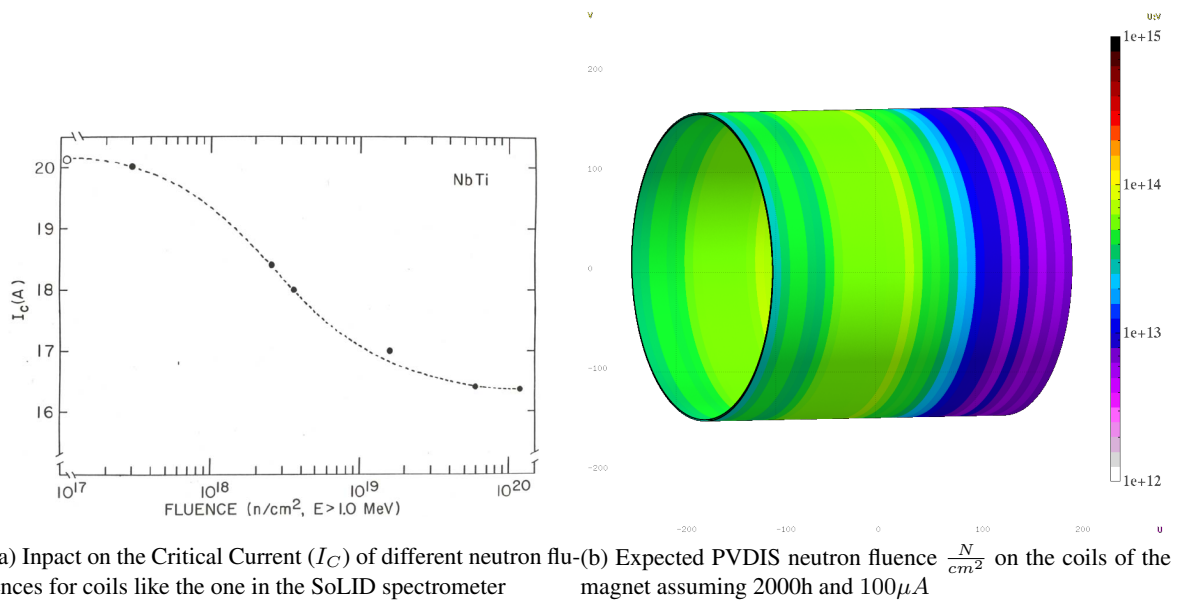
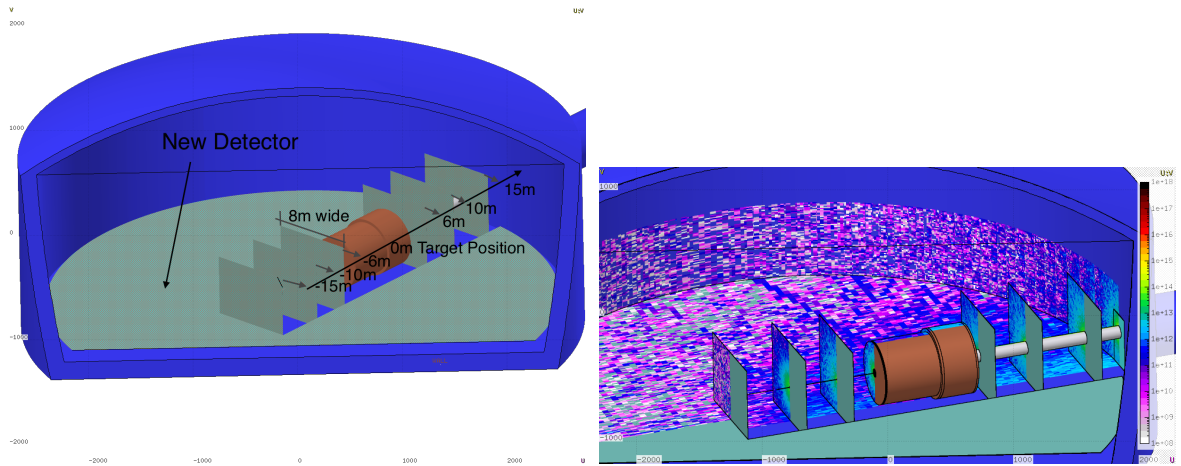
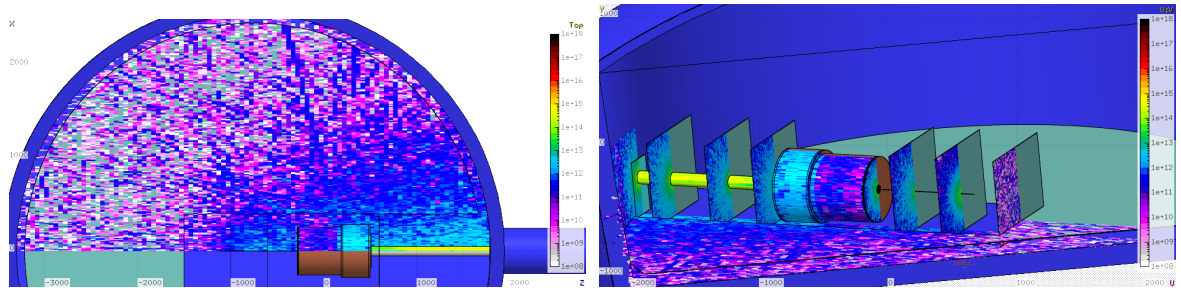


Figure 152: Expected exposure of the Solid magnet coil and expected impact of neutron fluence on Nb-Ti based coil for the Critical Current of the superconducting magnet.



(a) Position of the different planes where in the next plots (b) Estimate of radiation damage in the Hall with the SoLID spectrometer and the PVDIS configuration: A different view planes are put at different positions perpendicular to the beam-line; A plane is also put parallel to the floor at 1m of height



(c) Estimate of radiation damage in the Hall with the SoLID spectrometer and the PVDIS configuration: A different view (d) Estimate of radiation damage in the Hall with the SoLID spectrometer and the PVDIS configuration: A different view

Figure 153: Estimate of radiation damage in the Hall with the SoLID spectrometer and the PVDIS configuration. The leading part of radiation present in the Hall for the SoLID spectrometer is leaking through the downstream part of the beam-line assembly. In this plot is shown the 1MeV Neutron equivalent flux per cm^2 on the volumes surfaces estimated for 2000h of continuous running with a beam current of $100\mu A$ (This is the expected beam-time with the PVDIS configuration). In order to better show the behavior of the radiation leaking, different plane of observation have been inserted (at a distance from the target of $\Delta z = -15m$, $\Delta z = -10m$, $\Delta z = -6m$, $\Delta z = 6m$, $\Delta z = 10m$, $\Delta z = 15m$ (see Fig. 153a). The level of radiation leaking increases as one moves farther from the target, reaching a maximum $\leq 10^{15} \frac{N_{1MeV}}{cm^2}$. These levels of radiation is on the “mild to severe” damage range for commercial semiconductors (as one can see comparing them with Estimate of the tolerance of different material plots 140). This area is not expected to carry any delicate equipment. On the upstream section of the beam-line, the level of radiation leaking is tolerable to also commercial equipment (not rad-hard). A comparable plot of this one, with a projection plane on the zy axis, is show in figure 153c

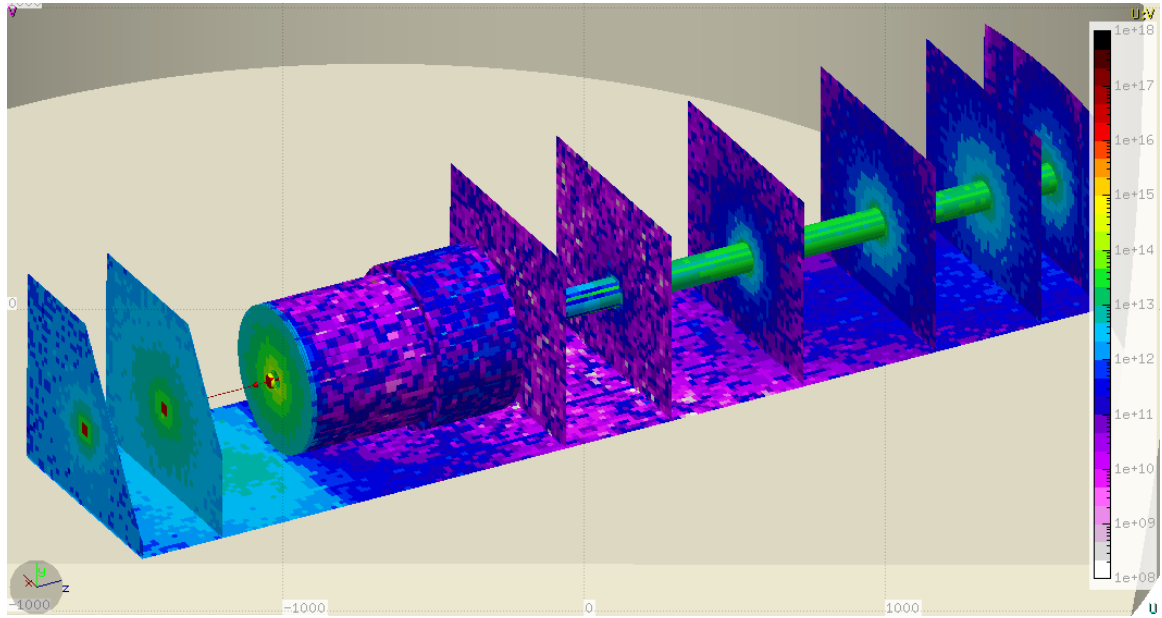


Figure 154: Estimate of radiation damage in the Hall with the SoLID spectrometer and the SIDIS ${}^3\text{He}$ configuration. The leading part of radiation present in the Hall for the SoLID spectrometer is originating from the target area and the closer surface of the magnet. In this plot is shown the 1MeV Neutron equivalent flux per cm^2 on the volumes surfaces estimated for 3000h of continuous running with a beam current of $15\mu\text{A}$ (This is the expected beam-time with the SIDIS configuration). In order to better show the behavior of the radiation leaking, different planes of observation have been inserted (at a distance from the center of the Cryostat of the magnet of $\Delta z = -10\text{m}$, $\Delta z = -6\text{m}$, $\Delta z = 6\text{m}$, $\Delta z = 10\text{m}$, $\Delta z = 15\text{m}$, $\Delta z = 20\text{m}$, $\Delta z = 24\text{m}$). The level of radiation leaking increases as one moves farther from the target, reaching a maximum $< 10^{14} \frac{\text{N}_{1\text{MeV}}}{\text{cm}^2}$. These levels of radiation is on the “mild to severe” damage range for commercial semiconductors (as one can see comparing them with Estimate of the tolerance of different material plots 140). This area is not expected to carry any delicate equipment.

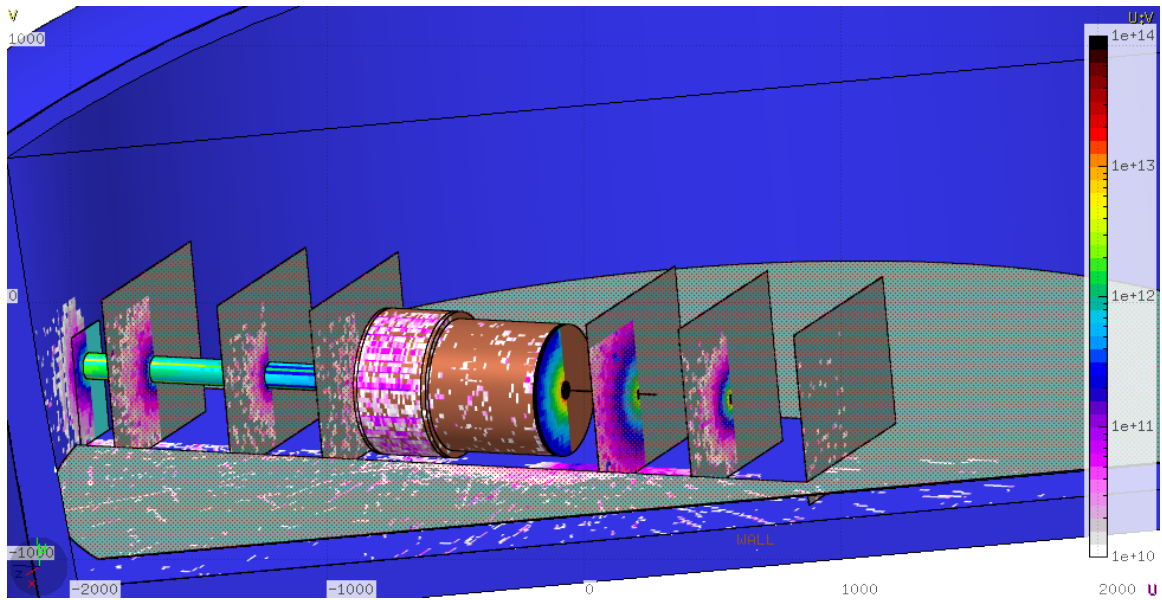


Figure 155: Estimate of radiation damage in the Hall with the SoLID spectrometer and the J/Ψ configuration with a 15cm Liquid Hydrogen target. The leading part of radiation present in the Hall for the SoLID spectrometer is originating from the target area and the closer surface of the magnet. In this plot is shown the 1MeV Neutron equivalent flux per cm^2 on the volumes surfaces estimated for 60 days of continuous running with a beam current of $3\mu A$ (This is the expected beam-time with the J/Ψ configuration). In order to better show the behavior of the radiation leaking, different planes of observation have been inserted (see Fig. 153a for reference of the position of each plane). The Color scale is different than in the previous cases in order to enhance the details in the desired region.

3747 **16 Slow Controls**

3748 Slow Controls typically covers the “infrastructure support” systems and logging for the detector
3749 package as a whole. This includes real-time controls and status monitoring of power, vacuum, tem-
3750 peratures, etc., in addition to integrated safety interlocks and alarm functions. Typical measurement
3751 and response times for such systems are on the order of a 100s of milliseconds to seconds. More
3752 rapid response times are also available if needed. Common examples of slow controls involve the
3753 high- and low-voltage power supplies for all detector apparatuses, gas composition and flow regu-
3754 lation, control of gain-monitoring systems, etc.

3755 This section *excludes* any discussion of slow controls for the target and solenoid magnet. Slow
3756 controls for those systems will be designed and implemented by their respective working groups.
3757 The systems covered here involve only the SoLID detector subsystems.

3758 Due to the obvious interdependence between the hardware and the software used to control it,
3759 details of several slow control components will need to wait until the hardware design is better
3760 developed (*eg.* gas systems). We will give an overview of some baseline requirements and expecta-
3761 tions that the Collaboration will abide by to ensure slow controls development and implementation
3762 will proceed smoothly.

3763 It is understood that any fast interlocks (*i.e.* millisecond level or faster) that cross system bound-
3764 aries need to be identified at the design stage. Examples may include tripping high-voltage if the
3765 gas flow is interrupted for the GEM system, disabling the flammable gas flows in the event of a fire
3766 alarm, etc.

3767 **16.1 General Requirements**

3768 The Collaboration agrees that all components must be able to interface with the EPICS (Experi-
3769 mental Physics and Industrial Control System) environment already present at Jefferson Lab. This
3770 imposes a common mid-level API for inter-system communication and allows the systems to take
3771 advantage of the well supported EPICS infrastructure at JLab. This includes local expert support
3772 from other experimental Halls (particularly Halls B & D), and the Accelerator Division for any
3773 necessary PLC, software and/or hardware IOC development, as well as taking advantage of JLab’s
3774 EPICS data archiver “MYA”.

3775 **16.2 Frontend GUIs**

3776 The graphical interface employed for all systems is expected to be based on the Control Systems
3777 Studio (CSS) environment. This is an Eclipse-based toolkit that is slowly replacing the legacy
3778 EDM/MEDM GUIs developed during JLab’s 6 GeV period. Hall D and Hall B already make exten-
3779 sive use of the CSS toolkit, and Hall C will be migrating its legacy M/EDM GUIs as time permits.

3780 The BEAST alarm handler, part of the CSS system, will be used to monitor EPICS variables
3781 and alert shift crew and/or external experts of problems.

3782 Systems that require lower-latency response times than softIOCs and EPICS polling systems
3783 can provide will investigate the CompactRIO (cRIO) standard successfully used in Halls B & D.

3784 The Hall B slow controls development experience, in particular, has been well documented by
3785 those involved and will provide an excellent local repository of interface code and management
3786 processes that SoLID can leverage.

3787 **16.3 High/Low Voltage Controls**

3788 High Voltage hardware will be standardized as much as possible. CAEN and Wiener systems are
3789 both in use as JLab. They each come with integrated EPICS support and pre-existing software sup-
3790 port on-site. Detector, sub-detector, and individual channel control and monitoring will be provided.
3791 Legacy LeCroy HV systems will *not* be supported.

3792 **16.4 DAQ Crate Control**

3793 It is desired to have realtime monitoring of VME and other data acquisition crate power systems and
3794 temperatures. All DAQ crates are expected to provide an integrated ethernet interface and EPICS
3795 support. Examples of such hardware include the Wiener 60xx series in common use across JLab.

3796 **16.5 Gas Systems Requirements**

3797 In addition to the necessary EPICS interface, the Collaboration agrees that the various gas sub-
3798 systems (Cerenkovs, GEMs, MRPC) will standardize any hardware that requires software support.
3799 This includes items such as mass flow controllers (MFCs) and hardware process controllers, etc.
3800 This will allow for a common spares inventory and simplify control software development and
3801 maintenance.

3802 **16.6 Detector Systems**

3803 The following list runs through the various sub-detectors and summarizes the necessary slow con-
3804 trols.

- 3805 • **EC:** HV control and monitoring.
- 3806 • **FA/LASPD:** HV control and monitoring.
- 3807 • **GEM Tracking:** HV/LV control and monitoring. The non-recirculating gas system will use
3808 Ar/CO₂ at STP and will employ a basic gas mixer system with flow monitoring and control.
- 3809 • **LGC:** HV control and monitoring. The CO₂ gas employed operates at STP and will be served
3810 by a simple non-recirculating “flow-through” system.
- 3811 • **HGC:** HV control and monitoring. The C₄F₁₀ gas employed is expensive and used in large
3812 quantities. Such a system will require a somewhat sophisticated recapture/purification/recirculation
3813 infrastructure involving PLC/IOC controls that remain to be designed.
- 3814 • **MRPC:** HV/LV control and monitoring. The MRPC gas system employs a 5% SF₆ + 90%
3815 R134 + 5% Isobutane mix that will likely require a recapture/recirculation infrastructure also
3816 involving a PLC/IOC system. This is still to be designed.

3817 In addition to the above items, gain-monitoring systems have been discussed that would also require
3818 some nominal controls. It is not expected that such systems would be a significant burden.

3819 **17 Electron Beam Polarimetry**

3820 The interpretation of the measurement of the parity-violating asymmetry relies on precise correc-
3821 tion for finite beam polarization, with an accurate absolute normalization to 0.4% accuracy at both
3822 11 GeV and 6.6 GeV. This will be achieved using two independent measurement techniques with
3823 independent sources of calibration errors, which can be directly cross-checked to high precision.
3824 This is an ambitious goal. The most precision electron beam polarimetry result to date in a physics
3825 publication is the 0.5% Compton polarimetry result by the SLD collaboration [304]. Compton po-
3826 larimetry is well-suited for the energy and intensity of the upgraded Jefferson Lab beam. Plans for
3827 upgrading the existing Hall A Compton polarimeter to achieve 0.4% precision are described below.

3828 The best candidate for a second, high-precision, independent measurement is Møller polarime-
3829 try. The use of iron foils in high magnetic fields can provide a precision well better than 1%, and
3830 may prove to be more precise to the level of 0.5%.

3831 **17.1 Compton Polarimetry**

3832 Compton polarimetry is a very promising technique for high precision polarimetry at beam en-
3833 ergies above a few GeV. Beam interactions with a photon target are non-disruptive, so Compton
3834 polarimetry can be employed at high currents as a continuous polarization monitor. The photon
3835 target polarization can be measured and monitored with a very high precision, and the scattering
3836 between a real photon and free electron has no theoretical uncertainty, such as the atomic or nuclear
3837 effects which can complicate other measurements. Radiative corrections to the scattering process
3838 are at the level of 0.3% and are very precisely known. While the SLD collaboration result, with
3839 a precision of 0.5%, demonstrates the feasibility of very high accuracy Compton polarimetry, that
3840 measurement was ultimately limited by the inability to detect individual scattered particles (due to
3841 the pulsed beam) and the high Bremsstrahlung background in the photon detector due to the prox-
3842 imity to the interaction region. Conditions at JLab are favorable for both of these concerns. The
3843 existing apparatus and plans for future improvements are described below.

3844 **17.2 The Hall A Compton Polarimeter Baseline Upgrade**

3845 As pictured in Fig. 156, the Hall A Compton polarimeter [305] is located in a chicane, about 15
3846 meters long, just below the beamline. After modification of the bend angle to accommodate 11
3847 GeV running with the existing chicane magnets, the electron-photon interaction point will be 21 cm
3848 below the primary (straight-through) beamline. After passing the electron-photon interaction point,
3849 the electron beam is bent about 3.5 degrees by the third chicane magnet and then restored to the
3850 main beamline. The scattered electrons are separated from the primary beam and detected using
3851 silicon microstrips, just before the fourth chicane magnet. Scattered photons pass through the bore
3852 of the third chicane magnet to be detected in a calorimeter.

3853 The photon target is a 0.85 cm long Fabry-Perot cavity crossing the electron beam at an angle
3854 of 1.4° . The laser system can be configured for infrared (1064 nm) or green (532 nm) light, and
3855 has achieved power levels of 10 kW of green light for polarimetry measurements. The laser light is
3856 polarized using a quarter-wave plate, and can be toggled between opposite polarizations of highly
3857 circularly polarized light. The feedback loop which locks the laser to the cavity resonance can
3858 be disabled to enable backgrounds from all non-Compton-scattering processes. To reduce overhead
3859 from the time required to re-lock the cavity, the transition between laser states is typically performed
3860 with a period of 1-2 minutes. The polarization of the transmitted light from the locked cavity and

3861 the reflected light from the unlocked cavity are each monitored and can be used to characterize the
 3862 laser polarization at the interaction point.

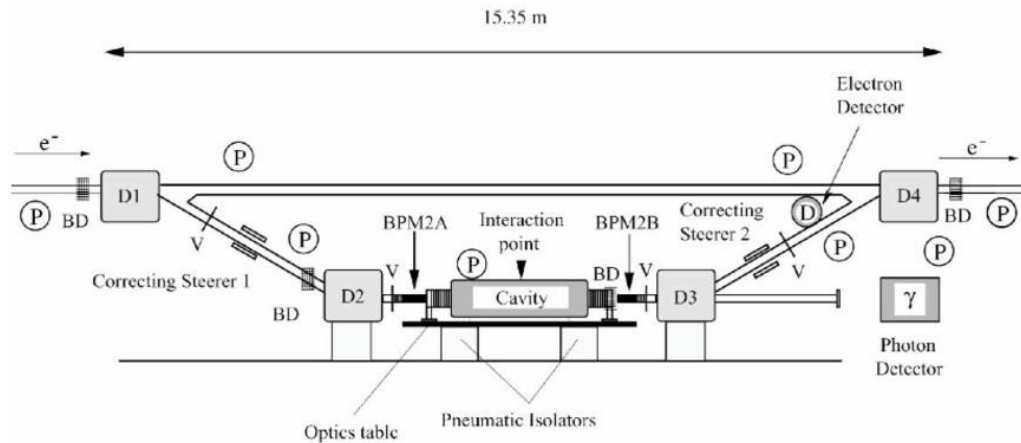


Figure 156: Schematic of the Hall A Compton polarimeter. Figure from [305].

3863 The vacuum in the interaction region is at the level of few $\times 10^{-8}$ torr, implying a photon back-
 3864 ground rate due to Bremsstrahlung scattering from residual gas of around $5 \text{ Hz}/\mu\text{A}$. The dominant
 3865 source of background in the photon detector is thought to be tails of the beam halo distribution
 3866 interacting with the apertures in the interaction region. In contrast, for the electron detector the
 3867 background is thought to be dominated by energy tail or position halo of the primary beam since
 3868 electrons from aperture scattering would presumably not cleanly transit the third dipole. When
 3869 well-tuned, the background rates in the photon and electron detectors have been seen to be roughly
 3870 similar: around $<100 \text{ Hz}/\mu\text{A}$ in recent use. At 11 GeV, with a 10 kW IR cavity, the Compton-
 3871 scattered rates would be approximately $20 \text{ kHz}/\mu\text{A}$ and the asymmetry will range from 17.8% to
 3872 -4% over the energy spectrum. At 6.6 GeV, a 10 kW green cavity will be used, which will provide a
 3873 rate of $13 \text{ kHz}/\mu\text{A}$ with an asymmetry ranging from 20.9% to -4.7% . If backgrounds remain com-
 3874 parable to recent operation, statistical precision of 0.4% would be possible in less than 5 minutes,
 3875 depending on the specific detection and analysis approach which is considered.

3876 Electrons are detected in a set of 4 planes of silicon microstrips located just before the 4th
 3877 dipole. Each microstrip instruments 192 strips with a pitch of $240 \mu\text{m}$. Custom readout electronics
 3878 pre-amplify and discriminate signals from the microstrips, implement a simple tracking algorithm
 3879 to reduce non-directional backgrounds, and count hits in each strip over specified integration gates
 3880 corresponding to the helicity pattern of the electron beam. Presently, this system is operating at low
 3881 efficiency with poor signal size for a minimum ionizing track compared to environmental noise on
 3882 individual strips. The baseline upgrade would include an improvement in this system to achieve
 3883 high efficiency and high signal-over-noise for the microstrip readout. The use of diamond mi-
 3884 crostrips, such as were recently successfully used for the Hall C Compton polarimeter [306], is
 3885 under consideration. Such diamond microstrips are more difficult to procure and in principle are
 3886 more challenging to instrument than silicon strips, however, they are more radiation hard and less
 3887 susceptible to low-energy photon backgrounds.

3888 The calorimeter for detecting scattered photons lies about 7 meters downstream of the interac-
 3889 tion point. The strong forward boost of scattered photons leads to a tightly collimated photon beam
 3890 ($<1 \text{ mrad}$), so the calorimeter size is determined by consideration of energy resolution through

3891 shower loss. The photon calorimeter is a GSO crystal scintillator of 6 cm diameter and 15 cm
3892 length, with a single photomultiplier tube. The PMT signal is split between two parallel data acqui-
3893 sitions: one with a fast-counting, buffered ADC self-triggered on pulses from the photon detector,
3894 and the other utilizing a 250MHz flash ADC (fADC) to integrate the total signal over periods corre-
3895 sponding to the helicity pattern of the electron beam. The fADC system can also record a very low
3896 rate of individual pulses for calibration. Each of these dual readouts can be analyzed independently.
3897 The fast counting ADC readout and the sample pulses in the fADC system can both be triggered
3898 using the electron detector, providing an electron-photon coincidence spectrum for calibration.

3899 **17.3 Upgrades Beyond the Baseline**

3900 There are several issues which must be addressed, related either to operation at the higher beam
3901 energy or to the very high level of precision which is proposed.

- 3902 • The electron beam halo — a term meant to describe a long tail on the momentum or position
3903 distribution of the beam — is expected to be larger at 11 GeV compared to 6 GeV operation,
3904 due to synchrotron light emission in the recirculation arcs which will increase the momentum-
3905 normalized beam emittance. For Compton polarimetry, a tail on the beam energy distribution
3906 is directly responsible for the dominant backgrounds in electron detection, while scattering of
3907 beam halo from narrow apertures in the interaction region is thought to dominate backgrounds
3908 in photon detection.
- 3909 • The measurement of the laser polarization must be performed with very high precision.
- 3910 • The total power of synchrotron radiation emitted by the beam in the chicane arcs will be more
3911 than an order of magnitude higher compared to Compton measurements in the 6 GeV era,
3912 and this radiation spectrum will be significantly stiffer. Dilution from this radiation would
3913 complicate photon and electron detection.
- 3914 • Photon detection must provide a well-characterized and linear response for photons in an
3915 energy range from about 3 GeV to low energies and over a large variation in signal rate, while
3916 being radiation hard and also insensitive or shielded from the synchrotron radiation power.

3917 These issues are addressed by several modifications which go beyond the baseline 11 GeV upgrade,
3918 listed below and described in the following sections. These improvements are expected to allow us
3919 to achieve the precision goals listed in Table 33.

- 3920 • **Laser system** A larger crossing angle for the photon and electron beams would allow larger
3921 electron beam apertures, and reduce backgrounds in the photon detector. This increase in
3922 crossing angle comes at the expense of lower luminosity, leading to a tradeoff in signal rate
3923 and background rate. With the high cavity power that has been achieved with this laser system,
3924 we do not expect to be limited by laser power even at increased crossing angle. The decision
3925 on crossing angle can be made when more is known about beam conditions at 11 GeV. The
3926 beamline through the chicane magnets is one inch inner diameter, which is about a factor of
3927 three larger than the aperture required by the present laser crossing angle. The luminosity
3928 would drop roughly linearly with crossing angle, and even with a factor of 1/3 the statistical
3929 power of the signal rate for a 10 kW cavity would still be sufficient assuming a reduced
3930 background fraction.

3931 In addition to the option to increase this crossing angle, a system for measuring laser po-
3932 larization inside the resonant optical cavity (although not while locked to resonance) must

Relative error (%)	electron	photon
Position asymmetries*	-	-
E_{Beam} and λ_{Laser} *	0.03	0.03
Radiative Corrections*	0.05	0.05
Laser polarization*	0.20	0.20
Background / Deadtime / Pileup	0.20	0.20
Analyzing power Calibration / Detector Linearity	0.25	0.35
Total:	0.38	0.45

Table 33: Goals for systematic errors for the Hall A Compton polarimeter at 11 GeV. Topics marked * are common systematic errors between the photon and electron analyses, while the others are largely independent between the detector systems.

3933 be developed and used, along with a thorough study of all optical components, to improve
3934 knowledge of the photon polarization.

3935 • **Chicane Modification** The synchrotron light power on the photon detector will be signifi-
3936 cantly reduced by installing shims to increase the fringe fields of the chicane dipole magnets
3937 in the interaction region. This would also soften the synchrotron energy spectrum, making
3938 shielding more effective. The effect of synchrotron light on the electron detector is being
3939 investigated, with the possibility to add some baffling to limit reflection into the detector.

3940 • **Photon Detector** The photon detection system used for recent running will be replaced with
3941 a detector better matched to the Compton photon energy spectrum for 11 GeV operation.

3942 These upgrades are described in more detail below.

3943 17.3.1 Laser System and Luminosity

3944 As described above, in the current configuration of the Hall A Compton, the electron beam interacts
3945 with green (532 nm) light in a resonant optical cavity at a crossing angle of about 1.4° . After
3946 accounting for the length of the optical cavity (about 85 cm) and the finite size of the cavity mirror,
3947 it is necessary to enforce an aperture on the electron beam of ± 5 mm. It is thought that this narrow
3948 aperture is the dominant source of background for 6 GeV running. At higher energies, synchrotron
3949 light emission in the accelerator recirculation arcs will increase the beam emittance and presumably
3950 lead to significantly larger backgrounds from this aperture scattering. In present use of the Compton
3951 polarimeter, frequent beam tuning is required to maintain operation with the signal-over-background
3952 > 10 . A large background signal is often associated with large fluctuations over the period of time in
3953 the laser on/off cycle used to measure backgrounds. This reduces the measurement precision, and
3954 potentially introduces a significant systematic error through instability in the phototube under large
3955 variations in rate. For this reason, it is desirable to keep the signal-over-background ratio large.

3956 The aperture can be widened only by increasing the laser crossing angle which would also
3957 lower the luminosity. Although the baseline upgrade plans do not make provision for changing this
3958 crossing angle, operability at 11 GeV may require larger apertures. At a finite crossing angle α , the
3959 luminosity for a continuous-wave electron and photon beam, with intersecting electron and photon

3960 waists sizes σ_e and σ_γ , is given by:

$$\mathcal{L} \approx \frac{1 + \cos \alpha}{\sqrt{2\pi}} \frac{I_e P_\gamma}{ek_0 c} \frac{1}{\sqrt{\sigma_e^2 + \sigma_\gamma^2}} \frac{1}{\sin \alpha} \quad (28)$$

3961 Here P_γ is the power of the photon beam, I_e is the current in the electron beam, and k_0 is the
3962 photon energy scattered at the kinematic maximum limit of colinear backscattering. As an example:
3963 at 10000 W stored power at 532 nm, the Compton scattering rate would be about 12 kHz/ μ A at
3964 1.4° crossing angle and about 4.8 Hz/ μ A at 3.5°. At the expense of approximately a factor of
3965 2.5 in luminosity, that larger crossing angle would allow a ± 0.5 inch aperture, comparable to the
3966 maximum aperture allowed by the 1" beam pipe diameter in the bore of the existing dipole magnets
3967 in the chicane.

3968 With an available laser power of 10 kW, the polarimeter is not expected to be limited by low
3969 signal rates even at the larger crossing angles. However, the drop in luminosity with increasing
3970 crossing angle suggests that any change must be optimized from the point of view of signal-over-
3971 background. Until beam tests at higher beam energies are performed to form reliable estimates of
3972 background levels, it is prudent to design for both large crossing angle and large luminosity.

3973 We propose the use of an infrared cavity storing 10 kW of optical power at 1064 nm for operation
3974 at beam energy above 8.8 GeV, and a cavity storing 10 kW of optical power at 532 nm for beam
3975 energies at 6.6 GeV and below. The primary disadvantages to the longer photon wavelength are
3976 the reductions in analyzing power and softening of the energy spectrum (17% analyzing power and
3977 1.8 GeV maximum photon energy for IR at 11 GeV, compared to 32% and 3 GeV for 532 nm).
3978 The advantages for the IR system would be a greater available luminosity and system reliability.
3979 While the cross-section is very similar between the two photon energies, at 1064 nm there are twice
3980 as many photons per unit energy. At 10 kW, an IR cavity would provide a rate of 9 kHz/ μ A
3981 at the increased crossing angle to allow the full ± 0.5 " electron beam aperture, or 23 kHz/ μ A at the
3982 original design 1.4° crossing angle. The 532 nm system requires an additional stage to frequency-
3983 double the original 1064 laser light. Without this doubling stage, the IR system can inject higher
3984 power to the cavity, enabling higher cavity power or the same cavity power with reduced cavity
3985 gain. A lower gain cavity will typically be more robust, and and less sensitive to radiation damage
3986 of the cavity optics. At beam energies below 8.8 GeV, the improvement in analyzing power and
3987 higher scattered photon energy endpoint are worth the possible trade-off in ease of operability.

3988 Precision electron beam polarimetry also requires precise determination of the polarization of
3989 the photon target. This has proved to be the dominant systematic error contribution in recent Hall A
3990 Compton polarimeter measurements, in part because the use of a high-gain resonant cavity signifi-
3991 cantly complicates this determination. In a resonant cavity, the polarization state of the stored light
3992 can not be directly measured without destroying the resonance. For the present Hall A polarimeter,
3993 the laser polarization is inferred from measurements of the light that transmits through the cavity.
3994 A transfer function, relating the polarization of light in the Compton Interaction Region (CIP) to
3995 the polarization measured in the transmitted beam outside the vacuum vessel, is determined from
3996 measurements with an un-locked cavity. The highly-reflective cavity mirrors must be removed for
3997 these measurement, and the cavity must be open to air, which implies a relaxation of stress-induced
3998 birefringence of the vacuum entrance and exit windows. Contributions from birefringence in the
3999 cavity mirror substrate and stress on the vacuum windows can be characterized separately, but as
4000 a practical matter these corrections are difficult to determine with high precision. For the Hall A
4001 polarimeter, previous studies have quoted the uncertainty in beam polarization to be 0.35%, but in
4002 recent operation the uncertainty could not be bounded to better than 0.7%.

4003 An improved technique has been used in Hall C to control the laser polarization uncertainty. The

4004 polarization of light arriving at the cavity entrance can be inferred from light reflected back from
 4005 the cavity and analyzed with the same apparatus used to create the initial polarization state, mea-
 4006 suring a single power level [307]. This technique was employed in Hall C to maximize the circular
 4007 polarization of light injected in the cavity and to monitor the polarization during the run. It was
 4008 verified to work by two methods. In the first, with the cavity under vacuum in running conditions,
 4009 a scan over a broad range of initial polarization states was performed, and the recorded analyzed
 4010 reflected power was shown to be well described by the simple hypothesis of optical reversibility. A
 4011 more direct verification was made with the cavity opened, directly measuring the polarization of the
 4012 injected light in the cavity and correlating this with the analysis of the reflected light. The correla-
 4013 tion is shown over the full range of the scan, and zoomed in for measurements at maximum circular
 4014 polarization, in Fig. 157. In operation, the Hall C Compton polarimeter ran with the reflected light
 4015 very near minimum, with an implied uncertainty on the circular polarization within the cavity of
 4016 0.1%.

4017 These studies demonstrate that this technique may provide knowledge and monitoring of the
 4018 circular polarization in the cavity to the level of 0.1%. An *in situ* measure of the polarization would
 4019 be a valuable confirmation of this procedure. Modifications to the interaction region will be made
 4020 to allow an insertable, vacuum-compatible analysis assembly for measurements of the beam in the
 4021 CIP. The power level for such measurements will necessarily be very low, as the highly reflective
 4022 mirrors of the cavity will attenuate incident light, but such a direct measurement would include all
 4023 effects of birefringence and depolarization in the injection of optical power into the cavity.

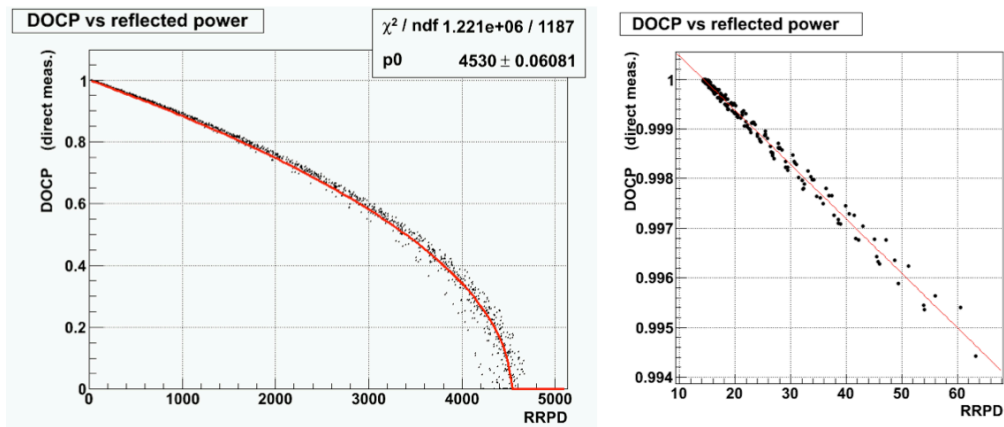


Figure 157: Measured degree of circular polarization in the Hall C Compton laser cavity vs. the polarization-analyzed reflected light, measured over a broad scan of initial polarization states. The figure on the right is zoomed in the region of maximum circular polarization.

4024 17.3.2 Alternative Laser System

4025 An alternative laser system has also been considered, based on the use of a short-pulse RF laser
 4026 synchronized to the electron bunch frequency. Such a system would concentrate laser power on
 4027 the electron bunches, in effect creating an electron-photon collider. For a laser with narrow pulse
 4028 structure (≈ 10 ps) and repetition frequency sub-harmonic to the electron beam ($f_{laser} = 499$ MHz

4029 / n with integer n), the the ratio of luminosity for the same average power goes as:

$$\frac{\mathcal{L}_{pulsed}}{\mathcal{L}_{CW}} \approx \frac{c}{f_{beam}\sqrt{2\pi}} \frac{1}{\sqrt{\sigma_{e,z}^2 + \sigma_{\gamma,z}^2 + \frac{1}{\sin^2\alpha/2} (\sigma_e^2 + \sigma_\gamma^2)}}. \quad (29)$$

4030 Here f_{beam} is the electron repetition rate and $\sigma_{e,z}$ ($\sigma_{\gamma,z}$) is the longitudinal size of the electron (laser)
 4031 pulse. For the parameters relevant to the proposed system, this corresponds to an enhancement of
 4032 luminosity per unit power of between 20-50. Commercially available mode-locked laser systems
 4033 has been identified providing 45 W at 1064 nm, with 100 MHz repetition rates and 10 ps pulse
 4034 widths. Assuming an average injected power of 30 W at the 3.6° crossing angle, such a pulsed laser
 4035 would provide 330 Hz/ μ A with a single-pass beam, that is, without the resonant optical cavity.

4036 Although the relatively low rates would be expected to be a disadvantage, it may turn out to
 4037 be operable depending on the characteristics of the 11 GeV electron beam. The statistical preci-
 4038 sion (0.4% in about 3 hours) would be sufficient for a high precision measurement. The primary
 4039 advantage of such a system would be a more straightforward determination of the laser polarization,
 4040 relative to a high-gain optical cavity. There are other advantages as well. Locking and unlocking
 4041 a cavity takes time, so to maintain a high duty factor for a cavity system the locked and un-locked
 4042 periods used to determine backgrounds are long (≈ 1 minute) relative to the fluctuations in the back-
 4043 ground. On the other hand, a laser can be turned off or deflected to a dump quickly, so background
 4044 measurements for such a single pass system could take place quickly, potentially providing superior
 4045 control of background fluctuations even if the signal-over-background ratio is smaller. Similarly,
 4046 without the requirement to maintain the delicate balance of signal levels necessary to robustly lock
 4047 a high-gain cavity, systematic studies varying laser power or position would be simplified.

4048 Should the rate from such a system be unmanageably small relative to backgrounds, it could be
 4049 roughly doubled using a “butterfly” cavity to recirculate the exit beam through the interaction point.
 4050 A more powerful option would be a hybrid system in which the RF pulses are stored in a resonant
 4051 optical cavity. A moderate cavity gain ≈ 20 would double the Compton signal rate compared to the
 4052 10 kW, gain ≈ 3000 CW default design. At such a low gain, the cavity lock would be relatively easy
 4053 to acquire, potentially enabling more rapid background measurements than the high-gain system.
 4054 The polarization measurement would also likely be simpler than for a high-gain cavity system, as the
 4055 injection beam in the interaction region would still be similar to the beam stored through relatively
 4056 few resonant reflections.

4057 Such a cavity would require the dual resonance condition of being both an integral number of
 4058 optical and RF wavelengths. This is not a particularly difficult condition to maintain. The injec-
 4059 tion laser must be mode-locked to ensure coherence between pulses. Locking mode-locked lasers
 4060 to Fabry-Perot cavities has been actively pursued over the last decade in development studies for
 4061 Compton-based X-ray sources [308, 309] and for a polarized positron source for the ILC [310, 311],
 4062 with significant technical success beyond the requirements for this proposed system.

4063 The above discussion demonstrates the utility and technical feasibility of the alternative proposal
 4064 for a 10 ps pulse length, 100 MHz, 1064 nm laser system operating either as an injection laser for a
 4065 gain ≈ 20 resonant cavity or as a 30 W single-pass system. This alternative proposal would require
 4066 new investment for acquisition of the injection laser and high-power optics. In addition, the pos-
 4067 sibility of time-dependent polarization in the short RF laser pulse may additionally complicate the
 4068 laser polarization determination. The alternative system remains as a backup should complications
 4069 in determining the laser polarization inside the high-gain laser cavity prove to be insurmountable.

4070 **17.3.3 Chicane Magnet Modification**

4071 At 11 GeV, significant synchrotron radiation is emitted when the electron beam is bent in a magnetic
 4072 field. The total radiated power rises as β^4 for the same bend radius. At 11 GeV, this radiation load
 4073 will be a significant background in the photon detector and may overwhelm the signal from Compton
 4074 scattering. Figure 158 shows the energy spectrum of synchrotron light attenuated by lead shielding
 4075 between 1–5 mm thick, depending on the beam energy. On the left, the spectrum for 11 GeV with
 4076 unmodified magnets is compared to calculations for the recent runs of HAPPEX-III (3 GeV) and
 4077 PV-DIS (6 GeV). On the right, the energy spectrum (“Fringe 2”) is shown when iron extensions,
 4078 15 cm in length, are added to the dipole magnets in order to provide an extended region of reduced
 4079 field. This reduced magnetic field produces synchrotron light with lower energy range and with
 4080 reduced intensity, for the portion of the electron beam trajectory that projects to the photon detector.
 4081 With this modification, the bending strength of the magnet remains the same but the synchrotron
 4082 light radiated into the detector is reduced by a factor of 10^4 , to a level comparable to HAPPEX-
 4083 III. The magnetic field extensions were modeled using TOSCA, and have been constructed. Field
 4084 measurements have been taken to verify the magnetic model for both the integral Bdl and the shape
 4085 of the fringe field with and without the field extensions. These field extension pieces have been built
 4086 and will be ready for installation at the start of 11 GeV operations.

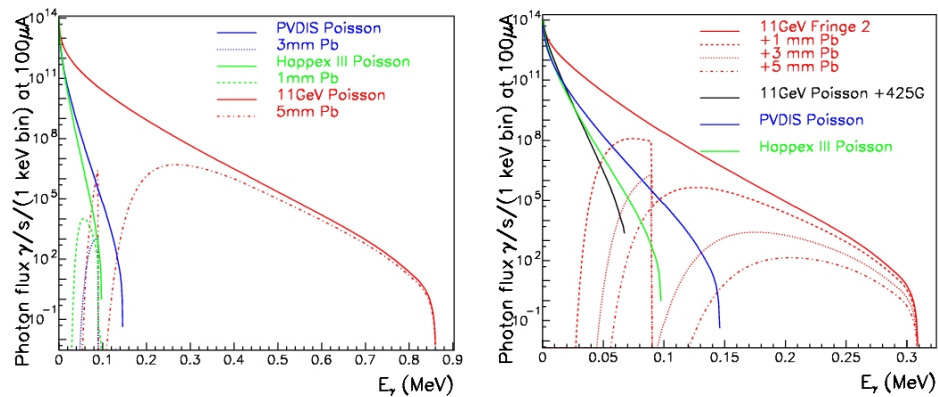


Figure 158: Energy spectrum of synchrotron radiation penetrating lead shielding of thickness listed. Plot on left shows unmodified chicane magnets, plot on right shows energy spectrum for proposed magnetic shims which reduce the field for the bend radiating into the Compton photon detector acceptance. Note the different horizontal scales between the plots.

4087 **17.3.4 Photon Detection**

4088 The specific calorimeter to be employed is not yet determined. The present calorimeter is a GSO
 4089 crystal scintillator, which has excellent light yield suitable for measurements at low energies. The
 4090 crystal is too small to contain most showers at higher energies, and a new calorimeter will be re-
 4091 quired for precision measurements at 11 GeV. In the past, Hall A has used an undoped lead tungstate
 4092 ($PbWO_4$) array. This may be suitable for 11 GeV operation; the relatively low light yield for $PbWO_4$
 4093 is not an issue for higher photon energies of the proposed measurements or for the integrating mea-
 4094 surements, and the high speed of this material reduces pile-up issues in counting measurements.
 4095 Designs for multi-layer sampling calorimeters, using either scintillation or Cherenkov light, will
 4096 also be considered.

4097 **17.4 Systematic Uncertainties**

4098 While the proposed system should assure operability and sufficient statistical precision at 11 GeV,
4099 the challenge will be achieving an absolute measurement of beam polarization with a precision of
4100 0.4%. Table 33 summarizes the goals for various contributions to systematic uncertainty. The first
4101 four rows list sources of uncertainty which are highly or completely correlated between the electron
4102 and photon analyses. Other potential systematic errors arise in detector readout or calibration and
4103 are mostly or entirely decorrelated between the analyses. Each of these separate categories of po-
4104 tential systematic uncertainty: correlated, electron-only, and photon-only, will be discussed in the
4105 following sections.

4106 **17.4.1 Sources of Correlated Error**

4107 Any error associated with the Compton scattering process will be a common source of systematic
4108 error between the electron- and photon-detector analyses. One example lies in the energy normaliza-
4109 tion of the scattering process. The analyzing power is a function of both electron energy and photon
4110 energy, so these must be precisely determined. The photon wavelength will be determined to better
4111 than 0.1 nm and the electron energy to 0.05%, which leads to an uncertainty at the level of 0.03%.
4112 A similarly small uncertainty will come from radiative corrections, which are calculable [312] with
4113 high precision and will contribute at the level of 10^{-3} .

4114 Helicity-correlated changes in luminosity of the laser/electron interaction point can introduce a
4115 false asymmetry. Various causes of luminosity variation must be considered, such as electron beam
4116 intensity, beam motion or spot-size variation. The control of helicity-correlated beam asymmetries
4117 is now a standard technology at Jefferson Lab, and typically achievable results (few part per mil-
4118 lion intensity, 10's of nanometers beam motion, $<10^{-3}$ spot size changes) will suitably constrain
4119 the electron-photon crossing luminosity variations. Another possible source of false asymmetry
4120 would be electronics pickup of the helicity signal, which could potentially impact an integrating
4121 photon analysis. However, the demands of the primary experiment for isolation of the helicity sig-
4122 nal exceed those for polarimetry by several orders of magnitude. In addition, the laser polarization
4123 reversal provides an additional cancellation for asymmetries correlated to the electron beam helicity.
4124 For these reasons, beam asymmetries are expected to be a negligible source of uncertainty in this
4125 measurement.

4126 A more significant potential source of error comes from the uncertainty in the photon polar-
4127 ization. As described above, the determination of photon polarization will be improved with the
4128 analysis of light reflected from the cavity input mirror, which will allow precise control and mea-
4129 surement of the polarization state injected into the cavity. This will be supplemented by an insertable
4130 stage to measure the polarization in the interaction region directly. The circular polarization of the
4131 laser will be determined and cross-checked with a precision of 0.2%. If studies do not demonstrate
4132 that this can be achieved within the high-gain cavity, the alternative laser system will need to be
4133 developed.

4134 **17.4.2 Systematic Errors for the Electron Detector**

4135 The electron detector is composed of 4 planes of silicon microstrips normal to the electron beam
4136 trajectory and positioned on the low-energy side of the beam trajectory in the dispersive chicane.
4137 Electrons which have given up energy to a scattering process are separated from the primary beam
4138 by the third chicane dipole, and the energy of a detected electron is implied by the distance of the
4139 track from the primary beam with a dispersion of about 0.45% of the beam energy per millimeter.
4140 Models of the chicane magnets are used to calculate the electron energy as a function of position

4141 in the detector. The effects of electronics noise and non-directional backgrounds are reduced by
 4142 triggering on tracks which are restricted to very small angles relative to the beam. The trigger can
 4143 be adjusted for the range of track angles and number of planes used in the track, including a single
 4144 plane trigger. The efficiency of individual strips can also be measured using data from the multiple
 4145 planes.

4146 The silicon detector may also be sensitive to synchrotron light, and while the detector is not
 4147 in line-of-sight to synchrotron emission in dipole 3, synchrotron photons rescattered in the beam
 4148 pipe may be a problem. The 11 GeV upgrade includes a gate valve installed on the straight-through
 4149 beam pipe, to block synchrotron light from the first dipole of the chicane during operation of the
 4150 polarimeter.

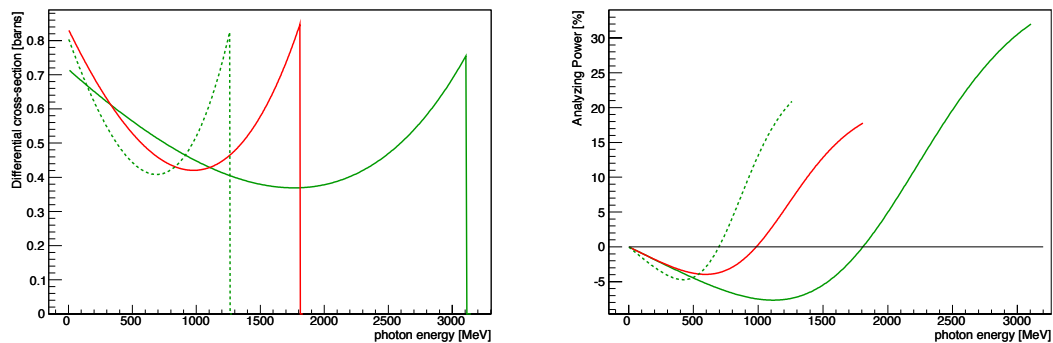


Figure 159: *The cross-section and asymmetry plotted versus Compton scattered photon energy for the Hall A polarimeter at 11 GeV for 532 nm (green solid line) and 1064 nm (red line) laser options, and at 6.6 GeV for the 532 nm laser (green dotted line).*

4151 The cross-section and asymmetry as a function of Compton scattered photon energy is plotted in
 4152 Figure 159 for 11 GeV electron beam. The Compton edge (the kinematic endpoint of the Compton
 4153 energy spectrum) is observed in the electron detector and used to calibrate the distance of the detec-
 4154 tor from the primary beam. In addition, the asymmetry as a function of photon energy k exhibits a
 4155 zero crossing. Determining the location of this asymmetry zero crossing (0xing) provides a second
 4156 absolute energy calibration point, so together the Compton edge and 0xing can be used to calibrate
 4157 two parameters: the detector location relative to the beam and the strength of the magnetic field
 4158 in dipole 3. In this way, survey results and magnetic field maps serve as a cross-check to a beam-
 4159 based self-calibration of the Compton energy spectrum. The precision of this calibration is limited
 4160 by delta-ray production in the microstrips, which distorts the measured spectrum, and efficiency
 4161 variations between the microstrips.

4162 In operation at low beam energies, the 0xing is close to the primary beam: for HAPPEX-II, the
 4163 separation was approximately 5 mm. At this proximity, background rates were extremely sensitive
 4164 to beam tuning in the injector and RF phase corrections in the linacs, presumably due to energy
 4165 tails. At 11 GeV with the IR laser, the 0xing will be around 16mm from the primary beam, which
 4166 should allow for robust operation. The analyzing power for the measured electron distribution can
 4167 be very accurately determined with use of this self-calibration, with the systematic error dependent
 4168 upon the specifics of the analysis approach.

4169 For an example of a specific analysis technique, consider an asymmetry measured from the
 4170 Compton edge to some selected cut-off in the electron spectrum. This would need to be compared
 4171 to the theoretically expected average asymmetry, which would be sensitive to the energy cut-off

4172 threshold. In an analysis that computed a single count-rate asymmetry from the integrated rate
4173 from the Oxing to Compton edge, an error in determining the Oxing would act approximately as a
4174 dilution effect (as the asymmetry is small in the neighborhood of the Oxing). While there may be
4175 statistical variation in determining the Oxing, this would be merely a source of statistical noise. If the
4176 systematic bias in determining the Oxing is estimated to be within $1/10$ μ strip width (about $25 \mu\text{m}$),
4177 this would imply a systematic bias in the analyzing power of about 0.15%. While this is a useful
4178 estimate of the error due to energy calibration, this analysis relies on integrating the rate-weighted
4179 average asymmetry over the accepted energy range, and so would likely suffer a larger contribution
4180 of systematic error due to efficiency variations in the μ strips.

4181 Other analysis techniques which would be less sensitive to efficiency variations would rely on
4182 averaging asymmetries over a range of strips, rather than averaging the count rate. In this case, both
4183 energy calibration points are needed to determine the expected asymmetry at each μ strip. Because
4184 the Compton edge will be extracted from the rate spectrum, efficiency variation between the silicon
4185 strips must be minimized and well-known to avoid biasing this determination. In addition, careful
4186 study of the contribution of delta-ray production, which distorts the asymmetry spectrum at the
4187 Oxing and the rate spectrum at the Compton edge, will also be important. Here also, a high strip
4188 efficiency will be helpful, by providing a high-efficiency for vetoing events with multiple tracks.
4189 Strip-by-strip efficiencies can be calculated by comparing track-hit efficiency between the multiple
4190 planes of the μ strip detector, and comparisons between planes can also help benchmark corrections
4191 for delta-ray production. A uniform and high-efficiency detector will be an important component of
4192 this system.

4193 It is worth noting a measurement using only the last, single silicon strip at the Compton edge
4194 will be capable of 0.4% statistical precision on time-scales of around one hour. The rate of change
4195 of the asymmetry in this region is only 0.5% / mm. Locating this strip, relative to Compton edge, to
4196 a little better than half its own width should provide a robust accuracy on the analyzing power better
4197 than 0.4%. This technique would be sensitive to determination of the location of the Compton edge,
4198 but otherwise very insensitive to other calibration parameters.

4199 Similarly, if the electron detector can be moved close to the primary beam (about 9 mm from the
4200 primary beam for the IR laser at 11 GeV) the asymmetry minimum could be detected. The statistical
4201 power is much lower in this region, with a single strip requiring 20 hours to achieve 0.4% statistical
4202 precision on the polarization (assuming signal-noise ratio of 10:1). However, here the asymmetry is
4203 not changing with position, so there is minimal calibration error in selecting a strip in this minimum.
4204 Beam position and angle may vary the asymmetry minimum over hundreds of microns during this
4205 time span, but such changes can be tracked using beam position monitors or the Compton edge,
4206 and the analyzing power varies by only about 0.4% of itself over a range of $\pm 300 \mu\text{m}$, suggesting
4207 minimal corrections will be necessary .

4208 Cross-checks between calibrations and techniques should provide convincing evidence that the
4209 system is well understood. Given these considerations, it seems likely that the calibration of the
4210 electron detector will be understood at the level of 0.3% or better.

4211 Regardless of the analysis, contributions from deadtime and pileup will need to be understood.
4212 The fast-counting DAQ can take very high rates with low deadtimes, and deterministic deadtime in-
4213 tervals are enforced in readout and acquisition electronics stages. While the total Compton-scattered
4214 data rates may as high as 1 MHz, rates in individual strips will be reduced by segmentation to
4215 < 15 kHz, which will allow dead-time and pile-up systematic errors to be controlled at the level
4216 of 0.2%. The high statistical power of the measurement is of significant use here; high precision
4217 studies can be performed to benchmark models of the readout system against changes in the laser
4218 power or the parameters of the triggering (preamp levels, logical gate lengths, coincidence levels,
4219 etc).

4220 Backgrounds are also a potential but small source of systematic uncertainty. Backgrounds are
4221 studied with the laser cavity unlocked, allowing both the background level and asymmetry to be
4222 well determined. However, high backgrounds could impact the systematic error due to deadtime or
4223 pile-up corrections. There is also the possibility of backgrounds from Compton-scattered electrons,
4224 which can produce delta rays when scattering in the detector or in its shielding. These tracks can
4225 themselves be sufficiently forward-going to pass the trigger, thus changing the analyzing power as a
4226 function of energy. Simulation will be used to avoid such problems, and studies of track distribution
4227 and electron-tagged photon energy spectra can be used to identify such effects in the data.

4228 Finally, it is perhaps obvious, but worth stating, that beam properties at 11 GeV will be important
4229 for the precision of the electron detector analysis. If simulations reveal that halo backgrounds for
4230 the electron detector are likely to be large in the region ~ 15 mm from the primary beam, then the
4231 green laser option would be required for high precision polarimetry. Using 532 nm light in a cavity
4232 would put the zero-crossing about 33 mm from the primary beam. It is also worth noting that the
4233 single-strip analyses would be also be improved with the higher resolution and larger asymmetries
4234 (and larger distances from the primary beam) available from a green laser.

4235 **17.4.3 Systematic Errors for the Photon Detector**

4236 The precise determination of the analyzing power as a function of energy is more difficult for the
4237 photon calorimeter than for the electron detector due to the width and shape of the detector response
4238 function. In order to fit the asymmetry as a function of detected photon energy, the analyzing power
4239 must be calculated as a convolution of the response function with the theoretical analyzing power
4240 curve. The response function shape and energy calibration can be simulated, and studied using the
4241 photon tagging through coincidence triggers with the electron detector.

4242 In general, determining the effect of a low-energy threshold on the analyzing power depends
4243 sensitively on the shape of the response function; at low energies this is a major source of uncer-
4244 tainty. At high energies, the improved resolution and consistency of the response function shape
4245 over the range of interest should significantly reduce this problem. As noted above, the photon
4246 calorimeter will be upgraded to better contain showers from high energy photons, with the primary
4247 objective to provide a response function which scales linearly over a broad range of energy.

4248 The pulse-counting analysis in the photon detector is also sensitive to pile-up, which distorts
4249 the asymmetry distribution. Background and rate distributions will serve as inputs to simulation for
4250 corrections to the analyzing power. In the current Hall A analysis, pile-up corrections are estimated
4251 at the level of 1%, and the effect can be controlled at a level better than 10% of itself. Deadtime
4252 corrections, which can vary significantly with background conditions, will also represent a potential
4253 systematic uncertainty.

4254 Uncertainties related to the threshold, response function shape, absolute energy calibration,
4255 deadtime and pile-up can also be eliminated by integrating the photon calorimeter signal, with-
4256 out threshold [313]. These previous problems are then replaced with a requirement on the linearity
4257 of the average response to the photon energy. Because the analyzing power integral is energy-
4258 weighted, the statistical figure-of-merit is not badly degraded by the negative asymmetry region at
4259 low photon energies.

4260 The PREX experiment, with a beam energy near 1 GeV, relied on the integrating photon method
4261 for polarimetry at the level of 1% precision. Simulations of the photon response function were
4262 sufficient to control the analyzing power uncertainties for those measurements. The dominant un-
4263 certainty in the asymmetry measurement arises from variation in the photomultiplier response with
4264 changes in average rate which introduces a systematic error through background subtraction.

4265 At high energies, with the ability to study response function with the electron-detector-tagged

4266 photon beam over a large fraction of the energy range, the photon detector analyzing power nor-
4267 malization uncertainty in the range of 0.3% should be achievable. Characterization of the pho-
4268 totube response as a function of rate and pulse-size will also be important. As described above,
4269 Bremsstrahlung scattering from apertures in the interaction region, coupled with the characteristics
4270 of the 11 GeV electron beam, present a possible source of background.

4271 **17.5 Summary of Compton Polarimetry**

4272 The prospects for 0.4% Compton polarimetry are excellent. This ambitious goal will require vig-
4273 orous and dedicated efforts to reduce sources of systematic uncertainty. It is expected that some
4274 significant fraction of data production time will be used for studies of the Compton polarimeter sys-
4275 tem which are not disruptive to the experiment, for example, scans of detector positions, laser power
4276 and polarization, and data acquisition parameters. The scattering asymmetry at 11 GeV is relatively
4277 large which, for some analysis approaches, will provide statistical precision at the level of $\sim 0.5\%$ in
4278 a few minutes of data collection. Given this high statistical power, these studies will be an effective
4279 method for constraining many of the possible experimental systematic uncertainties.

4280 The future use of the Hall A polarimeter at 11 GeV will be a very different situation from
4281 the recent operation. The dominant systematic errors in recent operation lay in the determination
4282 of the analyzing power and laser polarization. Operating at lower energies the asymmetries were
4283 significantly lower and therefore the statistical power was worse. In addition, the limits of systematic
4284 uncertainty had not been pushed by demands of the experiment precision.

4285 The 0-Xing “self-calibration” of the electron detector was attempted for the first time for the
4286 HAPPEX-II and HAPPEX-He measurements. The situation was complicated due to the low beam
4287 energy of around 3 GeV, which not only reduced the average asymmetry but also reduced the ra-
4288 tio of Compton-scattered photon energies and the electron energies. At 3 GeV, the zero-crossing
4289 was about 5 mm from the primary beam, which was as close as the electron detector could get to
4290 the beam. Geometric efficiencies at the edge were a significant complication in this approach. In
4291 addition, the microstrip detector was damaged and displayed low and uneven efficiency, which com-
4292 plicated the analysis. The estimated systematic errors for that analysis which were not associated
4293 with these efficiency issues are consistent with Table 33. A similar technique has been successfully
4294 employed in the Hall C Compton polarimeter at 1 GeV, where a larger chicane and green laser were
4295 used to optimize for the low beam energy during the Qweak experiment. While analysis is ongoing,
4296 the current status indicates that the ultimate precision will be significantly better than 1%.

4297 For the photon detector, the integration readout method has been successfully used in the HAP-
4298 PEX-3 and PREX experiments, with the primary limitations being the characterization of the photo-
4299 tube response over the range of signal levels. The rapid access to high statistical power expected for
4300 11 GeV operation, which is so powerful for cross-checking potential sources of systematic uncer-
4301 tainty, has never before been available to the Hall A Compton. Coincidence measurements between
4302 the photon and electron detectors will also provide a significant cross-check to the response function
4303 and energy calibrations. As described above, recent improvements in available laser power, analy-
4304 sis techniques, laser polarization measurements, and the favorable kinematics of the higher electron
4305 beam energy have opened the door to 0.4% precision Compton polarimetry for the SoLID program.

4306 **17.6 Møller Polarimetry**

4307 This section describes our plans for precision Møller polarimetry in Hall A. Møller polarimetry
4308 will provide a useful cross check on beam polarization measurements performed with Compton
4309 scattering, gathering high statistics in a short amount of time and with different attendant systematic

4310 errors. The principal challenge is to achieve high precision ($\sim 0.5\%$ on the beam polarization)
 4311 through careful control of the systematic effects.

4312 Electron-electron scattering, with arbitrary spin orientation for the beam and target, has been
 4313 calculated in lowest order QED by many authors [314–317], and the basic formulas for (non parity-
 4314 violating) polarized Møller scattering are given in many places. For example, following [318], the
 4315 cross section at high energies in the center of mass frame can be written as

$$\frac{d\sigma}{d\Omega_{\text{cm}}} = \frac{\alpha^2 (3 + \cos^2 \theta)^2}{s \sin^4 \theta} [1 - P_{\text{long}}^{\text{B}} P_{\text{long}}^{\text{T}} A_{\text{long}}(\theta) - P_{\text{tran}}^{\text{B}} P_{\text{tran}}^{\text{T}} A_{\text{tran}}(\theta) \cos(2\phi - \phi_{\text{B}} - \phi_{\text{T}})] \quad (30)$$

4316 Here, $s = (2E)^2$ for electron energy E , θ is the scattering angle, $P_{\text{long,tran}}^{\text{B,T}}$ are the longitudinal and
 4317 transverse polarizations of the beam and target electrons, ϕ is the azimuthal scattering angle, and
 4318 $\phi_{\text{B,T}}$ are the azimuthal angles of the beam and target polarizations. The analyzing powers are

$$A_{\text{long}}(\theta) = \frac{(7 + \cos^2 \theta) \sin^2 \theta}{(3 + \cos^2 \theta)^2} \quad \text{and} \quad A_{\text{tran}}(\theta) = \frac{\sin^4 \theta}{(3 + \cos^2 \theta)^2} \quad (31)$$

4319 which are maximized at $\theta = 90^\circ$ with $A_{\text{long}}(90^\circ) = 7/9$ and $A_{\text{tran}}(90^\circ) = 1/9$. The electron
 4320 laboratory scattering angle for $\theta = 90^\circ$ is $(2m/E)^{1/2}$, rather small for GeV electron beams.

4321 A Møller polarimeter makes use of Eq. 30 to measure the beam polarization vector $\vec{P}^{\text{B}} =$
 4322 $(P_{\text{long}}^{\text{B}}, P_{\text{tran}}^{\text{B}})$ by incorporating a target with a known electron polarization vector $\vec{P}^{\text{T}} = (P_{\text{long}}^{\text{T}}, P_{\text{tran}}^{\text{T}})$
 4323 into a spectrometer to detect one or both of the scattered electrons. By reversing the beam polar-
 4324 ization vector $\vec{P}^{\text{B}} \rightarrow -\vec{P}^{\text{B}}$, one can deduce its magnitude, and perhaps its direction, through the
 4325 analyzing powers (31). The ideal Møller polarimeter, for determining longitudinal beam polariza-
 4326 tion $P_{\text{long}}^{\text{B}}$, is set at $\theta = 90^\circ$ with maximal (minimal) target longitudinal (transverse) polarization
 4327 $P_{\text{long(tran)}}^{\text{T}}$.

4328 We describe two techniques for getting as close as possible to the ideal Møller polarimeter.
 4329 One is based on iron foil targets, in which the outer atomic electrons are polarized, and the other
 4330 is based on an atomic hydrogen target. In the case of the iron foil target design, polarimeters at
 4331 Jefferson Lab have already described control of systematic errors near the 0.5% level. We describe
 4332 upgrades already in progress in Hall A in preparation the general 12 GeV program at Jefferson Lab
 4333 which will enable that level of performance. While potentially very precise, such a polarimeter re-
 4334 quires calibration from a body of magnetization studies with iron, and this normalization has never
 4335 been cross-checked to the required precision. In addition, iron foil polarimeters require dedicated
 4336 measurements at low current, and so measured polarization must be interpolated between spot mea-
 4337 surements and extrapolated to the high currents used for production. Møller polarimetry with an
 4338 atomic hydrogen target, in contrast, would be able to provide a continuous, non-invasive polariza-
 4339 tion measurement and would not require external calibration for accuracy at the few 10^{-3} level, but
 4340 would be a new technology requiring significant technical R&D.

4341 The strategy for Møller polarimetry, therefore, is to complete the upgrade of the Hall A iron foil
 4342 polarimeter and seek to maximize the accuracy of this device. A cross-calibration with the upgraded
 4343 Compton polarimeter should demonstrate that normalization of the target foil polarization is under
 4344 control. The atomic hydrogen polarimeter option could be pursued if it is needed to confirm results
 4345 of those studies.

4346 17.7 The Hall A Upgrade: “High Field” Iron Foil Targets

4347 Nearly all high energy Møller polarimeters operated to date [322, 323, 326–331] make use of tilted
 4348 ferromagnetic foil targets. High permeability alloys coupled with \sim few hundred gauss magnetic

Variable	Hall C	Hall A:	
		High Field Foil	Hydrogen
Target polarization	0.25%	0.25%	0.01%
Target angle	‡	‡	*
Analyzing power	0.24%	0.20%	0.10%
Levchuk effect	0.30%	0.20%	*
Target temperature	0.05%	0.05%	*
Dead time	‡	0.10%	0.10%
Background	‡	0.10%	0.10%
Others	0.10%	0.10%	0.30%
Total	0.47%	0.42%	0.35%

*: Not applicable ‡: not estimated

Table 34: Systematic error summary for Møller polarimeters at JLab, including anticipated uncertainties for future prospects. The Hall C polarimeter [319] uses a high field pure iron target [320, 321] with a simple two-quadrupole spectrometer. Uncertainties quoted for that system are taken from a publication detailing calibration of the analyzing power. The current Hall A Møller polarimeter [322, 323] uses a tilted ferromagnetic allow target, and a spectrometer with a dipole magnet following three quadrupoles. A high-field pure iron target upgrade is underway with plans for an additional quadrupole in the spectrometer for high energy operation. Uncertainties for this system are the expected performance after the upgrade. Research and development for a hydrogen gas target [324, 325] provides the basis for a second continuously-running high precision polarimeter to complement the Compton apparatus.

4349 fields preferentially polarize in the plane of the foil, so tilting the foil at a moderate angle gives
4350 a substantial longitudinal target polarization. Calculating the effective polarization, however, is
4351 typically the limiting systematic error, and such devices cannot ultimately do better than several
4352 percent precision.

4353 A different approach [319], implemented in Hall C at Jefferson Lab, using a high magnetic field
4354 perpendicular to the foil plane [320, 321], has reported 1% precision on the beam polarization. It is
4355 this target design that we are adopting for SOLID, and indeed are already preparing to implement
4356 in Hall A.

4357 Below we describe the principles of “high field” iron foil targets, the plans for redesign of
4358 the scattering chamber, and modifications to the existing spectrometer including simulations for
4359 operation at high energy.

4360 17.7.1 Ferromagnetic Foil Targets

4361 Materials respond to external magnetic fields because atomic electrons, with spin and orbital angular
4362 momentum, align themselves to an applied field. However, with a Bohr magneton equal to
4363 5.8×10^{-5} eV/tesla, the magnetic energy at several tesla is still much smaller than the thermal energy
4364 at room temperature, so the effects of magnetic fields in most materials (“diamagnetism” and
4365 “paramagnetism”) are quite small.

4366 Ferromagnetism, on the other hand, is a quantum mechanical phenomenon in which a subset
4367 of atomic electrons in some elements and alloys spontaneously align. These alignments happen in
4368 localized domains, which themselves are randomly oriented. However, the application of relatively

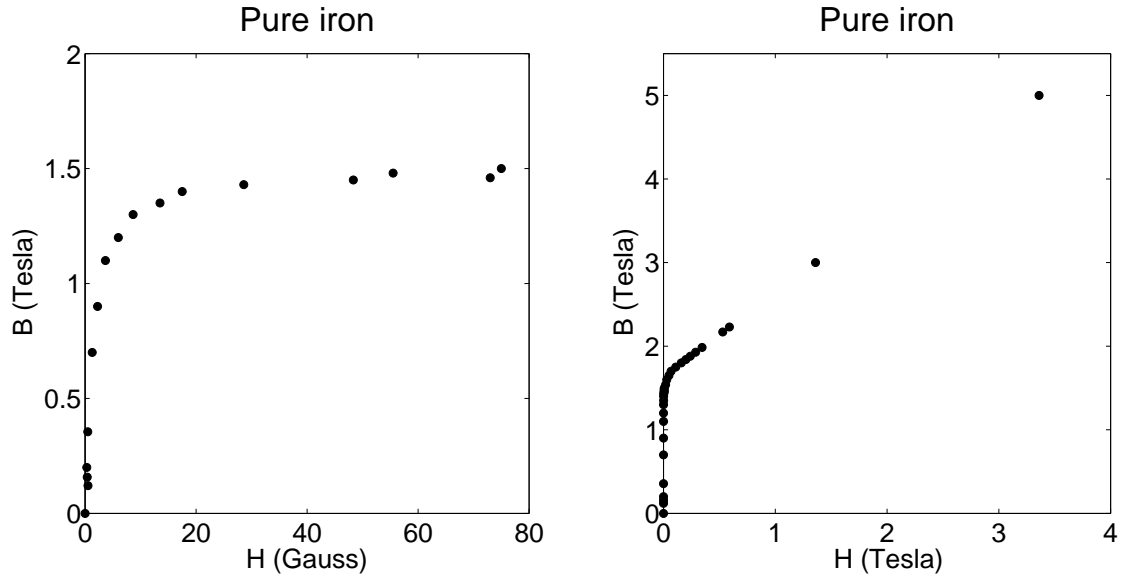


Figure 160: Magnetization curves for pure iron, from <http://www.fieldp.com/magneticproperties.html>. We use CGS units, so both B and H are properly measured in Gauss, but $1 \text{ Tesla} = 10^4 \text{ Gauss}$. Both plots are of the same data set, but the horizontal scale is much expanded on the right.

4369 small magnetic fields cause the domains themselves to line up, leading to large induced magnetic
4370 fields.

4371 Magnetostatics (in CGS units) is governed by the equations $\vec{\nabla} \cdot \vec{B} = 0$ and $\vec{\nabla} \times \vec{H} = 4\pi\vec{j}/c$
4372 where \vec{B} is the magnetic field, \vec{j} is the free current density, and \vec{H} absorbs the magnetic response
4373 of the medium. To be precise, $\vec{H} \equiv \vec{B} - 4\pi\vec{M}$ where the magnetization \vec{M} is the magnetic dipole
4374 moment per unit volume. It is the magnetization \vec{M} that we interpret, ultimately, as the polarization
4375 of target electrons.

4376 For *linear* materials (which *do not* include ferromagnets), we define the magnetic permeability
4377 μ through $\vec{B} = \mu\vec{H}$. It is nevertheless a habit to speak of μ for ferromagnetic materials in terms of
4378 vector magnitudes, that is $B = \mu H$. For most materials, μ is a constant slightly larger than unity.
4379 In ferromagnets, however, μ is a strong function of H and can be very large.

4380 Figure 160 shows magnetization data for pure iron. At several tens of gauss of “applied” field
4381 H , the magnetic field B saturates at ~ 1.5 tesla because the domains are aligned. The resulting
4382 magnetization corresponds to ~ 2 Bohr magnetons per iron atom, that is, roughly two electrons
4383 worth of magnetic dipole moment in *each* iron atom. As H reaches and exceeds several tesla, the
4384 magnetization field simply adds directly to the applied field. The value of μ rises to several thousand
4385 for a few gauss, and then decreases to unity for fields much greater than saturation.

4386 Møller polarimeters using “low field tilted” foil targets operate in the region where $\mu \gg 1$. In
4387 fact, they generally make use of special alloys that have exceptionally high values of μ , that is,
4388 saturate at relatively low values of H . In this case $\vec{B} = 4\pi\vec{M}$ to a very good approximation. Since
4389 $\vec{\nabla} \cdot \vec{B} = 0$ implies that perpendicular components of \vec{B} are continuous across the foil surface, and
4390 since $B = H$ outside the foil is hundreds of times smaller than the magnetization, the only way to
4391 meet the boundary condition is for \vec{M} to point in the plane of the foil. (Of course, this argument
4392 breaks down if the foil is at right angles to the applied field.) Thus a target tilted at some angle, say
4393 $\sim 20^\circ$ provides a dominantly longitudinally polarized target for an incident electron beam in the

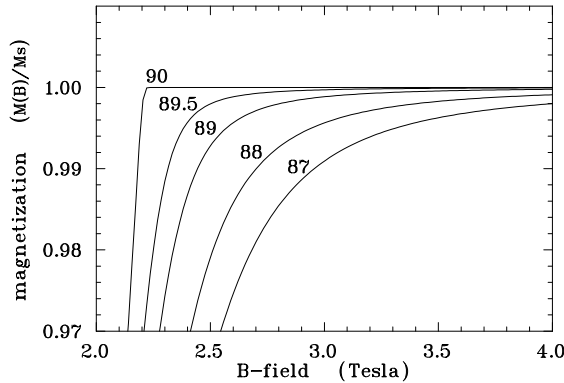


Figure 161: Simulations of foil magnetization for angles between the foil plane and the B-field direction close to 90 degrees. Errors due to imperfect alignment or a slight warp of the foil could produce such a result. Taken from [320, 321], which uses a calculation [336] of magnetization curves for uniformly magnetized prolate ellipsoidal domains.

4394 same direction as the applied field.

4395 The limiting precision of polarimeters using such targets, however, is extracting the target elec-
 4396 tron spin polarization from the magnetization. The ratio of “spin” magnetization M_s to the total can
 4397 be written as [332] $M_s/M = 2(g' - 1)/g'$, with g' close to, but somewhat less than 2. The attendant
 4398 uncertainties in g' for the alloys used in tilted target applications, limit one’s knowledge of the target
 4399 polarization to several percent.

4400 Measurements in *pure* iron or nickel, however, point to very precise knowledge of their magne-
 4401 tization parameters [333, 334]. The approach used by the Basel/Hall C group [319–321] is to not
 4402 only use pure iron foil targets, but to polarize them with a very high (several tesla) field, provided
 4403 by superconducting coils. This overcomes limitations of a not-so-large value of μ for pure iron.

4404 It is important to note that the magnetization of the foils in the strong longitudinal field has not
 4405 been measured, but is taken from published data on the properties of bulk iron, which claims an ac-
 4406 curacy of $\sim 0.1\%$. The orbital contributions to the magnetization of about 5% can be evaluated and
 4407 subtracted using the magneto-mechanical factor, measured by other dedicated experiments [335].
 4408 With strong external fields of 3-4 T several additional correction of about 0.5% have to be made to
 4409 compensate for extra orbital momenta and other complex effects. These corrections are tempera-
 4410 ture dependent. It will be important to carefully evaluate the literature on these measurements and
 4411 their interpretation to verify that the uncertainty is not larger than a few 10^{-3} . For example, it is
 4412 apparent that the anomalous magnetic moment of the electron has not been accounted for in recent
 4413 publications, amounting to a correction of more than 0.2% to the target electron spin polarization.

4414 Calculations of the longitudinal magnetization of a foil placed perpendicularly (or nearly so) to
 4415 an applied field are quite difficult. Figure 161, taken from [320, 321], shows the magnetization
 4416 (relative to its maximum value) of a pure iron foil as a function of applied magnetic field, for
 4417 different angles between the field and the normal to the foil. To be sure, this calculation is in fact of
 4418 a model of non-interacting prolate ellipsoidal domains [336], and the extent to which it applies to a
 4419 pure iron foil is not clear.

4420 A polarimeter based on this “high field” target was constructed in Hall C at Jefferson Lab [319].
 4421 The device has performed well, with experimenters claiming accuracy of 1% or better on the lon-
 4422 gitudinal beam polarization. Much of the updated design of the Hall A Møller polarimeter is based
 4423 on the Hall C experience.

4424 17.7.2 Simplified Møller Scattering Target Assembly

4425 Quite a number of small, systematic effects need to be considered in order to achieve 0.5% uncer-
 4426 tainty on the longitudinal beam polarization. For example, Figure 161 gives an idea of the tolerance

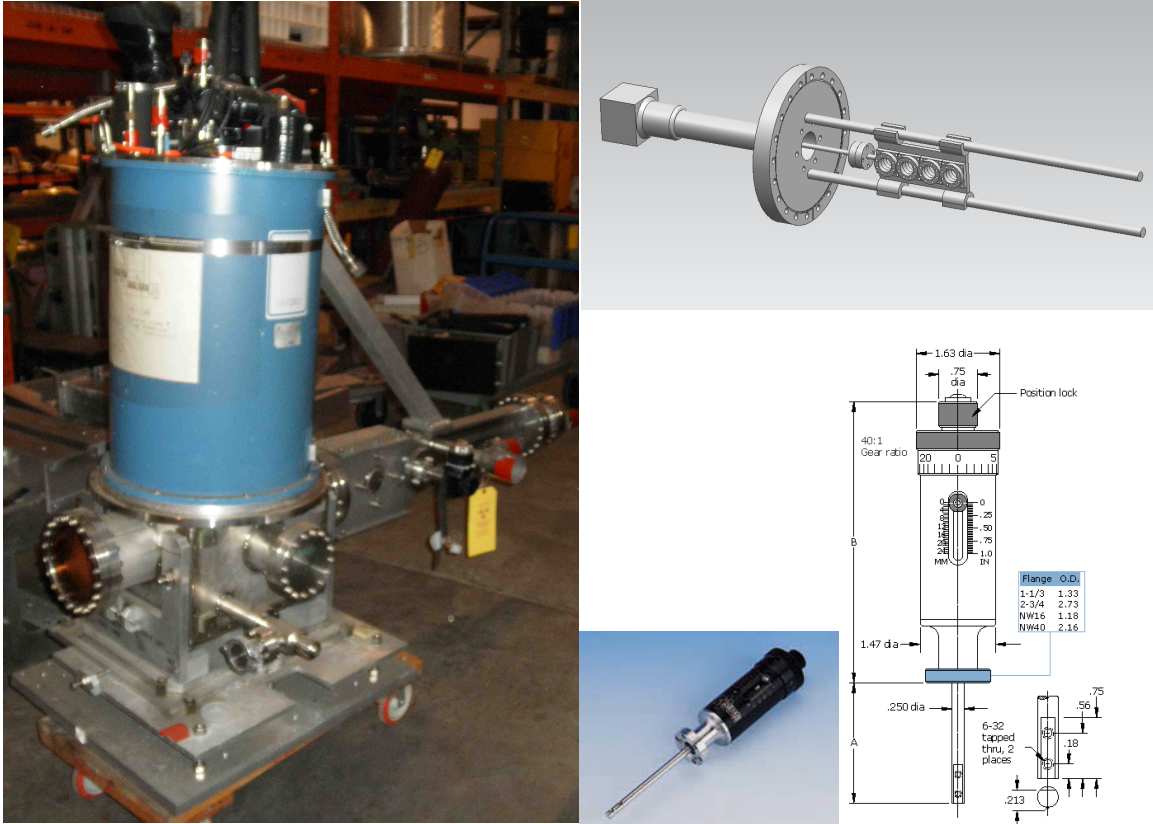


Figure 162: *Left*: Existing Hall A target chamber with ladder actuator extending off to the right. The magnet cryogenic system sits on top of the chamber. Our plan is to replace the actuator assembly, here shown supported by a boom attached to the cryo system. *Right*: Design concept for a new ladder actuator system, based on the Hall C design, along with a photo and schematic of the MDC660034 linear motion feedthrough.

4427 needed on iron target alignment. In order to be assured of at least 99.8% of the maximum target
 4428 polarization for a field of ~ 3 T, the tolerance on the foil angle misalignment is $\sim 1^\circ$.

4429 Figure 162 includes a photograph of the high-field foil target chamber previously in place in
 4430 Hall A, and some details of our current plans for the upgrade. Our plan is to retain the cryogenic
 4431 magnet system and the target chamber and overall adjustment mechanism, but to replace the target
 4432 actuator assembly. Originally designed to provide adjustments in many degrees of freedom, the
 4433 existing actuator assembly proved unwieldy for regular use. It was also very heavy, and required
 4434 stabilization through a connection to the dewar for the cryogenes. The redesign relies on precision
 4435 construction with fewer adjustable degrees of freedom, and will be much lighter.

4436 In order to interpret the target polarization to high precision, it is imperative that the foil be
 4437 saturated. This can be confirmed by studying the Møller scattering asymmetry as a function of
 4438 applied magnetic field. The cryogenic magnet is limited to fields less than 4 T, so according to
 4439 Fig. 161 we need to have the target angle precise to about 1° . It would be useful to in fact confirm
 4440 the behavior suggested by the figure, by making these measurements with the target arm rotated by
 4441 various angles close to 90° .

4442 **18 Supports and Infrastructure**

4443 **18.1 Magnet Support**

4444 The initial plan used for estimating the cost is to build a stationary frame and distribute the approx-
4445 imate 1000 ton load of the modified CLEO-II magnet section using eight 200 ton enerpac jacks.
4446 Steel plates and large steel blocks and/or large I-beams will be used to distribute the load out over a
4447 safe area. The 200 ton jacks will be used for vertical alignment and have locking rings which allow
4448 for a full mechanical connection and not rely on hydraulic pressure for stationary support.

4449 **18.2 Endcap Support Structure and Motion Mechanism**

4450 The endcap will have a support structure that cradles each half the cylindrical ring. The structure
4451 will be integrated into a track system that is mounted to steel plates resting upon the concrete floor.
4452 The initial design concept for the track system requires a set of longitudinal (downstream direction)
4453 tracks for moving the endcap away from the magnet. A second set of tracks that would separate
4454 the endcap halves in the lateral direction would ride on top of the longitudinal tracks. The endcap
4455 support structure would then be attached to the top lateral track system. Motion can be achieved by
4456 using hydraulic or electric cylinders to push and pull the entire system into position.

4457 **18.3 Support Structure for Equipment Located Inside Cryostat Bore**

4458 The magnet will be located adjacent to the existing Hall A center pivot/target mount area and will
4459 have limited access to the front of the magnet. The insertion of the large angle detector packages
4460 that will reside internal to the cryostat will be accomplished from the downstream side of the magnet
4461 using a supporting framework to roll the packages in and out. This will require the detector hut to
4462 be moved downstream to allow access to the cryostat.

4463 An internal frame system is needed to mount the lead baffles in the PVDIS experiment. See
4464 Figure 163. The frame cannot come into contact with the inside bore of the cryostat. This requires
4465 the frame to span the entire length of the cryostat and mount to the return yoke iron. The rails of the
4466 frame will be fabricated from 4 inch diameter schedule 80 welded stainless steel pipe. Either 304
4467 or 316 grade stainless is acceptable. The downstream end of the rails will have a hemispherical cap
4468 and a stainless steel foot welded on and will be bolted to the downstream collar. The upstream end
4469 of the rail will either be bolted or welded to an annular stainless steel plate. The upstream end of the
4470 frame will be mounted to the frontcup (magenta body inside the red front collar). Since the frontcup
4471 has to be movable to balance the magnetic field on the coils the annular plate will be attached to the
4472 frontcup with studs. This will allow the rail framework to remain stationary if the frontcup has to be
4473 adjusted. The same rail system can be used for the SIDIS experiment for mounting the large angle
4474 calorimeter and GEMs.

4475 **18.4 Power Requirements**

4476 The projected electrical power load is 1.6MVA, maximum current for magnet at 3266A. The present
4477 power consumption for Hall A is less than 1 MVA. So upgrade to the Hall substation to have 2 MVA
4478 is required. (MOLLER Experiment has included the cost (\$300k) for this in their MIE).

4479 The CLEO-II magnet is designed to have a low cryogenic heat load with passive cooling. The
4480 HRS arms will not be operational during SoLID, so it is expected that the refrigeration heat load
4481 will be less than needed for HRS. The refrigeration need for the cryotarget is discussed in the target
4482 section (Section 5).

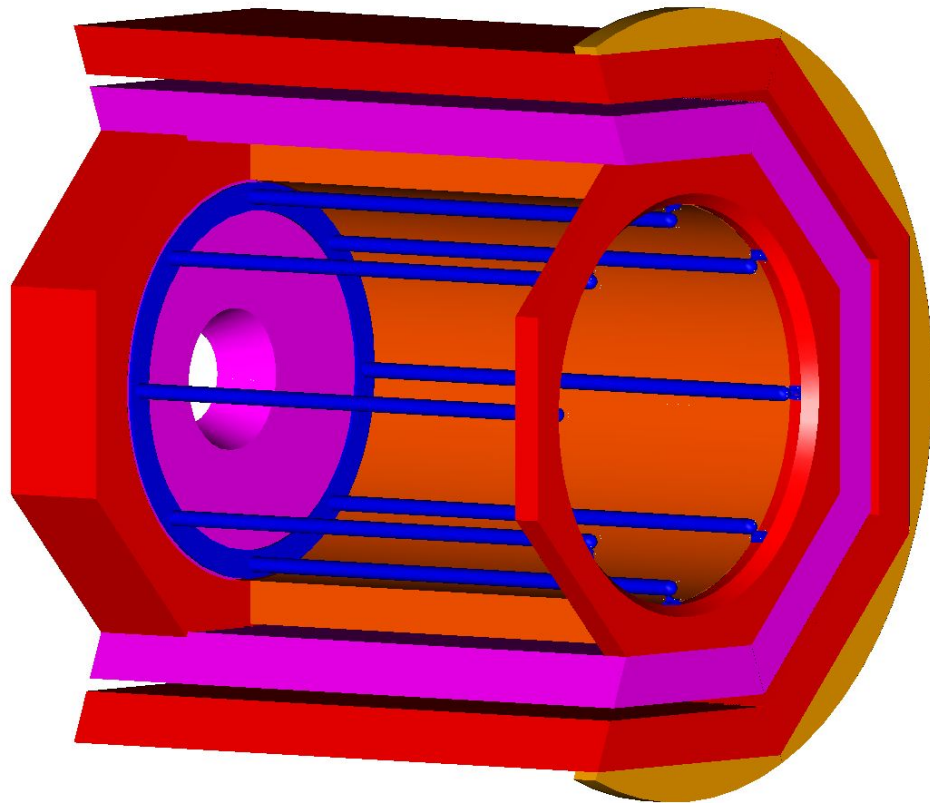


Figure 163: The internal rail system will be used to mount all parts inside the barrel, including PVDIS baffle, SIDIS large angle calorimeter and GEM's

4483 **19 Installation**

4484 **19.1 Experimental Layout**

4485 An initial check of the experimental equipment layout in Hall A has been done and no major ob-
4486 structions have been found. The experiment layout puts the HRS arms at 90 degrees to the beamline
4487 on the left and right. The target is at the nominal pivot location with the center of the CLEO-II
4488 magnet 350 cm downstream of the target center. The SoLID magnet and detectors encompass an
4489 area of 5.8 meters in diameter and 7.3 meters long. With the magnet on beamline center, clearance
4490 to the Hall floor ranges from 10 to 38 cm. This is sufficient area to support the load. The weight
4491 of the CLEO-II magnet, detector hut and detectors is estimated to be 1300 tons. The floor in this
4492 installation region is designed for 250 tons for a 12 square foot pad.

4493 **19.2 Magnet Moving and Placement**

4494 In evaluating the use of the CLEO magnet for SoLID consideration is given to how the CLEO
4495 magnet can be transported into Hall A and how Hall A structurally meets the requirements of CLEO.
4496 The footprint of SoLID utilizing the CLEO magnet will be approximately a 1000 ton load with
4497 dimensions of 24 feet long by 19 feet in diameter. Hall A is 164 feet in diameter. In the area
4498 required to install SoLID, the floor is constructed to carry 250 to 500 tons per 12 square feet.

4499 The existing Hall A equipment consists of the two High Resolution Spectrometers mounted at
4500 the center pivot and all related infrastructure. To accommodate installation of SoLID the target will
4501 need to be mounted 115 cm downstream from the existing support location in order for the magnet
4502 to clear the HRS bearing assembly. Placing the CLEO magnet on beamline height gives 15 inches
4503 clearance to the floor for adequate support and alignment. The location of the HRS arms during
4504 SoLID have two options: remove the existing beam line and move both HRS arms to beam left
4505 locations or place both HRS arms 90 degrees to the beam line. The second option allows more
4506 clearance for SoLID during operation but requires more planning and infrastructure modifications
4507 during installation. These options will be studied further.

4508 The bird's eye view Figure 164 and the back side Figure 165 show the SoLID in Hall A with
4509 two HRS arms on the side. The SoLID detector hut is cut in half and the right side of the return
4510 yoke layers are removed showing the cryostat in orange color.

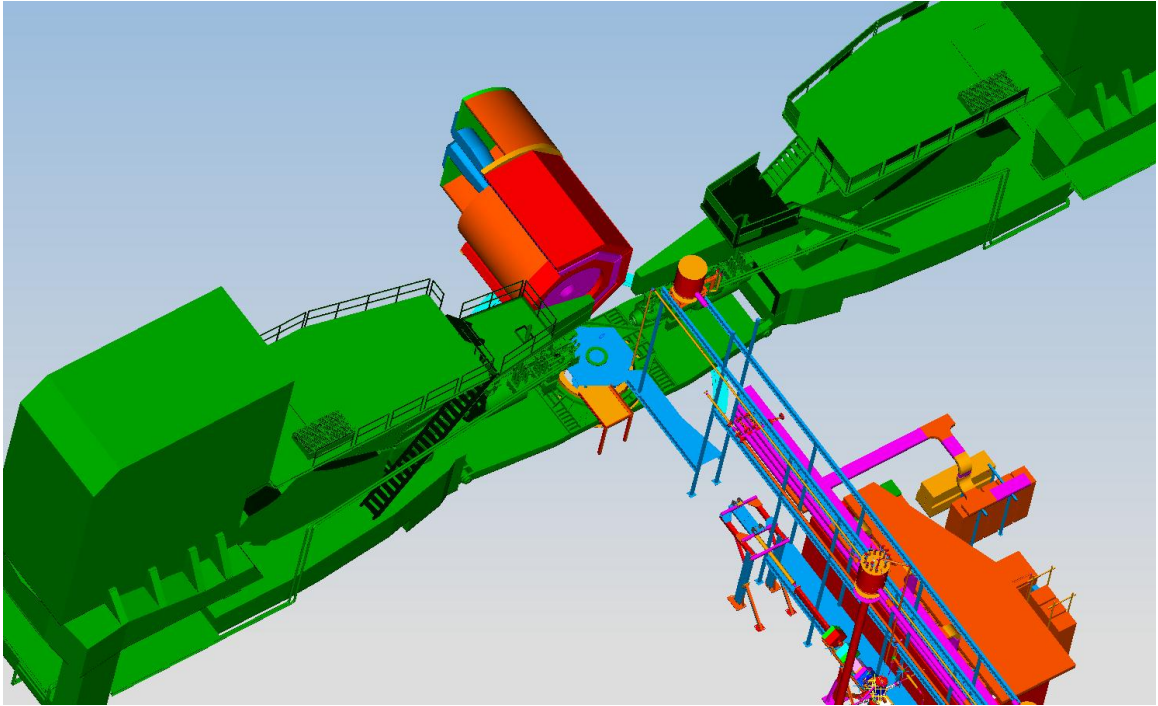


Figure 164: The bird's eye view of SoLID in Hall A

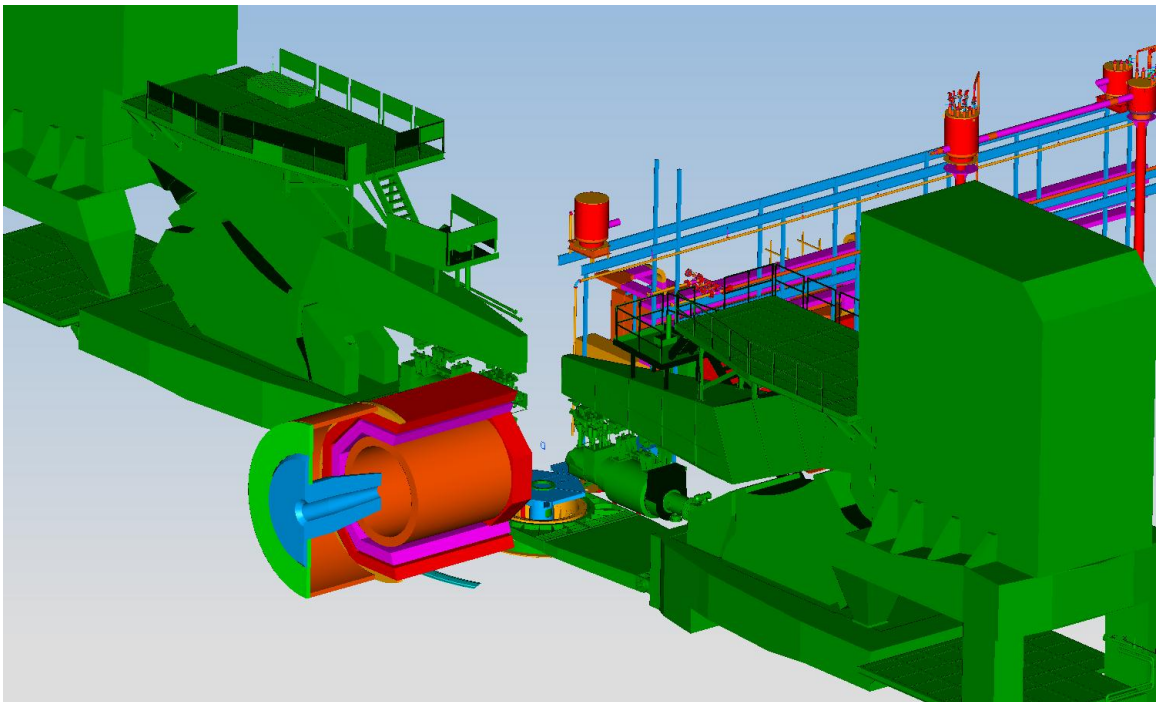


Figure 165: The back side view of SoLID in Hall A

4511 The CLEO-II magnet was disassembled and loaded on trucks for shipping by the Cornell per-
 4512 sonnel with oversight by Jefferson Lab. The coils and cryostat of the CLEO-II magnet have arrived
 4513 at JLab in 2016 and the exterior steel is being shipped as of Spring 2017.

4514 We have identified all of the parts of the CLEO magnet, with sizes and weights. We have
 4515 identified specifically the parts to reuse in building the SoLID magnet, and these have a total weight
 4516 of 1,053k lbs. The cryostat (35k lbs) and power supply are stored in an environment-controlled area
 4517 of approximately 400 square feet. Jefferson Lab projects the use of the CMSA site for storage of all
 4518 parts.

4519 In developing the installation plan for SoLID, the largest part to transport is the cryostat. The
 4520 cryostat is 12.3 feet long, 11.8 feet in diameter and weighs 22 tons. The height of the truck ramp
 4521 into Hall A is limited to 17 feet in height. This will require the cryostat to be moved into the Hall on
 4522 a roller structure rather than a flatbed type truck. This type of procedure has been completed several
 4523 times at Jefferson Lab. See Figure 166, Figure 167, and Figure 168.

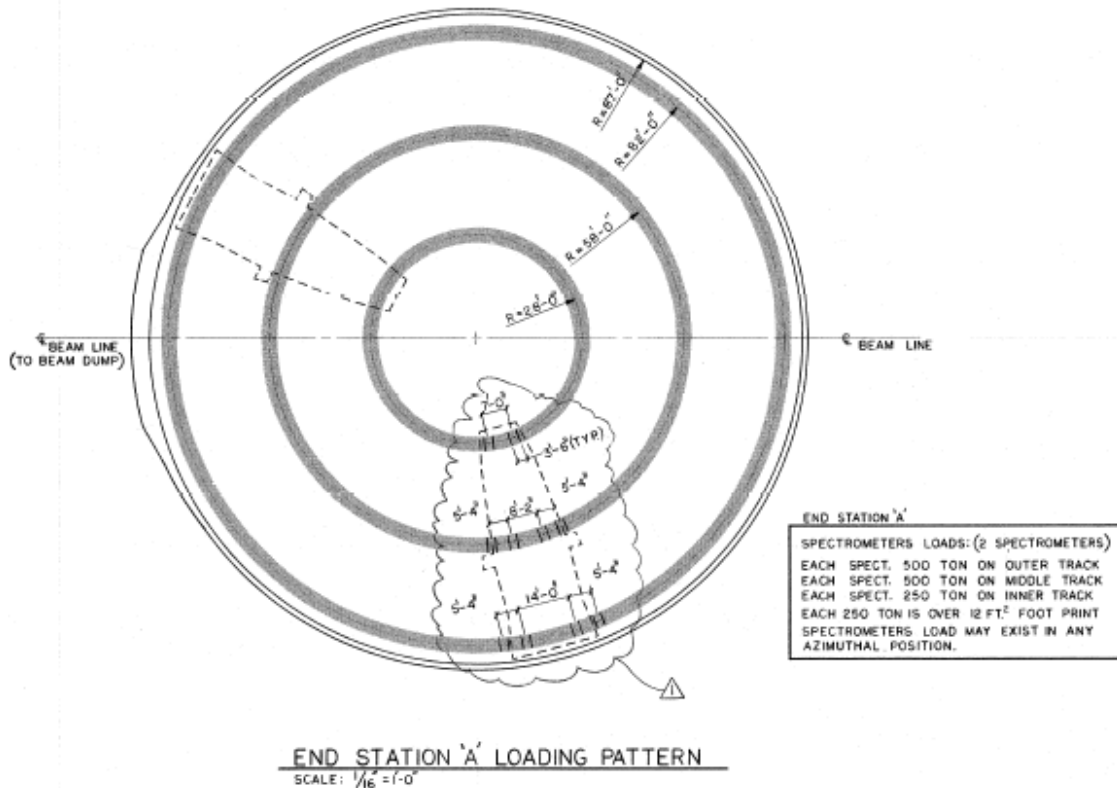


Figure 166: Hall A loading pattern.

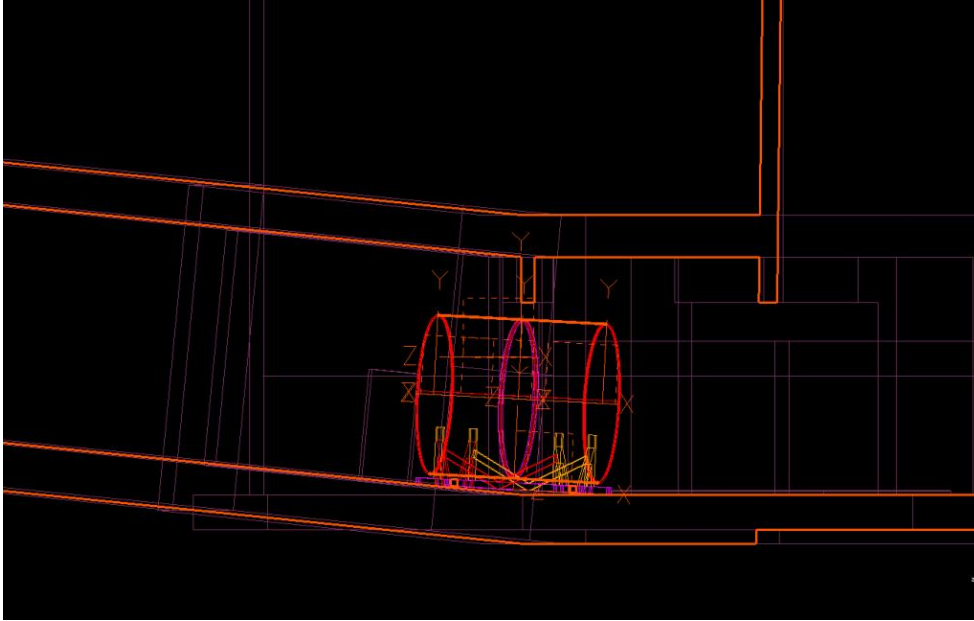


Figure 167: The plan of moving CLEO cryostat through Hall A ramp.

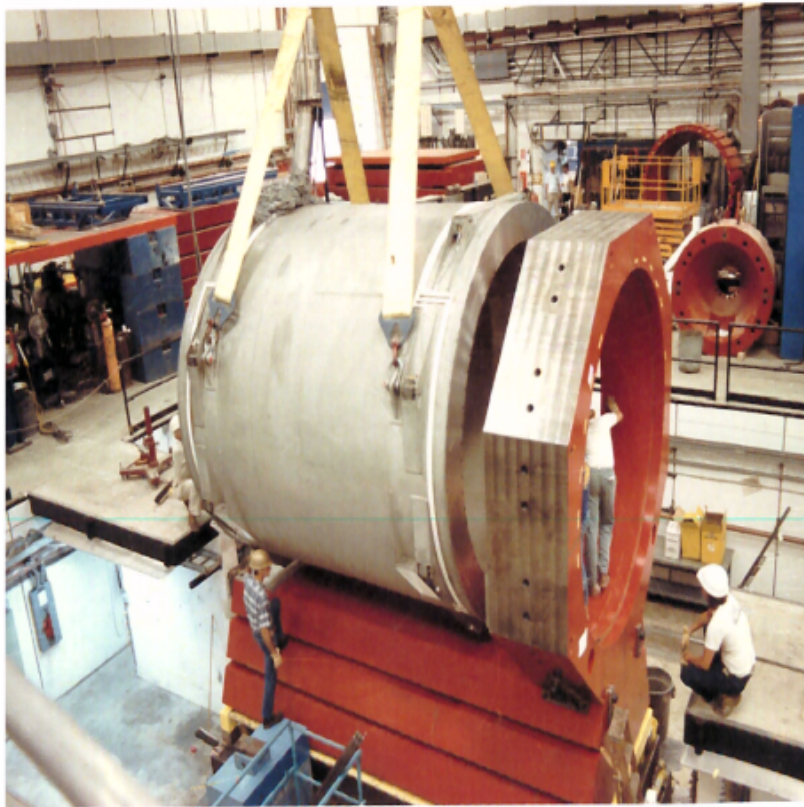


Figure 168: CLEO cryostat lifted during the installation at Cornell.

4524 **19.3 Helium Dewar Support and Upper Access Platform**

4525 An upper personnel access platform that is capable of supporting the helium dewar will be mounted
4526 to the top of the magnet. A similar platform was used for the CLEO II experiments. See Figure
4527 169.

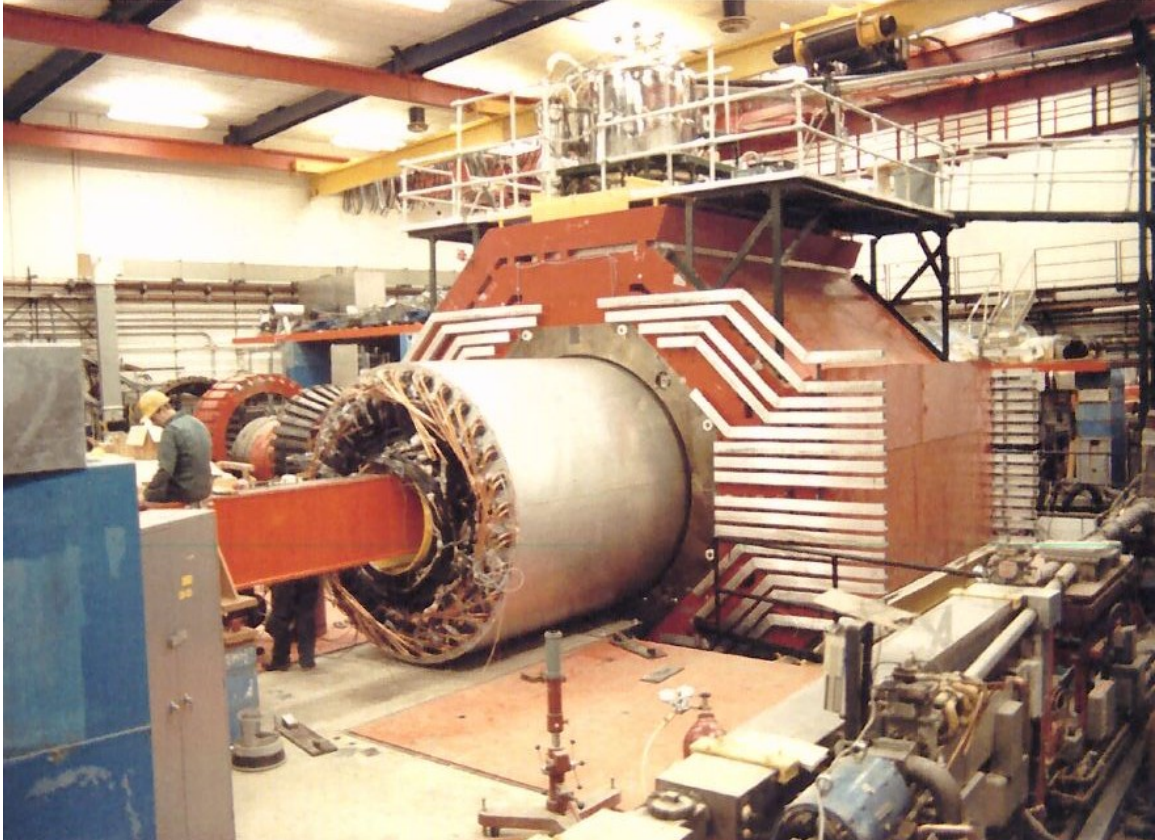


Figure 169: Helium dewar support upper access platform and detector loading inside of cryostat.

4528 **19.4 Endcap Forward Angle Detector Package Installation Structure**

4529 The basic design concept for the detectors mounted inside the endcap will have them supported by
4530 individual rails mounted to the inner circumference of the cylindrical ring and on rails attached to
4531 the outer horizontal circumferential surface of the nose if needed. The heavy gas Cherenkov will
4532 be separated into six sections with each section utilizing two rails to attach the section to the outer
4533 circumference of the endcap. A counterweight balanced installation device that is slung from the
4534 crane can be used to orient and position each section onto the rails. Personnel access to the endcap
4535 will be through man lifts and/or a specialized scaffolding as needed.

4536 **19.5 Large Angle Detector and Baffle Installation Mechanism**

4537 An installation mechanism is needed to load the large angle detector packages and baffle system into
4538 the internal support structure mentioned in the last section. This mechanism will likely be mounted
4539 to the longitudinal track system used for the endcap movement and can utilize the tracks for rolling
4540 the detectors and baffles into the cryostat and transferring the load to the internal frame. Depending

4541 on the final design of the detectors and baffle system the support could be a simple beam that runs
4542 through the middle of the detectors and baffles. See Figure 169 for similar approach at BNL

4543 **19.6 Light Gas Cherenkov Installation Structure**

4544 The light gas Cherenkov will mount to the external downstream end of the magnet and will not
4545 traverse with endcap. When the endcap is in the operational position the light gas Cherenkov will
4546 be enclosed within the cylindrical ring along with the rest of the forward angle detectors. The light
4547 gas Cherenkov detector will be made up of six pie shaped sections that will need to be bolted to
4548 the downstream side of the magnet. A space frame similar to a scaffolding system would hold
4549 and position each section while being attached to magnet. The space frame would attach to the
4550 rail system and could be movable along the rails if needed. The space frame will be suitable for
4551 personnel access to allow workers to perform the installation and maintenance of the detectors.

4552 **20 Project Status and Proposed Management Organization**

4553 The SoLID spectrometer was initially proposed in 2009 for two experiments: SIDIS experiment
4554 (PR12-09-014, later became E12-10-006) and the PVDIS experiment (PR12-09-012, later became
4555 E12-10-007). Both experiments aim to achieve high precision which require very high statistics.
4556 A spectrometer/detector system with a large acceptance and also able to handle high luminosity is
4557 needed. Therefore SoLID is designed to have a large solid angle and broad momentum acceptance
4558 and can handle luminosity up to $10^{39}\text{s}^{-1}\text{cm}^{-2}$ with a baffle system in the PVDIS configuration
4559 and $10^{37}\text{s}^{-1}\text{cm}^{-2}$ without a baffle system in the SIDIS configuration. With these unique features,
4560 SoLID is ideal for inclusive and semi-inclusive DIS experiments and is also good for measurements
4561 of certain exclusive reactions. The SoLID base equipment consists of a solenoid magnet (CLEO-II
4562 magnet), tracking detectors (GEMs), electron PID detectors (electromagnetic calorimeter and light
4563 gas Čerenkov detector) and hadron PID detectors (MRPC, heavy gas Čerenkov and EC), DAQ sys-
4564 tem, supporting structure and infrastructure needed for the spectrometer. Leveraging the unique
4565 capabilities of SoLID, currently, there are five high impact (four “A” rating and one “A⁻”) experi-
4566 ments approved using SoLID, including a near threshold J/ψ production experiment in addition to
4567 three SIDIS and one PVDIS experiments. Three more run-group proposals were also approved.

4568 The pre-conceptual design has gone through many iterations, including careful studies, detailed
4569 simulations, pre-R&D testings and a number of internal reviews. Among the various internal re-
4570 views, it is worth mentioning the two brainstorming sessions in September 2011 and January 2012,
4571 organized by the JLab physics division, and the dry run review in June 2012 with external experts
4572 (outside SoLID collaboration, including people from outside JLab). A formal pre-conceptual de-
4573 sign report was submitted to the JLab management in July 2014. A Director’s Review was help in
4574 February 2015. These reviews helped greatly in optimizing, improving and finalizing the concep-
4575 tual design. Detailed simulations with realistic background (including neutron backgrounds) and
4576 pre-R&D activities focusing on the major challenges have significantly improved the reliability of
4577 the conceptual design.

4578 **20.1 Collaboration and Organization**

4579 The SoLID collaboration has more than 250 members from over 70 institutions over 13 countries.
4580 SoLID has attracted international attention with many groups committed to make significant con-
4581 tributions, including noticeably the contributions to the R& D efforts for large detector projects
4582 (GEMs, MRPC and EC) from several Chinese groups and Heavy Gas Cherenkov detector from the
4583 Regina group in Canada.

4584 The proposed SoLID Organization Chart is shown in Figure 170.

4585 **Project Manager**

4586 Function: The Project Manager (PM) will be in charge of executing the project and report
4587 to JLab management. The collaboration will provide advice and oversight, and members of the
4588 collaboration will work under the PM in various roles to execute the project. For example, all
4589 subsystems coordinators will report to the PM. The PM has the authority and responsibility to
4590 manage the SoLID project.

4591 Jian-ping Chen is the initial PM.

4592 **Executive Board**

4593 Function: The Executive Board (EB) makes decisions on scientific and organizational choices,
4594 and provides high level oversight on all matter pertaining to preparation and operation of the SoLID
4595 project.

4596 The Chair of EB is the science leader, and is the principle contact between the collaboration

4597 and the lab management/DOE. The Chair will provide oversight and input to the PM for the SoLID
 4598 project. The Chair, together with the PM, is responsible for the performance and assessment of all
 4599 subsystems.

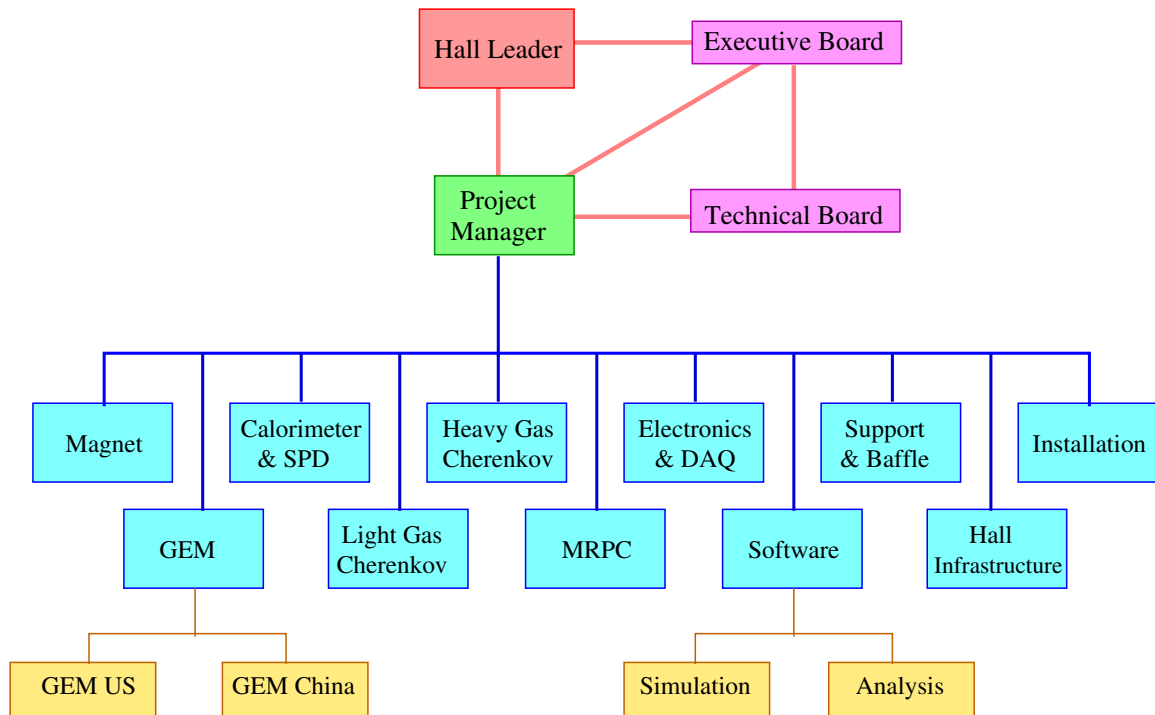


Figure 170: SoLID Organization Chart

4600 Initial members are the senior spokespeople plus the Hall Leader (ex-officio) and the PM (ex-
 4601 officio): Paul Souder (PVDIS), Haiyan Gao (SIDIS), Zein-Eddine Meziani (J/ψ), Thia Keppel
 4602 (Hall Leader, ex-officio) and Jian-ping Chen (PM, ex-officio).

4603 Paul Souder is the 1st Chair. It is expected that the Chair position will rotate.

4604 **Technical Board**

4605 Function: The technical Board (TB) advises the PM on all aspects of the Project, including any
 4606 changes in cost, scope or schedule.

4607 The TB will have a group of (usually senior) collaborators who represent the full range of
 4608 required technical expertise and usually a representative from each subsystem is expected to be on
 4609 this board. This group will be appointed by the EB. In addition, the TB will include the PM and also
 4610 project engineers when they are appointed. The membership of the TB can be periodically adjusted
 4611 by the EB as the situation warrants.

4612 The chair of the TB will be the PM. All EB members who are not already in the TB are ex-officio
 4613 members, along with the Hall leader.

4614 Initial members: Jian-ping Chen (Chair), Paul Souder, Haiyan Gao, Zein-Eddine Meziani, Thia
 4615 Keppel (ex-officio); Alexandre Camsonne, Eugene Chudakov, Tom Hemmick, Xiaodong Jiang,
 4616 Nilanga Liyanage, Bob Michaels, Xin Qian, Paul Reimer, Yi Wang, Zhengguo Zhao, Xiaochao
 4617 Zheng

4618 **Sub-System Lead Coordinators and Institutions**

- 4619 • **Magnet:** Robin Wines / Paul Reimer; JLab, Argonne

- 4620 • **GEM-US:** Nilanga Liyanage / Bernd Surrow ; UVa, Temple
- 4621 • **GEM-China:** Zhengguo Zhao / Xiaomei Li; USTC, CIAE, Lanzhou, Tsinghua, IMP
- 4622 • **Calorimeter:** Xiaochao Zheng / Wouter Deconick / Chufeng Feng; UVa, W&M, Shandong
- 4623 (China), Argonne
- 4624 • **Light Gas Cherenkov:** Zein-Eddine Meziani / Michael Paolone; Temple
- 4625 • **Heavy Gas Cherenkov:** Haiyan Gao / Zhiwen Zhao / Garth Huber; Duke, Regina (Canada)
- 4626 • **MRPC:** Yi Wang / Alexandre Camsonne; Tsinghua (China), JLab, Duke, Rutgers
- 4627 • **DAQ/Electronics:** Alexandre Camsonne / Ron Gilman; JLab, Stony Brook, Rutgers
- 4628 • **Simulation:** Seamus Riordan / Zhiwen Zhao ; Argonne, Duke, UVa, Syracuse, Stony Brook
- 4629 • **Reconstruction and Analysis:** Ole Hansen; JLab
- 4630 • **Supporting Structure and Baffle:** Robin Wines / Seamus Riordan; JLab, Argonne
- 4631 • **Hall Infrastructure Modification:** Robin Wines / Jessie Butler; JLab
- 4632 • **Installation:** Jessie Butler / Robin Wines; JLab, all user groups.

4633 The names listed are the coordinators for sub-systems. Institutions working on and responsible
 4634 for the sub-systems are also listed. Details of the responsibilities are described in the summary for
 4635 each sub-system. The list reflects the current situation and it is expected to be modified as more
 4636 groups join the effort as the SoLID project moves forward.

4637 **20.2 Cost estimation**

4638 Cost estimation has gone through many iterations in the last a few years. Procurement cost and
 4639 manpower estimations were first performed by the coordinators of subsystems. There are variations
 4640 in assumptions, including the number of years to complete the project. The final estimation made
 4641 adjustments to keep consistency for all subsystems in the assumptions. The length of the project
 4642 is assumed to be 4 years. Most of the procurement costs were estimated based on quotations from
 4643 vendors. Manpower were estimated from comparison with similar projects. JLab manpower was
 4644 estimated initially based on the estimation of similar projects from other halls. They were revised
 4645 later using the actual manpower used at the end of project completion in Hall D. The JLab budget
 4646 office provided valuable assistance in the cost estimation.

4647 **Bibliography**

- 4648 [1] D. Wang *et al.* (PVDIS Collaboration), *Nature* **506**, 67 (2014).
- 4649 [2] E. Eichten, K. D. Lane and M. E. Peskin, *Phys. Rev. Lett.* **50**, 811 (1983).
- 4650 [3] J. Erler, C. J. Horowitz, S. Mantry and P. A. Souder, *Ann. Rev. Nucl. Part. Sci.* **64**, 269 (2014).
- 4651 [4] S. Durr *et al.*, *Science* **322**, 1224 (2008).
- 4652 [5] Z. B. Kang, A. Prokudin, P. Sun and F. Yuan, *Phys. Rev. D* **93**, 014009 (2016).
- 4653 [6] Z. Ye, N. Sato, K. Allada, T. Liu, J.P. Chen, H. Gao, Z. B, Kang, A. Prokudin, P. Sun, and F.
4654 Yuan, *Phys. Lett. B.* **767**, 91-98 (2017).
- 4655 [7] M. Boggione, L. Gamberg, J. O. Gonzalez-Hernandez, T. C. Rogers and N. Sato, *Phys. Lett. B*
4656 **766**, 245 (2017).
- 4657 [8] SoLID Collaboration, SoLID Preliminary Conceptual Design Report, [http://hallaweb.
4658 jlab.org/12GeV/SoLID/download/doc/solid_precdr.pdf](http://hallaweb.jlab.org/12GeV/SoLID/download/doc/solid_precdr.pdf).
- 4659 [9] S. An et al, *NIM A* **594**, 39 (2008).
- 4660 [10] Mickey Chiu et al, Progress Report of (Sub) 10 Picosecond Timing Detectors for Generic
4661 Detector R&D for an Electron Ion Collider, [https://wiki.bnl.gov/conferences/
4662 images/c/c8/ERD10_Report_2015-06.pdf](https://wiki.bnl.gov/conferences/images/c/c8/ERD10_Report_2015-06.pdf).
- 4663 [11] European Muon, J. Ashman *et al.*, *Phys. Lett.* **B206**, 364 (1988).
- 4664 [12] B. W. Filippone and X.-D. Ji, *Adv. Nucl. Phys.* **26**, 1 (2001), hep-ph/0101224.
- 4665 [13] S. E. Kuhn, J. P. Chen, and E. Leader, *Prog. Part. Nucl. Phys.* **63**, 1 (2009), 0812.3535.
- 4666 [14] X. Artru and M. Mekhfi, *Z. Phys.* **C45**, 669 (1990).
- 4667 [15] P. J. Mulders and R. D. Tangerman, *Nucl. Phys.* **B461**, 197 (1996), hep-ph/9510301.
- 4668 [16] D. Boer and P. J. Mulders, *Phys. Rev.* **D57**, 5780 (1998), hep-ph/9711485.
- 4669 [17] X.-d. Ji, J.-P. Ma, and F. Yuan, *Phys. Lett.* **B597**, 299 (2004), hep-ph/0405085.
- 4670 [18] K. Hidaka, E. Monsay, and D. W. Sivers, *Phys. Rev.* **D19**, 1503 (1979).
- 4671 [19] J. P. Ralston and D. E. Soper, *Nucl. Phys.* **B152**, 109 (1979).
- 4672 [20] R. L. Jaffe and X.-D. Ji, *Phys. Rev. Lett.* **67**, 552 (1991).
- 4673 [21] V. Barone, *Phys. Lett.* **B409**, 499 (1997), hep-ph/9703343.
- 4674 [22] C. Bourrely, J. Soffer, and O. V. Teryaev, *Phys. Lett.* **B420**, 375 (1998), hep-ph/9710224.
- 4675 [23] J. Soffer, *Phys. Rev. Lett.* **74**, 1292 (1995), hep-ph/9409254.
- 4676 [24] W. Vogelsang, *Phys. Rev.* **D57**, 1886 (1998), hep-ph/9706511.
- 4677 [25] G. R. Goldstein, R. L. Jaffe, and X.-D. Ji, *Phys. Rev.* **D52**, 5006 (1995), hep-ph/9501297.

- 4678 [26] J. Ralston, private communications.
- 4679 [27] QCDSF, M. Gockeler *et al.*, Phys. Lett. **B627**, 113 (2005), hep-lat/0507001.
- 4680 [28] H.-X. He and X.-D. Ji, Phys. Rev. **D52**, 2960 (1995), hep-ph/9412235.
- 4681 [29] B. Q. Ma, I. Schmidt, and J. Soffer, Phys. Lett. **B441**, 461 (1998).
- 4682 [30] L. P. Gamberg and G. R. Goldstein, Phys. Rev. Lett. **87**, 242001 (2001), hep-ph/0107176.
- 4683 [31] I. C. Cloet, W. Bentz, and A. W. Thomas, Phys. Lett. **B659**, 214 (2008), 0708.3246.
- 4684 [32] M. Wakamatsu, Phys. Lett. **B653**, 398 (2007), 0705.2917.
- 4685 [33] B. Pasquini, M. Pincetti, and S. Boffi, Phys. Rev. **D72**, 094029 (2005), hep-ph/0510376.
- 4686 [34] J. C. Collins, Nucl. Phys. **B396**, 161 (1993), hep-ph/9208213.
- 4687 [35] Belle, K. Abe *et al.*, Phys. Rev. Lett. **96**, 232002 (2006), hep-ex/0507063.
- 4688 [36] HERMES, A. Airapetian *et al.*, (2010), hep-ex/1006.4221.
- 4689 [37] HERMES, A. Airapetian *et al.*, Phys. Rev. Lett. **103**, 152002 (2009), 0906.3918.
- 4690 [38] HERMES, A. Airapetian *et al.*, Phys. Rev. Lett. **94**, 012002 (2005), hep-ex/0408013.
- 4691 [39] COMPASS, M. G. Alekseev *et al.*, (2010), 1005.5609.
- 4692 [40] COMPASS, V. Y. Alexakhin *et al.*, Phys. Rev. Lett. **94**, 202002 (2005), hep-ex/0503002.
- 4693 [41] D. W. Sivers, Phys. Rev. **D41**, 83 (1990).
- 4694 [42] X. Qian *et al.*, Phys. Rev. Lett. **107**, 072003 (2011).
- 4695 [43] G. L. Kane, J. Pumplin, and W. Repko, Phys. Rev. Lett. **41**, 1689 (1978).
- 4696 [44] M. Anselmino, M. Boglione, and F. Murgia, Phys. Lett. **B362**, 164 (1995), hep-ph/9503290.
- 4697 [45] J. C. Collins, Phys. Lett. **B536**, 43 (2002), hep-ph/0204004.
- 4698 [46] A. V. Belitsky, X. Ji, and F. Yuan, Nucl. Phys. **B656**, 165 (2003), hep-ph/0208038.
- 4699 [47] D. Boer, P. J. Mulders, and F. Pijlman, Nucl. Phys. **B667**, 201 (2003), hep-ph/0303034.
- 4700 [48] S. J. Brodsky, D. S. Hwang, and I. Schmidt, Phys. Lett. **B530**, 99 (2002), hep-ph/0201296.
- 4701 [49] X.-d. Ji and F. Yuan, Phys. Lett. **B543**, 66 (2002), hep-ph/0206057.
- 4702 [50] L. P. Gamberg, G. R. Goldstein, and K. A. Oganessyan, Phys. Rev. **D67**, 071504 (2003),
4703 hep-ph/0301018.
- 4704 [51] M. Burkardt, Phys. Rev. **D69**, 057501 (2004), hep-ph/0311013.
- 4705 [52] M. Burkardt, Phys. Rev. **D72**, 094020 (2005), hep-ph/0505189.
- 4706 [53] S. J. Brodsky and S. Gardner, Phys. Lett. **B643**, 22 (2006), hep-ph/0608219.
- 4707 [54] J. Huang *et al.*, Phys. Rev. Lett. **108**, 052001 (2012).

- 4708 [55] T.-C. Meng, J.-C. Pan, Q.-b. Xie, and W. Zhu, Phys. Rev. **D40**, 769 (1989).
- 4709 [56] M. Anselmino, M. Boglione, and F. Murgia, Phys. Rev. **D60**, 054027 (1999), hep-ph/9901442.
- 4710 [57] A. Bacchetta, A. Schaefer, and J.-J. Yang, Phys. Lett. **B578**, 109 (2004), hep-ph/0309246.
- 4711 [58] Z. Lu and B.-Q. Ma, Nucl. Phys. **A741**, 200 (2004), hep-ph/0406171.
- 4712 [59] L. P. Gamberg, G. R. Goldstein, and M. Schlegel, (2007), 0708.2580.
- 4713 [60] A. Bacchetta, F. Conti, and M. Radici, Phys. Rev. **D78**, 074010 (2008), 0807.0323.
- 4714 [61] B. Pasquini and F. Yuan, Phys. Rev. D **81**, 114013 (2010).
- 4715 [62] F. Yuan, Phys. Lett. **B575**, 45 (2003), hep-ph/0308157.
- 4716 [63] D. Amrath, A. Bacchetta, and A. Metz, Phys. Rev. **D71**, 114018 (2005), hep-ph/0504124.
- 4717 [64] A. Bacchetta, L. P. Gamberg, G. R. Goldstein, and A. Mukherjee, Phys. Lett. **B659**, 234
4718 (2008), arXiv:0707.3372 [hep-ph].
- 4719 [65] H. H. Matevosyan, A. W. Thomas, W. Bentz, Phys. Rev. D **86**, 034025 (2012),
4720 arXiv:1205.5813 [hep-ph].
- 4721 [66] A. Kotzinian, H. H. Matevosyan and A. W. Thomas, arXiv:1403.5562 [hep-ph].
- 4722 [67] A. Metz, Phys. Lett. **B549**, 139 (2002).
- 4723 [68] J. C. Collins and A. Metz, Phys. Rev. Lett. **93**, 252001 (2004), hep-ph/0408249.
- 4724 [69] L. P. Gamberg, A. Mukherjee, and P. J. Mulders, Phys. Rev. **D77**, 114026 (2008), 0803.2632.
- 4725 [70] G. R. Goldstein and L. Gamberg, (2002), Transversity and meson photoproduction Proceed-
4726 ings of ICHEP 2002; North Holland Amsterdam, p. 452 (2003), hep-ph/0209085, Published in
4727 Amsterdam ICHEP 452-454.
- 4728 [71] Z. Lu and B.-Q. Ma, Phys. Rev. **D70**, 094044 (2004), hep-ph/0411043.
- 4729 [72] H. Avakian *et al.*, Phys. Rev. D **78**, 114024 (2008).
- 4730 [73] J. She, J. Zhu, and B.-Q. Ma, Phys. Rev. D **79**, 054008 (2009).
- 4731 [74] B. Pasquini, S. Cazzaniga, and F. Yuan, Phys. Rev. D **78**, 034025 (2008).
- 4732 [75] S. Boffi, A. V. Efremov, B. Pasquini, and P. Schweitzer, Phys. Rev. **D79**, 094012 (2009),
4733 0903.1271.
- 4734 [76] V. Barone, Z. Lu, and B.-Q. Ma, Phys. Lett. **B632**, 277 (2006), hep-ph/0512145.
- 4735 [77] V. Barone, A. Prokudin, and B.-Q. Ma, Phys. Rev. **D78**, 045022 (2008), 0804.3024.
- 4736 [78] M. Anselmino *et al.*, Phys. Rev. **D75**, 054032 (2007), hep-ph/0701006.
- 4737 [79] COMPASS, E. S. Ageev *et al.*, Nucl. Phys. **B765**, 31 (2007), hep-ex/0610068.
- 4738 [80] COMPASS, M. Alekseev *et al.*, Phys. Lett. **B673**, 127 (2009), 0802.2160.

- 4739 [81] M. Anselmino *et al.*, Eur. Phys. J. **A39**, 89 (2009), 0805.2677.
- 4740 [82] M. Anselmino *et al.*, Phys. Rev. **D72**, 094007 (2005), hep-ph/0507181.
- 4741 [83] M. Anselmino *et al.*, (2005), hep-ph/0511017.
- 4742 [84] M. Anselmino *et al.*, Phys. Rev. **D71**, 074006 (2005), hep-ph/0501196.
- 4743 [85] J. C. Collins *et al.*, Phys. Rev. **D73**, 014021 (2006), hep-ph/0509076.
- 4744 [86] V. Barone, A. Drago, and P. G. Ratcliffe, Phys. Rept. **359**, 1 (2002), hep-ph/0104283.
- 4745 [87] Jefferson Lab Experiment E12-10-006, Spokespersons: Chen, Gao (contact), Jiang, Peng, and
4746 Qian.
- 4747 [88] Jefferson Lab Experiment E12-10-006, Spokespersons: Chen, Huang (contact), Qiang, and
4748 Yan.
- 4749 [89] Jefferson Lab Experiment E12-11-108, Spokespersons: Allada, Chen, Gao (contact), Li, and
4750 Mezziani.
- 4751 [90] D. Crabb *et al.*, Phys. Rev. Letts. **64**, 2627 (2008).
- 4752 [91] C. Keith *et al.*, Nucl. Inst. Meth. **A501**, 327 (2003).
- 4753 [92] G. S. Atoian *et al.*, Nucl. Inst. Meth. **A531**, 467 (2004).
- 4754 [93] G. S. Atoian *et al.*, Nucl. Inst. Meth. **A584**, 291 (2008).
- 4755 [94] M. Anselmino and A. Prokudin, private communications.
- 4756 [95] J. Huang and Y. Qiang, *Maximum likelihood estimation of asymmetry and angular modulation*
4757 *for transversity (2010)*, URL <http://www.jlab.org/jinhuang/Transversity/MLE.pdf>.
- 4758 [96] Z. Ye *et al.*, Phys. Lett. B **767**, 91 (2017).
- 4759 [97] T. Hobbs and W. Melnitchouk, Phys. Rev. D **77**, 114023 (2008) [arXiv:0801.4791 [hep-ph]].
- 4760 [98] D. Wang *et al.* [PVDIS Collaboration], Nature **506**, no. 7486, 67 (2014).
- 4761 [99] S. Mantry, M. J. Ramsey-Musolf and G. F. Sacco, Phys. Rev. C **82**, 065205 (2010)
4762 [arXiv:1004.3307 [hep-ph]].
- 4763 [100] M. R. Buckley and M. J. Ramsey-Musolf, Phys. Lett. B **712**, 261 (2012) [arXiv:1203.1102
4764 [hep-ph]].
- 4765 [101] E. Eichten, K. D. Lane and M. E. Peskin, Phys. Rev. Lett. **50**, 811 (1983).
- 4766 [102] F. E. Close and A. W. Thomas, Phys. Lett. B **212**, 227 (1988).
- 4767 [103] E. Sather, Phys. Lett. B **274**, 433 (1992).
- 4768 [104] E. N. Rodionov, A. W. Thomas and J. T. Londergan, Mod. Phys. Lett. A **9**, 1799 (1994).
- 4769 [105] G. P. Zeller *et al.* [NuTeV Collaboration], Phys. Rev. Lett. **88**, 091802 (2002) [Erratum-ibid.
4770 **90** 239902 (2003)].

- 4771 [106] J. T. Londergan and A. W. Thomas, *Phys. Lett. B* **558** 132 (2003).
- 4772 [107] J. T. Londergan and A. W. Thomas, *J. Phys. G* **31** 1151 (2005).
- 4773 [108] M. Gluck, P. Jimenez-Delgado and E. Reya, *Phys. Rev. Lett.* **95** 022002 (2005).
- 4774 [109] I. C. Cloet, W. Bentz and A. W. Thomas, *Phys. Rev. Lett.* **102**, 252301 (2009)
4775 [arXiv:0901.3559 [nucl-th]].
- 4776 [110] W. Melnitchouk, I. R. Afnan, F. Bissey and A. W. Thomas, *Phys. Rev. Lett.* **84** 5455 (2000).
- 4777 [111] W. Melnitchouk and A. W. Thomas, *Phys. Lett. B* **377** 11 (1996).
- 4778 [112] S. I. Alekhin, *Phys. Rev. D* **63** 094022 (2001).
- 4779 [113] S. Kuhlmann *et al.*, *Phys. Lett. B* 476 297 (2000).
- 4780 [114] S. J. Brodsky and G. A. Miller, *Phys. Lett. B* **412**, 125 (1997).
- 4781 [115] S. J. Brodsky, I. A. Schmidt, and G. F. de Téramond, *Phys. Rev. Lett.*, **64**, 1011 (1990).
- 4782 [116] M. E. Luke, A. V. Manohar, and M. J. Savage. *Phys. Lett. B* **288**, 355 (1992).
- 4783 [117] A. B. Kaidalov and P. E. Volkovitsky, *Phys. Rev. Lett.*, **69**, 3155 (1992).
- 4784 [118] G. F. de Téramond, R. Espinoza, and M. Ortega-Rodriguez. *Phys. Rev. D* **58**, 034012 (1998).
- 4785 [119] V. I. Shevchenko, *Phys. Lett. B* **392**, 457 (1997).
- 4786 [120] A. Hayashigaki, *Prog. Theor. Phys.*, **101**, 923 (1999).
- 4787 [121] K. Yokokawa, S. Sasaki, T. Hatsuda, and A. Hayashigaki, *Phys. Rev. D* **74**, 034504 (2006).
- 4788 [122] T. Kawanai and S. Sasaki, *Phys. Rev. D* **82**, 091501 (2010).
- 4789 [123] K. Tsushima, D. H. Lu, G. Krein, and A. W. Thomas, *Phys. Rev. C* **83**, 065208 (2011).
- 4790 [124] K. Tsushima, D. H. Lu, G. Krein, and A. W. Thomas, *AIP Conf. Proc.* **1354**, 39 (2011).
- 4791 [125] M. Binkeley *et al.*, *Phys. Rev. Lett.* **48**, 73 (1982).
- 4792 [126] B. H. Denby *et al.*, *Phys. Rev. Lett.* **52**, 795 (1984).
- 4793 [127] M. D. Sokoloff *et al.*, *Phys. Rev. Lett.* **57**, 3003 (1986).
- 4794 [128] R. Barate *et al.*, *Z. Phys. C* **33**, 505 (1987).
- 4795 [129] P. L. Frabetti *et al.*, *Phys. Lett. B* **316**, 197 (1993).
- 4796 [130] S. Aid *et al.*, *Nucl. Phys. B* **472**, 3 (1996).
- 4797 [131] J. Breitweg *et al.*, *Z. Phys. C* **76**, 599 (1997).
- 4798 [132] S. Aid *et al.*, *Nucl. Phys. B* **472**, 2 (1996).
- 4799 [133] U. Camerini *et al.*, *Phys. Rev. Lett.* **35**, 483 (1975).
- 4800 [134] B. Gittelman *et al.*, *Phys. Rev. Lett.* **35**, 1616 (1975).

- 4801 [135] B. Knapp et al., Phys. Rev. Lett. **34**, 1040 (1975).
- 4802 [136] R. L. Anderson, *Excess Muons and New Results in Ψ Photoproduction*, SLAC-PUB-1471.
- 4803 [137] D. Kharzeev, nucl-th/9601029.
- 4804 [138] D. Kharzeev, H. Satz, A. Syamtomov, and G. Zinovjev, Eur. Phys. J. C **9**, 459 (1999).
- 4805 [139] S. J. Brodsky, E. Chudakov, P. Hoyer, and J.M. Laget, Phys. Lett. B **498**, 23 (2001).
- 4806 [140] A. Sibirtsev, S. Krewald, and A. W. Thomas, J. Phys. G **30**, 1427 (2004).
- 4807 [141] M. A. Shifman, A. I. Vainshtein, and V. I. Zakharov, Phys. Lett. B **65**, 255 (1976).
- 4808 [142] V. A. Novikov, M. A. Shifman, A. I. Vainshtein, and V. I. Zakharov, Nucl. Phys. **B136**, 125
4809 (1978).
- 4810 [143] . A. Shifman, A. I. Vainshtein, and V. I. Zakharov, Nucl. Phys. **B136**, 157 (1978).
- 4811 [144] A. Sibirtsev and M. B. Voloshin, Phys. Rev. D **71**, 076005 (2005).
- 4812 [145] R. B. Baldini, S. Pacetti and A. Zallo, arXiv:0812.3283 [hep-ph].
- 4813 [146] M. Ablikim *et al.* (BESIII Collaboration), Phys. Rev. Lett. **108**, 112003 (2012).
- 4814 [147] Gryniuk, Oleksii and Vanderhaeghen, Marc”, Phys. Rev. D **94**, 074001 (2016).
- 4815 [148] J. J. Wu, R. Molina, E. Oset, and B.-S. Zou, Phys. Rev. Lett. **105**, 232001 (2010).
- 4816 [149] P. Bosted *et al.*, Phys. Rev. C **79**, 015209 (2009).
- 4817 [150] Contact Person: E. Chudakov, PAC32 PR12-07-106 The A-dependence of J/Ψ Photopro-
4818 duction near Threshold.
- 4819 [151] Wang, Qian and Liu, Xiao-Hai and Zhao, Qiang”, Phys. Rev.” D **92**, 034022 (2015).
- 4820 [152] Contact Person: Z.-E. Meziani, PAC39 [https://www.jlab.org/exp_prog/
4821 proposals/12/PR12-12-006.pdf](https://www.jlab.org/exp_prog/proposals/12/PR12-12-006.pdf).
- 4822 [153] Contact Person: P. Souder, PAC34 [http://hallaweb.jlab.org/collab/PAC/
4823 PAC34/PR-09-012-pvdis.pdf](http://hallaweb.jlab.org/collab/PAC/PAC34/PR-09-012-pvdis.pdf).
- 4824 [154] Contact Person: H. Gao, PAC34 [http://hallaweb.jlab.org/collab/PAC/
4825 PAC34/PR-09-014-transversity.pdf](http://hallaweb.jlab.org/collab/PAC/PAC34/PR-09-014-transversity.pdf).
- 4826 [155] Contact Person: J. Huang, PAC37 [http://www.jlab.org/exp\\$\\$_prog/PACpage/
4827 PAC37/proposals/Proposals/NewProposals/PR-11-007.pdf](http://www.jlab.org/exp$$_prog/PACpage/PAC37/proposals/Proposals/NewProposals/PR-11-007.pdf).
- 4828 [156] Contact Person: H. Gao, PAC38 [http://wwold.jlab.org/exp\\$\\$_prog/
4829 proposals/11/PR12-11-108.pdf](http://wwold.jlab.org/exp$$_prog/proposals/11/PR12-11-108.pdf).
- 4830 [157] X. Qian et al., Phys. Rev. C **81**, 055209 (2010).
- 4831 [158] S. J. Brodsky et al., Phys. Lett. B **498**, 23 (2001).
- 4832 [159] K. Schilling and G. Wolf, Nucl. Phys. **B61**, 381 (1973).

- 4833 [160] R. Fiore et al., Phys. Rev. D **80**, 116001 (2009).
- 4834 [161] Aaij, Roel et al. (LHCb Collaboration), Phys. Rev. Lett., **115**, 072001 (2015).
- 4835 [162] C. Adloff et al., Eur. Phys. J. C **13**, 371 (2000).
- 4836 [163] L. W. Whitlow, Ph. D. thesis, Stanford University, SLAC-Report-357 (1990).
- 4837 [164] Developed by J. W. Lightbody and J. S. O’Connell in 1988.
- 4838 [165] D. E. Wiser, Ph. D. thesis, Univ. of Wisconsin (1977).
- 4839 [166] X. Qian, Ph. D. thesis, Duke University.
- 4840 [167] T. Abe, Computer Physics Communications **136**, 126 (2001).
- 4841 [168] PYTHIA, <http://projects.hepforge.org/pythia6/>, 2006.
- 4842 [169] Y. Kubota et al., Nucl. Instr. and Meth. A **320** (1992).
- 4843 [170] Poisson Superfish, http://laacg1.lanl.gov/laacg/services/download_sfp.html.
- 4844
- 4845 [171] G. Atoian et al., Nucl. Instr. and Meth. A **584**, 291 (2008).
- 4846 [172] W. Anderson et al., arXiv:1103.4277 [physics.ins-det].
- 4847 [173] B. Azmoun et al., IEEE Trans. Nucl. Sci. **56-3**, 1544 (2009).
- 4848 [174] C. Lu and K. T. McDonald, Nucl. Instr. and Meth. A **343**, 135 (1994).
- 4849 [175] Y. Wang et al., Chin. Phys. C **33**, 374 (2009).
- 4850 [176] S. J. Brodsky, P. Hoyer, C. Peterson, and N. Sakai, Phys. Lett. **93B**, 451 (1980).
- 4851 [177] S. J. Brodsky, C. Peterson and N. Sakai, Phys. Rev. D **23**, 2745 (1981).
- 4852 [178] W. C. Chang and J. C. Peng, Phys. Lett. B **704**, 197 (2011).
- 4853 [179] B. W. Adams *et al.*, “A Brief Technical History of the Large-Area Picosecond Photodetector
4854 (LAPPD) Collaboration,” arXiv:1603.01843.
- 4855 [180] “eRD14: PID Consortium for an integrated program for Particle Identification (PID) at
4856 a future Electron Ion Collider,” [https://wiki.bnl.gov/conferences/images/6/6f/
4857 ERD14_progress_report_Dec_2015.pdf](https://wiki.bnl.gov/conferences/images/6/6f/ERD14_progress_report_Dec_2015.pdf).
- 4858 [181] E12-10-007 “Precision Measurement of Parity-violation in Deep Inelastic Scattering Over a
4859 Broad Kinematic Range” Contact person: P. Souder.
- 4860 [182] E12-10-006, “Target Single Spin Asymmetry in Semi-Inclusive Deep-Inelastic ($e, e'\pi^\pm$) on
4861 a Transversely Polarized ^3He Target at 8.8 and 11 GeV”, Spokesperson: J.-P. Chen, H. Gao
4862 (contact), X. Jiang, J.-C. Peng, and X. Qian.
- 4863 [183] E12-11-007, “Asymmetries in Semi-Inclusive Deep-Inelastic ($e, e'\pi^\pm$) Reactions on a Longi-
4864 tudinally Polarized ^3He Target at 8.8 and 11 GeV”, Spokesperson: J.-P. Chen, J. Huang (contact),
4865 Y. Qiang, and W.-B. Yan.

- 4866 [184] E12-11-108 “Target Single Spin Asymmetry in Semi-Inclusive Deep-Inelastic ($e, e'\pi^\pm$) on a
4867 Transversely Polarized Proton Target”, Spokespersons: K. Allada, J.-P. Chen, H. Gao (contact),
4868 Z.-E. Meziani, and X.-M. Li.
- 4869 [185] M. Anselmino and A. Prokudin, *private communications*. Predictions are based on the ex-
4870 tractions of Ref. [186].
- 4871 [186] M. Anselmino *et al.*, proceedings of the XVI International Workshop on Deep Inelastic Scat-
4872 tering and Related Subjects, DIS 2008, London, U.K. 2009. e-Print: arXiv:0807.0173.
- 4873 [187] W. Vogelsang and F. Yuan, *private communications*.
- 4874 [188] B. Pasquini, *private communication*.
4875 S. Boffi, A. V. Efremov, B. Pasquini and P. Schweitzer, Phys. Rev. **D79**, 094012 (2009)
4876 arXiv:0903.1271.
- 4877 [189] X. Qian *et al.* (JLab Hall A Collaboration) Phys. Rev. Lett. **107**, 072003 (2011).
- 4878 [190] J. Huang *et al.* (JLab Hall A Collaboration) Phys. Rev. Lett. **108**, 052001 (2012).
- 4879 [191] X. Qian, Modern Phys. Lett. **A27**, 1230021 (2012).
- 4880 [192] Y. Zhang *et al.* Chinese Physics **C36**, 610 (2012).
- 4881 [193] L. W. Whitlow, SLAC-Report-357 (1990).
- 4882 [194] J. W. Lightbody and J. S. O’Connell, Computers in Physics 2, 57 (1988).
- 4883 [195] D. E. Wiser, Ph. D. thesis, Univ. of Wisconsin (1977).
- 4884 [196] E12-12-006, “Near-Threshold Electroproduction of J/ψ with a 11 GeV Beam”, Spokesper-
4885 sons: K. Hafidi, Z.-E. Meziani (contact), X. Qian, N. Sparveris, and Z.-W. Zhao.
- 4886 [197] Study of modifying CLEO II magnet for SoLID, E.Chudakov
4887 (https://userweb.jlab.org/~gen/jlab12gev/cleo_mag/)
- 4888 [198] Y. Kubota *et al.*, Nucl. Instr. and Meth., **A320** 66 (1992)
- 4889 [199] D. M. Coffman *et al.*, IEEE Transactions on Nuclear Science, **37** 1172 (1990)
- 4890 [200] X. Qian *et al.*, Phys. Rev. Lett. 107, (2012) 072003. J. Huang *et al.*, Phys. Rev. Lett. 108
4891 (2012) 052001.
- 4892 [201] T.D. Averett, *et al.*, Nucl. Instr. and Meth. A 427 (1999) 440.
- 4893 [202] J. Maxwell *et al.*, to be submitted to Nucl. Instr. and Meth. A.
- 4894 [203] D.G. Crabb, C.B. Higley, A.D. Krisch, R.S. Raymond, T. Roser, and J.A. Stewart, Phys. Rev.
4895 Lett. 64, (1990) 2627.
- 4896 [204] C.D. Keith, *et al.*, Nucl. Instr. and Meth. A 684 (2012) 27.
- 4897 [205] C.D. Keith, *et al.*, Nucl. Instr. and Meth. A 501 (2003) 327.
- 4898 [206] Design Report rfq 14231, Oxford Instruments Nanotechnology Tools Ltd.

- 4899 [207] F. Sauli, Nucl. Inst. and Meth. **A 386**, 531 (1997).
- 4900 [208] B. Ketzer *et al.*, Nucl. Phys. B (Proc. Suppl.) **125**, 368 (2003).
- 4901 [209] M. Villa, *et al.*, Nucl. Inst. and Meth. **A 628** 182 (2011).
- 4902 [210] M. Alfonsi *et al.*, Nucl. Inst. and Meth. **A 617**, 151 (2010).
- 4903 [211] D. Abbaneo *et al.*, Nucl. Inst. and Meth. **A** (2010).
- 4904 [212] M.J. French *et al.*, Nucl. Instr. and Meth. **A 466** 359 (2001).
- 4905 [213] F.Sauli, RD51-NOTE-2012-007 REVISED 21.09.2012.
- 4906 [214] D. Abbaneo *et al.*, RD51-NOTE-2012-012 16.11.2012.
- 4907 [215] William Whyte, “Cleanroom Technology: Fundamentals of Design, Testing and Operation”
4908 (2001) ISBN 978-0-470-74806-0
- 4909 [216] P. Walker, V. Weber, *et al.*, Journal of Photographic Science, **18** 150 (1970).
- 4910 [217] J. M. Shaw, J. D. Gelorme, *et al.*, IBM Journal of Research and Development. **41** 81 (1997)
4911 ISSN: 0018-8646
- 4912 [218] Rensheng Wang, Yan Huang, Zhigang Xiao *et al.*, Nucl. Inst. and Meth. **A701** 54 (2013)
- 4913 [219] S. P. Malace, B. D. Sawatzky and H. Gao, “Studies of single-photoelectron response and
4914 of performance in magnetic field of a H8500C-03 photomultiplier tube,” JINST **1309**, P09004
4915 (2013) [arXiv:1306.6277].
- 4916 [220] Composite Mirror Applications, Inc. 1638 S. Research Loop, Suite 100 Tucson, Arizona
4917 85710. <http://www.compositemirrors.com>
- 4918 [221] LHCb RICH Technical Design Report, The LHCb Collaboration: lhcb-rich.web.cern.ch/lhcb-rich/richtdr/tdr.pdf
- 4919
- 4920 [222] Hamamatsu flat panel type multianode photomultiplier tube assembly H8500 series specifi-
4921 cations are found at [http://jp.hamamatsu.com/products/sensor-etd/pd002/
4922 pd394/H8500C/index_en.html](http://jp.hamamatsu.com/products/sensor-etd/pd002/pd394/H8500C/index_en.html)
- 4923 [223] Amuneal Manufacturing Corporation. 4737 Darrah Street Philadelphia, PA 19124, USA.
4924 www.amuneal.com
- 4925 [224] GEMC: a GEant4 Monte Carlo. <https://gemc.jlab.org/>
- 4926 [225] GEANT4: a toolkit for the simulation of the passage of particles through matter: [http:
4927 //geant4.cern.ch/](http://geant4.cern.ch/)
- 4928 [226] M. Artuso *et al.*, Nuclear Instruments and Methods A, 558 373-387 (2006).
- 4929 [227] A. Bulla, Ph.D. thesis (1997); E. Foktitis *et al.*, Nuclear Instruments and Methods A 371 255
4930 (1996).
- 4931 [228] G.J. Barber *et al.*, Nuclear Instruments and Methods A 593 624-637 (2008).

- 4932 [229] JLab approved experiments E-12-09-014 and E-12-10-006
4933 http://www.jlab.org/exp_prog/proposals/09/PR12-09-014.pdf
4934 http://www.jlab.org/exp_prog/proposals/10/PR12-10-006.pdf
4935
- 4936 [230] S. P. Malace, B. D. Sawatzky and H. Gao, “Studies of single-photoelectron response and
4937 of performance in magnetic field of a H8500C-03 photomultiplier tube,” JINST **1309**, P09004
4938 (2013) [arXiv:1306.6277].
- 4939 [231] G. S. Atoian *et al.*, Nucl. Instrum. Meth. A **584**, 291 (2008).
- 4940 [232] H. Avakian *et al.*, Nucl. Instrum. Meth. A **417**, 69 (1998).
- 4941 [233] E. Picatoste Olloqui [LHCb Collaboration], J. Phys. Conf. Ser. **160**, 012046 (2009).
- 4942 [234] Y. V. Kharlov *et al.*, Nucl. Instrum. Meth. A **606**, 432 (2009).
- 4943 [235] D. A. Morozov *et al.*, J. Phys. Conf. Ser. **160**, 012021 (2009).
- 4944 [236] ATLAS Tile Calorimeter Technical Design Report (1996).
- 4945 [237] L. Aliaga *et al.* [MINERvA Collaboration], Nucl. Instrum. Meth. A **743**, 130 (2014)
4946 doi:10.1016/j.nima.2013.12.053 [arXiv:1305.5199 [physics.ins-det]].
- 4947 [238] M. J. Varanda, M. David, A. Gomes and A. Maio, Nucl. Instrum. Meth. A **453**, 255 (2000).
4948 doi:10.1016/S0168-9002(00)00642-2
- 4949 [239] LHCb Tracker Upgrade Technical Design Report.
- 4950 [240] Y. Wang, *et al.*, Nucl. Instr. and Meth. A 538 (2005) 425.
- 4951 [241] Y. Wang, *et al.*, Nucl. Instr. and Meth. A 537 (2005) 698.
- 4952 [242] A. Akindinov, *et al.*, Nucl. Instr. and Meth. A 602 (2009) 709.
- 4953 [243] A. Akindinov, *et al.*, Nucl. Instr. and Meth. A 533 (2004) 74.
- 4954 [244] Y. Wang, *et al.*, Chinese Physics C. 33 (2009) 374.
- 4955 [245] J.B. Wang, *et al.*, 2012 JINST 7 P10004.
- 4956 [246] JLab E-08-027, A. Camsonne, J. P. Chen, D. Crabb and K Slifer, spokespersons;
4957 http://www.jlab.org/exp_prog/proposals/08/PR-08-027.pdf
- 4958 [247] V. Gyurjyan *et al.*, J. Phys. Conf. Ser. **331**, 032013 (2011). <https://claraweb.jlab.org/docs/claraweb>
4959 [org/docs/claraweb](https://claraweb.jlab.org/docs/claraweb)
- 4960 [248] D. Lawrence, J. Phys. Conf. Ser. **119**, 042018 (2008). <https://www.jlab.org/JANA>
- 4961 [249] M. Al-Turany *et al.*, J. Phys. Conf. Ser. **396**, 022001 (2012). <https://fairroot.gsi.de>
4962 [de](https://fairroot.gsi.de)
- 4963 [250] C. Green *et al.*, J. Phys. Conf. Ser. **396**, 022020 (2012). <http://art.fnal.gov>

- 4964 [251] See for example E. Sexton-Kennedy, *A Review of Event Processing Frameworks used in HEP*,
4965 Talk at CHEP 2015, [http://indico.cern.ch/event/304944/contributions/](http://indico.cern.ch/event/304944/contributions/1672690/)
4966 [1672690/](http://indico.cern.ch/event/304944/contributions/1672690/)
- 4967 [252] R. Brun and F. Rademakers, Nucl. Instr. Meth. Phys. Res. A **389**, 81 (1997). [http://](http://root.cern/)
4968 root.cern/
- 4969 [253] ROOT/C++ Analyzer for JLab Hall A, <https://hallaweb.jlab.org/podd>. Code
4970 repository <https://github.com/JeffersonLab/analyzer>
- 4971 [254] <https://github.com/sPHENIX-Collaboration/coresoftware>
- 4972 [255] <https://cdcvcs.fnal.gov/redmine/issues/15372>
- 4973 [256] M. Al-Turany *et al.*, J. Phys. Conf. Ser. **664**, 072001 (2015).
- 4974 [257] Fluka, <http://www.fluka.org>
- 4975 [258] Geant4, <http://geant4.cern.ch/>
- 4976 [259] GEMC, <https://gemc.jlab.org/>
- 4977 [260] Poisson superfish, [http://laacg1.lanl.gov/laacg/services/download_](http://laacg1.lanl.gov/laacg/services/download_sf.phtml)
4978 [sf.phtml](http://laacg1.lanl.gov/laacg/services/download_sf.phtml)
- 4979 [261] Tosca, [http://www.chilton-computing.org.uk/inf/eng/](http://www.chilton-computing.org.uk/inf/eng/electromagnetics/p001.htm)
4980 [electromagnetics/p001.htm](http://www.chilton-computing.org.uk/inf/eng/electromagnetics/p001.htm)
- 4981 [262] C. Altunbas *et al.*, Nucl. Inst. Meth. A **490**, 177 (2002).
- 4982 [263] J. Huston, H.L. Lai, P. Nadolsky, W.K. Tung, J. Pumplin, and D.R. Stump, JHEP 07 (2002)
4983 012.
- 4984 [264] David E. Wiser, and Pions at SLAC Energies,” PhD thesis, Wisconsin University Madison,
4985 1977, <http://wwwlib.umi.com/dissertations/fullcit?p7719743>
- 4986 [265] S. Riordan, X. Zheng, Z. W. Zhao and N. Ton, unpublished (2014).
- 4987 [266] R. Beminiwattha, [https://hallaweb.jlab.org/DocDB/0002/000212/001/](https://hallaweb.jlab.org/DocDB/0002/000212/001/HallD_Gen_Summary.pdf)
4988 [HallD_Gen_Summary.pdf](https://hallaweb.jlab.org/DocDB/0002/000212/001/HallD_Gen_Summary.pdf)
- 4989 [267] Mark Ito, private communication (2014).
- 4990 [268] Eugene Chudakov, private communication (2014).
- 4991 [269] V. M. Budnev, I. F. Ginzburg, G. V. Meledin and V. G. Serbo, Phys. Rep. **15**, 181 (1975).
- 4992 [270] J. Beringer *et al.* (Particle Data Group), Phys. Rev. D **86**, 010001 (2012).
- 4993 [271] Yung-Su Tsai, Rev. Mod. Phys. **46**, 815 (1974).
- 4994 [272] R. E. Kalman, Transactions of ASME Journ. Basic Engineering **82**, 35 (1960).
- 4995 [273] R. Mankel, Rept. Prog. Phys. **67**, 553 (2004).

- 4996 [274] M. Capogni, E. Cisbani, G.M. Urciuli, *Note on GEM digitization modeling*, http://www.iss.infn.it/cisbani/atmp/sbs/ft/gemc/diginote_0.2.pdf.
4997
- 4998 [275] H. Avakian *et al.* Nucl. Instrum. Meth. A **417**, 69 (1998).
- 4999 [276] A. Bacchetta, M. Diehl, K. Goeke, A. Metz, P. J. Mulders, and M. Schlegel, JHEP **0702**, 093
5000 (2007).
- 5001 [277] S. Dulat *et al.*, Phys. Rev. D **93**, 033006 (2016).
- 5002 [278] D. de Florian, R. Sassot and M. Stratmann, Phys. Rev. D **75**, 114010 (2007).
- 5003 [279] M. Anselmino, M. Boglione, U. D’Alesio, A. Kotzinian, F. Murgia and A. Prokudin, Phys.
5004 Rev. D **71**, 074006 (2005).
- 5005 [280] M. Anselmino, M. Boglione, U. D’Alesio, A. Kotzinian, S. Melis, F. Murgia, A. Prokudin
5006 and C. Turk, Eur. Phys. J. A **39**, 89 (2009).
- 5007 [281] M. Anselmino, M. Boglione, U. D’Alesio, S. Melis, F. Murgia and A. Prokudin, Phys. Rev.
5008 D **87**, 094019 (2013).
- 5009 [282] C. Lefky and A. Prokudin, Phys. Rev. D **91**, 034010 (2015).
- 5010 [283] L. P. Kaptari, A. Del Dotto, E. Pace, G. Salmè and S. Scopetta, Phys. Rev. C **89**, 035206
5011 (2014).
- 5012 [284] A. Del Dotto, private communication
- 5013 [285] I. Akushevich, N. Shumeiko and A. Soroko, Eur. Phys. J. C **10**, 681 (1999).
- 5014 [286] I. Akushevich, A. Ilyichev and M. Osipenko, Phys. Lett. B **672**, 35 (2009).
- 5015 [287] J. Pumplin, D. R. Stump, J. Huston, H. L. Lai, P. M. Nadolsky and W. K. Tung, JHEP **0207**,
5016 012 (2002).
- 5017 [288] “SoLID Preliminary Conceptual Design Report”, The SoLID Collaboration, unpublished
5018 (2014).
- 5019 [289] A. Narayan *et al.*, Phys. Rev. X **6**, no. 1, 011013 (2016).
- 5020 [290] H. Spiesberger, Phys. Rev. D **52**, 4936 (1995).
- 5021 [291] M. E. Christy and P. E. Bosted, Phys. Rev. C **81**, 055213 (2010).
- 5022 [292] E12-10-006, “Target Single Spin Asymmetry in Semi-Inclusive Deep-Inelastic ($e, e'\pi^\pm$) on
5023 a Transversely Polarized ^3He Target at 8.8 and 11 GeV”, Spokesperson: J.-P. Chen, H. Gao (con-
5024 tact), X. Jiang, J.-C. Peng, and X. Qian.
- 5025 [293] E12-11-007, “Asymmetries in Semi-Inclusive Deep-Inelastic ($e, e'\pi^\pm$) Reactions on a Longi-
5026 tudinally Polarized ^3He Target at 8.8 and 11 GeV”, Spokesperson: J.-P. Chen, J. Huang (contact),
5027 Y. Qiang, and W.-B. Yan.
- 5028 [294] E12-11-108 “Target Single Spin Asymmetry in Semi-Inclusive Deep-Inelastic ($e, e'\pi^\pm$) on a
5029 Transversely Polarized Proton Target”, Spokespersons: K. Allada, J.-P. Chen, H. Gao (contact),
5030 Z.-E. Meziani, and X.-M. Li.

- 5031 [295] S. Martoiu, H. Muller and J. Toledo, Conference Proceedings: 2011 IEEE Nuclear Science
5032 Symposium Conference Record, 2036 (2011).
- 5033 [296] M.J. French *et al.*, Nucl. Instr. and Meth. **A 466** 359 (2001).
- 5034 [297] A. Neiser *et al.*, Journal of Instrumentation **8**, C12043 (2013).
- 5035 [298] E12-12-006, “Near-threshold Electroproduction of J/ψ with a 11 GeV Beam”, Spokesper-
5036 sons: K. Hafidi, Z.-E. Meziani (contact), X. Qian, N. Sparveris, and Z.-W. Zhao.
- 5037 [299] *The FLUKA code: Description and benchmarking* G. Battistoni, S. Muraro, P.R. Sala, F.
5038 Cerutti, A. Ferrari, S. Roesler, A. Fassio, J. Ranft, Proceedings of the Hadronic Shower Simu-
5039 lation Workshop 2006, Fermilab 6–8 September 2006, M. Albrow, R. Raja eds., AIP Conference
5040 Proceeding 896, 31-49, (2007)
- 5041 [300] *FLUKA: a multi-particle transport code* A. Ferrari, P.R. Sala, A. Fassio, and J. Ranft, CERN-
5042 2005-10 (2005), INFN/TC_05/11, SLAC-R-773
- 5043 [301] *Photodisintegration of deuterium and big bang nucleosynthesis* K.Y.Hare and others, *Phys.*
5044 *Rev. D* **68**, 072001 (2003)
- 5045 [302] *Displacement damage in silicon, on-line compilation* A. Vasilescu and G. Lindstroem
5046 available at [http://hepweb03.phys.sinica.edu.tw/opto/Irradiation/](http://hepweb03.phys.sinica.edu.tw/opto/Irradiation/Documents/NIEL_scaling/gunnar.htm)
5047 [Documents/NIEL_scaling/gunnar.htm](http://hepweb03.phys.sinica.edu.tw/opto/Irradiation/Documents/NIEL_scaling/gunnar.htm)
- 5048 [303] [https://solid.jlab.org/DocDB/0000/000025/001/zana_solid_radiation_](https://solid.jlab.org/DocDB/0000/000025/001/zana_solid_radiation_and_activation_mar_2017.pdf)
5049 [and_activation_mar_2017.pdf](https://solid.jlab.org/DocDB/0000/000025/001/zana_solid_radiation_and_activation_mar_2017.pdf)
- 5050 [304] K. Abe *et al.* [SLD Collaboration], *Phys. Rev. Lett.* **84**, 5945 (2000) [arXiv:hep-ex/0004026].
- 5051 [305] N. Falletto *et al.*, “Compton scattering off polarized electrons with a high finesse Fabry-Perot
5052 cavity at JLab,”, “*Nucl. Instrum. Meth.*”, A459, 212-425, 2001.
- 5053 [306] A. Narayan, D. Dutta, V. Tvaskis and J. W. Martin, *Nuovo Cim. C* **035N04**, 134 (2012).
- 5054 [307] N. Vansteenkise, P. Vignolo, and A. Aspect, “Optical Reversibility Theorems for Polariza-
5055 tion: Application to Remote Control of Polarization”, *J. Opt. Soc. Am. A*, Vol. 10, No. 10, (1993)
5056 2240.
- 5057 [308] R.J. Loewen, “A compact light source: Design and technical feasibility study of a laser-
5058 electron storage ring X-ray source,” SLAC-R-0632 (2003).
- 5059 [309] S. Miyoshi *et al.*, Photon generation by laser-Compton scattering at the KEK-ATF, NIM
5060 A623 (2010) 576.
- 5061 [310] A. Variola *et al.*, The LAL Compton Program,, NIM A608 (2009) S83.
- 5062 [311] V. Brisson *et al.*, High finesse Fabry-Perot cavities in the picosecond regime, NIM A608
5063 (2009) S75.
- 5064 [312] A. Denner and S. Dittmaier, “Complete o() QED cor-
5065 rections to polarized Compton scatter-
ing”, *Nucl. Phys. B* **540** 58 (1999).
- 5066 [313] M. Friend *et al.*, “Upgraded photon calorimeter with integrating readout for Hall A Compton
5067 Polarimeter at Jefferson Lab”, [arXiv:1108.3116 [physics.ins-det]].

- 5068 [314] G. W. Ford and C. J. Mullin, “Scattering of Polarized Dirac Particles on Electrons,” Phys.
5069 Rev. **108**, 477 (1957); Erratum, Phys. Rev. **110**, 1485(E) (1958).
- 5070 [315] A. M. Bincer, “Scattering of Longitudinally Polarized Fermions,” Phys. Rev. **107**, 1434
5071 (1957).
- 5072 [316] P. Stehle, “Calculation of Electron-Electron Scattering,” Phys. Rev. **110**, 1458 (1958).
- 5073 [317] A. Raçzka and R. Raçzka, “Møller Scattering of Arbitrarily Polarized Electrons,” Erratum,
5074 Phys. Rev. **110**, 1469 (1958).
- 5075 [318] G. Alexander and I. Cohen, “Møller scattering polarimetry for high-energy e^+e^- linear col-
5076 liders,” Nucl. Instrum. Meth. A **486**, 552 (2002) [hep-ex/0006007]. This paper contains the basic
5077 formulas for Møller polarimetry, as well as references to calculations of higher order QED cor-
5078 rections.
- 5079 [319] M. Hauger *et al.*, “A high-precision polarimeter,” *Nucl. Instrum. Meth.*, vol. A462, pp. 382–
5080 392, 2001, nucl-ex/9910013.
- 5081 [320] Matthias Loppacher, “Møller Polarimetry for CEBAF Hall C”, Inaugural Dissertation, Uni-
5082 versität Basel (1996).
- 5083 [321] L. V. de Bever, J. Jourdan, M. Loppacher, S. Robinson, I. Sick, J. Zhao, “A Target for Precise
5084 Møller Polarimetry”, Nucl. Instrum. Meth. A **400**, 379 (1997).
- 5085 [322] A. V. Glamazdin, V. G. Gorbenko, L. G. Levchuk, R. I. Pomatsalyuk, A. L. Rubashkin,
5086 P. V. Sorokin, D. S. Dale and B. Doyle *et al.*, “Electron beam Møller polarimeter at JLab Hall
5087 A,” *Fizika B* **8**, 91 (1999) [hep-ex/9912063].
- 5088 [323] E. A. Chudakov, A. V. Glamazdin, V. G. Gorbenko, L. G. Levchuk, R. I. Pomatsalyuk,
5089 P. V. Sorokin, “Electron beam Møller polarimeter at Hall A, JLab”, *Prob.Atom.Sci.Tech.* **40**,
5090 43 (2002)
- 5091 [324] E. Chudakov and V. Luppov, “Møller polarimetry with atomic hydrogen targets,” *IEEE Trans.*
5092 *Nucl. Sci.*, vol. 51, pp. 1533–1540, 2004.
- 5093 [325] E. Chudakov and V. Luppov, “Moeller polarimetry with atomic hydrogen targets,” *Eur. Phys.*
5094 *J.*, vol. A24S2, pp. 123–126, 2005.
- 5095 [326] P. S. Cooper, M. J. Alguard, R. D. Ehrlich, V. W. Hughes, H. Kobayakawa, J. S. Ladish,
5096 M. S. Lubell and N. Sasao *et al.*, “Polarized electron Electron Scattering at GeV Energies,” Phys.
5097 Rev. Lett. **34**, 1589 (1975).
- 5098 [327] B. Wagner, H. G. Andresen, K. H. Steffens, W. Hartmann, W. Heil and E. Reichert, “A Møller
5099 polarimeter for CW and pulsed intermediate-energy electron beams,” Nucl. Instrum. Meth. A
5100 **294**, 541 (1990).
- 5101 [328] J. Arrington, E. J. Beise, B. W. Filippone, T. G. O’Neill, W. R. Dodge, G. W. Dodson,
5102 K. A. Dow and J. D. Zumbro, “A Variable energy Møller polarimeter at the MIT Bates Linear
5103 Accelerator Center,” Nucl. Instrum. Meth. A **311**, 39 (1992).

- 5104 [329] K. B. Beard, R. Madey, W. M. Zhang, D. M. Manley, B. D. Anderson, A. R. Baldwin,
5105 J. M. Cameron and C. C. Chang *et al.*, “Measurement of the polarization of a pulsed elec-
5106 tron beam with a Møller polarimeter in the coincidence mode,” *Nucl. Instrum. Meth. A* **361**,
5107 46 (1995).
- 5108 [330] H. R. Band, G. Mitchell, R. Prepost and T. Wright, “A Møller polarimeter for high-energy
5109 electron beams,” *Nucl. Instrum. Meth. A* **400**, 24 (1997).
- 5110 [331] P. Steiner, A. Feltham, I. Sick, M. Zeier and B. Zihlmann, “A high-rate coincidence Moller
5111 polarimeter,” *Nucl. Instrum. Meth. A* **419**, 105 (1998).
- 5112 [332] G. G. Scott and H. W. Sturmer, “Magnetomechanical Ratios for Fe-Co Alloys,” *Phys. Rev.*
5113 **184**, 490 (1969).
- 5114 [333] J. Crangle and G. M. Goodman, “The Magnetization of Pure Iron and Nickel,” *Proceedings*
5115 *of the Royal Society of London, Series A*, **321**, 477 (1971).
- 5116 [334] C. D. Graham, Jr., “Iron and Nickel as Magnetization Standards,” *J. Appl. Phys.* **53**, 2032
5117 (1982).
- 5118 [335] G. G. Scott, “Review of gyromagnetic ratio experiments,” *Rev. Mod. Phys.*, vol. 34, pp. 102–
5119 109, Jan 1962.
- 5120 [336] E. C. Stoner and E. P. Wohlfarth, “A Mechanism of Magnetic Hysteresis in Heterogeneous
5121 Alloys,” *Phil. Trans. Royal Soc. London, Series A* **240**, 599 (1948).
- 5122 [337] L. G. Levchuk, “The Intraatomic motion of bound electrons as a possible source of a system-
5123 atic error in electron beam polarization measurements by means of a Møller polarimeter,” *Nucl.*
5124 *Instrum. Meth.*, vol. A345, pp. 496–499, 1994.
- 5125 [338] M. Swartz, H. R. Band, F. J. Decker, P. Emma, M. J. Fero, R. Frey, R. King and A. Lath *et*
5126 *al.*, “Observation of target electron momentum effects in single arm Møller polarimetry,” *Nucl.*
5127 *Instrum. Meth. A* **363**, 526 (1995) [hep-ex/9412006].
- 5128 [339] D. Gaskell, D. G. Meekins, and C. Yan, “New methods for precision Møller polarimetry,”
5129 *Eur. Phys. J.*, vol. A32, pp. 561–564, 2007.
- 5130 [340] E. Chudakov and V. Luppov, “Møller polarimetry with atomic hydrogen targets,” tech. rep.,
5131 JLab, 2005. http://www.jlab.org/~gen/hyd/loi_3.pdf.
- 5132 [341] I. F. Silvera, “Ultimate fate of a gas of atomic hydrogen in a liquid-helium chamber: Recom-
5133 bination and burial,” *Phys. Rev. B*, vol. 29, pp. 3899–3904, Apr 1984.
- 5134 [342] I. F. Silvera and J. T. M. Walraven, “Stabilization of atomic hydrogen at low temperature,”
5135 *Phys. Rev. Lett.*, vol. 44, pp. 164–168, Jan 1980.
- 5136 [343] I. F. Silvera and J. T. M. Walraven, “Spin polarized atomic hydrogen,” *Progress in Low*
5137 *Temperature Physics, vol. X*, pp. 139–370, 1986.
- 5138 [344] T. Roser *et al.*, “Microwave driven extraction of stabilized spin polarized atomic hydrogen,”
5139 *Nucl. Instrum. Meth.*, vol. A301, pp. 42–46, 1991.
- 5140 [345] M. Mertig, V. G. Luppov, T. Roser, and B. Vuaridel, “Continuous density measurement of
5141 atomic hydrogen by means of a bolometer,” *Rev. Sci. Instrum.*, vol. 62, pp. 251–252, 1991.

- 5142 [346] M. D. Miller and L. H. Nosanow, “Possible ”new” quantum systems. ii. properties of the
5143 isotopes of spin-aligned hydrogen,” *Phys. Rev. B*, vol. 15, pp. 4376–4385, May 1977.
- 5144 [347] M. Poelker, J. Grames, J. Hansknecht, R. Kazimi, J. Musson, *Phys. Rev. ST Accel. Beams*
5145 **10**, 053502 (2007).
- 5146 [348] [https://hallaweb.jlab.org/12GeV/SoLID/download/doc/Estimated_](https://hallaweb.jlab.org/12GeV/SoLID/download/doc/Estimated_SoLID_Offline_Effort.ods)
5147 [SoLID_Offline_Effort.ods](https://hallaweb.jlab.org/12GeV/SoLID/download/doc/Estimated_SoLID_Offline_Effort.ods)
- 5148 [349] [https://halldsvn.jlab.org/repos/trunk/docs/offline/](https://halldsvn.jlab.org/repos/trunk/docs/offline/ProjectProgress/OfflineComputingActivities2013.xlsx)
5149 [ProjectProgress/OfflineComputingActivities2013.xlsx](https://halldsvn.jlab.org/repos/trunk/docs/offline/ProjectProgress/OfflineComputingActivities2013.xlsx)
- 5150 [350] EventDisplay3D project in the *art* workbook, available from [https://cdcvs.](https://cdcvs.fnal.gov/redmine/projects/art-workbook)
5151 [fnal.gov/redmine/projects/art-workbook](https://cdcvs.fnal.gov/redmine/projects/art-workbook)

5152 **Appendix A Summary of Recommendations from the 2015 SoLID Di-**
5153 **rector’s Review and the Responses (Where Are They Ad-**
5154 **ressed in the Main Text)**

5155 The SoLID Director’s Review was held at JLab on 23-24 February 2015. The committee consisted
5156 of: Paul Brindza (JLab), Marcel Demarteau (ANL), Nancy Grossman (ANL), David Mack (JLab),
5157 Richard Majka (Yale), Naomi Makins (UIUC), Curtis Meyer (CMU)(chair), Ernest Sichtermann
5158 (LBL), William Wisniewski (SLAC) and Bolek Wyslouch (MIT). A summary of all recommenda-
5159 tions made by the committee is provided below, with each recommendation ordered by number to
5160 improve readability.

5161 **A.1 On the physics relevance and risks**

5162 **On the completeness and credibility of the discussion of the experimental reach, including**
5163 **statistical, systematic and theoretical uncertainties**

5164 *Recommendation 1:* End-to-end simulations with realistic subsystem responses and material bud-
5165 gets, and complete track finding and reconstruction should be developed.

5166 reply in Section 12

5167 *Recommendation 2:* Acceptances, efficiencies, and systematic uncertainties should be simulated for
5168 each of the core measurements.

5169 reply in Section 13

5170 *Recommendation 3:* For the PVDIS measurements, the viability of the elastic scattering calibration
5171 procedure, to determine absolute Q^2 should be demonstrated by simulations for similar scattering
5172 angles to those probed in DIS, and with realistic misalignments.

5173 reply in Section 13.3

5174 *Recommendation 4:* Bin migration effects should be simulated for the measurements of the sharply
5175 rising J/ψ production cross section near threshold.

5176 reply in Section 13.4

5177 **On the ability to handle the desired luminosities and backgrounds including impacts on both**
5178 **the apparatus and the beam line downstream of the target**

5179 *Recommendation 5:* The signal and background trigger rates should be simulated for the J/ψ mea-
5180 surements.

5181 reply in Section 14

5182 *Recommendation 6:* The dead-time(s) in the DAQ chain should be modeled.

5183 reply in Section 14

5184 *Recommendation 7:* The development of a simulation framework with realistic reconstruction and
5185 analysis should be pursued with high priority and increased resources.

5186 reply in Section 12

5187 **On the implications for the relevance of the physics results in the context of possibly competing**
5188 **experiments at both Jefferson Lab and internationally.**

5189 *Recommendation 8:* Better comparisons with the expected results on programs such as SBS and
5190 particularly CLAS12 are needed to clarify the need for the SoLID SIDIS program. Crisp demon-
5191 strations of the improvements possible with SoLID should be developed.

5192 reply in Section 2.2.6

5193 *Recommendation 9:* The SoLID Collaboration should investigate the possibility of kaon identifica-
5194 tion, especially given their high luminosity.

5195 reply in Section 2.5.2 and 11.7

5196 *Recommendation 10:* The SoLID collaboration should investigate the feasibility of carrying out a
5197 competitive GPD program. Such a program would seem particularly well suited to their open geom-
5198 etry and high luminosity. If SoLID's luminosity is sufficiently high to permit a program of precise
5199 Double Deeply Virtual Compton Scattering (DDVCS) measurements, it would make a groundbreak-
5200 ing contribution to GPD studies.

5201 reply in Section 2.5.1

5202 **A.2 On the viability of approach and the experimental technique**

5203 **On any R&D required to meet the technical challenges of the experiment**

5204 *Recommendation 11:* Develop an overall R&D plan for the project with a timeline.

5205 reply in Section 20

5206 *Recommendation 12:* Close interaction between the US and Chinese groups in the development of
5207 GEM foils to assure good quality control is highly recommended.

5208 reply in Section 7

5209 *Recommendation 13:* Investigate the schedule risk when GEM foils are not produced in a timely
5210 way and continue to pursue Tech-Etch as a potential supplier for the foils.

5211 reply in Section 7

5212 *Recommendation 14:* The calorimeter group is encouraged to contact other groups (ALICE, LHCb
5213 SiPMs and possibly CMS) to understand the detector design choices these groups have made and
5214 resources needed for construction.

5215 reply in Section 10

5216 *Recommendation 15:* The stability tests of the conductivity of the glass for the mRPCs should be
5217 extended for a much longer period and the risk associated with the R&D needs to be identified.

5218 reply in Section 11

5219 *Recommendation 16:* The collaboration is strongly encouraged to develop an end-to-end realistic
5220 simulation and reconstruction to further optimize cost and physics reach and derive clear perfor-
5221 mance requirements for the individual subdetectors.

5222 reply in Section 12

5223 *Recommendation 17:* The collaboration is encouraged to explore the power of extended kaon iden-
5224 tification (through Cherenkov or TOF).

5225 reply in Section 2.5.2 and 11.7

5226 **On the proposed magnet concept and choice, including magnet configuration modifications (if 5227 any), magnet cool-down and infrastructure requirements**

5228 *Recommendation 18:* The Committee strongly recommends testing the CLEO magnet coils (cold
5229 test), power supply and controls, before installation in Hall A.

5230 reply in Section 4

5231 *Recommendation 19:* A new magnet power supply should be included in the total cost of SoLID.

5232 reply in Section 4

5233 *Recommendation 20:* Evaluate the schedule impact of mapping the magnetic field in situ in Hall A.

5234 reply in Section 4

5235 **On the proposed detector concept and associated electronics and data acquisition**

5236 *Recommendation 21:* The plans for the High Level Trigger and the needs for slow control need to
5237 be worked out in detail and the implications for resources need to be evaluated.

5238 reply in Section 14 and 16

5239 *Recommendation 22:* The implications of the need for these resources in the context of availability
5240 of resources at the laboratory need to be understood.

5241 reply in Appendix C

5242 *Recommendation 23:* Closer communication with the other JLab experiments and the JLab com-
5243 puting center is strongly encouraged.

5244 reply in Section 12.1 and Appendix C

5245 *Recommendation 24:* Having a functional simulation and reconstruction routines as soon as possible
5246 should be a high priority in the software effort. Such software will pay off many times over in
5247 experimental design and avoiding pitfalls.

5248 reply in Section 12

5249 **On the beam line design, including collimation and shielding**

5250 *Recommendation 25:* Complete radiation calculations to determine activation and absorbed dose on
5251 components of concern and mitigate as appropriate.

5252 reply in Section 15

5253 *Recommendation 26:* It should be confirmed that the baffle design, including the support structure,
5254 is optimized for background rejection and signal acceptance. Furthermore the baffle design should
5255 minimize generation of secondary backgrounds.

5256 reply in Section 6

5257 **On the cryogenic and polarized target system concepts and integration**

5258 No recommendation was presented in the report.

5259 **On the beam polarimetry requirements.**

5260 No recommendation was presented in the report.

5261 **A.3 On the understanding, completeness, and credibility of the resources needed for** 5262 **the SoLID project.**

5263 **On the experience, expertise and quantity of the scientific and technical manpower for the** 5264 **project**

5265 *Recommendation 27:* Compare the resource levels you have assumed in some key areas (particularly
5266 in software, data acquisition and project management) to make sure the estimates align with other
5267 similar projects or there is a good reason they do not.

5268 reply in Section 14 and C

5269 *Recommendation 28:* Redo the cost estimate using an average cost per type of resource.

5270 *Recommendation 29:* Create a high level resource loaded schedule to get a more realistic schedule,
5271 funding and resource profile. This will also allow JLab to better determine their ability to support
5272 the FTE needs.

5273 *Recommendation 30:* Revisit the comments of the 2012 Internal Review Report in conjunction with
5274 the recommendations from this report.

5275 **On utilities (power, cabling, LCW, cryogenics) requirements for the project**

5276 *Recommendation 31:* A cost benefit analysis for any systems being reused should be carried out,
5277 including the magnet power supply.

5278 *Recommendation 32:* Appoint a small team to facilitate the integration planning for SoLID.

5279 **On requirements from Jefferson Lab on for instance engineering needs, electron beam, polar-**
5280 **ized source, and cryogenic target requirements**

5281 *Recommendation 33:* We strongly recommend tests at JLab of the CLEOII magnet coils (cold test),
5282 ideally with the new power supply and controls, before installation into the hall.

5283 *Recommendation 34:* An effort should be made to clearly specify resources required from JLab that
5284 are not explicitly in the project (effort, non-effort, equipment, building space, etc.).

5285 **On general experiment installation and alignment issues, including potential interaction with**
5286 **other Hall A programs and operations**

5287 *Recommendation 35:* The project should develop a preliminary resource loaded schedule for the
5288 installation and the corresponding space-management plan for the hall floor.

5289 *Recommendation 36:* The project should start planning the process of how to change from one
5290 SoLID configuration to another in order to better understand the time and effort involved and if
5291 there are any potential issues such as radiation levels.

5292 **Appendix B Summary of Subsystems**

5293 In responding to the recommendations from JLab physics division, we add this section, aiming to
5294 provide a brief description of the key assumptions for each subsystem, namely where the subsystem
5295 will be built, which groups will build it, where the fund comes from, how long it will take and what
5296 is needed from JLab to support it. Anything unique to the system which drives the project will also
5297 be listed.

5298 **B.1 Magnet**

5299 The solenoid magnet provides the magnetic field required for measuring the momentum of the track
5300 in the experiment. The detectors for SoLID will be mounted on the magnet yoke. The collaboration
5301 has identified the CLEO-II magnet as the one to be used for SoLID after modifications. The JLab
5302 Hall A engineering team, with assistance from JLab Engineering Division and also from the SoLID
5303 collaboration, is responsible for the transportation and modification of the magnet.

5304 The coils and cryostat of the magnet have arrived at JLab and the exterior steel is being shipped.
5305 The transportation (disassembling and shipping) the magnet from Cornell to JLab and initial refurb-
5306 ishing to verify the magnet is in good state for specific modifications for physics experiments is
5307 covered from the JLab Physics Division (operation fund). The cost for refurbishing and modifica-
5308 tions specific to SoLID is to be part of the SoLID MIE to DOE.

5309 The refurbishing and modification specific to SoLID will take 2.5 years. JLab will perform most
5310 of the work. Space will be needed at JLab for refurbishing, modification and storage. We will also
5311 need JLab support for the cryogenic and control systems.

5312 **B.2 GEM**

5313 • **Where the system will be built and who will build it:** It is assumed that the SoLID GEM
5314 tracker will be built in China by the five member institutions of the Chinese SoLID GEM
5315 collaboration: CIAE, LZU, THU,USTC and IMP. The GEM module development, design
5316 prototyping and benchmarking would be done in collaboration with the GEM detector groups
5317 at the University of Virginia (Liyanage) and Temple University (Sorrow). The GEM module
5318 and Electronics fabrication activities would be divided among the Chinese collaboration as
5319 follows:

5320 – USTC: The main institution for GEM module fabrication, readout electronics develop-
5321 ment and fabrication.

5322 – CIAE: GEM foil fabrication and GEM module fabrication.

5323 – LZU: GEM module fabrication

5324 – THU and IMP: GEM module fabrication and testing.

5325 • **Who will fund it ?**

5326 The funding for the SoLID GEM tracker will be sought from the Chinese funding agencies.
5327 Only the pre R&D funds and R&D funds (of the order of \$ 400 k) for the activities conducted
5328 at the University of Virginia and Temple University will be requested from the US DoE.

5329 • **How long will it take ?**

5330 The pre-R&D phase of the project would take at least 2 years. This would be especially true
5331 if the GEM foils fabricated in China are to be used for the project as assumed. A well focused

5332 and intense pre-R&D program in China is required to ensure that the manufacturing capabil-
5333 ities and capacities for full size GEM foils, and that GEM module assembly facilities setup
5334 and several full size prototype module constructed and tested at each of the five institutions.

5335 After the successful conclusion of the pre-R&D program, it would take at least two more
5336 years for the R&D, construction, testing, installation and the commissioning phase.

5337 • **what is needed from JLab to support it ?**

5338 Jlab engineering support will be needed for the design of the GEM module mounting struc-
5339 ture, and DAQ support will be needed to integrate the GEM readout into the hall A DAQ
5340 framework.

5341 **B.3 Light Gas Čerenkov**

5342 The light gas Čerenkov prototyping and construction will be done by the Temple University Nuclear
5343 Physics Group. All of the construction will be done at Temple, with the possible exception of
5344 any specific materials needed to adapt and integrate the subsystem into the larger SoLID detector.
5345 Funds for the project will be requested by the group from DOE and/or NSF. The light gas Čerenkov
5346 detector will also be designed at Temple University with the expectation that communication with
5347 the SoLID project engineers at Jefferson Lab, as well as access to schematics and documentation,
5348 will be made available concerning interfacing the sub-detector design with the larger SoLID design.

5349 **B.4 Heavy Gas Čerenkov**

5350 The Heavy Gas Cherenkov (HGC) will provide the required particle identification of pions in a
5351 background of kaons and protons. It will be built by Prof. Haiyan Gao's Medium Energy Physics
5352 group from Duke University with engineering and technical help from the Triangle Universities
5353 Nuclear Laboratory (TUNL), and by Prof. Garth Huber's group from the University of Regina in
5354 Canada.

5355 **B.5 Electromagnetic Calorimeter and Scintillator-Pad Detector**

5356 The Electromagnetic Calorimeter (EC), in combination with other detectors, provides the main
5357 trigger and the particle identification for the SoLID experiments. The EC consists of a Preshower
5358 and a Shower portion. The technologies that we chose for the EC – WLS-fiber-embedded scintillator
5359 for the Preshower with MAPMT readout and the Shashlyk-type modules for the Shower with regular
5360 PMT readout – have both been used in experiments at the LHC. The main goal of the pre-R&D is
5361 thus to adopt such technology and to optimize the design configuration of the EC to meet the physics
5362 requirement of SoLID, and to determine the best construction institution/site.

5363 The Scintillator Pad Detector (SPD) is needed only by the SIDIS program of SoLID. It consists
5364 of a forward- (FA) and a large-angle (LA) parts. Both FASPD and LASPD will serve as a photon
5365 veto in order to reduce the photon background to a manageable level. Design of the FASPD is
5366 very similar to the Preshower detector of the EC, with WLS fibers embedded in thin scintillators.
5367 The LASPD will also provide time-of-flight information and a 150-ps timing resolution is required.
5368 The LASPD will thus consists of thick scintillators with direct readout by field-resistant fine-mesh
5369 PMTs inside the solenoid.

5370 The pre-R&D stage of EC and SPD will likely take up to two years. The lead institutions on
5371 the EC includes University of Virginia (UVa), and the Chinese Shandong University (SDU) and Ts-
5372 inghua University (THU). The SDU group has extensive experience with scintillator manufacturing

5373 in China, and have produced preshower modules with similar light yield as those produced by the
5374 Russian IHEP (the sole manufacturer of EC for nearly all LHC experiments). For Shashlyk mod-
5375 ules, both THU and SDU groups have already constructed prototypes and are currently working on
5376 improving their light yield. The pre-R&D will focus on increasing the light yield, conducting beam
5377 tests to determine their PID performance, and to design an effective mass-quantity construction
5378 method.

5379 The SPD will be manufactured by the US Eljen company and further constructed at UVa. Pro-
5380 totype modules have already been made and tested with cosmic rays and their light yield has been
5381 characterized. The pre-R&D goal will be to determine the light yield uniformity for the FASPD,
5382 and to determine the timing resolution of the LASPD under SoLID-like running conditions.

5383 **B.6 MRPC**

5384 The Multi Gap Resistive Plate Chamber (MRPC) will be used by the SIDIS experiment for parti-
5385 cle identification by means of time of flight. A MRPC can achieve a timing resolution of 50 ps.
5386 Under more realistic conditions with large background rates, timing resolution of 80 ps has been
5387 demonstrated.

- 5388 • Who will build it :
5389 Tsinghua University
- 5390 • Where the system will be built:
5391 In Tsinghua University, Beijing
- 5392 • Rutgers university will take care of the readout electronics.
- 5393 • Who will fund it :
5394 NSFC (China) for the detector; the front en electronics will be funded by the DOE, and also
5395 the NSF through Rutgers University.
- 5396 • How long will it take :
5397 Two and half years
- 5398 • What is needed from JLab to support it:
5399 Beam tests will be needed at Jlab including electronics and DAQ system in order to test the
5400 detector and optimize it under realistic beam conditions. Since it is planned to include the
5401 MRPC in the trigger to reduce the background, a special board from JLAB will be required
5402 to send the logic signals to the L1 trigger.
- 5403 • Anything unique to that system that's a project driver : This is the first high rate TOF system
5404 in hadron physics experiments and is need for the particle identification.

5405 **B.7 DAQ**

5406 The SoLID experiment is a large acceptance detector designed to run at high luminosities. The
5407 trigger rates expected for PVDIS are of the order of 600 KHz and for SIDIS up to 100 KHz. This
5408 pipelined electronics is crucial to generate a selective trigger in the very large background present
5409 in the detector.

- 5410 • Where the system will be built and who will build :
5411 Two universities are collaborating on the SoLID DAQ :

- 5412 – The Rutgers University with the group of Pr. Ronald Gilman group will be in charge of
5413 the high resolution timing measurement aspects of the development and production for
5414 the electronics.
- 5415 – The University of Massassuchets group led by Prof. Rory Miskimen will help in the
5416 testing of the Flash ADCs similar to what was done for Hall D.
- 5417 ● Who will fund it ?
5418 The electronics will be funded by the DOE request.
- 5419 ● How long it will take
5420 The project will take 2 years of preRD, 4 years of R%D, production and testing, and installa-
5421 tion.
- 5422 ● What is needed from JLAB to support it
5423 Since SoLID will be using the Jefferson Laboratory Pipelined Electronics, the JLAB Fast
5424 electronics group will be largely involved in the development, tests and deployment of the
5425 electronics. An estimate of the electronics and DAQ group is summarized in the table in
5426 addition of the JLab physics staff person.

5427 Appendix C Software Development Effort Estimate

5428 A preliminary assessment of the effort required to carry out all SoLID offline computing-related
5429 tasks, assuming adoption of the *art* framework [250] as an example, yields approximately 586 FTE-
5430 weeks. With contingency and overhead, explained below, this number increases to a total of 976
5431 FTE-weeks, or about 22 FTE-years, assuming 44 work weeks per year per developer. A spreadsheet
5432 with this calculation can be found online [348].

5433 This estimate covers simulations, reconstruction, calibrations and alignment, data challenges,
5434 production and analysis, where “analysis” represents a baseline set of replay configurations (PVDIS,
5435 SIDIS-³He, SIDIS-*p*, *J/ψ*), data quality checks, plots, production output variables, corrections,
5436 cuts and histograms. Not included in the estimate are DAQ software (firmware, front-end and
5437 trigger programming, run control etc.), online analysis and monitoring, and the intellectual effort to
5438 understand and interpret the results of the simulations and experimental data analysis. The latter is
5439 excluded because it is largely an open-ended creative process.

5440 For each covered area, we have counted the work required to develop the actual software, test
5441 the code and validate results, coordinate efforts (meetings, wikis and similar), write and generate
5442 user and developer-level documentation, and to configure and monitor offline computing operations
5443 (simulation and production passes, data challenges). The time estimates at this point are subjective
5444 best guesses, based on our experience with similar efforts. They assume expert developers who are
5445 fully familiar with all task requirements, programming languages, framework paradigms, library
5446 APIs, tools etc. This yields a sum of 586 FTE-weeks. A contingency of 25% is added to this total
5447 to account for missed tasks, time overruns, etc. Furthermore, since developers are never the ideal
5448 experts assumed above, we estimated an average “developer efficiency” of 75%, *i.e.* on average
5449 each developer is assumed to spend an extra 1/3 of the estimated task time on preparations such as
5450 collecting requirements and learning. A more precise estimate of this efficiency factor would have
5451 to be made on a task-by-task basis under consideration of the personnel assigned to the task, infor-
5452 mation which is incomplete at this time. With contingency and overhead, the total effort estimate is
5453 976 FTE-weeks.

5454 In comparison to a similar project, GlueX have estimated their offline computing effort at 1866
5455 FTE-weeks [349]. (This number excludes 110 FTE-weeks that GlueX allocate for “online” tasks
5456 (beamline commissioning and monitoring), which is outside of our scope.) It is unclear if the GlueX
5457 numbers include developer overhead, *i.e.* the time spent on task preparations and learning discussed
5458 above, but given the generous allowances made generally, we assume that they do.

5459 The offline computing manpower requirements estimated by GlueX and SoLID are summarized
5460 in Table 35. To make the GlueX estimates comparable to ours, we combined certain line items of
5461 the GlueX offline computing effort document [349] as follows:

- 5462 • The quoted “Simulation” effort includes “Geant3 simulation”, “Geant4 simulation” plus 1/4
5463 of “Integration/QC” and “Coordination” (total of 16.5 FTE-weeks) from the Miscellaneous
5464 section.
- 5465 • “Reconstruction” counts all of “Reconstruction” plus “DAQ Translation”, “Event Viewer”,
5466 “Documentation”, “Integration of Slow Controls”, 1/2 of “Recon/analysis code Q/A” and
5467 again 16.5 FTE-weeks for integration and coordination.
- 5468 • “Calibration” is taken as the total of “Calibrations” plus 1/4 of “Integration/QC” (11 FTE-
5469 weeks).
- 5470 • “Production” comprises “DST Generation”, “MC Studies for Detector Optimization” and
5471 again 11 FTE-weeks of “Integration/QC”.

- 5472 • “Analysis” takes all of “Analysis” less 1/2 of “Recon/analysis code Q/A” already counted
5473 under “Reconstruction” plus 1/2 of “Coordination”.
- 5474 • The “Data Challenges” estimate is taken as is.

5475 These allocations make the top-level categories approximately comparable.

Task Group	Labor estimate (FTE-weeks)		Main reasons for difference (see text)
	GlueX [349]	SoLID [348]	
Simulation	192	240	Simulation to be integrated into framework.
Reconstruction	787	355	Adoption of existing framework. Re-use of algorithms. Smaller number of subsystems.
Calibration	275	103	Smaller number of subsystems.
Production	275	155	Standard data format. Re-use of workflow tools.
Analysis	275	100	No PWA analysis and no grid implementation of analysis.
Data Challenges	62	23	No PWA data challenge.
Totals	1866	976	

Table 35: Offline computing manpower requirements estimated by SoLID and GlueX

5476 SoLID estimates a larger simulation effort than GlueX, possibly because GlueX make approxi-
5477 mate estimates of time already spent on finished work, while SoLID is using a detailed breakdown
5478 of anticipated future tasks. Also, SoLID plans to integrate simulations into the overall software
5479 framework, while GlueX’s simulations are standalone.

5480 The estimated SoLID effort for reconstruction is significantly lower than GlueX’s. The differ-
5481 ence is to a great extent due to the fact that SoLID proposes to adopt an existing framework rather
5482 than write a new one and that SoLID anticipates to reuse well-tested existing algorithms for stan-
5483 dard tasks such as track fitting, *e.g.* from the `genfit` library, and calorimeter cluster reconstruc-
5484 tion. Documentation effort is reduced in SoLID’s case also due to the already very good user-level
5485 documentation of the proposed *art* framework. Furthermore, the difference can be attributed to
5486 the smaller number of detector subsystems in SoLID than in GlueX, 5 vs. 7, the lower complexity
5487 of these systems (one vs. two tracker systems, Cherenkovs vs. multiple calorimeter systems), and
5488 the more challenging multi-particle final state reconstruction and PID in GlueX. Lastly, a SoLID
5489 event viewer can be readily assembled from an existing MC geometry with minimal effort (days vs.
5490 months) using ROOT’s `TEve` framework within *art*, as demonstrated by *art* example code [350].

5491 Calibration effort for SoLID is also estimated lower than in GlueX, again in part due to fewer
5492 main detector systems, smaller channel counts and easier calibration of SoLID’s GEMs vs. GlueX’s
5493 drift chambers.

5494 The lower estimated time for Production (DST generation) is attributable to the fact that we do
5495 not anticipate spending time on developing and maintaining a custom file format (it is defined by
5496 *art*) and expect to be able to reuse the job control and workflow tools currently under development
5497 for GlueX and CLAS12.

5498 Finally, SoLID estimates much lower analysis effort than GlueX because no kinematic fitting
5499 and PWA analysis is foreseen for SoLID nor is SoLID planning a grid implementation at this point
5500 as the JLab compute farm resources are expected to be sufficient for us. For similar reasons, our
5501 estimate for data challenges is lower.